Evaluation of self-focusing image formation for the development of an unconventional near eye display for augmented reality applications

Vladimir Krotov

Année 2022

UNIVERSITÉ DE HAUTE-ALSACE

UNIVERSITÉ DE STRASBOURG

THESE

Pour l'obtention du grade de

DOCTEUR DE L'UNIVERSITÉ DE HAUTE-ALSACE

ECOLE DOCTORALE: Mathématiques, Sciences de l'Information et de l'Ingénieur (ED 269)

Discipline: Electronique, Optronique et Systèmes

Présentée et soutenue publiquement

par

Vladimir KROTOV

Le 08 décembre 2022

ETUDE DE LA FORMATION D'IMAGE PAR AUTO-FOCALISATION POUR LE DEVELOPPEMENT D'UN DISPOSITIF VISUEL NON CONVENTIONNEL DE LA REALITE AUGMENTEE

Sous la direction de Prof. Olivier HAEBERLE et encadrement de Dr. Christophe MARTINEZ

Jury:

Pr.	Olivier HAEBERLE	Université de Haute-Alsace	(Directeur de thèse)
Dr.	Christophe MARTINEZ	CEA-LETI	(Encadrant de thèse)
Pr.	Eric LACOT	Université Grenoble Alpes	(Rapporteur)
Pr.	Huges GIOVANNINI	Aix-Marseille Université	(Rapporteur)
Dr.	Elise GHIBAUDO	Grenoble INP	(Examinatrice)
Dr.	Kristina IRSCH	Institut de la Vision	(Examinatrice)

The worthwhile problems are the ones you can really solve or help solve, the ones you can really contribute something to. ... No problem is too small or too trivial if we can really do something about it.

Richard Feynman

Acknowledgements

Most cordially I want to thank my Ph.D. supervisors: Dr. Christophe Martinez and Pr. Olivier Haeberlé for their unprecedented support during my research and especially writing period. Without them, it would be impossible to write down this thesis. I'm thankful to them for giving to me the second chance to finalize the work that was started seven years ago. I want to thank them for their trust. It was a long journey from the first interview up to the last pages of the manuscript. I really appreciate the goodwill of both of them and their time.

I'm tremendously grateful to Christophe for his patience during the long hours of manuscript editing and discussion. Working by his side during my Ph.D. studies, I grasped the spirit of science or I hope to have done so. He instilled in me some habits of rigorous research that I try to apply. Thank you for all you have done for me, it was more than anyone deserves.

I'm especially grateful to Olivier for his kind attitude during the whole long period of being a UHA's Ph.D.-student: from the first enrolment up to the exceptional extension. Thank you for your continuous support during all this time, I remember the moments of sharing scientific and life knowledge during my visits to Mulhouse or his to Grenoble.

My special thanks to the colleagues of our laboratory: Benoit Racine, Florence Rigal, Frederic Sermet, Myriam Tournaire, Bernard Aventurier, Vanessa Gorge, Yann Lee, Marion Provost, Stéphane Getin, Sylvie Joly, Anis Daami, François Templier, Tony Maindron, François Olivier, Pierre Joly, Baptiste Caron, Nicolas Delpuech, Clément Abélard, Basile Meynard and many others. Especially, Stéphanie Le Calvez – the head of the lab. I warmly remember the days in the CEA due to the warm welcome and friendly atmosphere. I would also like to thank the members of the jury for reading this manuscript.

I want to mention two Ph.D.-students and my friends that were there: Elias and Philip and thank them for their support, encouragement, advice, and long-long conversations on the CEA-site during lunches and dinners at the canteens and in the city. I'm looking forward to seeing you again in Grenoble: it was a very good time and I keep warm memories of you.

I want to thank my wife Maria for her love and wisdom, endless patience and her support during the long process of writing. We met during our Ph.D.-studies, she started later and finished earlier than me. She helped me to find the strength to finish this work. I would have dedicated it to her if she had agreed, but she is a humble person. The dedication would have been: "пожив несколько лет с умною и сметливою женою, сделался вполовину меньше прежнего прост".

I want to thank my parents for the opportunity to study abroad: my mother for English classes enrolment and the choice of the university, and my father for the love of the French language and culture nurtured by French classic movies. I remember how ten years ago my parents showed me France and it strongly influenced my choice of country.

I would also like to thank the members of the jury for reading this manuscript.

Finally, I would like to acknowledge the CEA-LETI for the funding of the PhD program and for the possibility to work.

List of abbreviations

AR: Augmented Reality

CGH: Computer-Generated Hologram

CMOS: Complementary metal-oxide semiconductor

cpd: Cycles per Degree

DMD: Digital Micromirror Display

DOE: diffractive optical element

EB: Eye Box

EP: emissive point

EPD: Emissive point distribution

EUC: Emissive Unit Cell

FOV: Field of View

FWHM: Full Width at Half Maximum

HMD: Head/Helmet Mounted Display

HOE: Holographic Optical element

HVS: Human Visual System

HWHM: Half Width at Half Maximum

LCD: Liquid crystal display

LED: Light-emitting diode

MEMS: Micro-electro-mechanical systems

MPE: Maximum Permissible Exposure

MR: Mixed Reality

NED: Near eye display

NHZ: Nominal Hazard Zone

PSF: Point Spread Function

SLM: spatial light modulator

SNR: signal to noise ration

VAC: Vergence–accommodation conflict

VR: Virtual Reality

Table of Contents

Introduction

Visual perception is highly important and may be considered crucial for human beings [1]. It has the dominant role among our senses, which reflects the fact that our behaviours are highly visual-oriented [2]. However, our world is oversaturated with all types of visual data: every minute[1] people share hundreds of thousands of photos and videos on various social networks, send dozens of millions of messages via all types of messengers. This pushes us up to the limit of human perception capability: our brain evolved in circumstances tremendously different from those we live in now [3]. Somehow, it reminds the red Queen's race: "it takes all the running you can do, to keep in the same place and if you want to get somewhere else, you must run at least as fast as that!"[2]

One way to overcome the obstacle is to let algorithms of artificial intelligence like machine and deep learning to process these big data and provide to us digests and recommendations [4]. It could be based on the data coming from the Internet of things (IoT): all our smart devices – watches, phones, eyewear, even cars and houses – will be connected and exchanging data over the internet. At the same time, one will need a device to perceive the upcoming information visually and aurally for decision-making. Immersive technologies like augmented, virtual and mixed reality is a perfect way to deliver the information: its high efficiency in various domains of human activity like education, medicine, engineering, etc. has already been proven [5]–[14].

One of the embodiments of immersive technologies is a near-to-eye optical system, which displays information (**Figure A**). It could be a **H**ead/**H**elmet **M**ounted **D**isplay (**HMD**) or

[1] Reference: Here's What Happens Every Minute on the Internet in 2020 (visualcapitalist.com)

[2] Reference: Carroll, L., & Tenniel, J. (1899). *Through the looking-glass and what Alice found there*. London: Macmillan and Co., Limited.

smart glasses/eyewear.

Figure A. Artistic-view of Augmented Reality smart-eyewear: Information displayed over real screen.

Such **N**ear-**E**ye **D**isplays (**NED**s) smoothly comes into our daily life, transnational giants like Microsoft, Google, Facebook, Apple, Sony, etc. (the list could be long enough) commercialize their solutions or actively research and develop (R&D) them [15]. These devices are far from consumers expectations nourished by futuristic images from science-fiction books and movies. The design process of ergonomic (both aesthetic and high-performing) devices requires R&D-teams to compromise between numerous design parameters and properties[3]. Most of the parameters and properties are interrelated and there is always a trade-off between high performance and aesthetic user-expectations. This complex dilemma challenges R&D groups from all over the world to improve existing systems, or propose new breakthrough designs.

Several years ago, CEA-LETI proposed an unconventional concept of near-eye lensless retinal projection display [16]. It is based on a self-focusing effect that doesn't require any optics but only an observer's eye. In this thesis we provide the necessary background for understanding design considerations of such unconventional holographic retinal projection display, describing Augmented Reality state of the art and **H**uman **V**isual **S**ystem (**HVS**). Then we explain the concept in detail and present a theoretical overview of the self-focusing effect – the core of the concept. Our theoretical description is evaluated via simulations and validated experimentally for both the

[3] Reference: https://www.linkedin.com/pulse/why-making-good-ar-displays-so-hard-daniel-wagner

self-focusing effect and unconventional image formation. We introduce a possible approach of self-focusing image formation performance evaluation and discuss its main limitations and drawbacks.

The thesis consists of 4 chapters and a conclusion.

Chapter I provides the necessary context, research goals, challenges and contributions. Present state-of-the-art for Near Eye Display domain is depicted along with Human Visual Systems and let us present main issues related with NEDs.

Chapter II overviews our concept and introduces self-focusing effect with the basic related notions for our unconventional display such as **E**missive **P**oint (**EP**), **E**missive **P**oint **D**istribution (**EPD**) and **E**missive **U**nit **C**ell (**EUC**) and **spel** (elementary spot self-focused on the retina). We present design limitations for such self-focusing display and our attempts to overcome them.

Chapter III describes the first experimental validation of self-focusing effect. I introduce our setup and provide its characterization. Subchapters basically describe various experiments validation of the self-focusing effect.

Chapter IV is dedicated to unconventional image formation. I describe Double-Gaussian model for image formation simulations and compare it with experimental results. Self-focusing-image formation is analyzed and I introduce γ-parameter to evaluate quality of spel in addition to signal to noise ratio (SNR).

In the **Conclusion and Perspectives**, I highlight the main results, provide a list of publications, and overview of related research done by our group since 2018.

Chapter I: Near Eye Displays

Any sufficiently advanced technology is
indistinguishable from magic.
Clarke's Third Law

Chapter I provides the necessary context about **N**ear **e**ye **d**isplays (**NED**) such as classification of immersive technologies: **A**ugmented **R**eality (**AR**), Virtual reality (**VR**) and **M**ixed **R**eality (**MR**), its application and chronology of NED development. This background helps us to understand the key factor for NED design: **H**uman **V**isual **S**ystem (**HVS**), comfort and immersion requirements. This serves to better understand the state of the art of NEDs for both conventional and unconventional approaches. We finish by formulating the research goals, challenges and contributions.

1 Introduction

One may speculate that the chain of visual devices evolution leads from traditional displays via smartphones to Near Eye Displays. From user experience (UX) point of view there are two main parameters/axes that evolve and play a crucial role for UX: **portability/wearability** and **immersion** [17]. Portability of device could be assumed as a combination of device autonomy with wearable comfort. Immersion could be seen as degree of similitude of signals received from the device and from real world: roughly speaking, more an artificially created sound or image resembles the real one, higher the immersion. During the device evolution there is a **trend from zero portability in low immersion to their combination in high quality**. It can be seen for both visual and audio devices as it is shown in **Figure I.1.** Traditional speakers are large, not easily portable, and create a shared listening experience. Headphones and earbuds, on the other end of the spectrum, are small, portable, and create a personal listening experience. Similarly, televisions and monitors are large, not easily portable, and create a shared viewing experience. Near eye displays are the headphones of the display world, creating small, portable, personal viewing experiences.

Figure I.1. Some audio/visual devices development milestones that illustrate the evolution of paradigm (paradigm shift): from low immersion to high, from shared experience to personal, from small to large size and back to small: a) audio devices evolution chain, b) visual devices evolution chain.

Before any audio-visual device invention, a person should come to a venue such as a theater to listen to an opera or to watch a play. It provides the spectator an audio/visual experience with a high immersion and zero portability, totally shared with other spectators. The invention of sound recording with a gramophone (**Figure I.1.a**) makes it possible to augment portability since it's possible to listen to music in one's own place. The experience could also be shared with the smaller audience if any presents near the gramophone. However, low sound quality downgrades significantly the immersion of UX. Engineers searched the way to overcome this obstacle and proposed various systems to achieve high-quality sound. Such systems still had low portability, but enhanced immersion. Technological progress allowed to reduce the size of devices without significant loss in sound quality. So-called boomboxes became a kind of portable device that combines high portability with high immersion. Everyday use of such device that provides sharing experience with surrounding strangers was not acceptable in the individualistic type of western culture where loud music disturbs other people. This problem was solved with the commercial introduction of headphones previously widely used in the telecommunication and military sector with miniaturized portable cd-players like Walkman. Increased portability of the device with personalized experience was achieved with the cost of decreased sound quality. The pattern observed for audio media: bulky sound systems like boomboxes gave way to more compact and easily portable systems. In the next step of the audio device, development engineers tried to gain back the sound quality. New types of data storage like CD and USB changed the embodiment of the device, made from a huge gramophone to a tiny device the size of a pocket watch. Smartphones merged music player's functionality as well as many other devices, e.g. digital camera. One can remember how Apple eventually stopped to produce the music player iPod due to low demand caused by the presence of the iPhone or other smartphones as a substitute product.

The audio device development could be seen as a constant **trade-off between portability and immersion**. Finally, technology let us combine the both: the headphones in couple with smartphones provide high sound quality and absolute portability. The same process is observed for visual devices (**Figure I.1.b**) that starts from the invention of the cinematograph – an analogue of the gramophone for visual media. Cinematograph provided some portability but loose

immersion. Roughly speaking, the analogy can be drawn between audio and visual media taking into account a time delay in device development for visual media due to a set of complex tasks to solve for researchers and engineers. The next step was the television that brought the films in everyone house with a price of smaller immersion. It could be seen as increased portability: one did not have to go to the cinema anymore and could watch films in their own house. During the XX century, the augmented immersion trend was achieved by the increased image quality and screen size with progress of technologies. Liquid Cristal displays made possible to have large screens of relatively low weight and therefore higher portability. The perfect example is personal consoles and eventually laptops. Another consequent step is of visual device development is the most portable device: a smartphone. Analyzing the evolution of the development of compact electronic devices display systems, two trends can be distinguished: 1) **the size of the device is steadily decreasing**; 2) **the ratio of the display area to the size of the device itself is increasing**. The trend to reduce the size and weight of the electronic device is also associated with the desire to create an affordable, convenient, compact multifunctional device that is always at hand. In many respects, the creation of such devices became possible due to the appearance of compact screens with high brightness and contrast at relatively low power consumption. This has led to the fact that the smartphone is currently the most common electronic device. However, this device lack immersion. Immersive technologies could solve this problem in the embodiment of smart eyewear such as smartglasses and head mounted displays (HMD) with the core element Near eye Displays. Smart Eyewear could be the next step in the gadget evolution chain. One can observe an increase in demand for Augmented Reality glasses, which means manufacturers and developers will strive to improve technologies, and Augmented Reality glasses will become part of the future. In the field of developing AR glasses, many new players are currently appearing, for example, Facebook, Apple, Xiaomi. However, the most famous and technically developed AR devices at the moment are stand-alone glasses Google Glass, Epson Moverio, Microsoft Hololens. It could be seen as a result of maturity/saturation and eventual decline of the current Smartphone market. In the today stage, eye-ware prototypes became commercialized commodities mainly for industrial users and will soon become everyday devices for individual consumers. One can speculate that smart **eyeware will eventually substitute smartphones**.

2 Immersive technologies (AR, MR, VR)

In the end of 2021 - beginning of 2022 the Metaverse as a term becomes one of the hottest topics. If during the previous decade community spoke about Virtual and Augmented reality, then the narrative merged them into Mixed reality, and finally everybody now uses a term Metaverse, like Bernard Kress, a significant AR/MR inventor and an AR/MR visionary, told in his talk "everything is Meta- now, metamaterials, metasurfaces and metaverse."[4] Immersive technologies are a general notion for Mixed, Virtual and Augmented Reality. Its taxonomy is comprehensively described by S. Mann [18], an AR pioneer. A model of mixed (hybrid) reality, or the continuum of reality-virtuality was first described in 1994 [19]. As can be seen from **Figure I.2.** Virtual Reality is completely virtual environment that provides fully immersive experience. Mixed Reality is defined as a system in which objects of the real and virtual worlds coexist and interact in real-time, within the framework of the virtual continuum. Augmented Reality complements the real world with virtual elements and sensory data mostly for informative purposes [20].

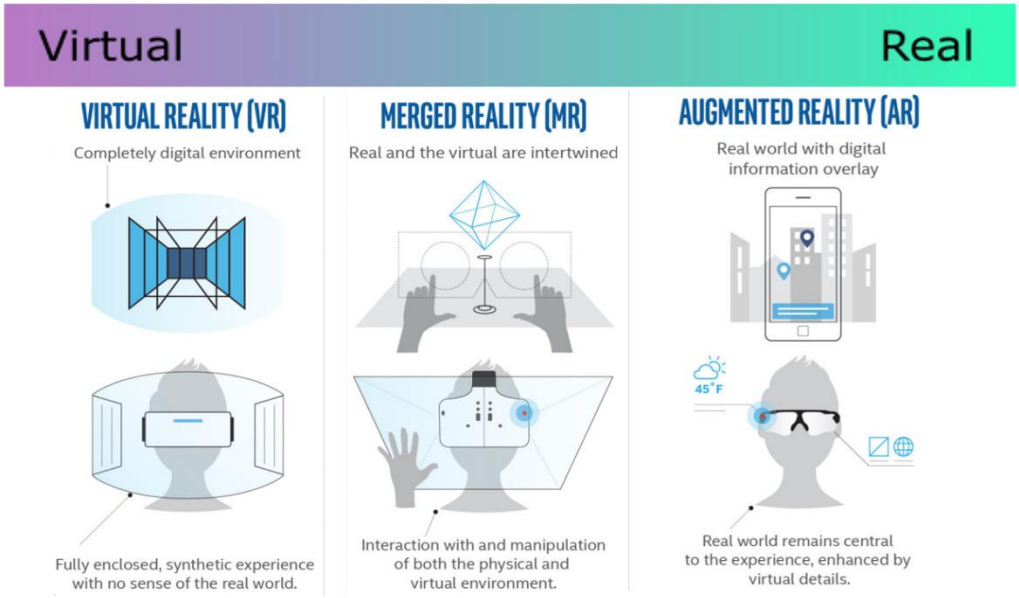

Figure I.2. VR/AR/MR taxonomy[5] in Virtual/Real spectrum: VR provides fully immersive experience, MR provides interactive experience and AR provides mostly informative experience.

[4] https://www.youtube.com/watch?v=4FeBFBXERLU

[5] https://www.appliedart.com/blog/vr-ar-or-mr-whats-the-difference-why-should-i-care

Therefore, immersive technologies are the key to a fundamentally new level of human interaction with the digital world, which plays an increasingly important role in the global economy, politics, and social relations [14]. Moreover, Immersive technologies are interactive, innovative technical solutions that open a world of new opportunities for social actors. The efficiency of using these technologies is achieved due to the "immersion effect" and maximization of user involvement in the process. Several years ago, Immersive technologies have received the most serious development in the entertainment and marketing industries, but this is not the limit, but only the first stage of their implementation [21]. Immersive technologies are finding more and more practical application in enterprises and bring changes to established business processes/tasks, so that one can get a fundamentally new experience [22]. With the competent use of the potential of these technologies, companies will be able to achieve increased profits through increased employee productivity, optimized work and production processes, attracted new customers and customers, and deepened professional competencies of their employees. "AR would simplify everyday human life is a gross understatement. It will radically change the way we consume digital information is more precise.", B. Kress cited an anonymous immersive technologies analyst. **Table I.1** summarizes applications of Immersive technologies in various industries by functions and foresees main outcomes.

Table I.1. Immersive technologies applications

What	Where	Potential Results
Management and interaction		
Visual cues that help the employee to complete the tasks of operation, repair and installation (assembly)	Aerospace industry, military-industrial complex, automotive industry, construction, healthcare, oil and gas industry, energy and utilities, technical and applied sciences	Increased productivity, streamlined workflow, reduced risk, remote collaboration
Immersive learning		
Creating a realistic training environment, which in normal conditions involves high risk or high costs for staff; reproduction of certain conditions and phenomena for the purpose of psychological rehabilitation	Consumer segment, healthcare, higher education / continuing education programs, industrial products	Risk reduction, cost reduction, enhanced therapeutic effect, conserving supplies
Improving customer experience		
introducing customizable and unique interaction methods with a company, brand or product	Automotive, banking and securities, consumer products, media and entertainment, tourism, services	Customer Experience Improvement with a company, brand or product, Customer engagement, increase marketing opportunities growth sales, increasing brand competitiveness
Design and analysis		
Data visualization, design, new forms of analysis	Aerospace and military-industrial complex, automotive industry, construction higher education, real estate, R&D	Cost savings, increased efficiency, identification of design flaws in the early stages, new methods of data analysis, reporting and forecasting

There are numerous applications for AR and VR in very diverse domains such industrial production, education, healthcare, consumer services [23]. The widespread introduction of immersive technologies contributes to the development of the world economy, a significant increase in productivity and efficiency in industrial enterprises within the framework of Industry

4.0[6], the formation of new approaches to the learning process and higher education levels, a qualitative increase in the level of healthcare and access to medical care due to the remote presence of a doctor [23]. Along with this, Immersive technologies create the new ways of communication and consumer services, form mass media for the modern generation [24]. Next-generation software and services could fundamentally change existing business processes and provide new opportunities for customer service employees who need hands-free technology. **Table I.2** presents Smart-Eyewear from market perspective devided by usage segments and product types.

Table I.2. Current product offering by users and segments

Product	Consumer		Enterprise			Medical		Defense	
	Daylong usage	Occasional indoor usage	Factory floor usage (shifts)	Heavy outdoor iddustry	R&D	Non surgical usage	Surgical usage	Training usage	Battlefield usage
#1	+++	+++	++	+++	+++	++	++	+	+
#2	+	+	++	+++	+++	+	---	---	++
#3	+	++	++	++	++	+++	+	+	++
#4	+++	+	+	---	---	+++	+	+	---
#5	-	+	++	---	++	--	+++	++	---
#6	-	+++	++	++	++	++	+	+	++
#7	--	++	+++	++	++	+++	+	++	+++
#8	---	+	+++	++	+++	+	+++	+++	+++
#9	---	++	++	+	+	+	++	+	+

Where:

- #1 is Audio only smart eyewear with prescrion corretion (e.g. Bose Frames, Huawei Smart Glasses)
- #2 is Rugged Smart Glasses – monocular, opaque (e.g. RealWear HMT1, Vuzix m300)
- #3 is Smart Glasses – monocular, see-thtough (e.g. Google Glass)
- #4 is Smart eyewear with display and prescription correction (e.g. Google Glass, North Focal, Lumus DK32)
- #5 Tetherd AR hedsets to PC (e.g. Meta 2, DreamWorld Glasses)

[6] https://www.weforum.org/agenda/2016/01/the-fourth-industrial-revolution-what-it-means-and-how-to-respond/

- #6 Standalone AR headsets (Epson Moverio, Lumus DK50/Vision Digilens Cristal)
- #7 Standalone AR headsets with 6DOF and gesture sensing (ODG R9M nReal AR glasses, Daqri, Atheer Labs)
- #8 High-end see-through untethered MR (e.g. HoloLens V1/V2)
- #9 Pod-tethered high-end see-through MR (Magic Leap One, Lenovo ThinkReality)

Outlined premises made Immersive technologies the investment mainstream with very promising outcomes according to standard investment metrics like Compound Annual Growth Rate (CAGR) which provides a constant rate of return over the time period [25]. According to Transparency market research[7]., "The Augmented Reality market was valued at USD 4.21 billion in 2017 and is expected to reach USD 60.55 billion by 2023, growing at a CAGR of 40.29% during the forecast period. The Virtual Reality market was valued at USD 5.12 billion in 2017 and is expected to reach USD 34.08 billion by 2023, growing at a CAGR of 33.95% during the forecast period. The base year considered for this study is 2017, and the forecast period considered is between 2018 and 2023" According to the late 2021 report Immersive technologies market is expected to cross USD 2.6 Trn by 2031, expanding at a CAGR of ~38% during the forecast period.

Some investors use the Gartner Hype Cycle to understand the current state of the art for making investment decisions. The Gartner Hype Cycle is an empirical heuristic to trace technologies for investment, it provides some qualitative insights about technology adoption by users. It's limited in prediction accuracy[8], however, it could be used as posterior adoption dynamics tracing. The Metaverse now in the peak of the inflated expectations from the end of 2021 (**Figure I.3**). The question is if it becomes mature and leaves this cycle. Immersive technologies are disappeared from the hype cycle in 2020 that means the experts considered them mature enough to be commercialized and therefore no longer be viewed as an emerging technology. VR was widely adopted in 2017 in the gaming industry. AR was place last time in 2018 into "through of disillusionment". The path of AR via the hype cycle was made in two decades: during the 00's it was climbing up onto the peak of inflated expectations and in 10's it was dropping down. The

[7] https://www.transparencymarketresearch.com/immersive-technologies-market.html

[8] https://www.linkedin.com/pulse/8-lessons-from-20-years-hype-cycles-michael-mullany

same 2018-year MR was going its way to becoming a commodity from prototypes. In 2014, Google began testing Google Glass, the first HMD for wild consumer market that failed the adoption due to law social comfort, aesthetics and functionality compared to smartphones. In 2016, Microsoft introduced HoloLens – an HMD for industries that along with industrial version of Google glass little by little were adopted by various industries mentioned above. These events contributed to the active continuation of work in the field of Augmented and Virtual Reality technologies.

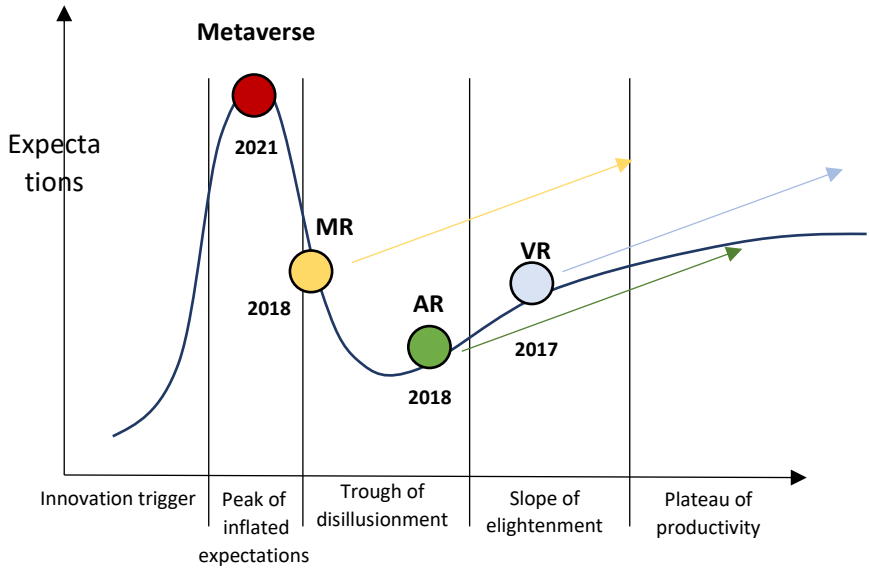

Figure I.3. Gartner Hype Cycle for immersive technologies, adapted from www.gartner.com: VR last appeared on the diagram in 2017 before become a commodity fully adopted by customers; AR and MR last appeared in 2018,Metaverse is on the peak of inflated expectations.

"Today everybody talks about the metaverse", said Bernard Kress during his opening remarks of SPIE AR,VR,MR Industry Talks 2022 [21]. "Earlier we talked about AR, VR, MR, today we are talking about the same concepts and architectures, but they all englobed in the metaverse. <…> Between you and the metaverse there is hardware and there is where we are stepping in". In other words, **NED is the hardware that will enable the Metaverse and Immersive technologies**.

Augmented Reality looks like something brand-new-made in its penetration into the consumer market. However, its roots can be traced back to World War II, and conceptually to Pepper's

ghost illusion technique firstly mentioned even in the end of the XVI century[9]. As Newton said "If I have seen further, it is by standing on the shoulders of giants", the development of the hardware for Augmented Reality, exactly like many other technologies, made a long path and we probably only in the middle of this way. Eventually, AR hardware could be reduced to contact lenses like it was demonstrated in the "Black Mirror" series and even further up to direct stimulation of the visual cortex. **Figure I.4** presents AR chronology with milestones from mid XIX century up to nowadays.

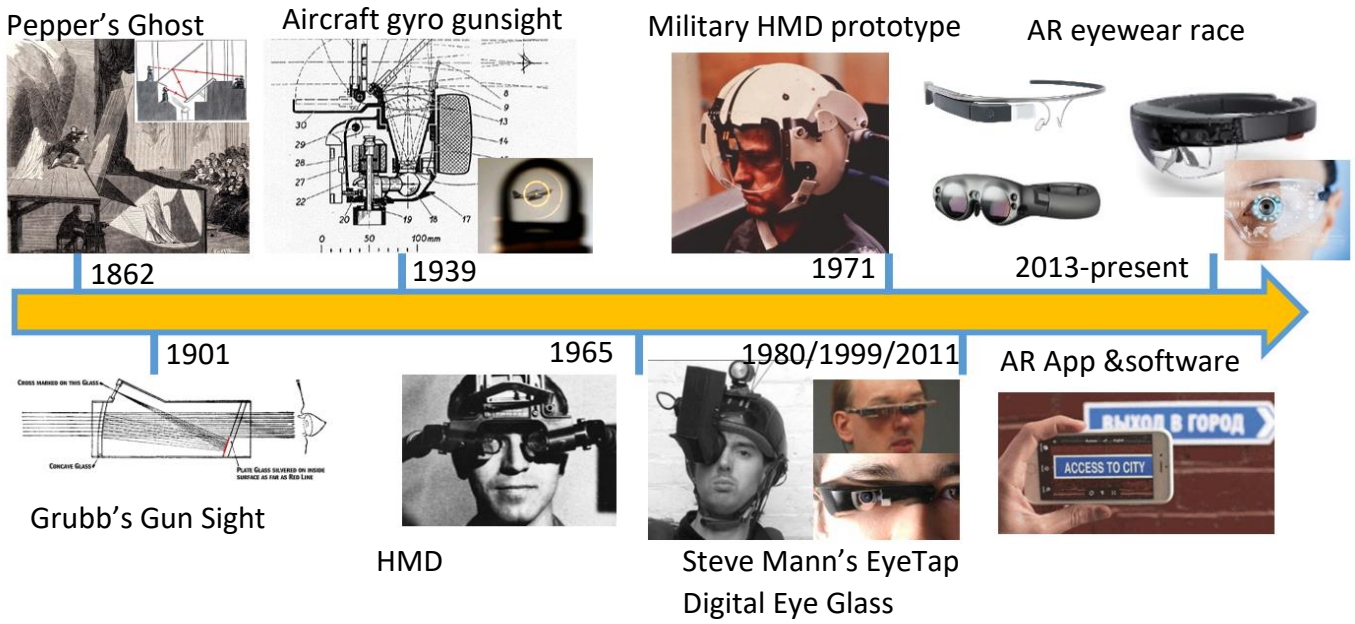

Figure I.4. AR-chronology and milestones: from XIX century to nowadays: from Pepper's Ghost to Smart Glasses through air force helmet

The first milestone arbitrary dated 1862 for an artistic application of AR. It can be argued that Pepper's Ghost was essentially the first Augmented Reality appearance in modern world. Basically, it was the first huge Head-up Display. In 1901, Frank Baum, author of famous "The Wonderful Wizard of Oz", first introduced in his novel "The Master Key" the idea of electronic glasses that overlay character data on real scene: "while you wear them every one you meet will be marked upon the forehead with a letter indicating his or her character[10]." In the same year Howard Grubb, an optical engineer and telescope maker from Dublin, invented and patented a

[9] https://newyork.museumofillusions.us/peppers-ghost/

[10] https://www.gutenberg.org/files/436/436-h/436-h.htm

collimating reflector sight. This sight could be assumed as a first ancestor of modern Head Up Displays. The Grubb's sight was widely adopted for on many types of weapons, especially in aircrafts since 1918. In 1939 British engineers developed the first gyro gunsight for fighter aircraft that eventually evolved into Head Up Display that we know now.

In 1965 Head Mounted Display called the Sword of Damocles was firstly introduced by Ivan Sutherland and his Harvard university research team. Helmet Mounted Displays found their application in military sector. In 1980, Steve Mann developed the EyeTap, a helmet that displays virtual information right in front of the user's eye. EyeTap is the first functional AR headset model. The helmet exists to this day: its dimensions have been significantly reduced to simple goggles in 2011. In 2013 the AR-eyeware race started when Google firstly introduced their smartglasses. Since then slowly but steadily all the biggest digital companies join this race and multi-million and even billion investments and acquisitions have been made. The essential part of such smartglasses is NED. NEDs allow to integrate of information with real-world objects in the form of text, computer graphics, and audio in real-time and expand user experience with the environment. There are several key factors for NED that lead to ultimate UX.

3 Key factors for Near Eye Display design

Bernard Kress defines two main factors for UX: **comfort** and **immersion**. The third parameter is the **cost** which is always beyond of research scope but could be a strong limitation factor. There are several types of comfort: wearable, visual and social. Even the lack of one of the components make the adoption of new commodity such as eyeware low probable. One could observe how appearance of Google Glass appeared in 2014 was ahead of its time. User adoption failure could be explained by the lack of social comfort and strong mismatch between over-enthusiastic user expectations nourished by science fiction and scarcity of device performance caused by the early development stage of technology.

Research teams struggle to design aesthetic and high-performing devices and face an inevitable compromise between several design parameters and properties. The list is long enough and comprehensively described in the literature [17], the main parameters are schematically presented in **Figure I.5**.

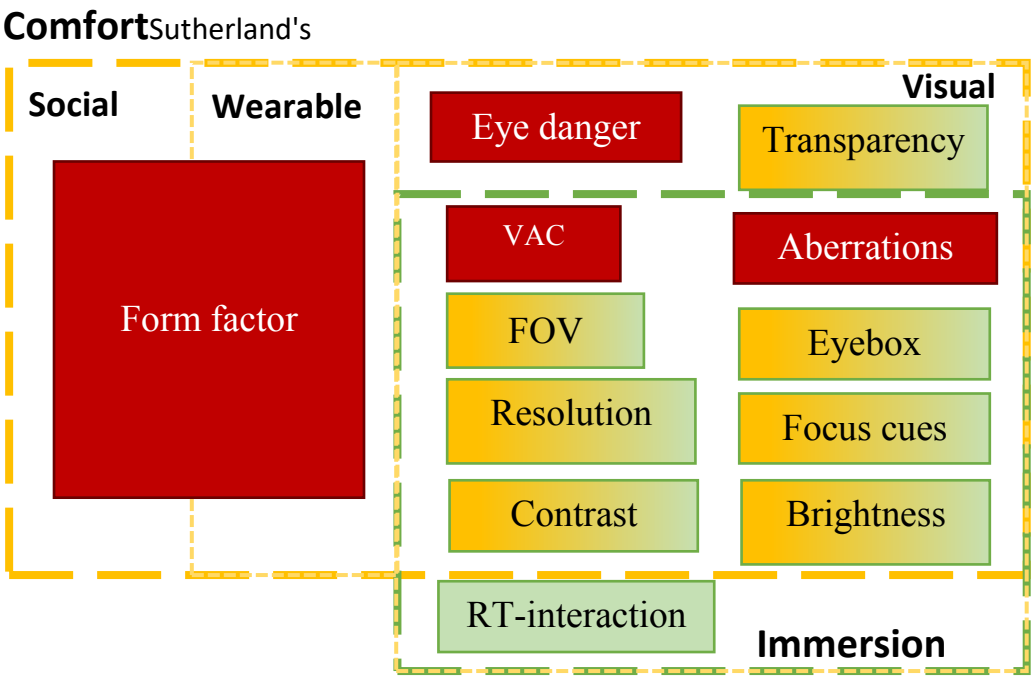

Figure I.5. Human-centric perspective on design features and constrains: comfort and immersion, adopted from [17], [26] : red factors should be overcome or diminished, green – expanded up to HVS characteristics.

It's convenient to follow Kress' classification of Comfort and Immersion. The are three different types of comfort: **Social, Wearable** and **Visual**. Visual comfort and immersion are interrelated: more visually comfortable the device, deeper the immersion. An ideal NED should be lightweight and compact to resemble a pair of eyeglasses to allow comfortable wearability and social acceptance. This is **Form Factor** constrain which prevents a massive adoption by individual consumers, because there is no social acceptance of such device and therefore there is no **social comfort**. However, people accept any type of wearables if it is a part of their job uniform. This is the reason why AR-headsets are widely implemented in the industry, healthcare, and education.

Therefore, a compact form-factor is one of the most important characteristics for smart-eyeware from customer adoption point of view. AR headsets may consist of the display unit, multiple sensors, computing units, communication units and a battery. Despite integrating all these components, it is important that these devices are lightweight so that the users can wear these devices for long hours. Several limitations in reaching these goals are related to the underlying technologies such as the interplay between battery size and weight, heat dissipation, run time,

and computational power, while other considerations arise from trade-offs between features and capabilities of the device design. If not considered carefully, the design may prevent users from having comfortable, long-lasting experiences.

Since smartglassess are limited by Form factor, NEDs face a long list of challenges to overcome visual comfort constraints and to be truly immersive: **Field of view** (**FOV)/EyeBox (EB)/resolution** challenge**, Vergence-Accommodation Conflict** (**VAC**) challenge, **Transparency/Brightness/Eye safety** challenge. it's almost impossible to solve all challenges and have a small and light headset. Some R&D-teams like Kelly Peng's "Kura AR" claimed to solve all issues [27], but there is no commercialized device yet, so maybe it's over positive statement. Most of the parameters and properties are interrelated and there is always a trade-off between these parameters and the **improvement in one parameter costs the loss in the others**. For example, if one wants to increase the FOV by expanding the numerical aperture (*NA*) of the collimation lens, the EB is reduced (as well as the angular resolution) and the size of the optics increases.

The trade-offs are caused by the existence of optical invariants: the light entering the system is equivalent to the light leaving the system (**Figure I.6**).

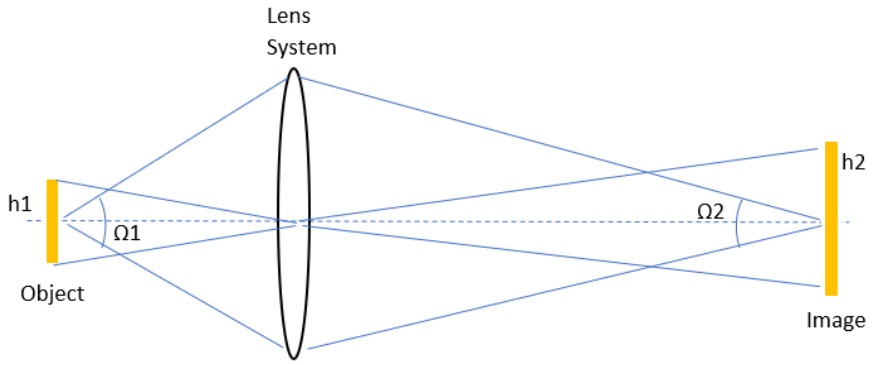

Figure I.6. Law of conservation of etendue: while h_2 increases Ω_2 must decrease

There are three invariants: the Lagrange invariant (or Optical), Abbe sine condition and Etendue, also known as throughput. These invariants allow to estimate a performance of various optical systems configurations. The Lagrange invariant states that in paraxial approximation a product of the aperture, angle value and height of field is constant in both image and object space [28]:

$$h \cdot \theta \cdot n = const, \tag{I.1}$$

Where h is the object height,θ is an aperture angle and n is refractive index. Abbe sine condition extends the Lagrange variant and it is valid for non-paraxial approximation free of spherical aberrations and coma:

$$h \cdot sin(\theta) \cdot n = const, \quad \text{(I.2)}$$

The etendue extends previous invariants into radiometry field adding the notion of conservation of energy. In a display, etendue is the product of the height of the imaging source size h_1 and the solid angle of light that enters the optical system Ω_1, which is equivalent to the product of the size of the EB h_2 and the FOV solid angle Ω_2 as described by the following equation:

$$etendue = h_1 \cdot \Omega_1 = h_2 \cdot \Omega_2 = const, \quad \text{(I.3)}$$

Practically, law of conservation of etendue means that if one seeks to increase both FOV and EB, a larger imaging source is required meaning the size of the device will likely increase. So, there is an interplay between the display size, FOV, and EB. Additionally, for a given imaging source, if one increases the FOV by decreasing the EB, the resolution of the output image will be spread across a larger angle meaning a decrease in the angular resolution.

However, the final detector is **Human vision system** (**HVS**) that has their limitations and from this human centric perspective researchers can find compromises. For example, one alternative often used to get around the limitations of etendue is pupil expansion. For pupil expansion, the radiance of the image source is split into multiple optical paths with separate exit pupils or EBs. In this manner, the luminance of the image is reduced, but with multiple EBs produced, the effective EB size is increased. Therefore, a NED should be adapted to the HVS.

3.1 Human visual system for near eye display design

Human visual system is a limiting factor for NEDs. Analyzing these limitations one can address the challenges of key factors to achieve the best possible comfort and immersion. HVS could be split into two levels: low and high [26]. Low-level refers to a psychophysical process in which the eye acquires visual stimuli, and it involves both the physical optics of the eye and anatomical structure of the retina. In contrast, high-level vision refers to a psychometric process in which the brain interprets the image. It describes the signal processing in the visual cortex, such as perception, pattern recognition, and feature extraction. To achieve appropriate results in the prototype image projection, it is necessary to understand the principles of the eye function and

structure. As an optical instrument, the eye contains two lenses: cornea and crystalline. The first one has a fixed optical power, the second one is an active optical element: it can change its shape to modify its optical power. This constitutes the so-called accommodation mechanism. The main characteristics of the human eye is presented in **TableI.3**:

Table I.3. Main characteristics of a human eye

Focal length	24 mm
Aperture	2-8 mm
Refractive index	~1.38
Dynamic range	From 10^{-6} to 10^{5} cd/m^2.
Diffraction resolution	0.02°
Field of view (FOV)	From 4.5°× 4.5° up to 160° × 175°
Autofocus	25 cm (< 50 years) and > 50 cm (> 50 years)
Spectral sensitivity	380-750 nm
Fovea centralis	4.5° (1.3mm) in diameter

Human visual acuity is limited by many factors including sensor cell distribution, pupil diffraction, lens aberrations, and contrast of stimulus. Humans are very sensitive to spatial resolution and thus this factor is very important to preserve in a display that will provide high information density. The acuity of human vision is typically measured by the highest spatial frequency that the visual system can resolve in terms of cycles per visual angle. The standard measure of "normal" or 20/20 vision is supported for a spatial frequency of **30 cpd** (cycles per degree), i.e. the ability to resolve a contrasting intensity cycle spanning **two arc minutes** (2'), or a feature spanning one arc minute [29]. However, the human visual system has such a high resolution only for a narrow region on the retina called the fovea (**Figure I.7**). Beyond this region, the resolution drops drastically and is very low in the peripheral FOV. It's caused by the cone density– photodetectors that are capable of color vision and are responsible for high spatial acuity as shown in **Figure I.7a**. This non-uniform resolution across the field-of-view provides an opportunity to provide high-resolution imagery without having to build very high-resolution display panels but poses a challenge to dynamically change the display as the eye looks in different directions.

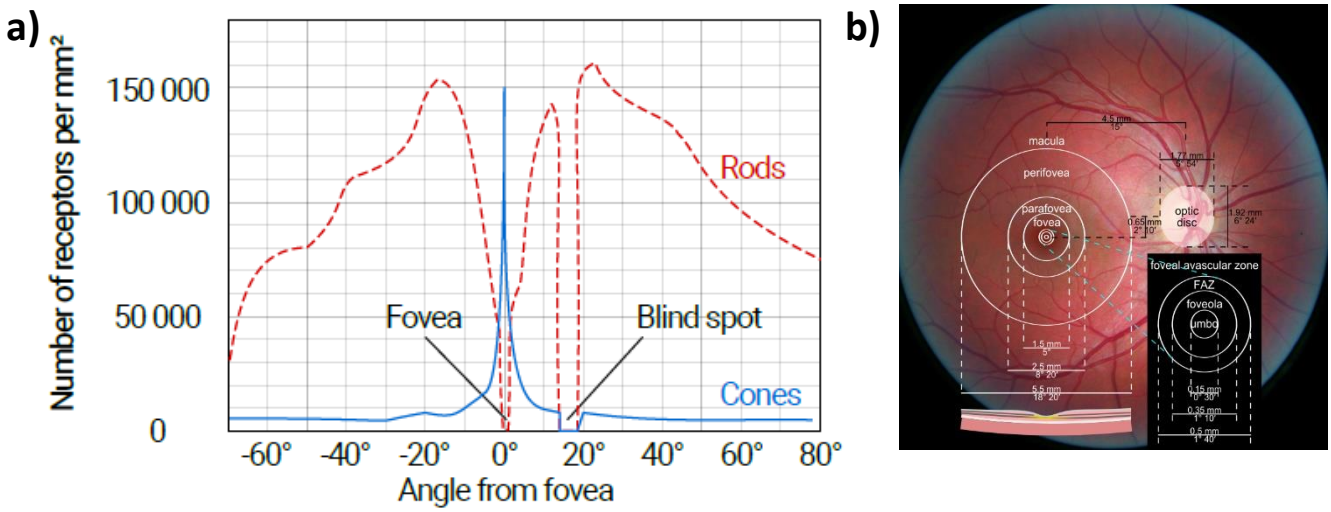

Figure I.7. Human retina region: a) Cones and Rods density near fovea region, b) linear/angular size of the fovea/macula region

The maximum acuity zone has FOV of about 2-3°. **Figure I.8a** presents FOV of an eye: Up to 10° one can read texts and symbols, up to 30° - distinguish shape and up to 60° – distinguish colors [29]. The human eye has a static FOV of approximately 150° wide, and the combined FOV between both eyes is about 190°. With eye motion, this FOV expands to approximately 290 [29]. Some researchers suggest that an ideal optical see-through (OST) NED should support augmented imagery over a 100° wide FOV while not occluding the viewer's peripheral sight [30]. Wider FOV is especially important for displaying imagery spatially registered to the world, which may appear anywhere in the viewer's FOV according to the viewing position; restricting this FOV may result in imagery disappearing or being cropped to the viewing window. Such cropping limits the region of the world that can be instantaneously augmented, reduces the realism of the augmented display, and requires active user effort to keep spatially registered content within the supported FOV. An example measure of a field of view is shown in **Figure I.8b**. A typical human monocular visual field extends 60° nasally limited by the nose, 60° superiorly limited by the eyebrow, 100° temporally limited by the pupil and 70° inferiorly limited by the cheek [31]. This means a total monocular FOV of 160° horizontal and 130° vertical. When eye motion is considered, an additional 50° may become visible as the eye rotates toward the temple.

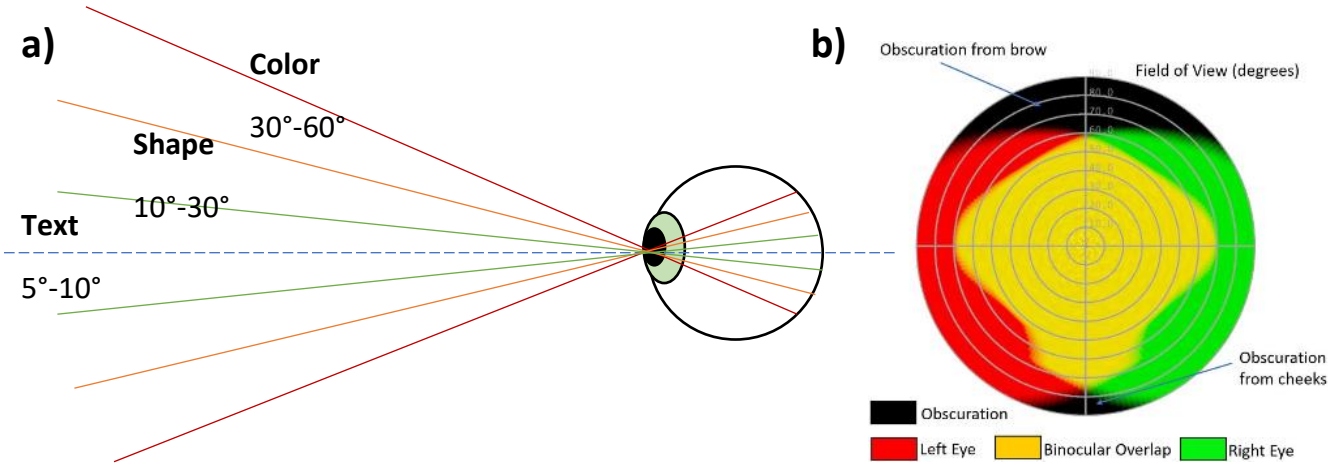

Figure I.8. Human eye's perception of the information and its field of view: b) Human binocular FOV region

Another important consideration for any NED is the EB, the viewing volume in which the eye can move relative to the display while the user still sees the whole projected image (**Figure I.9a**). Outside of the EB, the user may see vignetting (gradual darking of the image toward the edges), a corrupt image, a partial image, or no image at all. The EB should be appropriately sized to allow for eye rotation, shifting of the near-eye display on the head, and variation in human anatomy. An EB of 10 mm or larger is generally recommended for head worn displays [32]. However, the effective range of pupil motion within the EB depends on the pupil size; for a given EB size, a larger pupil has less freedom of movement. The EB position for a given display may be fixed, may be translated mechanically (e.g. by centering optical components over the eyes), or may be adjusted in software [33]. In particular, it is useful to adjust the EB position to account for varying interpupillary distances, which vary between 45 to 80 mm for virtually all adults [34]. Larger EBes are preferred, but EB sizes are usually balanced with other factors such as size (e.g. a larger imaging lens will generally produce a larger EB) and image quality (e.g. increasing EB size may increase the number of constraints on an optimized optical surface). In the computational designs proposed in this dissertation, EB size may be traded for non-traditional factors, such as resolution.

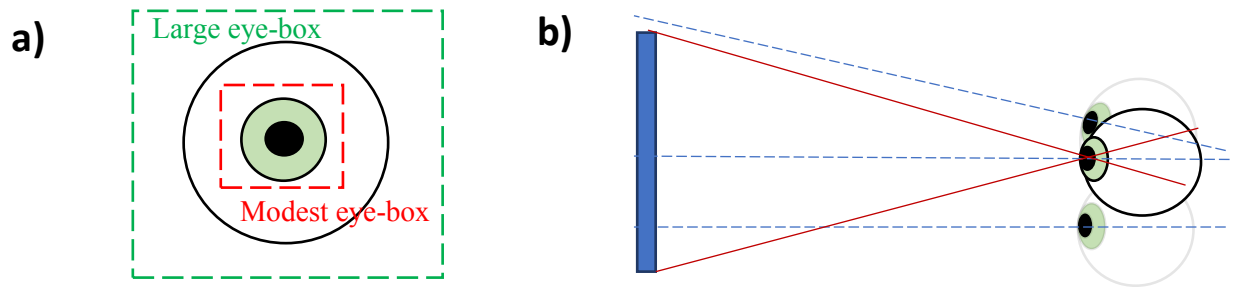

Figure I.9. EB and FOV relation: a) Eyebox refers to the range of pupil positions from where the virtual image by the AR display can be seen., b)

A wide EB is a challenge due to existence of **FOV/EB/resolution trade-off.** The EB is the same as the exit-pupil of the display. Many display technologies and prototypes have been demonstrated which have beautiful imagery but with narrow EBs [35]. For such displays, EB replication techniques may be useful.

Eye relief is the intended viewing distance of the display, measured from viewing center to the nearest display component. A suitably long eye relief is needed to allow space for viewer eyeglasses behind the display and to improve viewer comfort; an eye relief of 20 mm or more is recommended [32]. Eye relief is generally traded off among other factors in a display; **Figure I.10a** shows how EB size varies directly with viewer eye relief in a simple near-eye display design. In optical configurations where the field of view is limited by the size of the optical element nearest the eye, the FOV of the display also decreases with increasing eye relief. Incorporating corrective eyewear into the display itself (e.g. as with Google Glass) offers an opportunity to reduce the necessary eye relief. as experienced by the user

Figure I.10 summarizes the effects of eye relief, FOV, and eye pupil size on the perceived EB. The combination of all three parameters can help to build a more or less uniform EB, no matter the size of the human eye pupil.

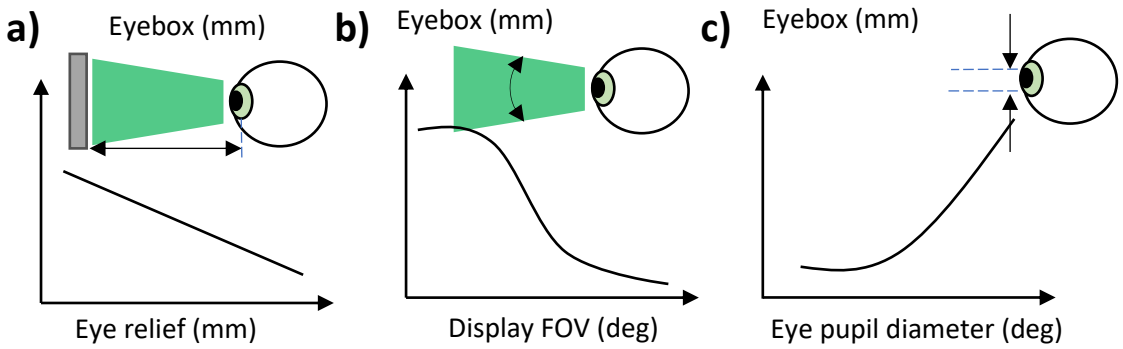

Figure I.10. The perceived eyebox size is a function of eye relief, display FOV and eye pupil diameter, adapted from B.Kress [36]

Due to the different sensitivities of the cone and rod cells, the human eye has a wide range of illumination sensitivity which can be broken down into 3 ranges shown in **Figure I.11**. **Scotopic** vision happens at low ambient illumination ranges when vision is mediated by the rods, a primary characteristic of which is loss of color sensitivity. **Photopic** vision occurs at ranges of high ambient illumination and is mediated by the cones. **Mesopic** vision occurs at the illuminace levels between the photopic and scotopic ranges when vision is mediated by both cones and rods [37].

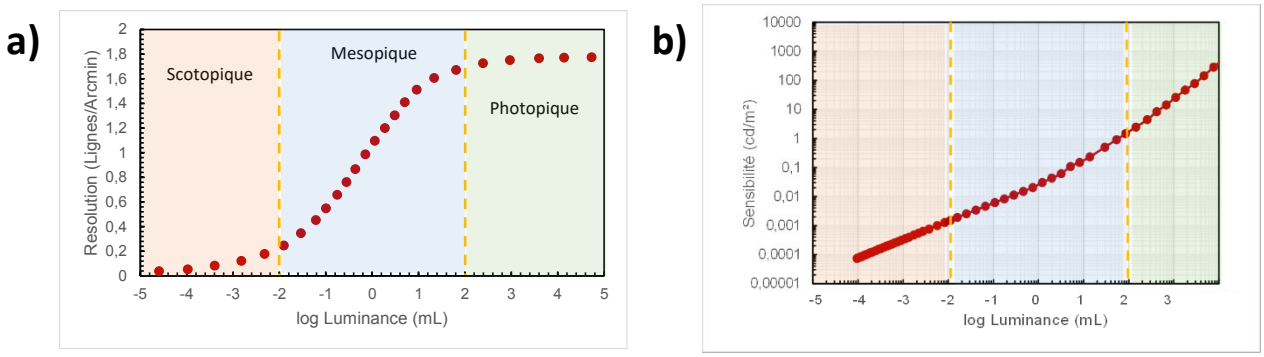

Figure I.11. Approximate ranges of vision regimes and receptor regimes across the HVS dynamic range: a) resolution grows from Scotopique to Photopique regimes, b) the growth trend for light sensitivity

The manner and quality that the real world is conveyed to the eye is important to consider from **Transparency/Brightness/Eye safety trade-off** point of view. OST- NEDs have the advantage of letting the light from the real-world scene pass directly to the user. However, some amount of attenuation is likely to occur. If the display is meant for outdoor use, attenuation of the bright

sunlight may be desired so that the lower luminance of the display may be perceived; however indoors, the same attenuation would darken the view undesirably. Ideally the attenuation will be at a level where virtual content may be overlaid on either bright or dark backgrounds with enough contrast to provide clear viewing. The contrast of virtual content could be enhanced with an occlusion capable display, but such displays exhibit additional problems with bulk, correct occlusion focus, and occlusion latency. The **luminance, contrast, and dynamic range** of the display are co-dependent; with a greater luminance, better contrast and dynamic range usually follow, so providing a greater maximum luminance is desirable. Additionally, reducing noise, as measured in peak signal-to-noise ratio, in the final is important to the final image quality.

There are two essential mechanisms of HVS: **accommodation** and **vergence**. Accommodation is the eye mechanism that allows to change the crystalline curvature and therefore focus the image into the retina from various distances. Vergence is an eye movement to obtain a binocular vision. The vergence and accommodation of human vision are neurally coupled and presenting unmatching depth and vergence cues will force a decoupling leading to an effect commonly known **as vergence–accommodation conflic**t (**VAC**) shown in **Figure I.12**.

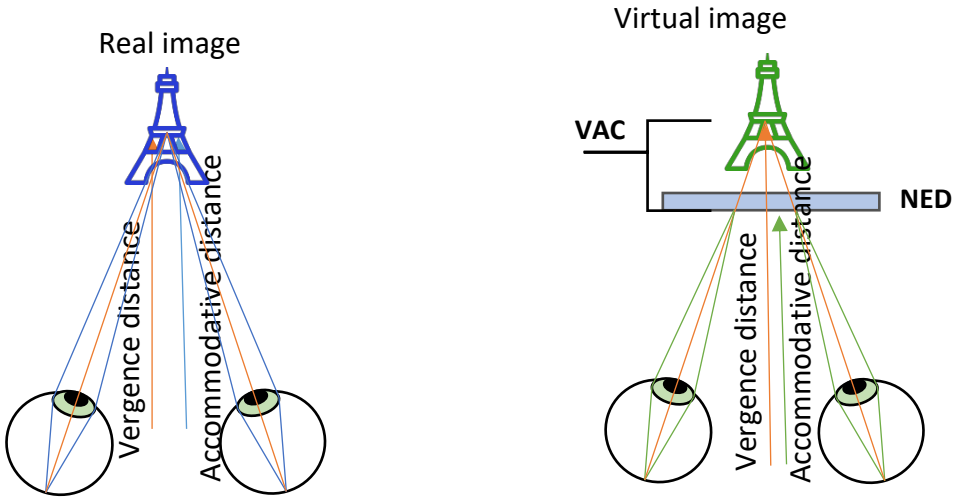

Figure I.12. Vergence-accommodation conflict: a) no conflict vergence and accommodative distances are the same, b). Conflict due to Vergence and accommodative distances mismatch

Assume, a viewer is fixated and focused on the real image of Eiffel Tour (**Figure I.12a**). Vergence and accommodation distance is the same and equals to distance to the image. In **VAC** case the

virtual image is located behind the NED and there is a mismatch between these distances (**Figure I.12b**). Thus, the disparity target leads the eyes to come closer to a certain distance, while the light rays coming from the virtual plane produce a blurring of the retina, which leads the eyes to adapt to another distance, giving rise to the conflict between these depth cues.

4 Near eye displays overview

A NED must perform three primary functions: to bring into focus (and usually magnify) a virtual image source placed near the eye, to relay the image into the eye, and to **combine the optical paths of the virtual image source and the see-through view of real scene**. Since both FOV and EB shall be large it is very hard to make the display small. Large displays lead to bulkiness, which leads to less practical glasses; the larger the glasses are the more likely the user is to bump into something. However, larger displays usually also result in heavier optics. Due to quality and refraction index requirements many optical elements of today's AR displays are made of glass, which can quickly become too heavy as size increases. The goal is to obtain a system that imitates the free viewing, or Newtonian viewing. Such systems form an image of a target on the retina with minimal accessory optics (**Figure I.13**).

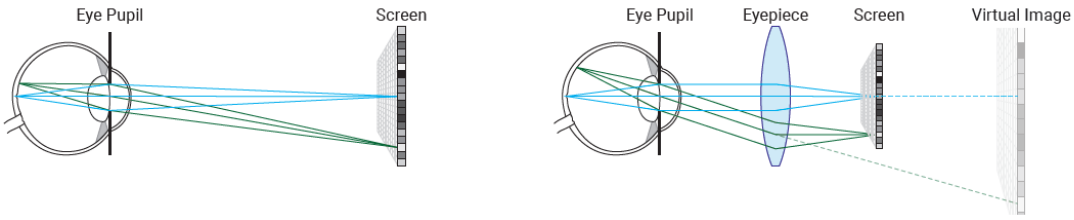

Figure I.13. Direct (Newtonian) view: a) free viewing, b) with a lens

R&D teams have proposed several classical optical designs [38], [39] and [40] to address improving FOV. As it was demonstrated in [41] and [42], combining an NED with projections promises a larger FOV, but it introduces new practical challenges. Throughout this refinement process, while attributes such as form-factor, weight, and FOV were improved, it wasn't until relatively recently when increasing the focal depth range was widely addressed as a means for solving VAC. Supporting accommodative cues is known to cause major complications in a NED's optical design. Several different techniques have been shown effective in providing more than a

single focal depth. Always-in-focus and extended-focus methodologies such as **Maxwellian View displays** are advantageous because user state does not need to be accounted for. They can imitate defocus blur during image generation, and may provide large FOV with a small form-factor, but are typically limited in angular resolution due to diffraction of the pupil. **Virtual retinal displays** can provide correct focal cues through beam shaping, but face a difficult trade-off with resolution and time. **Multifocal** approaches enable correct focal cues at the depths of the virtual images, but suffer from loss of resolution when interpolating to distances between the focal planes and a limited FOV. **Varifocal** techniques provide high angular resolution and accommodative cues, but historically suffer from limited FOV. Recent works have improved the FOV, making varifocal a good optical choice for reducing VAC while being computationally and optically simpler than other techniques. Computational methodologies such as **light fields** can provide accommodative cues while enabling wide FOV. However, light field displays demand a significant amount of image formation computation and are limited in angular resolution. Displays based on **computer generated holography** are capable of providing per-pixel focal depth, but due to current spatial light modulator (SLM) technology, have a very constrained etendue. I review designs that have enabled accommodative cues, investigate their characteristics, and provide a comparison of these solutions in **Table I.4**. Several review articles provide additional descriptions of the various focus-supporting display architectures [43], [44], [26] and [45].

Previously, I mentioned the Kura AR R&D team. They claimed the next characteristics: 150° FOV, 8k resolution, 70 pixels per degree, 2 million nits microLED, 30% light efficiency, 95% transparency, super slim design, glasses form factor and $899 cost. For most experts this seems to be a super-optimistic claim.

Table I.4 NED types and basic characteristics.

Display	Design	See-Through	FOV [deg]	Angular Resolution [cpd]	Frame Rate, [Hz]	Eye Box, [mm]	Focal Range	Blur	Eye Tracking
Average	HMD	Limited	35-65	8-25	45-75	5-14	1.5-6	Rendered	Pupil-driving
Maxwellian View and Afocal Dispalys									
[46]	Bench	V.High	25	<20	60	8	Afocal	Rendered	Required
[47]	Bench	No	-	4-7	60	2.1	7	Rendered	Pupil-driving
[48]	Glasses	V.High	31.5	12.5	60	7	>5	Rendered	None
[49]	Glasses	No	Large	3-15	-	0.8	Afocal	Rendered	None
[50]	Glasses	Limited	110	2-3	60	7	Afocal	Rendered	Pupil-driving
Virtual Retinal Displays									
[51]	Bench	High	70	low	frameless	3.5	3	~ Correct	None
[52]	Bench	High	-	low	60	-	14	~ Correct	None
[53]	Glasses	V.High	68	7-9	10	dynamic	3	Rendered	Required
Multiplane Displays									
[54]	Bench	No	26	22-38	12	≤1	1.33	~ Correct	None
[55]	Bench	No	-	27-47	45	≤1	1.8	~ Correct	None
[56]	Bench	No	18.3	21	75	≤1	1.33	~ Correct	None
[57]	HMD	High	40	9-12	60	6.3	3	~ Correct	None
[58]	Bench	High	31	23	67	4	3	~ Correct	None
[59]	HMD	No	18	2-12	60	-	3.25	~ Correct	Required
[60]	Bench	High	29.6	<30	60	23.5	3.05	~ Correct	Required
[61]	Bench	High	34-52	<10	60	10	6.5	~ Correct	None
Varifocal Displays									
[62]	Bench	High	28	10-14	85	3	8	Rendered	Required
[63]	HMD	No	36	5-6	75	4	9.8	Rendered	Required
[64]	HMD	High	60	18	60	15	5	Rendered	Required
[65]	Bench	High	75	-	60	30	7	Rendered	Required
[66]	HMD	High	75	4-5	60	25	10	Rendered	Required
Light Field Displays									
[67]	Glasses	No	33.3	2-3	15-70	7.6	3.3	~ Correct	None
[68]	Glasses	Limited	65	-	85	≤1	9.8	~ Correct	Pupil-driving
[69]	HMD	High	40	10-20	60	6.5	3	~ Correct	None
[70]	HMD	No	110	3-4	60	8	4.45	~ Correct	Pupil-driving
Holographic Displays									
[71]	HMD	High	-	-	-	3.14	-	~ Correct	None
[35]	Bench	V.High	>94	<12	20	≤1	6.9	~ Correct	Pupil-driving
[72]	Bench	No	15	<130	20	10	1.75	~ Correct	None

4.1 Maxwellian View Displays

The procedure of projecting an illuminating source on the eye's pupil instead of viewing it directly is called Maxwellian viewing [72]. Displays that are designed to follow this principle, where the screen plane is the optical conjugate of the retina and the illumination source is the conjugate of the eye's pupil plane, are called Maxwellian view displays (**Figure I.14a**). Since the source is imaged on the eye's pupil, and the image is formed on the retina, the result is typically always in focus. Several variants of the Maxwellian view displays have been proposed in the literature. Ando and Shimizu [46] utilize both a holographic optical element and a digital micromirror display (DMD) [73] to achieve retinal projection (**Figure I.14b**).

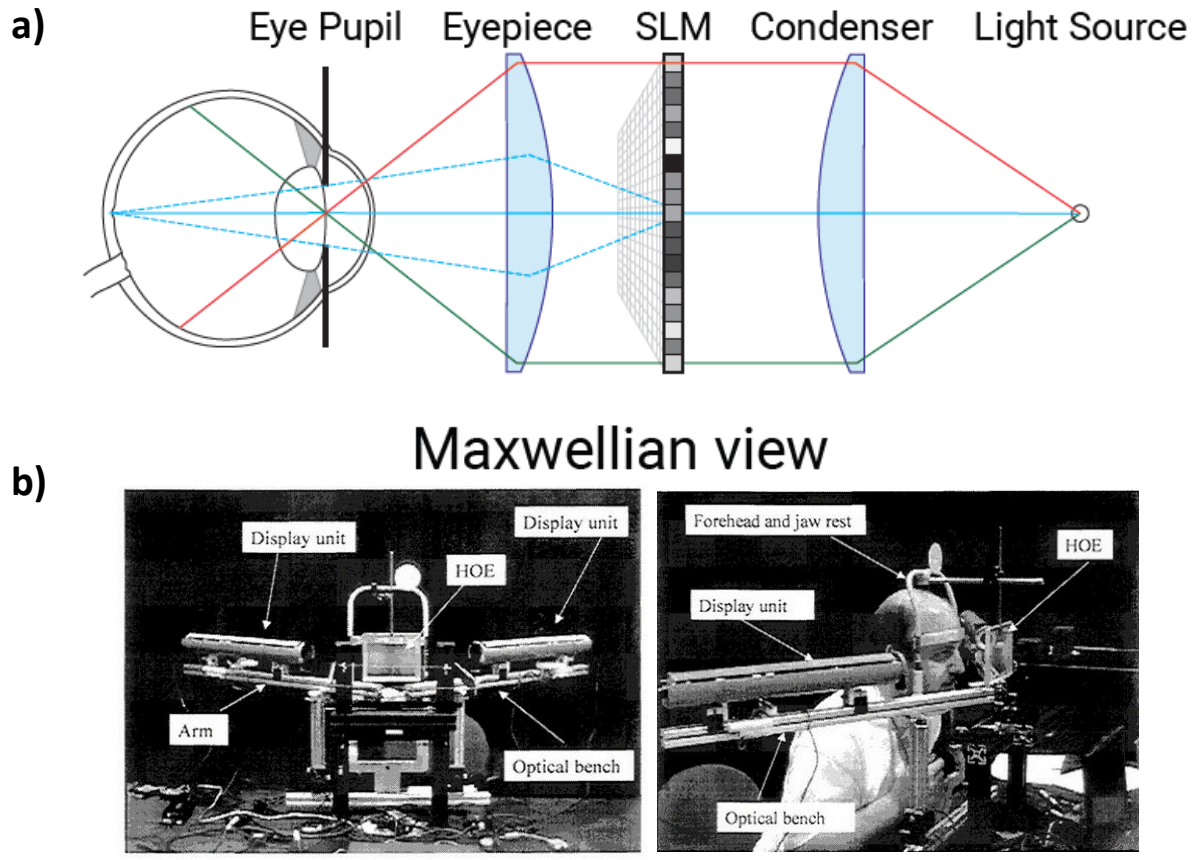

Figure I.14. Maxwellian view: Optical scheme, b) Bench prototype example [46]

While von Waldkirch et al. [47] use an LCD (liquid crystal display) and a set of collimation and projection lenses to achieve a quasi-accommodation-free Maxwellian viewing with

high resolution. However, such displays have a very small depth of focus and EB sizes. By using an elliptical scanning beam, they show that the depth of focus of a Maxwellian view retinal scanning display can be improved, whereas von Waldkirch et al. [48] show an improved depth of focus by using an oscillating fluid lens in the retinal projection system.

Yuuki et al. [49] combined LCD, pinhole array aperture mask, and micro-lens array to create a tessellated series of Maxwellian view displays capable of extended DOF. Alternative always-in-focus mechanisms, related to Maxwellian view in that they project an image directly on the retina, also offer sharp imagery regardless of the viewer's accommodation state.

The "**Pinlights**" always-in-focus AR display [50], by using a see-through sparse backlight mechanism behind an LCD, generates a tessellated series of retinal projectors capable of a wide FOV but limited in angular resolution.

4.2 Virtual Retinal Displays

Another method for projecting light directly onto the retina is by conditioning a narrow bundle of collimated rays and directing it into the eye in a steerable manner **(Figure I.15a**). By modulating the intensity and colour of the bundle of rays while raster scanning the light across the retina at a high frequency, full image generation is possible. This technique is called virtual retinal display, or retinal scanning display, and was first proposed by Kollin in 1993 [74].

A virtual retinal display was demonstrated in conjunction with micro-electromechanical system (MEMS) deformable mirror membrane devices (DMMDs) by McQuaide et al. [51]. Built on the principles of a Maxwellian view display, a laser is scanned onto the DMMD, which then reflects it through a series of mirrors directly into the pupil—forming an image on the retina. The surface convexity of the mirror is controlled by the applied voltage, thereby controlling the focus of the displayed objects.

Schowengerdt et al. [52] showed an achievable accommodation range of 0D to 14D by the DMMD. Creating a volumetric display by application of deformable mirror membranes was attempted by Schowengerdt and Seibel in 2006, where the membrane curvature was synchronized with per-frame swapping between two different images, thereby displaying the

images at different depths simultaneously. The prototype demonstrated a depth range of 0D to 16D in a continuous fashion.

More recently, in 2017 Jang et al. [53] demonstrated a Maxwellian view style virtual retinal HMD with multiple projectors and a holographic optical element (**Figure I.15b,c**). While the Maxwellian view capability of the display extends the depth of field, the small EB limitation is overcome by employing eye tracking and a moving EB.

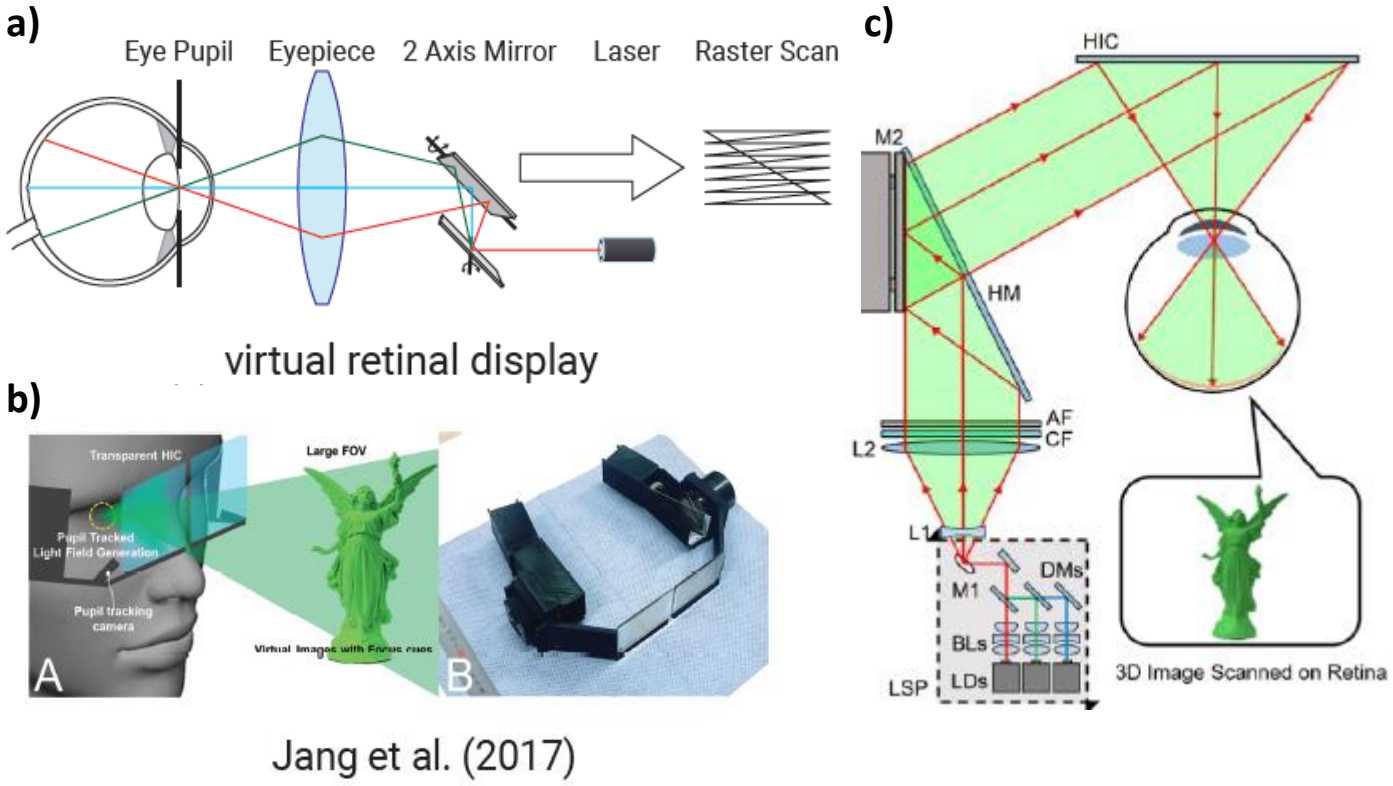

Figure I.15. Virtual retinal display layout: Optical scheme, b) prototype example [53], c) prototype's projection scheme: LDs – laser diodes, BL – beam-shaping lenses, DMs – dichroic mirrors, M1 – MEMS mirror 1, LSP – laser scanning projector, L1 - beam-shaping lens, L2 – collimation lens, CF color balancing filter, AF – attenuation filter, HM anti-refraction coated half mirror, M2 – fast steering mirror, HIC holographic image combiner.

4.3 Multiplane Displays

Multiplane displays are capable of generating virtual images at more than one focal depth . In the classical multiplane approach introduced by Rolland et al. [75] in 2000, virtual content displayed at one of the focal planes have correct focus cues, but generating virtual content

between the focal planes requires interpolation leading to less-correct focus and loss of resolution (**Figure I.16a**). These displays have large computational demands for decomposing and interpolating the virtual content and complex optical hardware that doesn't typically lead to a wearable form-factor. Much work has been done on improving scene decomposition and gaze-contingent multiplane capabilities ([75] and [76]). There are two approaches for generating multiplane displays: optical path multiplexing and temporal multiplexing.

In 2004 Akeley et al. [54] demonstrated the benefits of fixed-viewpoint optically-multiplexed multiplane desktop displays with a prototype capable of generating near-correct focus cues without any need for eye tracking (**Figure I.16b**). In 2009 Love et al. [55] used two fast switchable lenses per eye to create a time-multiplexed four-plane display. In 2014 the work by Hu and Hua [57] demonstrates a see-through, time-multiplexed, multiplane display in the form of a wearable NED utilizing a 1 kHz DMMD.

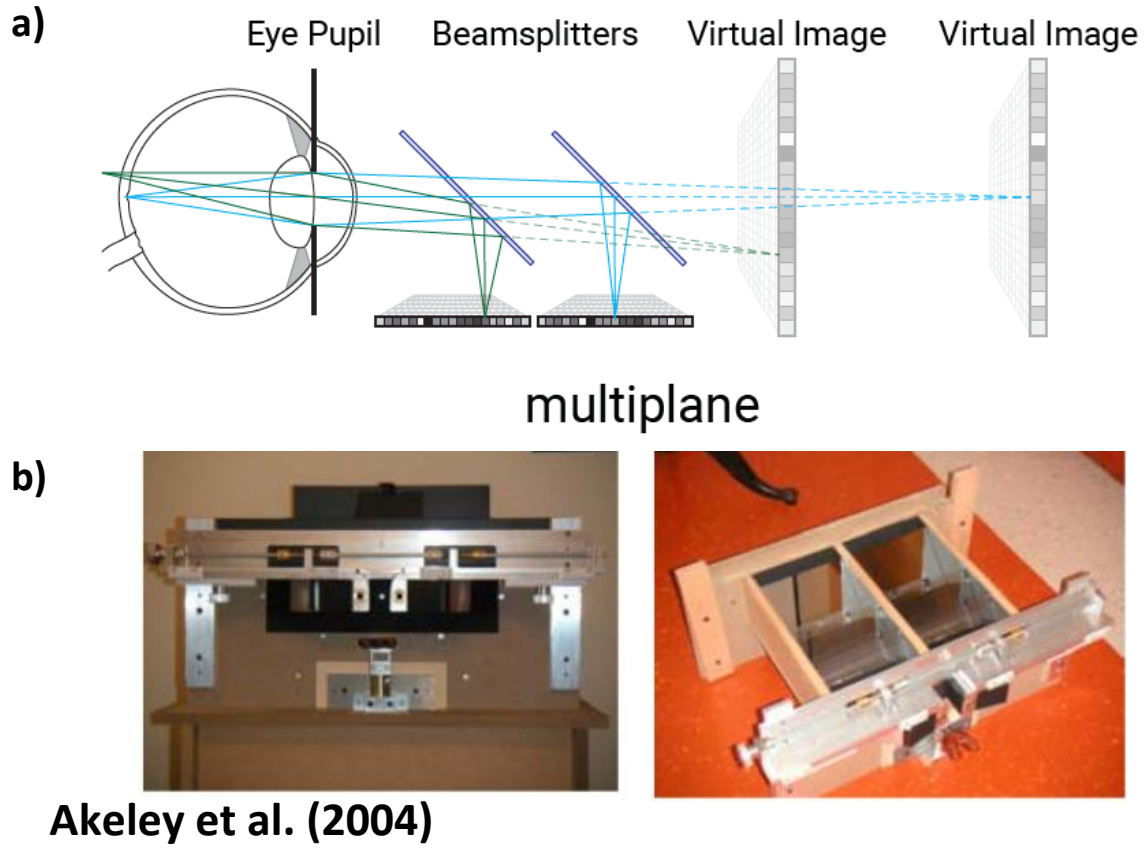

Figure I.16. Multiplane display layout: Optical scheme, b) bench prototype example [54]

Unfortunately, such a display design offers good resolution, but only with a small 32° FOV. In 2017 Mercier et al. [76] developed a bench-top prototype combining a three-plane display, gaze tracking, and focus tracking to demonstrate that despite multiplane displays showing near-correct focus cues without eye tracking, correct scene decomposition is dependent upon eye position. This means that eye tracking is required for displaying high quality images. In 2018 Rathinavel et al. [61] presented an extremely fast, time-multiplexed, multiplane display supporting 280 distinct depth planes. The density of depth planes is indistinguishable from a full volumetric display and shows the great potential of >20 kHz operating DMDs. However, the optical complexity in such approaches has thus far challenged their practicality in increasing FOV and decreasing form-factors.

In 2017 as an alternative to multiplane displays, Matsuda et al. [59] demonstrated a focal surface display, which uses a phase-only SLM to bend the focal plane of the image into a complex surface. These scene-optimized surfaces can improve the focal accuracy across simple scenes. They also propose combining multiple focal surface images into a multiplane focal surface display which would greatly reduce the number of focal planes required to accurately represent a scene.

Akin to multiplane planes, Konrad et al. [63] study an interesting scenario called monovision, where each eye is subjected to one focal depth, with one eye's focus being near and the other eye's focus being far. This approach leverages binocular single vision and suppression in an attempt at reducing VAC, with a loss of resolution. Detailed perceptual studies on monovision have also been conducted in 2017 by Johnson et al. [77] and Koulieris et al. [78] which found that not only did viewer comfort and visual performance not improve, but **monovision display**s do not drive accommodation to the simulated distance meaning they **do not resolve VAC**.

4.4 Varifocal Displays

Related to multiplane displays, varifocal displays elect to show a single, but moveable focal depth (**Figure I.17a**). The core idea being that the human eye can only focus at a single depth at a time, so if the displayed focus can be changed fast enough and the correct depth to display is known,

only this one focal depth need be displayed. A tunable lens system combined with a spherical mirror is used in the work of Liu et al. [62], presented in 2008, producing a small FOV but having a good accommodation range capable of switching depths within 74 ms. The study described in [63] by Konrad et al. also takes advantage of an electrically tunable lens system as relay optics and demonstrates a similarly small FOV VR prototype. Their solution switches depth from one extreme to another within 15 ms, and provides a better accommodation range. In 2017 Aksit et al. [64] uses holographic optical elements for intermediate image formation before relaying the final image into the eye, offering a wearable form-factor with good FOV (**Figure I.17b**). All of the above-mentioned varifocal display designs, suffer various drawbacks either in form-factor, depth-switching speed, or FOV.

Several studies show evidence that supporting accommodative cues through a varifocal mechanism improves visual comfort [77] and user performance [63]. Just as with always-in-focus displays, objects not located at the current focal depth should have appropriate rendered blur to provide the appropriate focal cues.

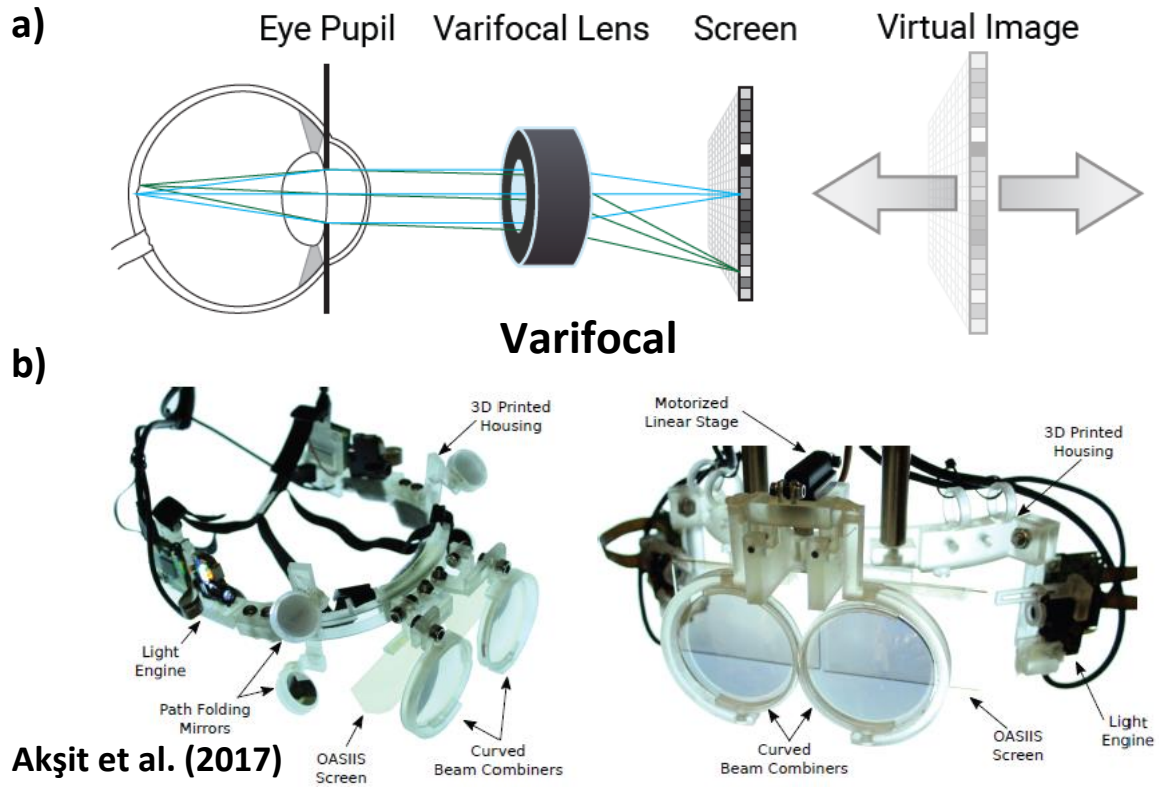

Figure I.17. Varifocal display layout: Optical scheme, b) prototype example [64]

4.5 Light Field Displays

Light field displays, in addition to the traditional color, intensity, and position, provide angular control of the light generation leading to capabilities for correct parallax, stereoscopic view, and multi-view (**Figure I.18a**). With enough angular resolution they can also depict correct focus cues in NEDs. Two approaches for creating light field displays have been presented thus far, integral and multi-layer. Integral imaging, first proposed by Lippmann [79], places an array of micro lenses, an aperture array, or both in between the viewer and the image such that as the viewing angle changes, so does the visible image (**Figure I.18b**). Alternatively, a multi-directional backlight can achieve the same effect as shown in 2013 by Fattal et al. [80] . Unfortunately, current implementations of integral light field NEDs sacrifice the spatial resolution for generating angular resolution. Lanman and Luebke [67] introduced a near-eye light field display that uses an array of microlenses, resulting in a very thin and light form-factor VR NED with a good possible field of view, but with a heavily compromised resolution. In 2014 Hua and Javidi [69] demonstrated a NED for AR applications that combines advancements of free-form relay optics with a computational integral imaging methodology. Unfortunately like with most designs the transition from VR to AR was accompanied by a loss in FOV. In 2015 Aksit et al. [81] used a pinhole mask in front of an LCD to create a light field at the eye and thus increase the apparent depth of field, but at the expense of resolution.

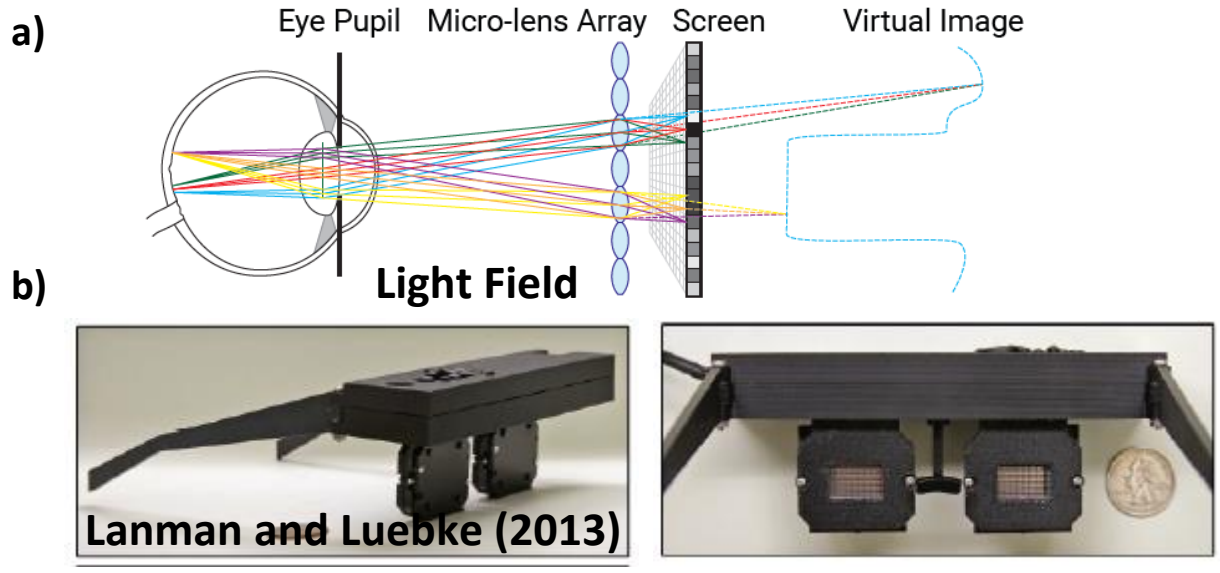

Figure I.18. Light-field display layout: Optical scheme, b) prototype example [67]

Multi-layer light fields use stacked SLMs with a single illumination source to add the angular control of the light. This approach works to increase the resolution above the integral approach, however it suffers from a loss of contrast as light must pass multiple SLMs and has a resolution limit from the compounding diffraction. In 2013 Maimone and Fuchs [68] detailed an AR near-eye multi-layer display with no reflective, refractive, or diffractive optical elements capable of occluding the real world. While having an impressive focal range, and decent FOV, the display suffered from noise, low resolution, and poor contrast. In 2015, Huang et al. [70] demonstrated a prototype which employs two LCDs and a pair of classical magnifiers. This light field stereoscope was capable of producing a wide diagonal FOV and an improved image resolution.

4.6 Holographic Displays

Holography, both analog and digital, can encode all optical complexities into a complex wavefront, enabling possibility of compact eyeglasses style near-eye displays. **Computer-generated holography** (**CGH**) simulates the physical processes of an optical hologram recording and reconstruction using numerical methods. As holographic displays work on the principle of diffraction, computing the diffracted wave field of light through a finite aperture is fundamental to holography. Holographic displays aim at creating an intensity image via interference of the diffracted wave field that is resulted from the modulation on the SLM (hologram) (**Figure I.19a**). Existing SLMs support only either amplitude or phase modulation, and typically a phase modulating SLM is preferred due to its higher diffraction efficiency. The phase on the SLM describes the delay introduced by the SLM element to the incident wave phase. Computing the appropriate phase modulation pattern on the hologram plane is the core challenge of CGH.

Many NED designs combine a digital holographic projector with various see-through analog holograms (G. Li et al.[82] and Maimone et al. [35] **Figure I.19b**). In 2020, the design by Maimone and Wang [83] use holographic optical elements and demonstrate compact form factor for virtual reality with a modest EB size. Holography also offers the power of correcting for any aberrations both in the optics or the eye lens (Yeom et al. [84]), along with rendering images with depth cues. Holographic displays suffer three major problems: EB size, holographic image quality

and computational cost. Current implementations of holographic near-eye displays have a very small EB and are computationally expensive. Due to the conservation of etendue, the EB sizes of holographic NEDs are often very small, sometimes even less than 1mm (Maimone et al. [35]).

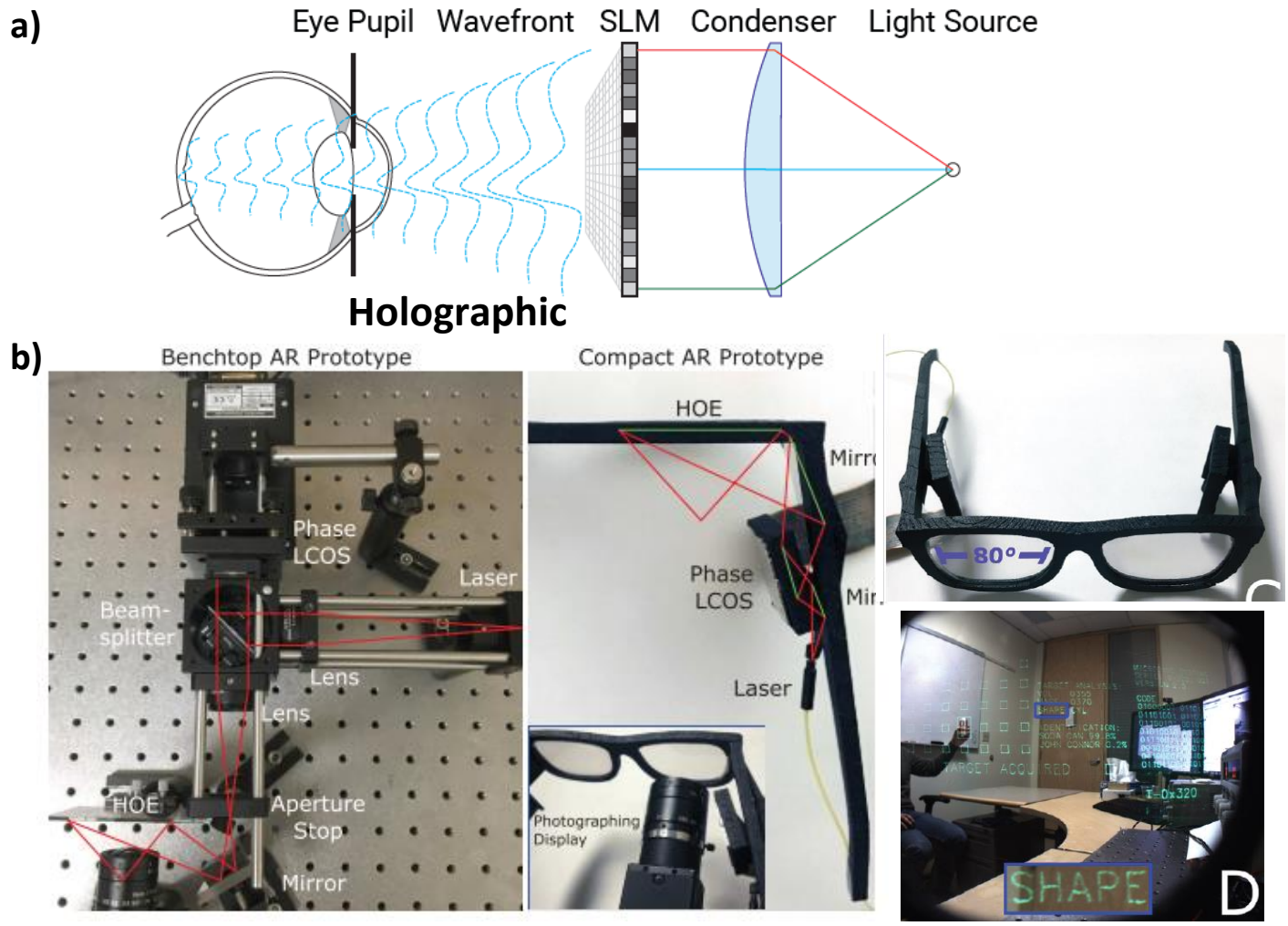

Figure I.19. Holographic display layout: Optical scheme, b) prototype example [35]

Unacceptable image degradation occurs if the eye pupil is not in the EB region. However, the EB can be expanded either by steering the exit pupil by tracking the eyes to relay images onto the retina, or create an array of exit pupils that collectively expand the EB (Jang et al. [53]). Other passive etendue expansion methods such as using scattering elements (Kuo et al. [85]) or diffractive/holographic optical elements (Xia et al. [86]) have also been proposed in 2020. While holographic optical elements have been used for a long time in NED designs enabling almost

eyeglasses-like thin form-factor, and a very wide FOV (Ando and Shimizu [46] and Aksit et al. [64]), true CGH NEDs are a relatively recent topic.

Holography promises good angular resolution with a thin form-factor by using phase and sometimes amplitude SLMs to manipulate of the wavefront of light causing interference to generate the image. In 2017, CGH based NED designs for VR and AR have been presented by Maimone et al. [35], showing superior quality imagery, the ability to provide per-pixel focus, wide FOV and eyeglasses form-factor. For such displays, however, a small EB, large computing demand, and theoretically limited resolutions still remain major concerns. In 2017 Shi et al. [72] demonstrated a real time rendering pipeline for computer-generated holograms using spherical waves and achieving high resolution and a much wider EB. Holographic displays precisely modulate the wave function of the image arriving at the pupil using a digital hologram displayed on a phase-only spatial light modulator (SLM) such as a phase-only liquid crystal on silicon (LCoS) panel. Conceptually, these displays can also provide accurate focus cues, vision correction, and non-Lambertian effects.

5 CEA Retinal Projection Display Concept overview

5.1 General principle of the concept

Conventional NEDs are strongly limited by optical design constraints related to the basic principles of geometric optics. To overcome these constraints and offer a device that meet the customers' expectations, innovative optical architecture concepts are studied by several research teams around the world. Among them a research team of CEA-LETI develops an unconventional image projection AR-prototype. In 2013, the laboratory proposed an ambitious concept based on the association of technologies in integrated photonics, holography and the implementation of diffractive effects. The main idea of the prototype is to emit directly the light-field into the retina and let the eye to focus them into it. It let us to design a smartglasses prototype without an optical system between the viewer's eye and the display.

Most development on smartglasses for AR applications is based on a conventional imaging scheme built on the following steps:

1) Sensing: perception of the surrounding environment by sensors [**camera**].
2) Processing: computation of the digital image in relation to the surrounding field of view [**micro-processor**].
3) Generating: a display creates the analogic image [**microdisplay**].
4) Transforming: the real image is transformed into a virtual image seen at large distance to be seen by the viewer [**optical system**].
5) Propagating: the photons produced in the image creation process are brought to the eye [**free-space or waveguide propagation**].
6) Combining: the virtual image is superimposed on to the surrounding scenery [**semireflective, grating, or holographic elements**].

These technological functions are difficult to integrate in a compact way, and most of the devices produced for AR applications are still closer to a smart helmet than to smart glasses. Based on this analysis CEA-LETI has tried to find an unconventional design that takes as a starting point an idealized image of lightweight, discreet smart glasses that has been brought to the consumer and uses alternative technologies to achieve a thin, light, and bright see-through device. We found that the difficulties encountered in the optical system design are due to the steps 3 to 6 that concern the manipulation of the image from the display to the eye. To circumvent these difficulties, an obvious solution is to emit directly the wavefronts related to the image in front of the eye. This led CEA-LETI to develop a new kind of display that mixes integrated photonics

One can see the difference between conventional and unconventional retinal imaging in **Figure I.20**. At a large distance each point of an image impacts the eye as a planar wavefront characterized by its wave vector $\vec{k}_p$ (**Figure I.20.a**). As the image comes closer, the wavefronts associated to the points of the image are no more planar. The eye has to accommodate to correct the curvature of the wave. As a result, a display located near the eye can't be seen with a good resolution. Each pixel emits a spherical wavefront $\vec{k}_s$, on a direction perpendicular to the display, that can't be corrected: the image is blurred (**Figure I.20.b**). To allow clear NED image formation, the conventional solution is to use a collimating lens that transforms the spherical wavefront

emitted by the pixel into a directive planar wavefront $\vec{k}_p$ (**Figure I.c**). However, the use of the lens induces severe constraints due to the pupil management, in particular on the strongly related parameters of FOV and EB. These constraints are particularly difficult to overcome in a see-through design where the displayed image has to be seen superimposed to the scene. Combiner or waveguide solutions have to be used to redirect the wavefront coming from the optical system [87], [88]. In order to improve near-eye optical design, light field displays, described in **Section 4.5**, have been developed (**Figure I.20.d**).

Another approach is to emit a coherent holographic wavefront that directly codes the image to be displayed this solution known as holographic display has been described in paragraph 4.6. In this case a phased array emits a planar holographic wavefront $\vec{k}_h$ with encoded phase (**Figure I.20.e**).

The CEA-LETI has introduced a concept of a lens-free near-eye display based on coherent multi beam emitters. In this design a set of emitting pixels generate multiple directive spherical wavefronts $\vec{k}_s$. If the wavefronts are phase adjusted, multiple interference can focus the beams onto a single image pixel (**Figure I.20.f**).

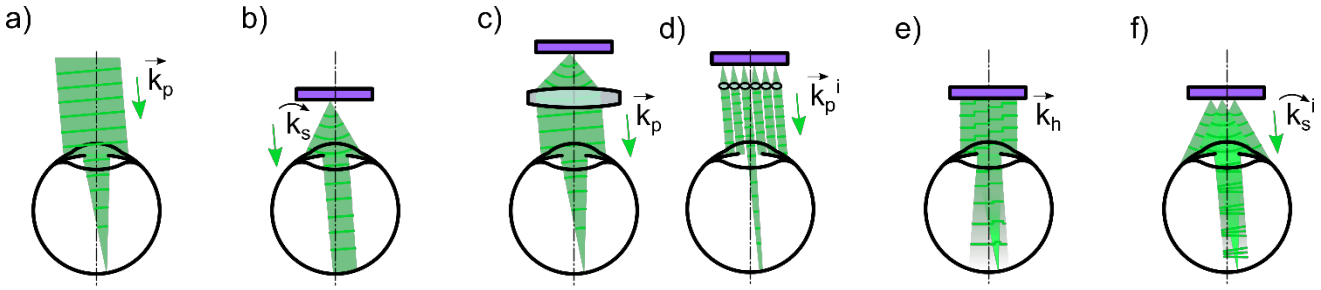

Figure I.20. Principle of various conventional and unconventional eye imaging configuration: a) point at infinity, b) near to eye display, c) collimating lens, d) integral imaging, e) phased array and f) multiple beam interferences.

The conceptual ideal of the concept is the next: several light fields are projected towards the eye from an integrated photonic circuit made up of thousands of waveguides. This transparent circuit is placed on the surface of a spectacle lens. An artistic representation of the concept is presented in **Figure I.21.** An array of lasers injects light into a photonic circuit of waveguides. This circuit consists of waveguides intersected by electrodes. Above the intersection points there is a

switchable out-coupling grating layer which serves as a diffractive grating to locally extract the light from the circuit. These extraction points form an **Emissive Points Distribution** (**EPD**) on the surface of the glass of eyeglasses. The orientation and the phase of the emission points are modified using a pixelated hologram deposited on the circuit. The light beams are projected into the eye where they are self-focused by eye lens into the retina to form an image.

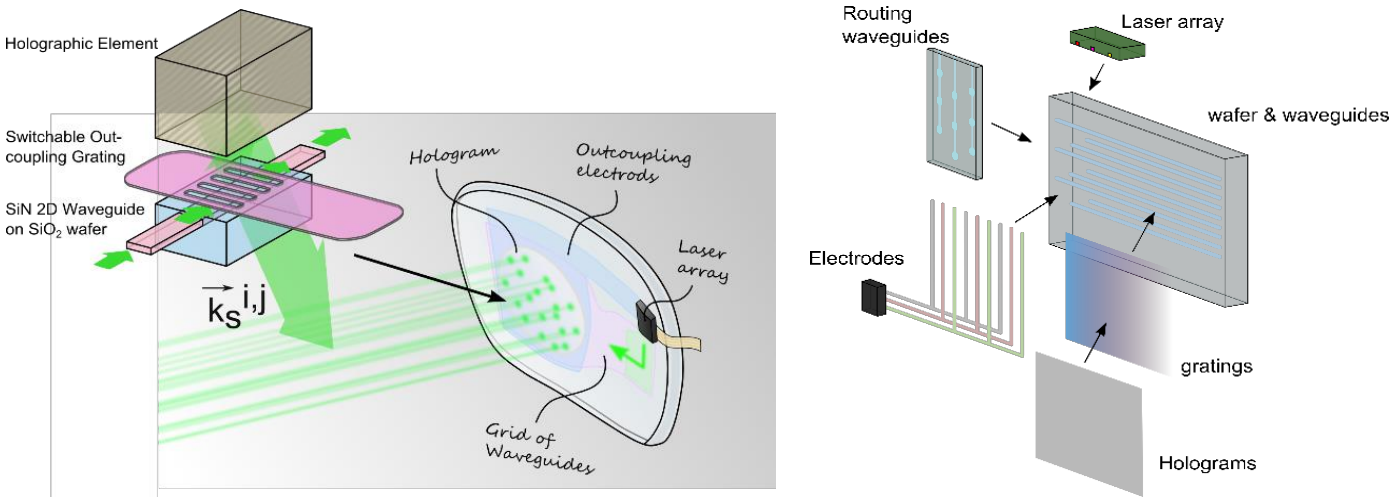

Figure I.21. Artist view of the see-through display device with a zoom on one emissive point element and the principle building blocks

The essential part of the concept is the **self-focusing effect** that allows lensless NED imaging. The self-focusing effect uses the interference of several spherical wavefront coming from NED's emissive points distribution. The combination of spherical wave fronts from several points then forms a planar wavefront which can be directly focused naturally on the retina like an image at infinity. This operation is comparable to the formation of wave fronts by Optical Phased Arrays which use the Huygens-Fresnel principle. The phase of the spherical wavefronts must be precisely tuned to properly form the planar wavefront. Otherwise, the self-focusing effect is disturbed by interferences without phase coherence and does not allow a well-defined focusing.

6 Research challenges and contributions

The primary contribution of this dissertation is the **theoretical description and experimental validation of the self-focusing effect for the NED-prototype image formation conceived in CEA-LETI**. It is particularly oriented towards the understanding, simulation and experimental evaluation of diffractive effects. The main challenges are described in three chapters.

In **Chapter II** I introduce the **basic notions** for our innovative unconventional image projection approach. I explain the main aspects of the prototype's operational principle, the imaging process of the unconventional display and propose an addressing solution for it. Each emissive point shall be able to be activated or deactivated simultaneously with the corresponding **Emissive Point Distribution (EPD)**. I overview the basic addressing approaches for conventional displays and explain the design limitation for such implementations in our case. The **EPD is a corner stone of the projection system**. An approach to find an optimal distribution is shown in and some guidelines are given to analyze it. I discuss several design issues for such self-focusing display, categorize design criteria and develop necessary conditions for optimal image formation. The position of the **self-focused spots on the retina called spels** is defined by the emission orientation of the collection of beams. Using simulation tools built in the laboratory, I evaluated the **performance of spel formation** according to emissive point distributions. These distributions are spatially distributed on the surface of the screen according to functions imposed by the addressing constraints of the screen. I propose a **metric to evaluate quality of spel-formation** and **simulate self-focusing projection** of our concept and analyze it.

Chapter III provides evidence of self-focusing effect describing its **validation process** with various pinhole distributions which imitates EPDs. I highlight the basic idea of the **experimental setup** to imitate the unconventional NED concept operation for self-focusing effect. I describe the setup and characterizes its two main parts: the **emissive system** and the **imaging system**. The emissive system is basically imitating our NED concept. The imaging system is a simplified eye model. I detail solution to overcome specific issues related to the spel evaluation experiment and the dynamic range. I demonstrate **experimental evidence** of the influence of the source position (shift and rotation) and of the eye pupil size variation. Finally, I present the results of self-focusing

simulation with a variation of the spectral characteristics to evaluate the **impact of the temporal coherence** on the image formation.

Chapter IV investigates image formation capability of self-focusing effect for a future development of unconventional image projection display concept. The task is accomplished with simulations based on **simplified spel-formation approach** and then **validated experimentally** with a **self-focusing image formation setup**. The rigorous spel-formation algorithms based on multiple source interference are approximated by two Gaussian functions called **Double-Gaussian (DG) model**. This model is used for two reasons: 1) to qualitatively evaluate the behaviour of the concept prototype as an image-forming device and 2) as a kernel of spel-superposition image formation algorithm. For theoretical evaluation of spel formation quality **γ-parameter** is introduced in addition to SNR. I perform **image formation simulations** with developed spel-superposition algorithm. **Simulation results are experimentally validated** on the assembled self-focusing image formation setup. A natural constraint for the display prototype so-called **resolution/sharpness conflict** is discussed**.**

7 Conclusion

Present state-of-the-art for Near Eye Display domain is depicted along with Human Visual System and let us present main issues related with NEDs and, in particular, our concept. Various existing approaches to achieve functionality performance and aesthetics are discussed, with emphasis on common, general-purpose designs. This work is accomplished by a bibliographic study to understand the particular design constraints and key-factors for AR NEDs. The comfort and immersion requirements demand the use of a complex optical system integrating in particular a combination element called "combiner". The formation of the virtual image of the screen by the device is accompanied by constraints related to the management of the pupils which limit the FOV and EB while leading to bulky systems. Known unconventional solutions are generally based on imaging concepts designed in an angular rather than a spatial way. Angular vision, even if it seems less familiar to us, is the central phenomenon of human vision system which perceives objects above all by their angular size. The angular resolution of the eye in the foveal and peripheral zone, its response to a dynamic signal, the influence of the pupil, all these elements

have been analyzed with the aim of optimizing our retinal projection device and with a view to the construction of an experimental digital analysis device simulating the human eye. On the basis of this knowledge, the thesis focused on the diffractive part which constitutes the physical phenomenon of image formation on the retina – **self-focusing effect**. To overcome the traditional optics between the eye and the display, our concept is based on a NED emitting angular beams, self-focused by the eye. This effect is based on the emission of a collection of elementary beams, tuned in phase and emitted along a common angular direction. Their penetration into the cornea and their propagation in the lens and the vitreous humor produces, by multiple interference, a self-focused spot called spel (elementary spot). Self-focusing effect is described in detail and simulated in **Chapter II**, experimentally validated in **Chapter III** and simulated for Image formation and compared with experimental results in **Chapter IV**.

Chapter II: Self-focusing effect: analysis, implementation and simulation

In the progress of scientific investigation, <...> doubt must necessarily succeed often to apparent certainty, and must again give place to a certainty of a higher order.

Thomas Young

In this chapter I describe the self-focusing effect implementation into our lensless NED concept. In the **Introduction** I provide some basic analogies to understand our concept and present some previous works related to the self-focusing effect in the visible range.

In the **Section 2** I show the general principal of the NED concept and point out the design trade-offs. I introduce basic related notions for our unconventional display such as **E**missive **P**oint (EP), **E**missive **P**oint **D**istribution (**EPD**), **E**missive **U**nit **C**ell (EUC) and **spel** (elementary spot self-focused on the retina).

The essential topic to be discussed is how I propose to solve the addressing problem for our unconventional image projection display. In the **Section 3** I briefly overview the basic addressing approaches for conventional displays and explain the design limitation for such implementations in our case. I explain the image projection process of our unconventional display and propose an addressing solution for it.

The EPD is a corner stone of the projection system. An approach to find an optimal distribution is shown in the **Section 4** and some guidelines are given to analyze it. I discuss several design issues for such self-focusing display, categorize design criteria and develop necessary conditions for optimal image formation. I present a method for producing such distributions taking into account proposed design considerations and possible trade-offs.

Finally, in the **Section 5** I provide a theoretical analysis of the self-focusing effect and present our self-focusing simulation model. I propose a metric to evaluate quality of spel-formation and simulate self-focusing projection of our concept. Then, I discuss the results obtained with various EPDs. Lastly, I present possible EPDs for experimental validation of self-focusing effect.

1 Introduction

The closest analogy to our concept could be a multiple interference phenomenon that was firstly described by Young with his double-slitexperiment [89]. Constructive interference produces so-called Young pattern or Young fringes (**Figure II.1**). The pattern is described as distinct peaks of same widths but different amplitudes due to the apodization by an envelope. Adding extra slits with constant distances makes peaks thinner, but it does not change their number and their positions. The width of envelope depends on the width of the emissive slits and the distance between the peaks depends on the period of the slits.

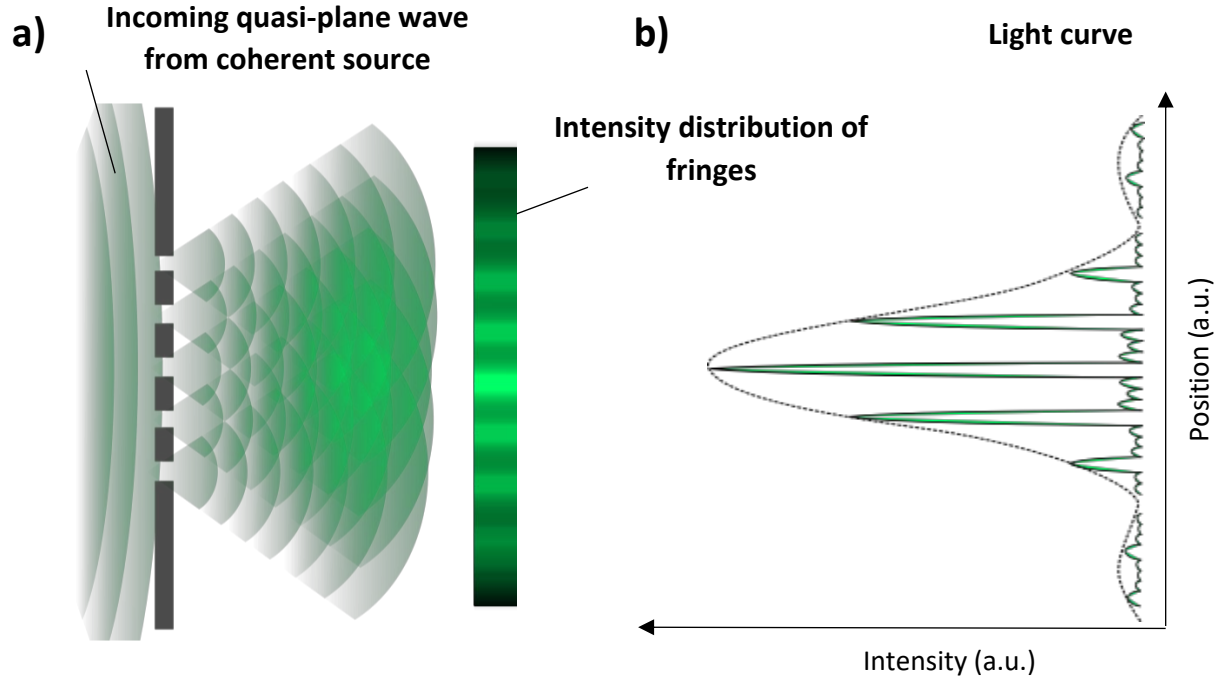

Figure II.1. a) Multiple interference, one dimensional five slits case, general principle. b) Diffraction envelope over interference fringes: distinct peaks of same widths and different amplitudes limited by an envelope that depends on the size of emissive slits. In this example, the five slits form the EPD and the diffraction pattern corresponds to the spel.

A very rough approximation of our concept is to consider a two-dimensional distribution of pinholes or apertures illuminated by monochromatic light. The ***ultimate design goal*** is to find the ***optimal Emissive Point Distribution that produces a self-focused pattern*** with a clear central peak and weak surrounding secondary peaks. This could be done if the Emissive Point

Distribution has in the same time two contradictory qualities: randomness or heterogeneity and uniformity or homogeneity of Emissive Points. This heterogeneity/homogeneity trade-off is complicated regarding the feasibility requirement. Furthermore, the emissive point in our concept is not just a simple pinhole, but a complex technological mix of photonics, electronics and holography. ***Each emissive point is an intersection between waveguides that bring light and electrodes that activate light emission with a particular intensity in a given angular direction through a holographic optical element (HOE) that can be considered as an oriented Bragg grating.*** Therefore, our EP has physical dimensions and there are finite possible allocations on the display surface and other requirements that will be discussed further.

Experimentally, the self-focusing effect (or lensless focusing) in the visible range of electromagnetic spectrum was validated by Hong. et al. in 2006 for optical data storage [90] (**Figure II.2**). The idea uses the same Huygens-Fresnel principle for lensless focusing: we can assume that a monochromatic optical pattern is a superposition of unfocused plane waves series converging from many different directions.

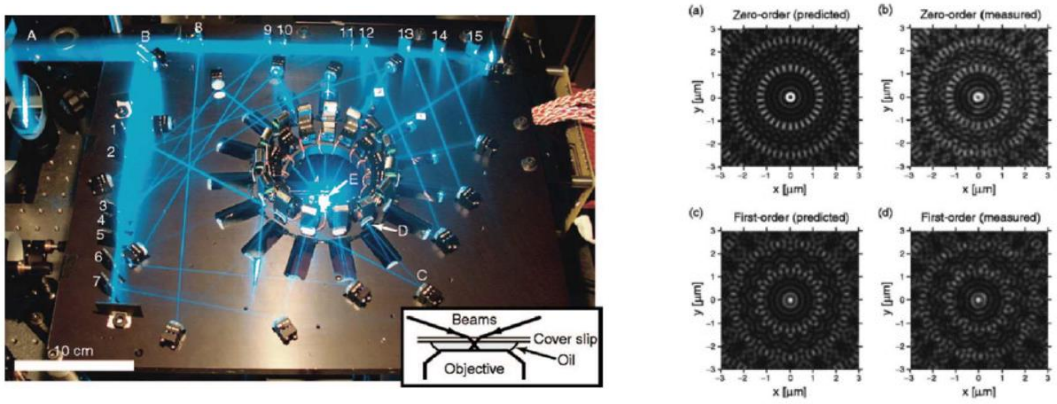

Figure II.2. Experimental application of the self-focusing effect for optical data storage [90]: on the left view of the setup, on the right the result of focusing for two orders of Bessel beam function (a) and (c) theory, (b) and (d) experiments.

A close technological analogy to our concept that has already found wide application is Optical Phased Arrays (OPA). In OPA an antennas array is used to shape the radiation using the phase of electromagnetic waves (**Figure II.3 a**). The Young's double slits experiment could be seen as the simplest optical phased array. Sun et al. showed in 2014 the possibility to create arbitrary image pattern with specific phase distributions on an antennas array [91].

The main similarity between this concept and ours is an emissive array operating in visible range fabricated as integrated photonic circuit with a high antennas' density (**Figure II.3 b**). However, there is an essential difference in the final wave front treatment: Sun et al. propose the use of a complex phase distribution obtained by the Fourier transform of the image to be projected. Therefore, the whole array is used simultaneously to produce the whole image. Consequently, each antenna emits a wave front according to this phase pattern for the corresponding image. However, there is also a quite important difference from image formation side. The OPA's approach has a strong constraint related to a moderate Field-of-View (FOV) [92]. The FOV of the final image directly depends on the emissive antenna size, which produces the resulting envelope.

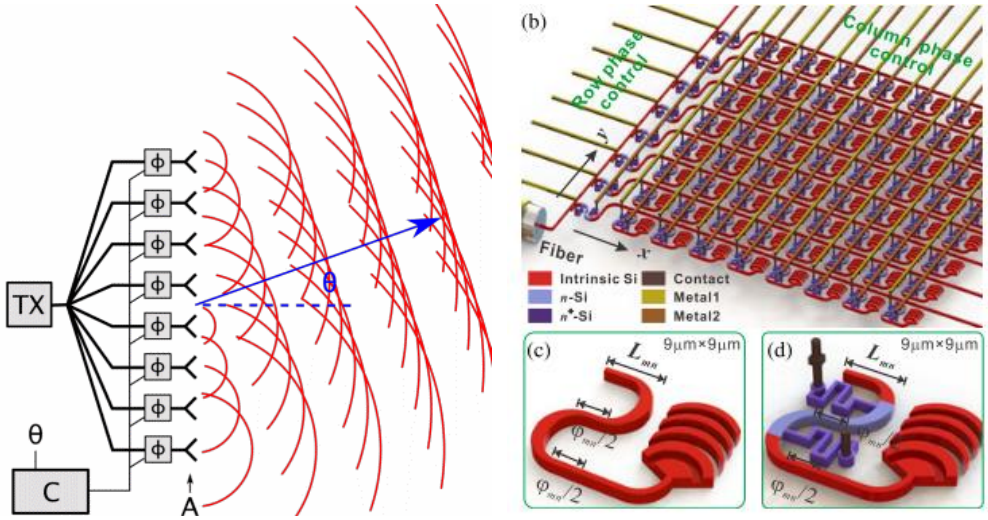

Figure II.3. a) Radar phased array can create a quasi-plane wave with arbitrary direction θ [93] b) Application of OPA in photonics: Sun et al. presented their approach to project an arbitrary image using a complex phase distribution

In our case, we hope to exceed this limit by introducing the geometric approach with angular orientation of emissive points grouped into ensembles. The envelope remains limited by the size of the emissive points but it is oriented angularly. Therefore, our approach is rather to produce the final image onto the retina as a geometrical combination of simple self-focusing patterns resulting from elementary coherent in-phase wavelets within one emissive distribution. Each emissive point associated with a particular distribution should emit wavelets in the same phase to form a quasi-planar wave front that is focused onto the retinal by the eye lens.

2 Self-focusing effect implementation

2.1 General concept

A conventional display is composed of pixels, elementary units of an emissive surface or a screen. Following the simple rules of geometrical optics, one can find the projection of such a pixel on the retina through a lens combination. Our concept proposes another approach to project image onto the retina. It is an unconventional approach to avoid an optical system between the viewer's eye and the display. Each pixel of a conventional display produces a spherical wave front and there is two conventional approaches to make it planar to let the eye focus the image on the retina. The first approach is to place the display at least to the near point distance (about 25 cm for a "normal eye"), the case of free viewing or so-called Newtonian viewing [94]. The second approach is the case of near-eye displays: an optical system is placed between the screen and the eye to make the incident wave front planar; otherwise, the wave front curvature produced by pixel cannot be corrected by the eye lens.

There are various unconventional solutions to design a NED without any intermediate optics between the viewer's eye and the display, some of them were overviewed in the previous chapter. Our approach relies on combining multiple coherent in-phase spherical wave fronts from **E**missive **P**oints (**EP**s) according to Huygens-Fresnel principle to produce a planar wave front envelope. This resulting wave front is quasi-planar and it can be focused by the eye lens onto the retina as a self-focused simple pattern or **spel** (from the French "**sp**ot **él**émentaire" or elementary spot). We call an ensemble of such **EP**s an **E**missive **P**oint **D**istribution (**EPD**). Therefore, each spel corresponds to a defined EPD – a number of EPs, and not simply to one emissive point as in a conventional case (pixel). The angular orientation of each EP is given by the corresponding angular orientation of its wave vector $\vec{k}$ (**Figure II.4)**.

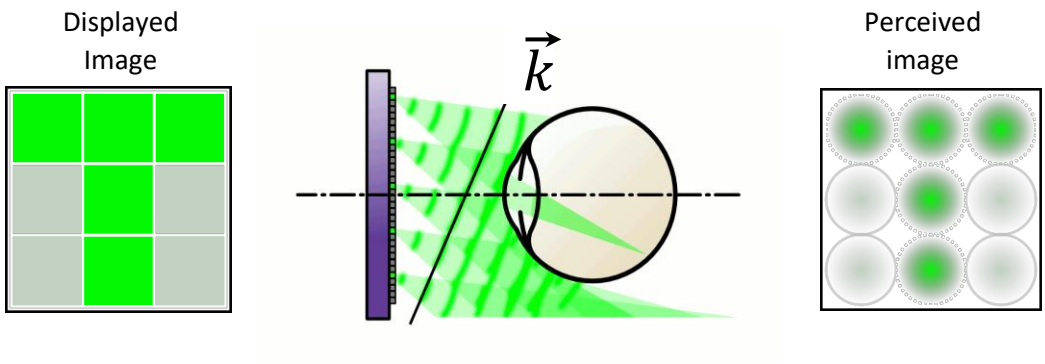

Figure II.4. An unconventional display working on the principle of self-focusing effect. A collection of emissive points distributed on the system aperture produces a beam interference following a given angular direction $\vec{k}$. it generates a planar wavefront that becomes a focus signal (spel) on the focal plane after passing through the eye lens

There are two key aspects the **operational principle** and the **imaging process** itself. The device is a merge of such technologies: photonics (a laser array and a waveguides grid), electronics (an activation electrodes network) and holography (a hologram layer).

Supposing, we would like to display an image as shown in **Figure II.4**. The first step **(1)** would be to generate the light by the laser. Then **(2)** it should be delivered via routing waveguide to addressing the waveguides grid. Further, **(3)** via waveguides grid, the light should travel without critical loss to emissive points. This stage is already a complicate task and it has been addressed in a dedicated research [95],[96]. Finally, **(5)** the electrode network should activate light emission and **(6)** the hologram layer should provide the required angular direction and phase for each EPD.

Let's take a look how such a system forms an image following a scanning principle. Briefly, for a 3x3 pixels image, the display activates 9 different EPDs, each forming a spot on a particular angular direction. With a laser array containing 3 lasers, the whole process is divided in three stages. Firstly, the display focalizes on the retina the three points corresponding to the first column, with different output power corresponding to the three lasers and the three angular directions. Secondly, the system projects the next column of image. Another set of amplitudes is given to the three laser sources and 3 other EPDs are activated in order to address the

corresponding angular directions. Thirdly, the same process is repeated for the last three image pixels. Due to vision persistence, the whole image observation is possible (**Figure II.5**).

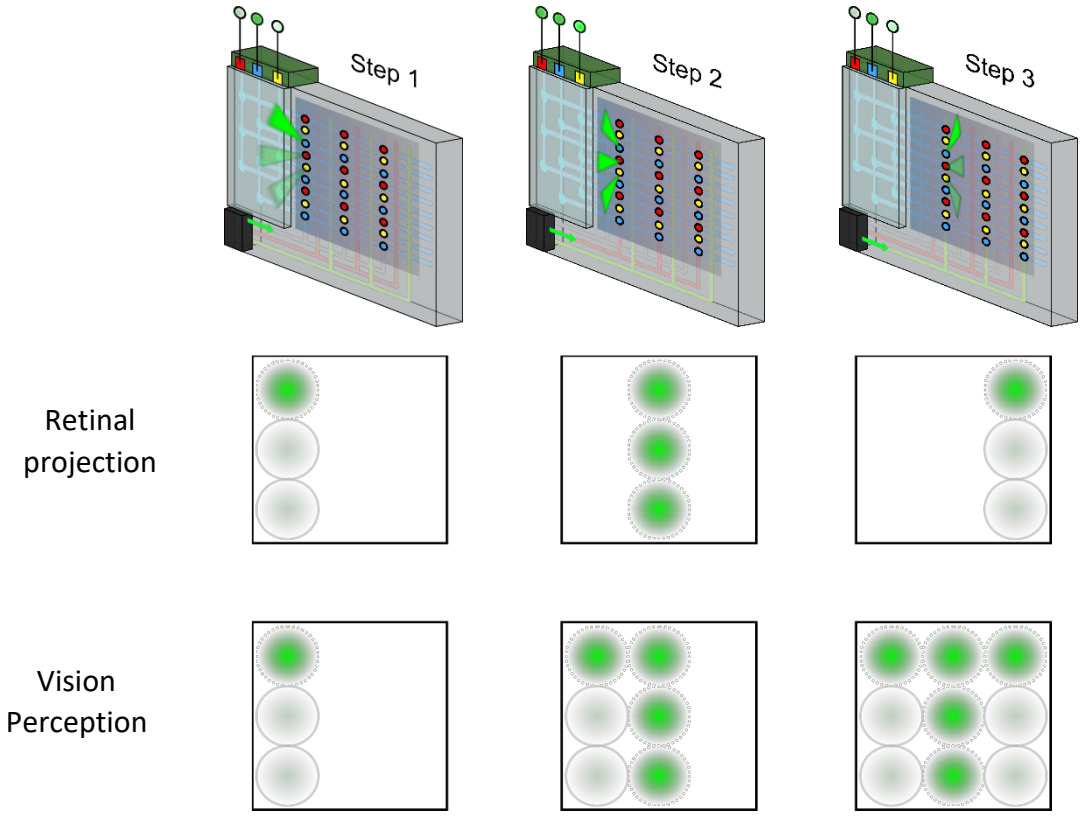

Figure II.5. Principle of the concept operation: three-steps projection of the 3x3 pixels image: on the left- imaging process and on the right - projection array activation process. For clarity only one beam emerging from an EPD is represented in the figure.

2.2 Emissive Points Distribution for self-focusing

Another important issue is the study of the best possible applicable EPD, which means we should know such parameters as the **number of emissive points** and the **kind of distribution**. The quality of a spel is directly related to these characteristics. Theoretically, the best achievable spel, corresponding to an Airy disk, is produced by a surface entirely covered with emissive points. This case is almost identical to the incidence of light from infinity through an aperture with a size equal to the emissive surface. Reducing the number of emissive points leads us to search a distribution, which has much less emissive points, but at the same time still focalizes a spot with acceptable quality. It has been shown that periodic types of EPD produce periodic side-peaks

around the central spot, while random ones reduce them almost to insignificant values, leaving only a central focalized spot [97]. Therefore, the EP number per EPD is a **trade-off between quality of spel** (SNR of PSF and its peak to surrounding area energy ratio) **and number of possible spels**. We call it **resolution/sharpness conflict.**

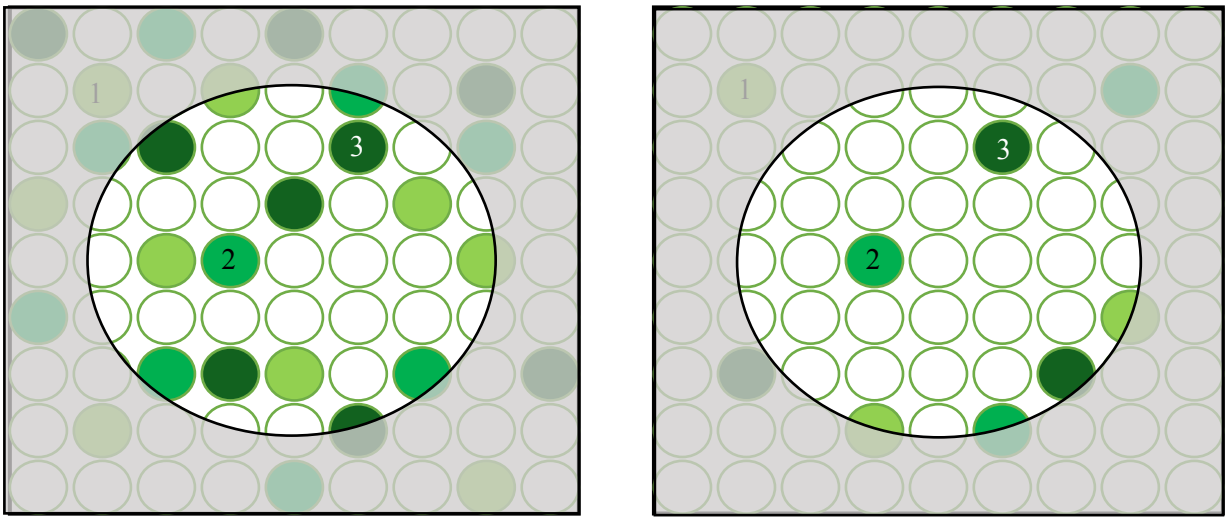

Figure II.6. A model emissive surface with two type of EP per EPD filling a) Emissive surface with 9 EP per EPD – 9 possible EPDs = 9 spels of "high quality", b) 3 EP per EPD – 27 possible EPDs = 27 spels of "low quality"

As a simple example, we consider a small emissive surface that can hold only 81 EPs – a square with a side of 9 EPs. (**Figure II.6)**. There are two limit cases: first, the highest resolution case in terms of maximum possible number of pixels to project. In this case one EP corresponds to one EPD. However, in this case the quality of self-focused spots or spels (sharpness) would be insufficient to distinguish the image (no interference). Second, the highest spel quality case when all EP corresponds to one EPD. The perfect spel quality will be useless, because such display is capable to project only one pixel. There is a whole spectrum of design possibilities between these two cases. As an example, **Figure II.6** shows two intermediate options: the design on the left provides 9 EPDs (= 9 pixels to project) with relatively "high" quality of spel. The design on the right provides 27 EPDs with relatively "low" resolution. Therefore, a compromise should be found. Moreover, if we consider the eye pupil size (in grey in **Figure II.6**) and more realistic number of pixel to project, say, a display with 300x300 pixels image resolution, the display requires 90000 EPDs. If each EPD has about 20 emissive points, there are $1.8 \cdot 10^6$ emissive points

on a given aperture S. If this aperture S cover ¼ of the surface of the whole display (for EB consideration), the addressing issue concerns $7.2 \cdot 10^6$ emissive points.

Each EPD must be related to one common coherent source located outside of the emissive surface. Bringing light to such high number of emissive points is a first challenge. Notably, there is another challenge to set all the on/off states for these points in order to generate dynamic video images. This first analysis underlines the fact that the addressing issue is a central theme for our development.

3 Display addressing techniques application to the CEA retinal projection concept

Although the activation of emissive points on a display surface is a well-known addressing issue, in our case, due to unconventional image formation principle, this issue presents specific constraints.

There are three main approaches to activate emissive regions in a display:

- direct drive (usually used in simple devices like digital watches, status indicators or calculators) and its extension, known as multiplex drive,
- passive matrix driving,
- active matrix driving.

3.1 Direct-driven display

The simplest displays are direct-driven displays. In this case, every single pixel or segment has its own connection line to the common electrode (**Figure II.7**). Main issue for this type of addressing is increasing the number of pixels that leads to higher number of connections to an electrical driver. Typically, *n* segments require *n+1* electrodes.

There is an extension of direct-driven method called multiplex drive, which makes it possible for increasing the number of connections. Using additional switches and electrodes, this kind of driven scheme with n connections requires only (*n/m + m*) electrodes where m is the number of common electrodes

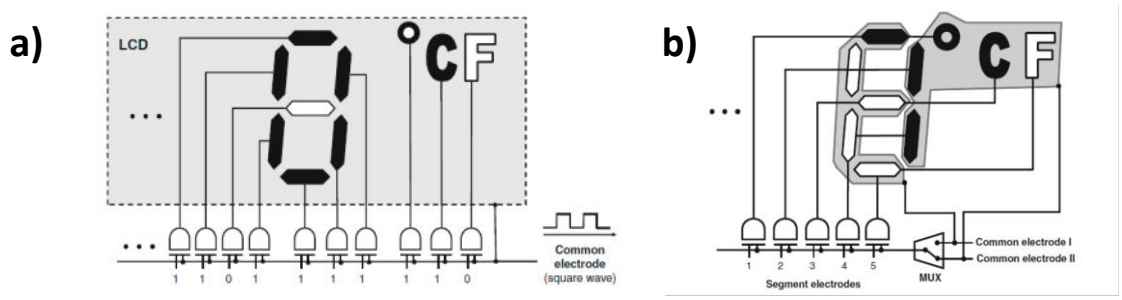

Figure II.7. Direct-driven display a) A display consisting in 10 segments controlled via its own connection line with one common electrode, b) Multiplex-driven display of the same number of segments using 5 segment electrodes and 2 common electrodes with a switch.

Due to technical limitations such as switching time, m is usually limited to $m \leqslant 4$. To overcome this issue in displays that require numerous pixels, an electrode-addressing matrix was proposed with two possible configurations: passive and active. Both of them address pixels via row and column electrodes, however while pixels of passive matrix are active only in a scanning row, active matrix driving stores information about on and off state, and therefore pixels of all frame are active during a scanning period [98].

3.2 Passive Matrix Displays

Passive matrix addressing system activates a segment sandwiched between intersection of row- and column-electrodes, controlled by a 4- or 8-bit microcontroller [98]. A resolution of MxN pixels requires $M+N$ electrodes. Every intersection of the matrix corresponds to a pixel position (**Figure II.8 a**). A passive matrix design scans sequentially each row by a pulse and is characterized by a frame period T. Pixel activation consists of pulses, with duration T/N. It is controlled by a Timing Controller (TCON) assembled via a microcontroller interface (µC IF) (**Figure II.8 b**).

In passive addressing matrix, each pixel is sandwiched between intersection of two electrodes: one row and one column, and sequentially scanned by a pulse. During this pulse, the data for a row is applied to the columns. Black pixel A is active, but pixels in the same row and column are also addressed by half the voltage. This situation is known as cross-talk.

To overcome the limitations of passive matrix driving, an active matrix configuration has been proposed in 1975 [98].

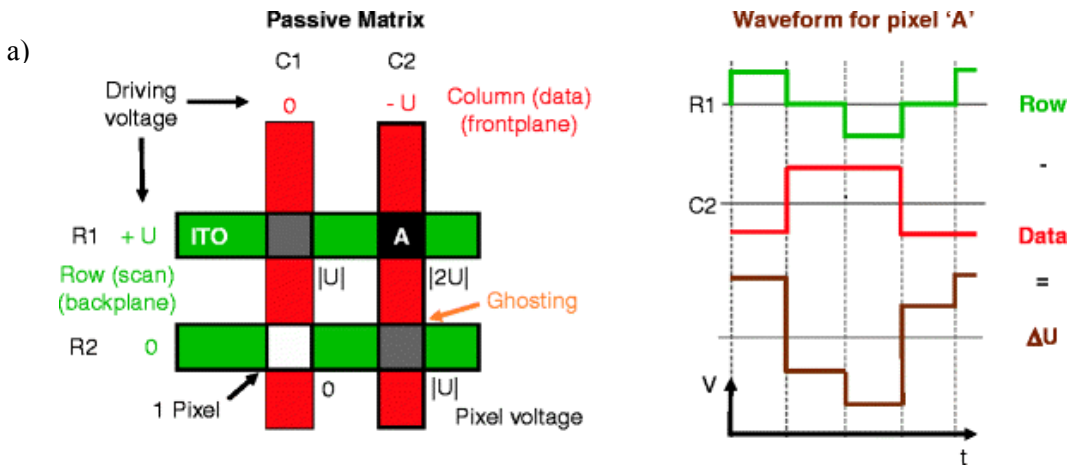

Figure II.8. Passive addressing [98] a) Passive matrix b) pixel activation scheme

3.3 Active Matrix Displays

The active matrix design uses not only row and column electrodes, but also a Thin Film Transistor (TFT) as a nonlinear switch for each pixel. There are several designs of active addressing but all of them have in common a switch for each cell. A row of pixels is selected by applying the appropriate voltage to the line connecting the TFT gates for that row of pixels. To load information to a pixel, a required voltage is transferred via its data column through its storage capacitor. During the whole frame, the voltage difference ΔU between data voltage and front plane voltage is kept non-zero, allowing the pixel for staying active. For the neighboring pixel, ΔU is equal to zero because no data is sent to the data column during the activation step.

For addressing a whole frame, display's rows are activated one by one sequentially, until the last row is reached. The pixels of a line emit light during all the refreshing period, on the contrary of passive addressing. The passive matrix uses persistence of vision to form an image, whereas on the case of active matrix, all pixels are active as long as an image remains the same. **Figure II.9** gives a comparison between passive and active addressing systems.

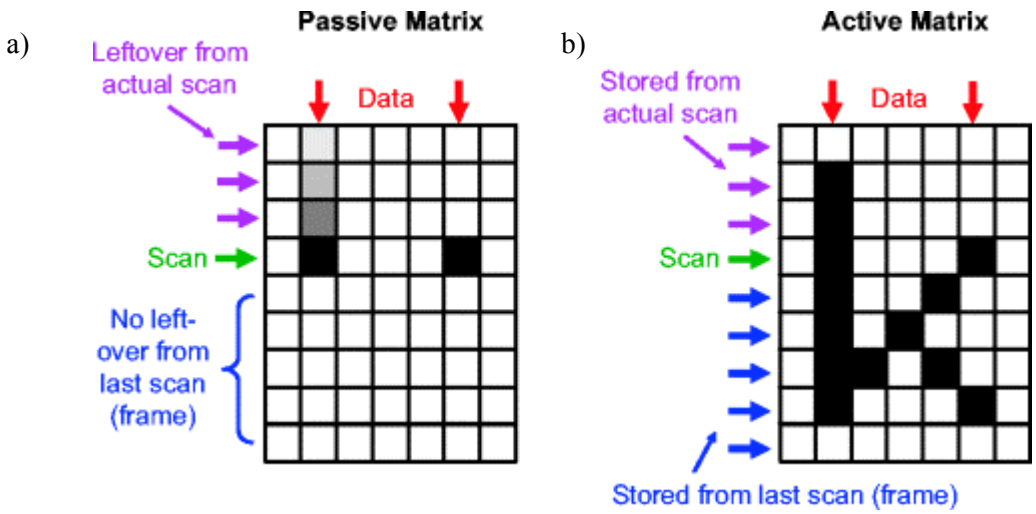

Figure II.9. Difference between passive and active matrix driving [99]. Pixels of passive matrix are active only in the scanning line, while pixels of the active matrix are active during whole scanning period.

Our concept requires a different approach in the addressing, due to the unconventional image formation process. As the display has no pixels in the conventional meaning, we propose to have a closer look on the elements of image formation in **Figure II.10**.

3.4 Addressing configuration in CEA retinal projection concept

A digital image processed by a microprocessor is used to produce light radiations that are projected directly on the retina, thanks to the self-focusing effect. This process requires several steps. The first is to match every pixel forming the digital image with an EPD. The second step is to activate all emissive points of every EPD. Each EPD produces a planar wave front with a given angular direction $\vec{k}$ from a superposition of elementary spherical wave fronts. The third step is the propagation of the planar wave front through the human eye, and the focalization of the energy into a spel, which amplitude corresponds to the pixel intensity.

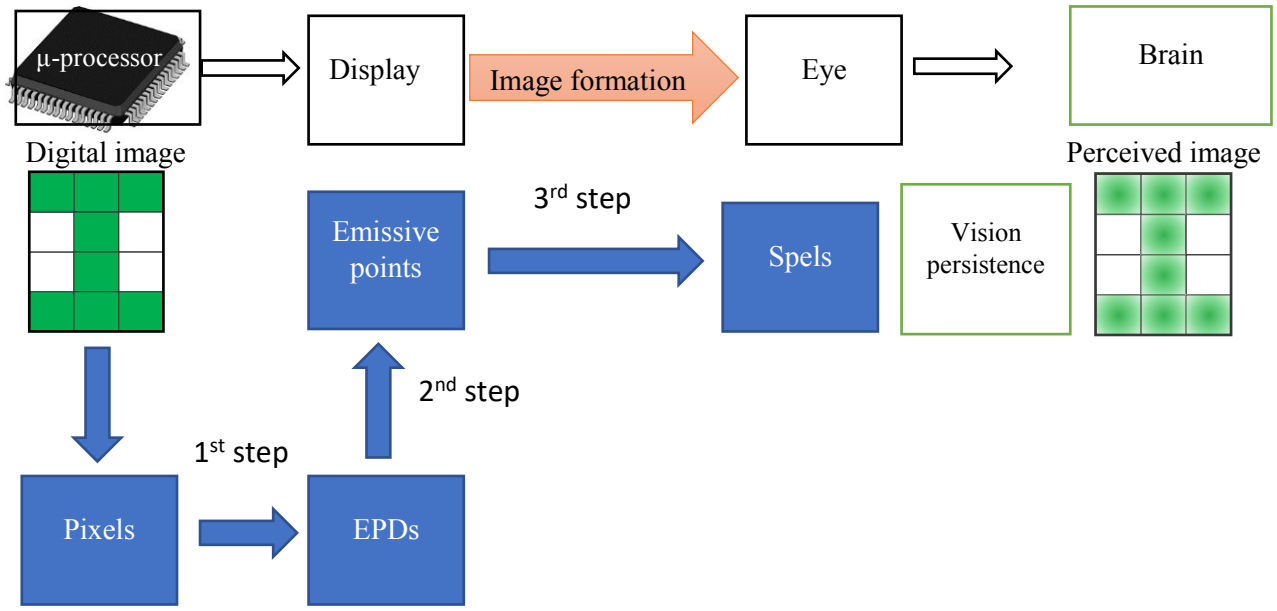

Figure II.10. **Unconventional image formation diagram.** A microprocessor-processed digital image consists in pixels that are matched with EPDs. EPDs are groups of emissive points that produce spels in the focal plane of the eye, which due to vision persistence gives the perception of an image.

The energy distribution of a spel depends directly on its EPD parameters, such as periodicity, randomness and number of emissive points [97]. The number of emissive points is limited by pupil size.

A specific condition of our concept is that every EPD should emit phase adjusted wave fronts to produce a spel, which means that emissive points should be activated simultaneously and also that the common source of light has to be coherent. Only in this case will the self-focusing effect appear thanks to multiple interferences (detailed description will be provided later). Considering a MxN pixels image, the first solution is to project simultaneously the whole image by $Q = MxN$ simultaneous EPDs. This configuration is associated to an active addressing case that activates the image in one step.

The signal can be modulated by the intensity of the laser source or by the efficiency of the emissive points. Therefore, there are two possible ways of signal modulation according to already presented addressing schemes. In the first case, the waveguides of the unconventional display

should correspond to the data columns (modulated laser). In the second case, the emissive point addressing electrodes should correspond to the data columns.

Regarding the first case, each EPD can be associated to Q different modulated laser sources that emit through a collection of fixed outcoupling gratings.

In the second case, Q different modulated outcoupling grating distributions emit light from one laser. **Figure II.11** shows the diagram of a simple 3x4 pixels image projection in an active addressing solution with the image modulation brought by intensity variation of the laser source. This configuration requires a large number of lasers. Each EPD is presented as a group of emissive points of the same color with the same emissive angular direction.

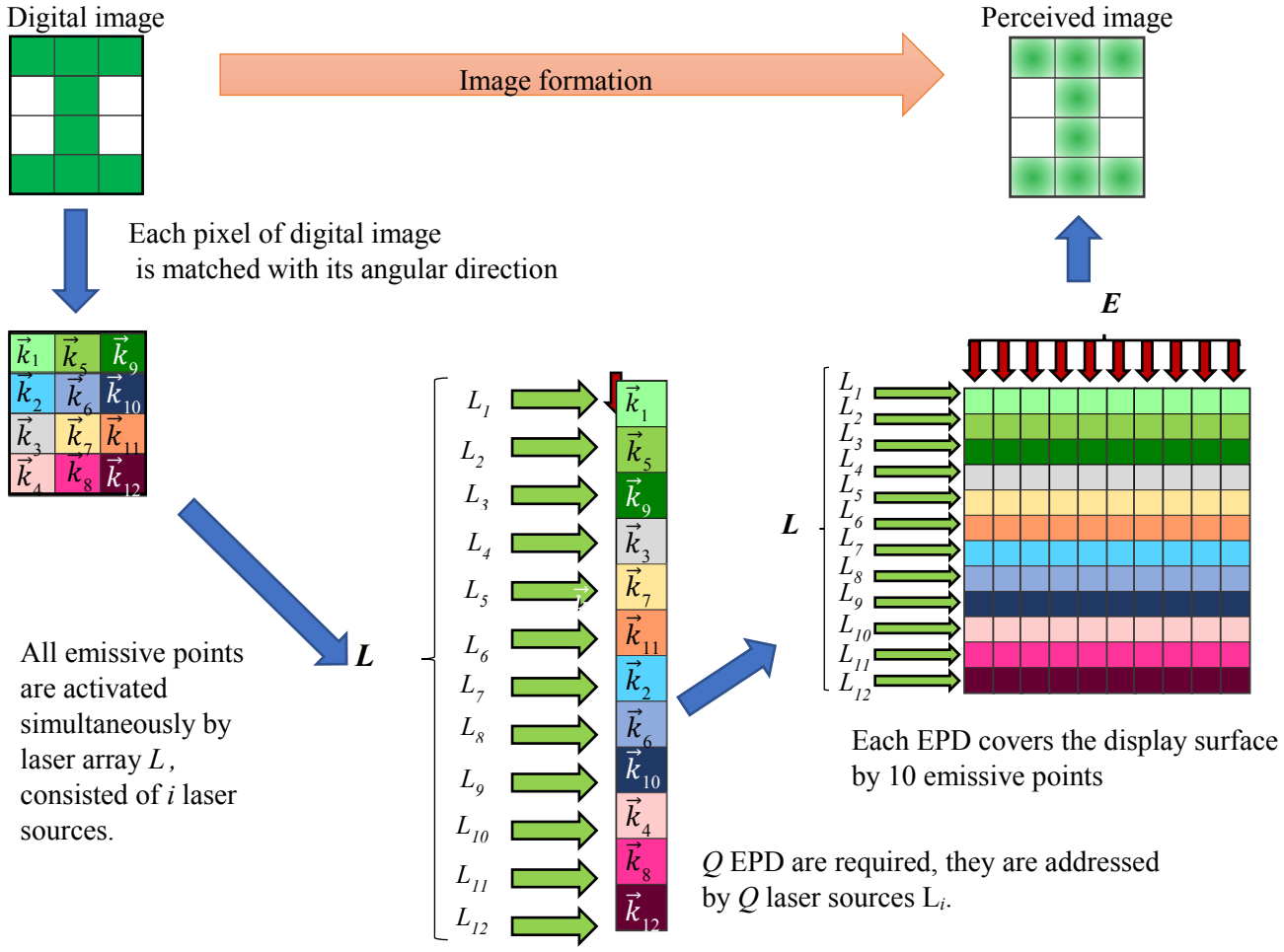

Figure II.11. **Active addressing or simultaneous activation scheme (laser source modulation case).** A pixel of the image corresponds to an emission point distribution (EPD). Each EPD is presented here as a group of emissive points of the same color.

In another addressing scheme the image modulation is brought by the modulation of the outcoupling gratings. **Figure II.12**. presents this configuration where one laser is modulated by Q electrodes. In this case, all the spels are formed by the same laser at the same moment. This case poses the problem of possible cross-interference between the spels due to the coherence of the laser required for the self-focusing effect. To avoid this problem each spel associated to one laser has to be projected successively in a sequential mode.

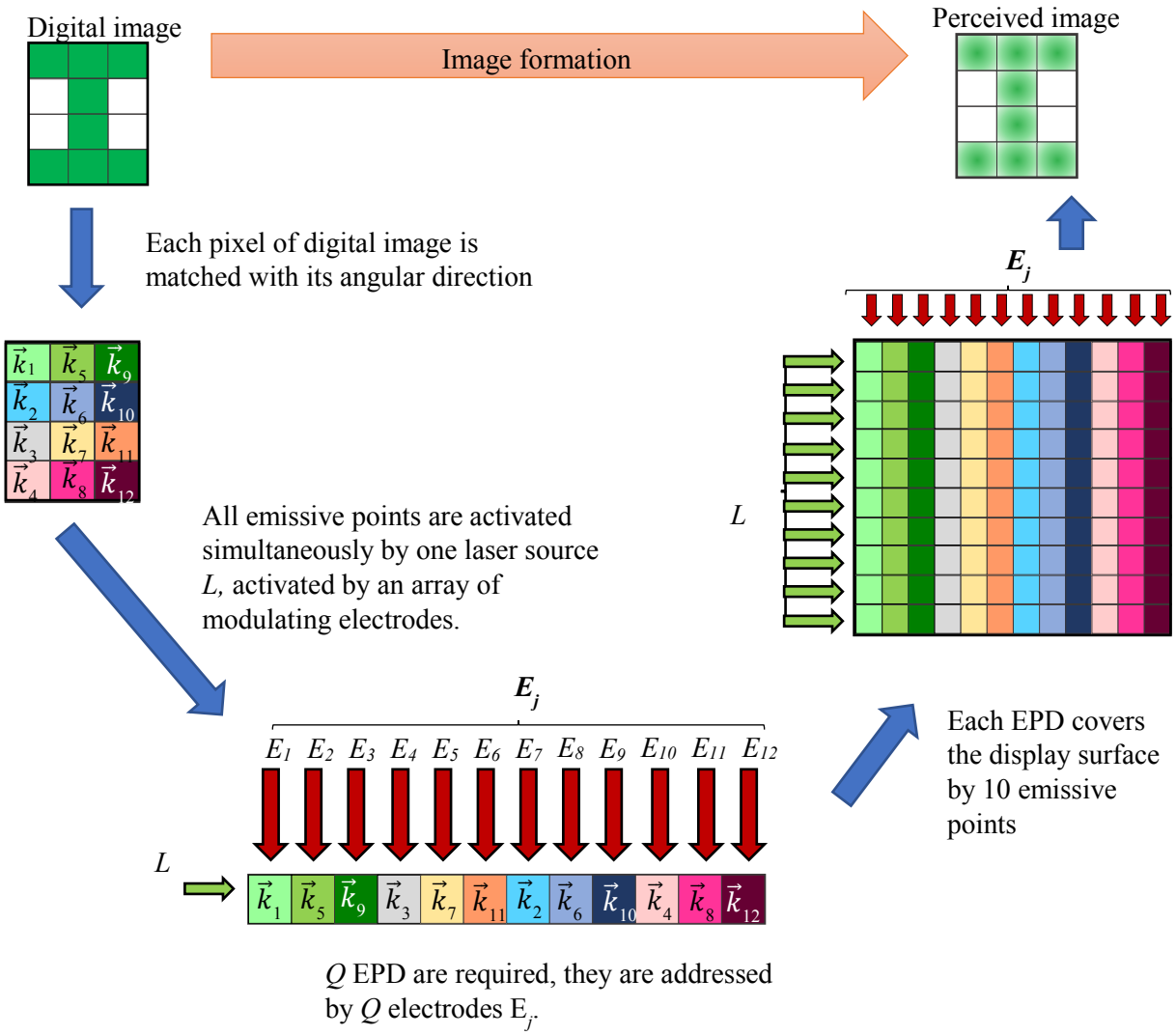

Figure II.12. **Active addressing or simultaneous activation scheme (electrode modulation case)**: each pixel of the image corresponds to an emission point distribution (EPD). Here, a 12-step sequence: all the rows are activated with the same laser source L_1. The columns are activated by modulating electrodes E_i. The surface of the display is covered by emissive points

The addressing of a huge number of emissive points at the same time with lasers and waveguides also pauses the problem of a very complex optical design in terms of waveguide architecture. To reduce this complexity, we can share the same waveguides to address different emissive points. In this case, also the image projection has to be done in a sequential way.

Consequently, the image needs a reduced number of spel n_{spel} during one step to form the image. This number is given in a simple way by the number of step n_{step} required to perceive the image:

$$n_{spel} = \frac{M \times N}{n_{step}} \qquad \text{(II.1)}$$

To implement this sequential approach, we consider an addressing scheme where the data columns are associated to the laser emission and the scan row are associated to the outcoupling gratings. In this case, as the lasers emissions fix the spels amplitudes, just one laser must be associated to one spel. **Figure II.13** describes the formation of the symbol I on a 3x4 image in the case of a passive addressing process or sequential activation scheme. We show here two possible configurations depending on the number of lasers. In the first case, we project two spels by steps thanks to two lasers L_1 and L_2. In order to address the 12 EPDs, 6 electrodes are therefore required **(Figure II.13 a).** In the other case, we choose to project 4 spels by steps, so that 4 lasers and 3 electrodes are required **(Figure II.13 b).**

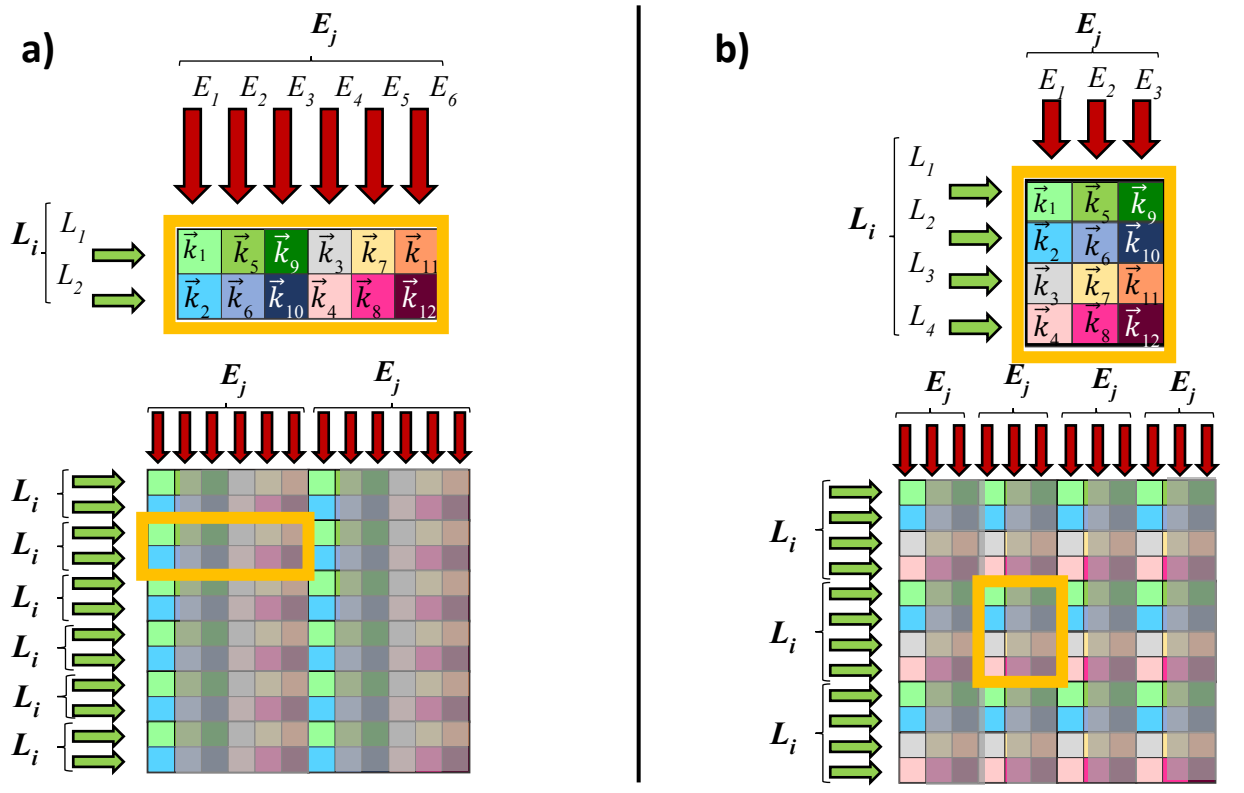

Figure II.13. **Passive addressing or Sequential activation scheme.** Two possible realizations are presented, including one with each pixel of the image corresponding to an emission point distribution (EPD).

The number of required lasers and electrodes are directly driven by the number of steps and by the number Q of EPD:

$$n_{elect} = n_{step} \tag{II.2}$$

$$n_{laser} = \frac{Q}{n_{step}} \tag{II.3}$$

Figure II.13 shows that the surface of the display is composed by groups of $n_{laser} \times n_{elect}$ emissive points. The display is formed by the repeating pattern highlighted in yellow. We introduce the **E**missive **U**nit **C**ell (**EUC**) term to refer to this elementary building block of the display. As shown in **Figure II.14**, EUC is a region with sides Λ_1 and Λ_2, composed by one emissive point from each EPD. The size of the EUC is given by the following relations:

$$\Lambda_1 = n_{elect} \times d_E \quad \text{(II.4)}$$

$$\Lambda_2 = n_{laser} \times d_W \quad \text{(II.5)}$$

where d_W and d_E are the distances between rows of waveguides and between columns of electrodes. The intersection between the waveguides and the electrodes defines the emissive points.

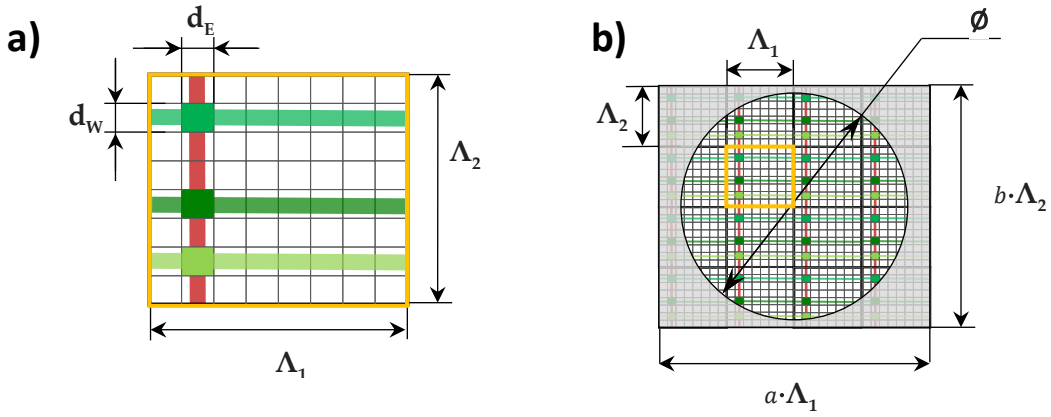

Figure II.14. a) **Emissive unit cell (EUC)** consisting in an ensemble of one emissive point of every EPD, b) it can be assumed as a Λ_1 /Λ_2 periodic elementary unit of the display surface. The number of effective EUCs is limited by the pupil size **ø**.

The total number of emissive points N_{EP} on the surface of the display is given by the number of EUCs and the number Q of EPD. If we consider a display covered by a x b EUC, N_{EP} is given by:

$$N_{EP} = a \times b \times Q \quad \text{(II.6)}$$

A major limitation factor of our display is related to the eye pupil size ø. The number $\overline{N}_{EUC}$ of EUC that effectively enter the eye and contribute to the formation of the spels is defined in a first approximation by ø:

$$\overline{N}_{EUC} = \frac{\pi \times \text{ø}^2}{4 \times \Lambda_1 \times \Lambda_2} \quad \text{(II.7)}$$

On the other way, the number of EPDs is given geometrically by the size of the EUC. So, **equations** (**II.2**) to (**II.5**) give:

$$Q = \frac{\Lambda_1 \times \Lambda_2}{d_e \times d_g} \quad \text{(II.8)}$$

There is a compromise to find between the number of EUCs that improves the efficiency of the EPD and the number of EPDs that fixes the number of pixels for the image. It is an inevitable conflict between number of projected spels and their quality:

$$\overline{N}_{EUC} = \frac{\pi \times \text{ø}^2}{4 \times d_e \times d_g \times Q} \quad \text{(II.9)}$$

Another limitation is that emissive points should be distributed more or less randomly over the whole display surface to achieve efficient self-focusing-effect. Otherwise, the focalized spot is surrounded by parasite signals that make image formation impossible. Designing an efficient random distribution of emissive points is not an easy task. We present later some proposals to achieve this goal, but firstly we analyze the possible theoretical geometric configurations for the EUCs between periodic and random distributions.

4 Types of Emissive Points Distributions

In this section I present design considerations for emissive point distributions, show possible EPD design solutions, provide an algorithm for EPD calculation and analyze possible EPD using histograms.

The emissive points distributions play a dominant role for self-focusing, therefore the best feasible distribution to implement has to be found. I will introduce some possible solutions and discuss their advantages and disadvantages. Overall, the best theoretical solution for the image formation is a random distribution, however it is impossible to make it technologically. On the other hand, the easiest solution for the concept fabrication is a lattice distribution, but not acceptable from the image formation point of view. Hence, we need to find a compromise, i.e. a realistic-pseudo-random (further referred as a realistic-random for short) distribution has to be found.

In this study I use 3 main types of distributions with 2 variations for each of them: periodic and quasi-periodic, random and quasi-random, realistic-random (Cross-Sinusoidal (CS) and Cross-Random-Sinusoidal (CRS)). Design acceptability from practical point of views is discussed. It should provide in the same time adequate image formation capability in terms of image quality and pixel number along with feasibility of such EPD manufacturing.

4.1 EPD design considerations

Now, being familiar with addressing features of this new NED concept, I present requirements for EPD. The ultimate goal is to **design an emissive surface that projects maximal number of pixels with the maximal possible quality of spels**. There is always a trade-off between number of pixels/spels and spels quality. One can define three necessary condition to fulfil the EPD acceptability criterion: 1) Randomness or Heterogeneity, 2) Uniformity or Homogeneity and 3) Feasibility.

- **Randomness** of Emissive points location for each EPD or Heterogeneity:

Randomness in our case means a low periodicity of EPs within one EPD. Requirement of randomness stems from the fact that periodic EPDs produce low quality spel due to the various diffraction orders.

- **Uniformity** of EPD or Homogeneity:

Uniformity condition comes from the need to produce the highest quantity of EPD. This means the highest number of pixels to be projected into the retina as spels. It could be done if one finds out how to cover the whole display surface with grid of waveguides that don't overlap but have random intersections with a grid of electrodes (each EP is a result of the intersection between a waveguide and an electrodes.). This is an interesting mathematical task that has to be rigorously analyzed and the first result are promising [100], [101].

The proposed approach is to divide the emissive surface into regions called Emissive Unit Cell. This is a block with sides Λ_1 and Λ_2, that contains one EP from each EPD. This guaranties a uniform coverage of the emissive surface by EPs, however the position inside the EUC should be as random as possible to fulfil the randomness condition. The size of the EUC defines the number of EPs per EPD and the level of possible randomness: with a large EUC there is more space for possible position of EP inside the EUC, however a large EUC induces a low number of EPs per EPD. We will see this trade-off in the case of Quasi-Random distribution – the distribution chosen as a model to study self-focusing effect parametrization.

EPD uniformity is defined as follows: **each EUC contains one EP per EPD**. In other words: an **EPD is uniform when each of its EP corresponds to a given EUC**. This notion of uniformity of EPD leads to introduction of the principle of Elementary Unit Cell – a spatial period for EP.

- Design **Feasibility**

The design of waveguides has to be realistic in terms of fabrication and have characteristics that allow the concept to remain operational. The biggest constraint is given by the waveguide curvature limit. Generally, curvature losses increase exponentially as curvature radius decreases. So, one would like to have smooth curvature along the entire length of the waveguide. In the following sections various types of EPD that intend to fulfill some of these necessary conditions we described.

Finding an optimal EPD is an iterative process: one has to to define an EPD, to study and to analyze its spel-formation qualities along with its feasibility and then optimize the chosen EPD. Below I describe how such distributions are calculated for simulations.

4.2 Periodic and Quasi-Periodic distribution

To produce a Periodic EPD we need just to create a 2D grid of EP. Each EP is an intersection between two straight lines: horizontal and vertical (waveguides and electrodes). The coordinates of the EPD $x_{i,j}$ and $y_{i,j}$ are then given by the equation:

$$\begin{aligned} x_{i,j} &= \Lambda_1 i; \\ y_{i,j} &= \Lambda_2 j. \end{aligned} \qquad \text{(II.10)}$$

To maintain clarity in our equations we omit the initial positions on the 2D grid x_0 , y_0 that put each EP to the center of an EUC as shown in **Figure II.15**.**a**.

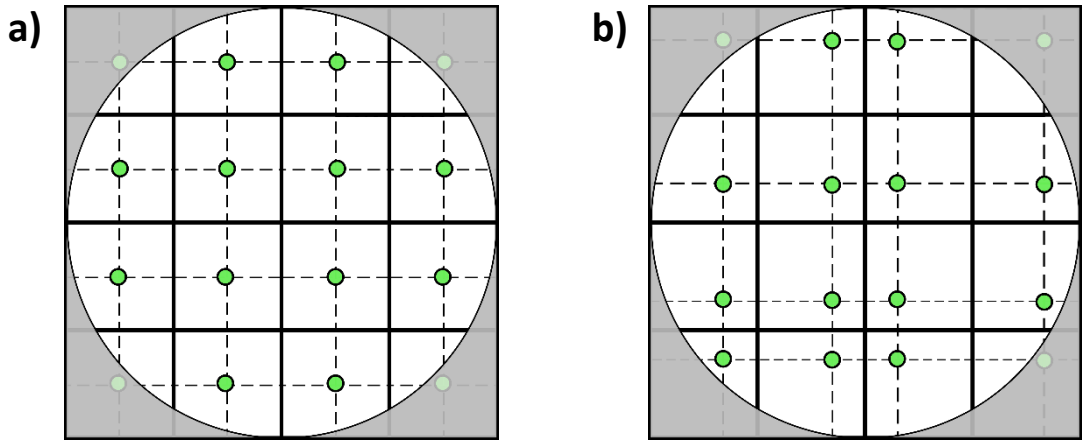

Figure II.15. a) Periodic EPD. Each EUC has an EP in its centre. Period of EUC is equal to distance between EPs. b) Quasiperiodic distribution. Each EUC contains a EP, but the distance between EP is variable, when EUC is constant.

Although Periodic type of EPD could be easily fabricated with perfect homogeneity and the maximum number of possible EPDs, it has no randomness. This leads to poor spel quality due to constructive interference in the various diffraction orders of the periodic distribution. It makes image formation impossible due to high intensity of side peaks.

We can introduce some irregularity without harming neither uniformity not feasibility. It is the principle of the Quasi-Periodic distribution:

$$x_{i,j} = x_i = \Lambda_1(i + rnd);$$
$$y_{i,j} = y_j = \Lambda_2(j + rnd); \quad \text{(II.11)}$$

Where rnd is a random number $\in$ [0; 1].

Quasi-Periodic distributions (**Figure II.15b**) have same strengths and weaknesses as Periodic ones, but the measure of randomness is higher for these EPDs.

4.3 Random and Quasi-Random distributions

Completely random distribution is non-feasible due to fabrication constraints, and because it breaks a requirement for uniformity of emissive points distribution (**Figure II.16a**). This requirement states that every EPD should contains equal number of emissive points in every EUC for the optimal image formation. However, this type of EPD should represent the ideal case in terms of randomness condition. The coordinates of the EPD can be written in this case as follows:

$$x_{i,j} = rnd \times a \times \Lambda_1$$
$$y_{i,j} = rnd \times b \times \Lambda_2 \quad \text{(II.12)}$$

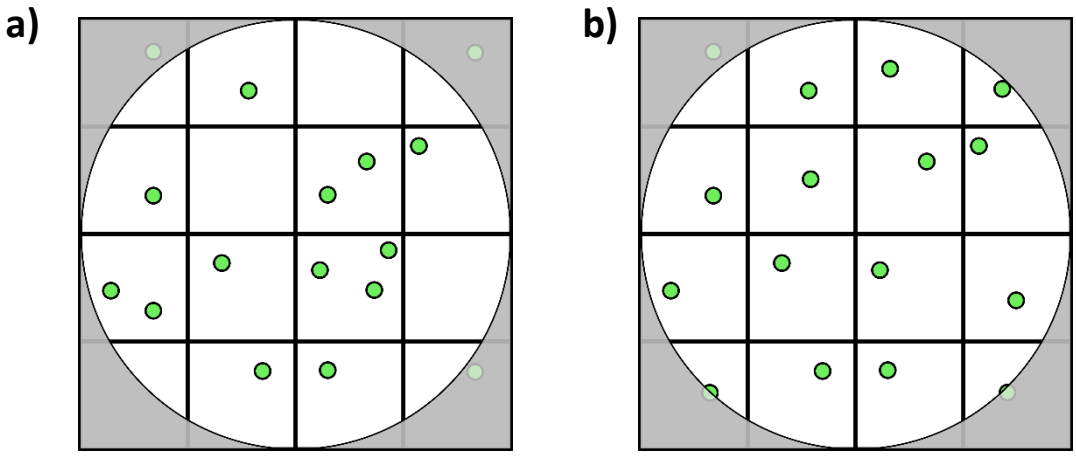

Figure II.16. Completely random distribution: non-feasible and non-uniform: there are void EUC and the EUC with multiple EP for a given EPD.

Quasi-Random EPD is another ideal distribution (**Figure II.16b**). The spel quality could be high and the EPD could fulfil the uniformity condition. We can express the coordinates as follows:

$$x_{i,j} = \Lambda_1(i + rnd)$$
$$y_{i,j} = \Lambda_2(j + rnd) \quad \text{(II.13)}$$

However, this type of EPD may be hard to manufacture, as it does not consider any constraint on the waveguide design (such as curvature limit). It corresponds to a pure theoretical concept that can serve as a reference for comparison with more realistic EPD.

4.4 Realistic-Random distribution

On the basis of our analysis on the requirement of waveguides with limited curvature, I propose to study two types of Realistic-Random distributions based on sinusoidally shaped waveguides: the Cross-Sinusoidal Distribution (CS) and the Cross-Random-Sinusoidal Distribution (CRS) (**Figure II.17**). The first type of EPD is completely uniform, i.e. each EUC contains one EP per EPD, however the level of randomness depends on the size of the EUC. If an EUC is small enough (close to EP size ~ 5 µm) the CS-distribution with this EUC degenerates into a periodic one. A CRS distribution is more random and less uniform according to the already mentioned trade-off between randomness and uniformity. It is inspired by the quasi-periodic configuration applied to the CS distribution.

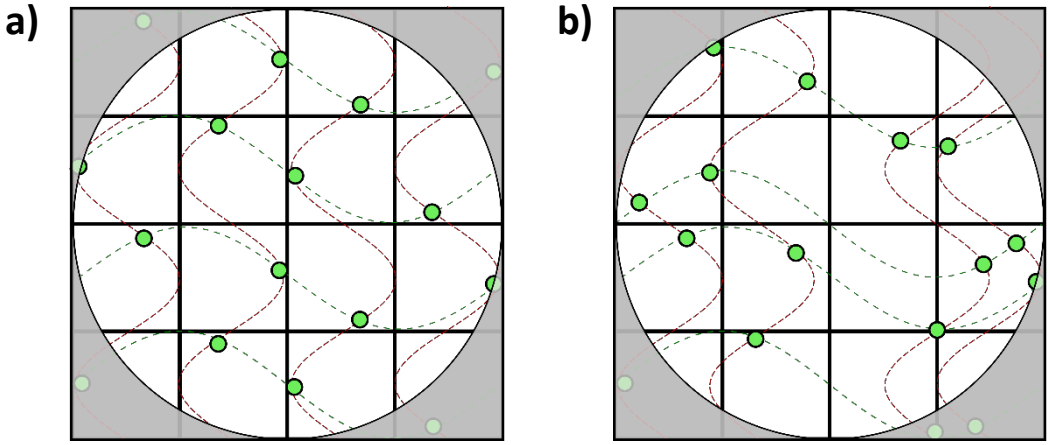

Figure II.17. a) CS distribution uses intersection between simple sinusoids and b) RRS distribution adds more randomness to the CS configuration

Compared to previous cases, the CS and the CRS cannot be expressed by a simple set of coordinates equations. To find these optimal Realistic-Random distributions we have to implement an Intersection calculation method.

4.5 Intersection Calculation Method

To produce a Realistic-Random distribution we developed a simple tool: considering three design conditions, we propose to use sinusoidal curves for the waveguides and the electrodes instead of straight lines to introduce enough randomness and in the same time keep uniformity. We assume that each EP corresponds to the intersection between a waveguide and an electrode. The main constraints of such a design are: 1) energy loss due to curvature of waveguides; 2) less EPs per emissive surface, due to the larger distance between the curves comparing with straight lines. The EUC sizes Λ_1 and $\Lambda_2$limit the maximal amplitude of such curves. There are two extreme cases: first, the EUC covers almost the whole emissive surface. Second, the EUC is close to waveguide/electrode interspacing: such distribution degenerates into a Periodic or Quasi-Periodic one. The whole spectrum of possible designs lays between these two limits. To overcome the design constrains we have to fulfil two requirements: first, our net of waveguides that covers our emissive surface should have a **regular spacing** between them (not necessarily within an EPD, but rather between all waveguides). The second requirement is that the waveguide curvature should be as smooth as possible to provide simultaneously lossless

propagation in terms of energy, and adequate randomness for the designed EPD to ensure acceptable spel formation.

With respect to Eq. (**II.12**) and (**II.13**), this can be done in two ways. First by keeping a periodic distribution for the Cross-Sinusoidal EPD:

$$(x_{i,j}, y_{i,j}) = \mathrm{f}_e(x + \Lambda_1 i, y) \cap \mathrm{f}_g(\mathrm{x}, y + \Lambda_2 j) \tag{II.14}$$

Secondly, by introducing a random access addressing for the Cross-Random-Sinusoidal EPD:

$$(x_{i,j}\,, y_{i,j}) = \mathrm{f}_e(x + \Lambda_1(i + rnd), y) \cap \mathrm{f}_g\big(x, y + \Lambda_2(j + rnd)\big) \tag{II.15}$$

Initially, since we have non-bijective functions, we propose the parametric representation of our path function f defined by a velocity vector. To simplify our analysis, we use a numerical method for its resolution.

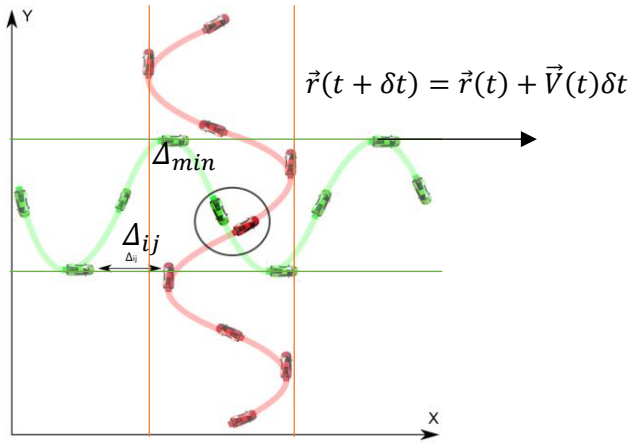

Figure II.18. Principal idea of Intersection calculation method for Realistic-Random EPD: we look for intersections between waveguides (in green) and electrodes (in red). Each curve is assumed a trajectory of a particle moving with varying speed.

For the determination of the intersections between f_e and f_g we choose to describe these functions as the trajectory of a moving particle with local dependency on a 1D parameter t and with absolute coordinates $(x_{i,j}\,, y_{i,j})$. The location $\vec{r}(x, y)$ of the particle **Figure II.18** is given by the time varying relation:

$$f: \quad \vec{r}(t + \delta t) = \vec{r}(t) + \vec{V}(t)\delta t \tag{II.16}$$

The velocity function $\vec{V}(t)$ that fixes the trajectory is defined by a time varying amplitude and direction:

$$\vec{V}(t) = \begin{bmatrix} v_0(t)\cos(\alpha(t)) \\ v_0(t)\sin(\alpha(t)) \end{bmatrix} \quad \text{(II.17)}$$

In this work, we choose a simple sinusoidal model with the following definition:

$$\begin{aligned} v_0(t) &= v_0 = const. \\ \alpha(t) &= \alpha_0 \cos\left(\frac{2\pi}{t_0}t\right) \end{aligned} \quad \text{(II.18)}$$

To find an optimal Realistic-Random Distribution, we variate the amplitude v_0 and the period $a(t)$.

Finally, as shown in **Figure II.18b**, in order to find the intersections of the trajectories it is necessary to find t_1 and t_2 that minimize the distance Δ_{ij} for each pair of $(x_{i,j}, y_{i,j})$ of the f_e and f_g. It corresponds to the minimal distance between a waveguide *i* and an electrode *j*:

$$\Delta_{min} = min\sqrt{(x_{1i} - x_{2i})^2 + (y_{1i} - y_{2i})^2} \quad \text{(II.19)}$$

One deduces a set of intersection points that defines an EPD for a particular set of waveguide/electrode parameters. In order to characterize these EPD, I introduce the histogram of the nearest neighbor for all the EP of the EPD.

4.6 The histogram of the minimal distance: an evaluation method of the distributions

This last subsection is to establish a first mathematical tool for further research to improve EPD performance in spel projection. [100]. Standard tools of descriptive statistics, i.e. histograms of the minimal distance distributions are used to analyze the emissive points distributions. This could help evaluating randomness of EPDs.

Say, one has a distance $|u_{pq}|$ between two arbitrary Emissive Points within the same EUC and EPD. Finding the minimum of this distance, one obtains the closest distance s_p between the nearest EP neighbours for an EUC for a given EPD:

$$s_p = \min(|u_{pq}|)_{q \in EPD}, \quad \text{(II.20)}$$

Using calculated s_p, a histogram of the closest distance for all EP for a EPD is built. I assume a square EUC: $\Lambda_1 = \Lambda_2 = \Lambda$ for all EPD. The histogram is plotted with a constant number of bins $N_h = 45$ in the range of 0 to Λ:

$$h_q = \sum_{p=1}^{N_{EPD}} I\left[0 < \left(s_p - q\frac{2\Lambda}{N_h}\right) \leq \frac{2\Lambda}{N_h}\right] \quad \text{(II.21)}$$

This evaluation method is expected to give a good view on the randomness condition of the EPD design. Indeed, for a periodic distribution (ideal feasibility) the histogram is theoretically a Dirac function and for a pure random distribution (ideal Randomness) it is a Gaussian distribution.

4.7 Example of EPD simulation

4.7.a Periodic and Quasi-Periodic

The first limit case (a periodic distribution) highlights that all 221 EP have their closest neighbour at the distance 600 µm the given EUC period for this EPD. From this, one can verify that each periodic distribution produces a Dirac delta function histogram centred at the period value (with expected value µ = the period (600 µm for the given case) and dispersion σ = 0). We seek to avoid such a narrow histogram (**Figure II.19**). Therefore, a mathematical criterion for the optimal distribution could be a dispersion σ maximisation.

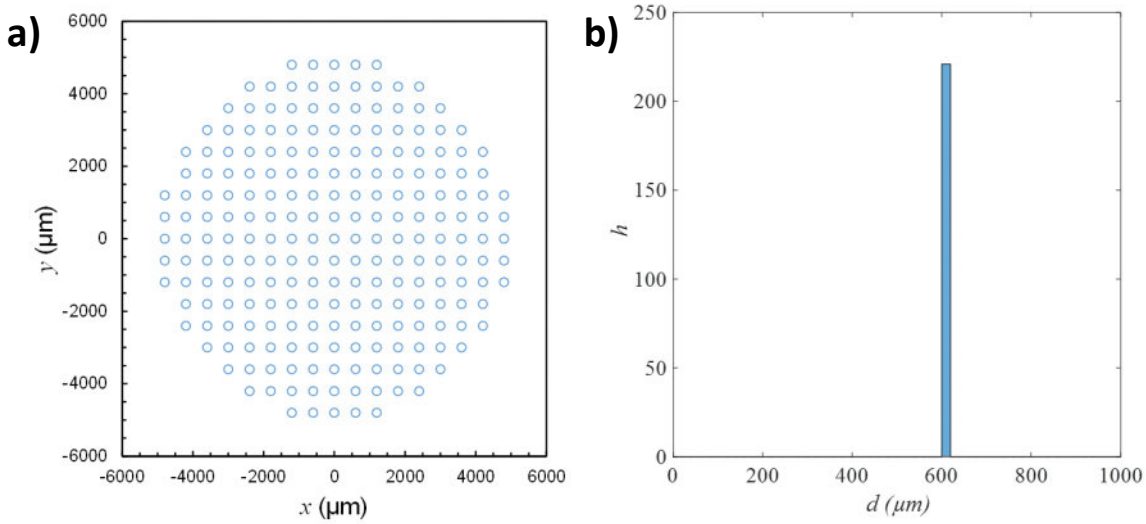

Figure II.19. a) Periodic EPD with 600 µm period and b) its histogram: the Dirac delta function shows the absence of randomness in the distribution

Randomly varying randomly a column-row period introduces some randomness into a distribution with our Quasi-periodic EPD (**Figure II.20 a**). The Dirac delta is no more present in the histogram. However, strong periodicities are present. It shows that the model is not ideal for randomness condition. As expected, the histogram spreads between 0 and 2Λ. A Quasi-Periodic distribution can be fitted by a Gaussian bell centred at 500 µm. The obtained distribution is close to normal distribution: it's perfectly seen that the expected value shifted from 600 µm to about 300 µm and σ ~ 169 µm. However, a "Manhattan profile" of histogram with high peaks and gaps between them (**Figure II.20 b**) is observed.

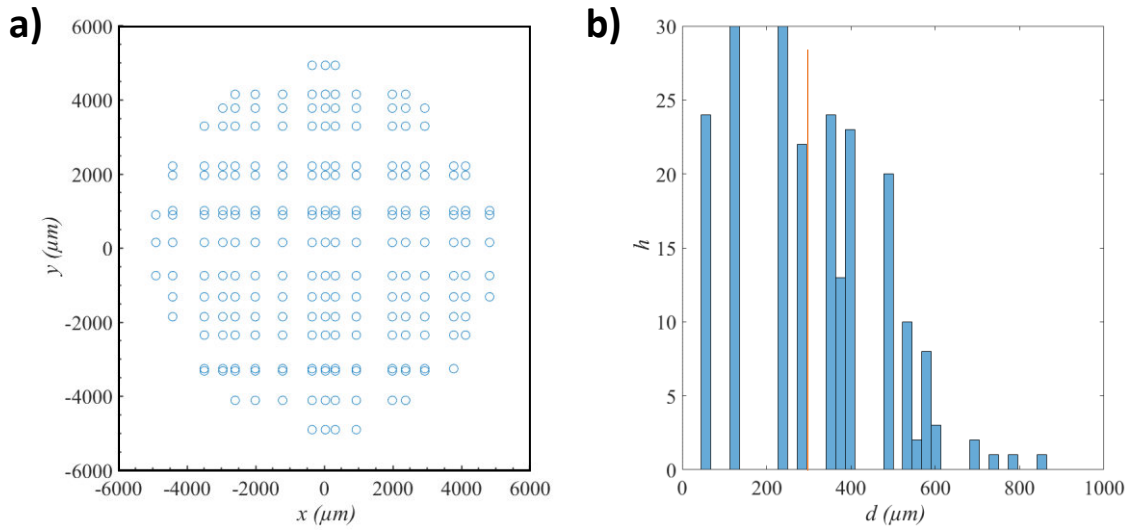

Figure II.20. a) Quasi-Periodic EPD with Λ=600 µm and b) its histogram: some randomness is introduced due to varying EP column and row period. The histogram is centered at µ = 303 µm with σ ~ 169 µm

4.7.b Random and Quasi-Random distribution

A pure random distribution in **Figure II.21** shows a Gaussian distribution centered at 318 µm with σ ~ 161 µm. There are however several void regions, which means a lack of uniformity.

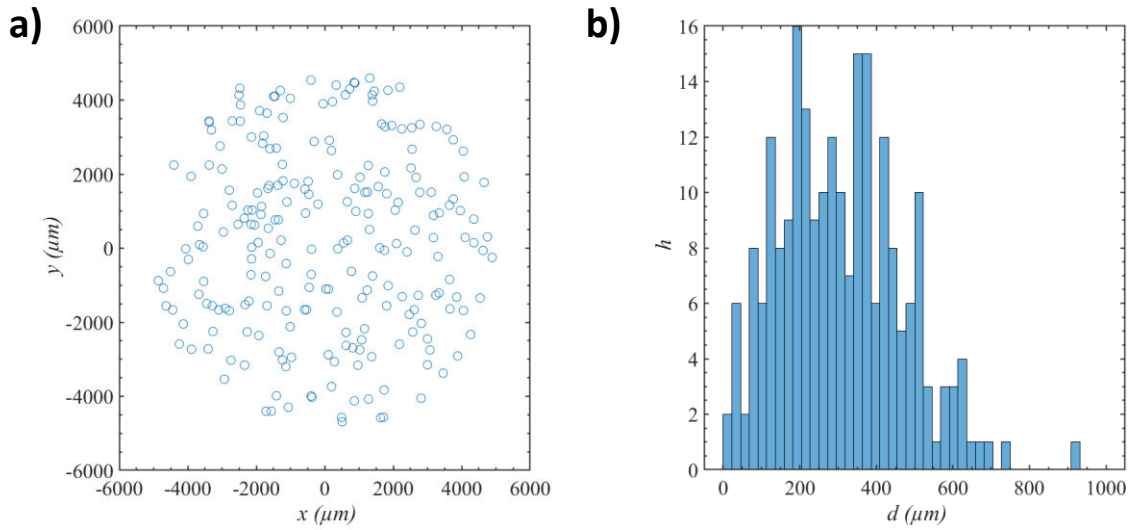

Figure II.21. a) Pure-Random EPD with Λ=600 µm and b) its histogram: the distribution could be fitted by a gaussian bell centered at about µ = 318 µm and σ ~ 161 µm

The EUC introduction into pure Random distribution (**Figure II.22**) shifts the expected value from 318 µm to 440 µm closer to Λ. However, it sacrifices the dispersion, which decreases from 161 to 110 µm.

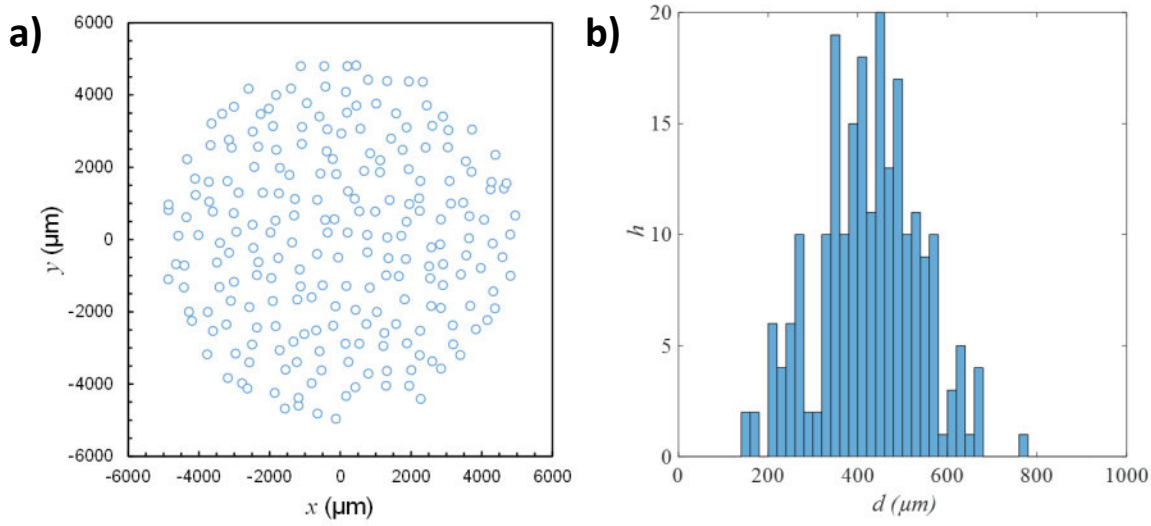

Figure II.22. a) Quasi-Random EPD with Λ=600 µm and b) its histogram: the distribution could be fitted by a Gaussian bell centered at about 440 µm.

4.7.c Realistic-Random distribution

There are two kinds of Realistic-Random distributions. The first kind is Cross-Sinusoidal (CS) EPD with equal spacing between the curves that represents waveguides and electrodes. The second kind is Cross-Random-Sinusoidal (CSR) EPD with randomly varying spacing between the curves. There is a Homogeneity/Heterogeneity trade-off: the CS distribution is more uniform, but the CRS distribution has more randomness.

A Cross- Sinusoidal distribution

Cross-Sinusoidal distribution could be described as an intermediate case between a Periodic distribution and a Quasi-Random one or just a truncated Quasi-Random distribution. The tails of Quasi-Random distribution have disappeared with a reduction of the dispersion to 40.5 µm. The histogram is centered at 573 µm, which is almost Λ that is close to the Periodic distribution.

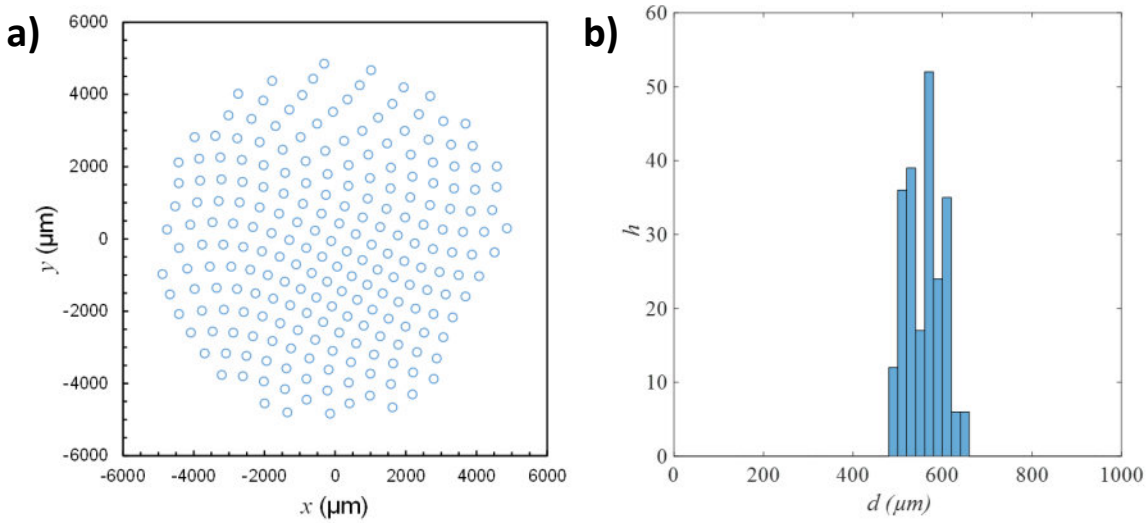

Figure II.23. a) Realistic-Random (CS) EPD with Λ=600 µm and b) its histogram: the distribution could be fitted by a Gaussian bell centered at about 573 µm and σ = 40.5 µm

B. Cross-Random-Sinusoidal distribution

Introducing some variation into the CS distribution leads to something intermediate between a Quasi-Periodic and a Quasi- Random distribution. The CRS distribution visually reminds a

combination of the Pure-Random distribution and Quasi-Periodic distribution. The gaps between peaks are moderately filled. It is centered at 440 µm with σ = 115 µm – these are almost the same characteristics than the Quasi-Random distribution.

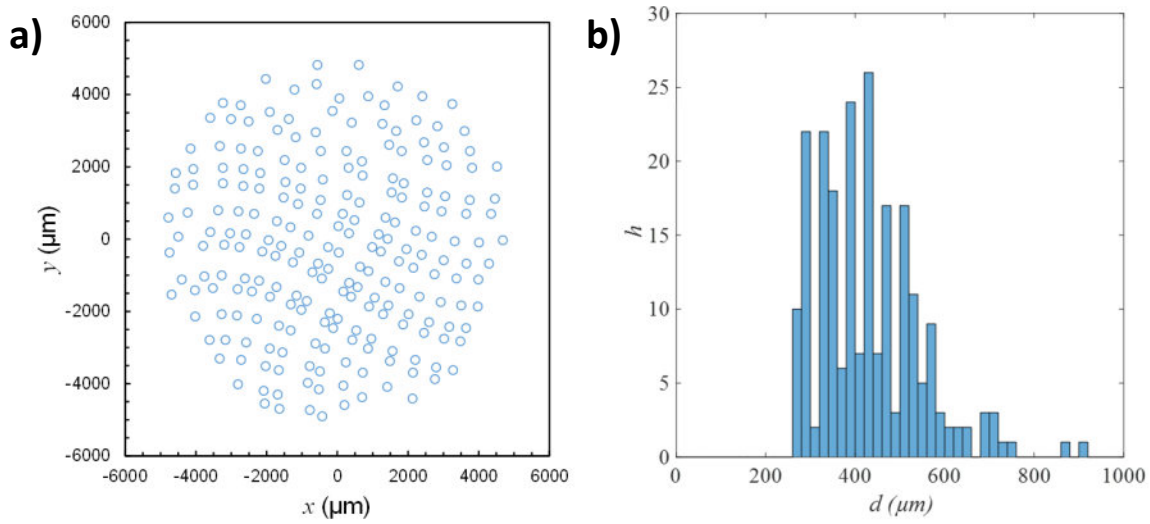

Figure II.24. a) Realisti-Random (CRS) EPD with Λ=600 µm and b) its histogram: the distribution centered at 440 µm with σ = 115 µm

4.7.d Discussion

The periodic and quasi-periodic distributions are completely feasible and provide uniformity, but lack required randomness. On the contrary, random and quasi-random distributions are non-feasible, but represent the best distribution model for the ideal case of spel formation from quality/quantity aspect.

Designing Realistic-Random distributions has been tried to overcome this issue and leads to a design compromise that fulfils all the EPD's design consideration criteria. Such constructions are completely feasible, although it has design limitations due to energy losses in waveguide bends [102]. This case was analyzed in detail by B. Meynard [95].

I introduced three design considerations or conditions. The first necessary condition ensures a high quality of spel. The second condition ensures the highest number of pixels that could be projected as spels. This is guaranteed by a homogeneous or uniform coverage of the EPs on the emissive surface. An ideal EPD would be a random, but an even coverage of the display surface

by the EPs. As can be seen, the first and second condition are related to a Heterogeneity and Homogeneity conflict. There is also a conflict of Heterogeneity and Feasibility, therefore one has to find a compromise to design an appropriate EPD. These conflicts are summarized in the **Table II.1**.

Table II.1: Types of EPD and their acceptability criterion conditions

Type of EPD	Randomness	Uniformity	Design feasibility
Periodic	No	Absolutely	Yes
Quasi-Periodic	Weak	Absolutely	Yes
Random	Strong	No	No
Quasi-Random	Strong	Absolutely	No
Realistic Random CS	Modest	Quasi-Uniform	Yes
Realistic Random CRS	Moderate	Modest	Yes

The histograms of the distributions give a first view on the EPD quality. However, to evaluate the efficiency of the EPD design, one must go further and simulate the influence of this design onto the spel formation.

5 Self-focusing simulations for addressing design

In this section I will detail the theoretical basis of self-focusing effect, explain the simulation algorithm I used and provide results of self-focusing along with their analysis. Histograms are a qualitative approach to evaluate EPD, however a more quantitative approach is needed. Signal to Noise ratio (SNR) is the first criteria to choose a particular distribution. The second criterion γ is the ratio between central peak energy and the total energy of the signal.

5.1 Theoretical analysis

Self-focusing is based on Huygens-Fresnel principle that implies the superposition principle: "Every point on a wavefront is itself the source of spherical wavelets, and the secondary wavelets emanating from different points mutually interfere. The sum of these spherical wavelets forms the wavefront"[11]. The resulting wavefront is assumed as the envelope of the spherical wavelets generated from the Emissive Points. The beam coherence is also implied in the process to make

[11] https://www.mathpages.com/home/kmath242/kmath242.htm

possible the interference – redistribution of intensity. The intensity distribution of self-focusing effects act like in the Fraunhofer diffraction pattern, which does not change if the aperture is shifted to the side in the plane of the screen without changing its orientation. The picture in the focal plane of the lens is always symmetrical with respect to its axis, regardless of the position of the aperture. In our case we have a large number *N* of identical emissive points with the same angular orientation.

For a Periodic arrangement of the EPs, when their angular orientation and inter-distances are equal, the phase difference between the waves diffracted from adjacent EPs has a fixed value. The interference of these waves significantly affects the diffraction pattern in directions for which the phase difference is a multiple of 2π. The amplitude of the diffracted waves is *N* times greater, and the intensity is N^2 times greater than from one EP. With a random arrangement of EPs, the phase relationships between waves from individual EPs are randomly distributed. Therefore, for each direction of observation, there is a simple addition of the intensities of the waves diffracted from all the EPs.

Wavelets are summed in amplitudes and mutually interfere in intensity. However, rather than spherical wavelets, the model developed for this work uses Gaussian Beam model propagation, a paraxial approximation of wave optics. Beams of coherent radiation with a Gaussian intensity distribution profile have the highest directivity, compatible with the wave nature of the radiation. A Gaussian beam is the closest approximation that diffraction can allow to a parallel beam of light with a limited cross section. In this and the next subsection I heavily rely on our article in term of theory and formula usage [97].

I implemented a paraxial approximation of wave optics to the multiple interference phenomenon. For each EP $M_{u,v}$ (**Figure II.25a**) I simulate a beam propagation in the direction given by the wavevector $k_{i,j}$(**Figure II.25b**).

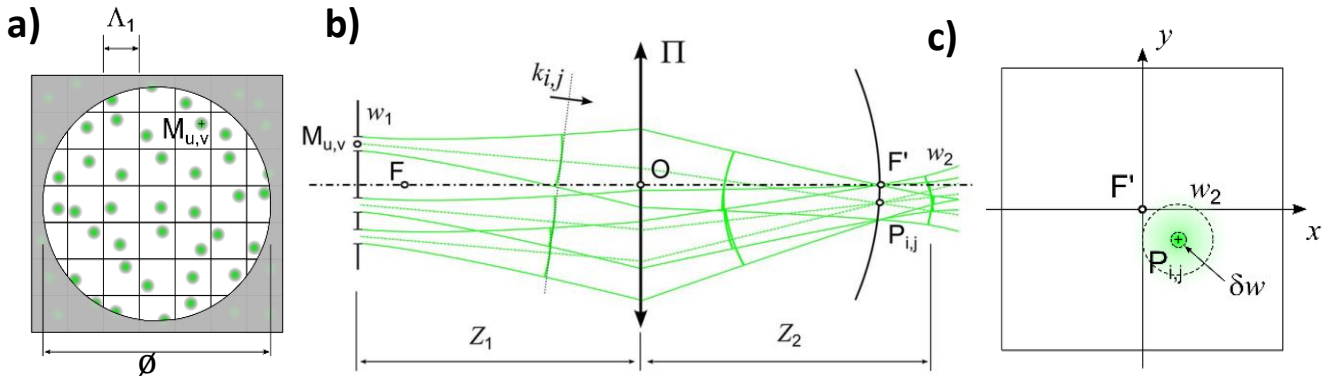

Figure II.25. From display to eye: self-focusing constructive gaussian beam interference. **a)** EPD on the display plane limited by eye pupil, **b)** beam propagation from the display to the retina through eye lens, **c)** focused spot on the retina (spel)

The theoretical development for self-focusing simulation has been introduced by C. Martinez in 2018 [97]. I use this theoretical approach for my simulations. **Figure II.25** summarizes this development. Each emissive point $M_{u,v}$ from the EPD$_{i,j}$ produces a directive beam with the wavevector $k_{i,j}$. The eye lens superimposes all the beams coming from the EPD at a location $P_{i,j}$on the retina, located at the focal image of the eye lens. The beam amplitude generated on the retina by the point $M_{u,v}$ is expressed as:

$$E_{u,v}(\vec{r}) = E_0 \times e^{-i(\overrightarrow{k_{u,v}}.\vec{r}+\varphi_{u,v})} \quad \text{(II.22)}$$

The wave vector $k_{u,v}$ is calculated as a function of the $M_{u,v}$ and $P_{i,j}$ coordinates. All the beams coming from the EPD that can enter the pupil Π of the eye are summed. The energy figure on the retina shows a maxima on the point $P_{i,j}$ that is the focus point relative to the emissive distribution $M_{u,}$ The interference function can then be expressed as:

$$I(\vec{r}) = \sum_{u,v}^{M_{u,v}\in\Pi} \sum_{u\prime,v\prime}^{M_{u\prime,v\prime}\in\Pi} {E_0}^2 \left[cos\left(\left(\overrightarrow{k_{u,v}} - \overrightarrow{k_{u\prime,v\prime}}\right).\left(\vec{r} - \overrightarrow{r_{i,j}}\right)\right)\right] \quad \text{(II.23)}$$

The area of the amplitude on the retina cannot be infinite. To limit its spreading our model therefore uses the Gaussian approximation that defines the amplitude factor E_0:

$$E_0(x, y, Z_2) = \sqrt{\frac{2P_0}{\pi {w_2}^2}} \times e^{-\left(\frac{x^2+y^2}{{w_2}^2}\right)}, \quad \text{(II.24)}$$

Where P_0 is the total power emitted by each EP. The size of the beam on the retina is given by w_2 and can be expressed by the relations of Gaussian optics. As the emissive point $M_{u,v}$ of waist w_1 is located close to the object focal plane of the eye lens, the waist formed in the image focal plane is given by:

$$w_2 = \frac{1}{n}\frac{f\lambda}{\pi w_1}, \quad \text{(II.25)}$$

where n is the refractive index in the eye and f is the focal distance of the eye lens.

5.2 Simulation algorithm for multiple interferences

In the section 4, I described how to create various EPDs, defining the EP coordinates in the display plane. The multiple interference algorithm relies on these coordinates $M_{u,v}$ to calculate the final pattern. The operational principle of this interference algorithm if presented on the. **Figure II.26.** Firstly, the pupil aperture Ø to set active emissive points is defined. Simulations consider a specific case where the emitted beams from the EPD are parallel to the axe of propagation O_z. The position $M_{u,v}(X_{u,v}, Y_{u,v},)$ of the EP on the plane of the display corresponds to the point $M'_{u,v}(X_{u,v}, Y_{u,v},)$ on the plane of the eye pupil. The position is defined by the same coordinates with the distance Z_0 between the eye pupil and the retina. It fixes the angles of incidence $\alpha_{u,v}$ and $\theta_{u,v}$ in radians of the beam $\vec{k}_{u,v}$ that intersect the axis O_z on the plane of the retina:

$$\alpha_{u,v} = atan\left(Y_{u,v}/X_{u,v}\right);\ \theta_{u,v} = atan\left(\frac{\sqrt{X_{u,v}^2 + Y_{u,v}^2}}{Z_0}\right), \quad \text{(II.26)}$$

Then, the general system parameters are set as follows:

- eye lens pupil aperture Ø varies from 2 to 8 mm,
- focal length f = 51 mm (corresponds to the mimetic eye lens used in **Chapter III**)
- the wavelength λ = 532 nm,
- the radius of emissive point waist w_1
- the pixel size of our detector that simulates the retina: 2.5 µm
- the size of the image plane that imitates our detector: 200 pixels

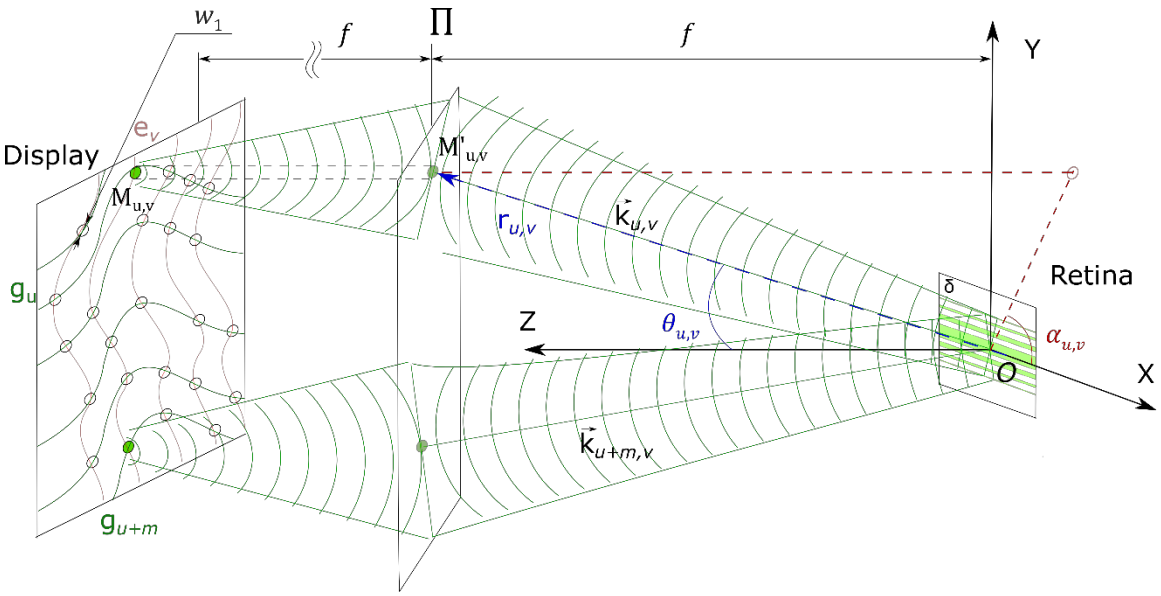

Figure II.26. Principle of multiple interference simulation:

Secondly, one calculates the distribution of energy on the retina on a coordinate grid X, Y given on an area defined by the waist w_2,as described by **equation II.25.** For each point of the EPD inside the eye pupil, primarily we calculate the wavevector $\vec{k}_{u,v}$of the wave front that corresponds to the angles $\alpha_{u,v}$ and $\theta_{u,v}$:

$$\overrightarrow{k_{u,v}} = \frac{2\pi}{\lambda}\begin{bmatrix} sin(\theta_{u,v})\cos(\alpha_{u,v}) \\ sin(\theta_{u,v})\, sin(\alpha_{u,v}) \\ \cos(\theta_{u,v}) \end{bmatrix}, \qquad \text{(II.27)}$$

Then, one calculates the field $E_{u,v}$ that corresponds to this wavevector as presented in **equation II.22,** assuming phase offset equal to zero: $\varphi_{u,v}$=0. This field is summed to a common field that will express the interference pattern.

One then calculates the envelope to limit spreading as the amplitude factor E_0 from the **formula II.24,** where P_0 = 1mW is the power emitted by an EP. Finally, one calculates superposition of wave. In the final step the multiple interference effect with the multiplication of the composite beam and its complex conjugate that give the spel intensity, writen as follows:

$$I(\vec{r}) = \left[\sum_{u,v}^{M_{u,v}\in\Pi} E_{u,v}(\vec{r})\right] \times \left[\sum_{u,v}^{M_{u,v}\in\Pi} E_{u,v}(\vec{r})\right]^* = E_{tot} \times E_{tot}^* \qquad \text{(II.28)}$$

The final expression for the simulated spel intensity is calculated from the summation of the planar beam given in **equation II.28** with a Gaussian beam intensity weighting and energy limitation related to the Gaussian beam extension on the retina of waist w_2.

5.3 Signal to Noise Ratio for EPD evaluation

I have shown previously how an EPD can be evaluated from EP location point of view. The randomness of the distribution with the dispersion of the histogram has been characterized. This method gives a first quantitative view of the device efficiency in the emissive plane. However, one needs to characterize its impact on the retina plane. Using tools to simulate the spel on the retina, I have studied two parameter to evaluate it in a quantitative way. These two parameters are the SNR and γ-parameter, described in **Figure II.27**.

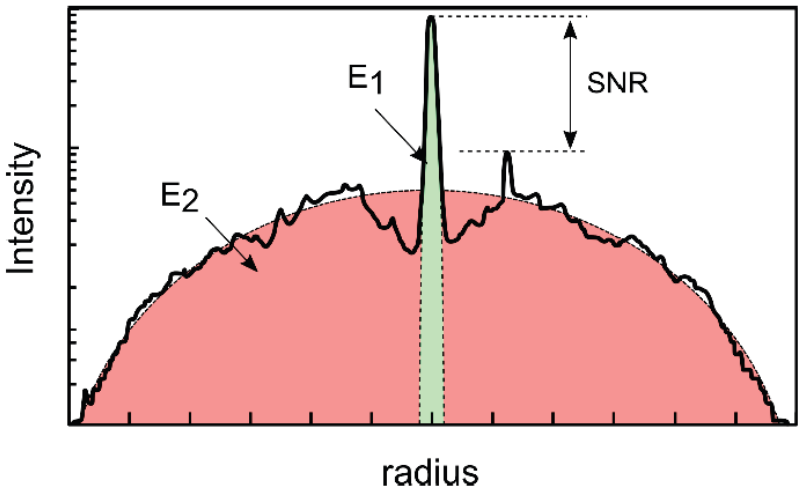

Figure II.27. Parameter SNR and γ characterizing the Point Spread Function resulting from self-focusing.

SNR is a ratio between the intensity of the central peak and the highest Intensity of the surrounding:

$$SNR = 10log\left(\frac{I_{peak}}{I_{ghost}}\right) = 10log\left(\frac{I_S(0)}{max\left(I_s(\vec{r})\right)_{r>\delta w}}\right) \quad \text{(II.29)}$$

Another important measure of spel quality is the ratio between central peak energy and the total energy of the signal called γ-parameter:

$$\gamma = -10\log\left(\frac{E_1}{E_1 + E_2}\right) \quad \text{(II.30)}$$

The Point Spread Function (PSF) characterizes the response of an optical system to the smallest feature it can represent as one can see in **Figure II.28**. It corresponds to the image of a theoretical

emissive point located at infinity. Here it corresponds to the notion of spel. In order to characterize the spel, I evaluate the parameter related to the perfect PSF.

The Airy disk is the diffraction limit for the PSF of any optics with a circular aperture. It is given in its normalized form by the following equation:

$$I_{Airy}(x) = \left(2\frac{J_1(\sigma)}{\sigma}\right)^2, \tag{II.31}$$

where J_1 is the 1st order of the Bessel function and σ is a spatial coordinate in the focal plane defined by the following equation [103]:

$$\sigma = \frac{2\pi}{\lambda} a \sin(\theta) \tag{II.32}$$

Where a is the radius of the aperture, and θ is the angle of observation.

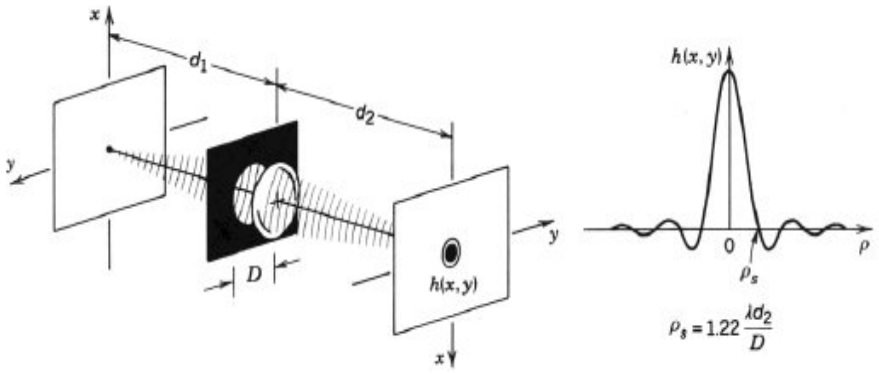

Figure II.28. a) Single lens image formation. b) PSF of the system ([104])

The equation of the Airy function allows for calculating the limit value of the SNR-parameter: it is expressed by the ratio of Airy function at σ=0 with the value of the first maximum. This first maximum is found at σ = 1,635 π:

$$SNR_{Airy} = 10log\left[\left(2\frac{J_1(1{,}635\pi)}{1{,}635\pi}\right)^2\right] = 17.57\ dB \tag{II.33}$$

One can also express a limit value for the $\boldsymbol{\gamma}$**-parameter** with the Airy function. I analyse this aspect relative to imaging in the **Chapter IV**.

The PSF of a spel and the Airy function are compared as shown in **Figure II.29**. The central peaks up to the first minimum perfectly fit. However, the noise level of a spel is evidently higher. In the close to peak region the difference between the spel noise and the Airy secondary peaks for the Random EPD is a few dB, but further from the centre it starts increase up to about 20 dB. This behavior cannot be seen using SNR criterion, however it's crucial for image formation, therefore in the **Chapter IV** the γ-parameter will be used instead.

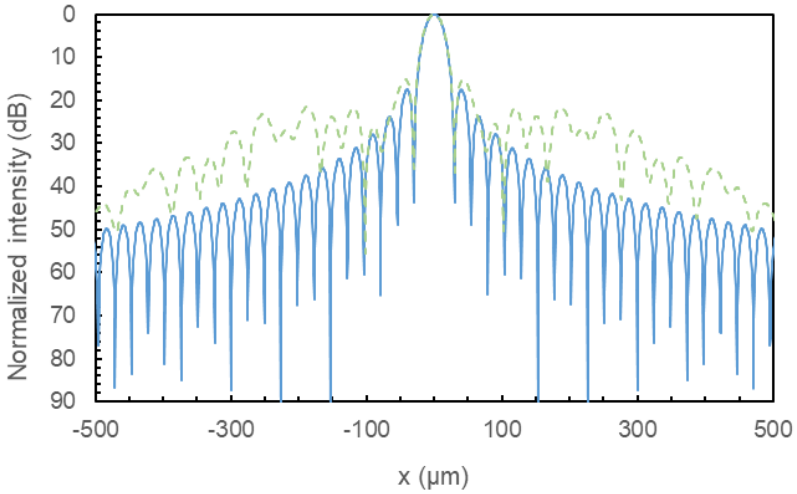

Figure II.29. Comparison between intensity cross section of the self-focusing signal in the Random EPD (dotted green curve) and the Airy function (blue curve).

5.4 Simulation results

Simulations aim at justifying the theoretical analysis of the self-focusing effect and provide the necessary design considerations for the fabrication of aperture distributions – a simplified analog of EPD. The SNR as spel quality criteria is chosen first and calculations are carried out with a variation on the next parameters:

- Distribution type: Periodic, Quasi-Periodic, Quasi-Random, Realistic (CS and CRS).
- Size of Emissive surface region D_e from 2 to 8 mm, D_e is assumed equal to the pupil aperture ø, where $Z_1 = f$, see **Figure II.30** .

- Observation position for the pupil aperture ø = 4mm: 9 positions all along the whole Emissive surface limited by D_{EB}= 10mm (**Figure II.30**), the first glance at the HDM eye-box issue.
- Number of emissive points given by Λ – the size of the EUC, Λ varies from 400 µm to 1000 µm with a 200-µm step .
- Size of EP: it impacts the SNR due to the beam etendue and transmitted energy.

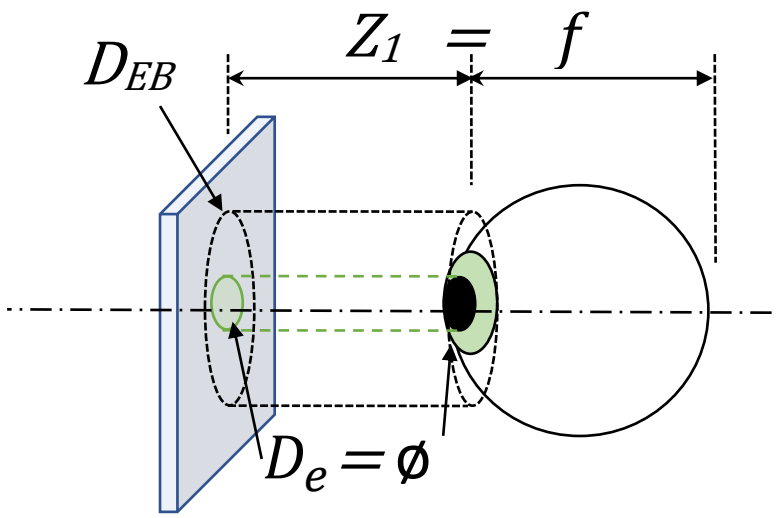

Figure II.30. Eye-Box and pupil size

5.4.a Self-focusing of various EPD-types

I performed a first set of simmulations to understand how randomness affects SNR. Initial characteristics for these simulation are: Λ = 600 µm, w_1=25 µm. Wavelength corresponds to the reference wavelength for the hologram recording setup developed in the laboratory: λ = 532 nm. The focal distance is f = 51 mm to be consistent with the characterization setup that will be introduced in the next chapter.

Simulations indead confirm that a periodic EPD creates periodic self-focusing pattern. The typical diffraction pattern from a periodic distribution is shown in **Figure II.31b**. The central peak is surrounded by strong secondary peaks (**Figure II.31c**) with the SNR estimated at about 0.16 dB (**Table II.2**). Changing the observation position has no influence due to the absolute uniformity of the EPD. The subsequent peaks' locations for periodic distribution depend on the EUC size $\Lambda = \Lambda_1 = \Lambda_2$, and can be calculated as follows:

$$\begin{cases} x_i = x_0 + i\dfrac{\lambda f}{\Lambda}, \\ y_i = y_0 + i\dfrac{\lambda f}{\Lambda}; \end{cases} \quad \text{(II.34)}$$

where (x_0, y_0) is the coordinates of central peak and i is an index integer.

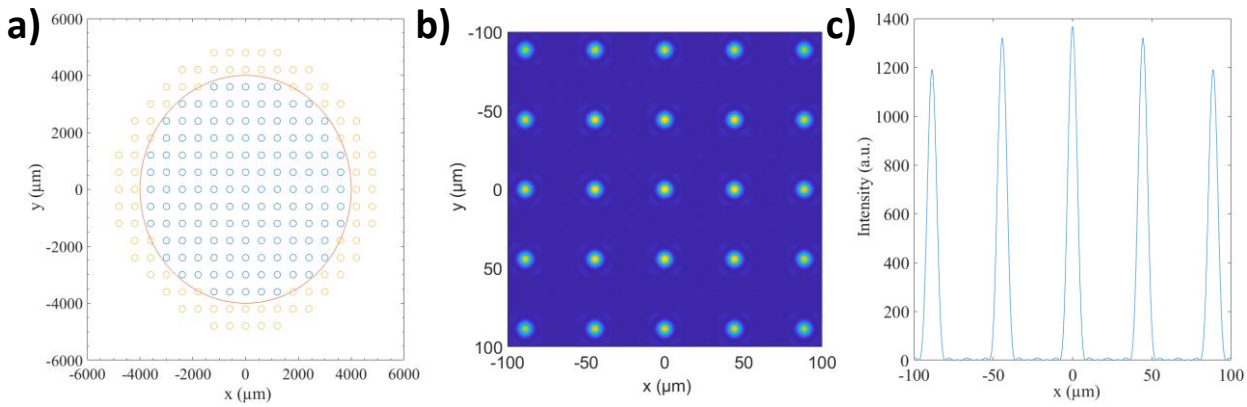

Figure II.31. Self-focusing simulation of Periodic distribution: a) Periodic EPD, b) its diffraction pattern, c) cross-section of the diffraction pattern

The introduction of a periodicity modification in case of the Quasi-Periodic distribution significantly improves the SNR up to about 4.62 dB in case of the whole emissive surface activation limited by maximum pupil aperture Ø= 4 mm (**Table II.2,** see below, near 5.4.c sub-section). The diffraction pattern presented in **Figure II.32b** has the form of a cross for relatively weak noise in terms of intensity with the thin and clear peak in the center. However, the reduction of the pupil aperture seriously decreases the SNR for the Quasi-Periodic EPD and in case of 2mm it performs almost equal to the Periodic ones with an SNR = 0.42 dB.

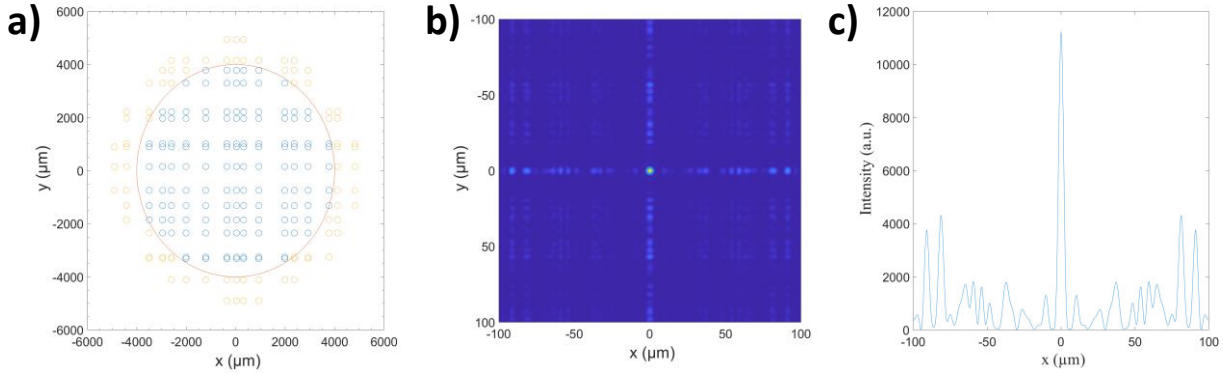

Figure II.32. Self-focusing simulation of Quasi-periodic distribution: a) Quasi-Periodic EPD, b) its diffraction pattern, c) cross-section of the diffraction pattern

The Quasi-Random distribution produces a pattern (**Figure II.33**) that gets closer to the diffraction limit with a SNR of 10.63 dB for the emissive surface limited by the 8 mm pupil aperture corresponding to 138 EPs. This case will be considered as an ideal reference and will serve for comparison with other distributions. We assume this EPD to be uniform, therefore there is no significant difference in term of the SNR for an arbitrary position of the pupil aperture.

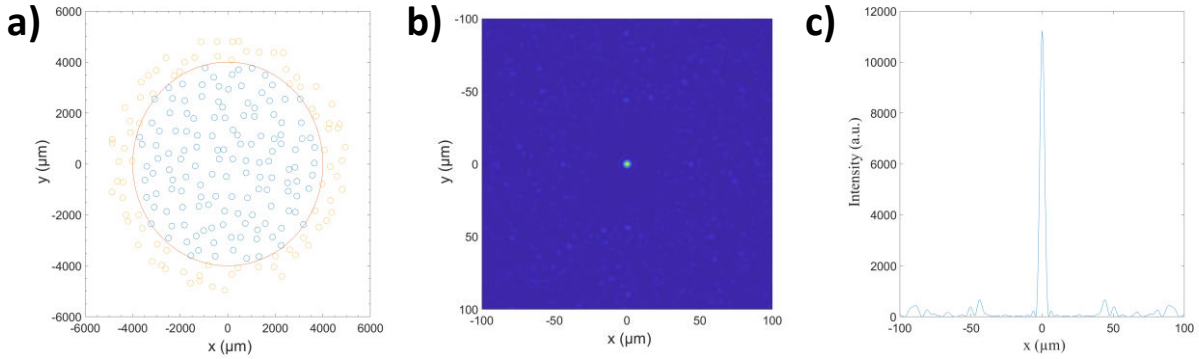

Figure II.33. Self-focusing simulation of Quasi-Random distribution: a) Random EPD, b) its diffraction pattern, c) cross-section of the diffraction pattern

The Cross-Sinusoidal distribution, the first case of Realistic-Random EPD (**Figure II.34a**), produces a diffraction pattern with an SNR equals to 4.79 dB. The noise has a regular profile as for the Quasi-periodic EPD that is slightly rotated counterclockwise around the center (**Figure II.34b**)). This shape becomes more evident in the case of a reduced pupil aperture Ø= 4mm (**Figure II.34c**). It is induced by a low randomness in the centre of the EPD, which recalls a clockwise rotated periodic distribution as it could be seen from **Figure II.34 a**.

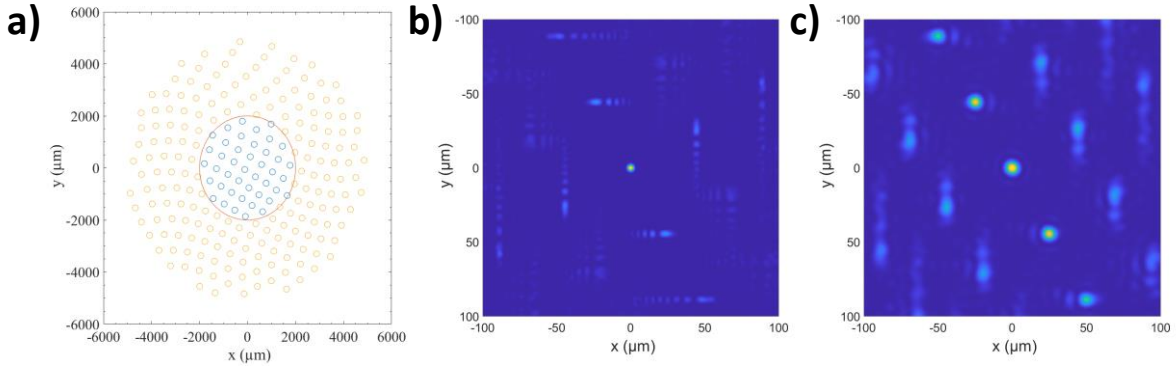

Figure II.34. Self-focusing simulation of Cross Sinusoidal distribution: a) CS EPD with the pupil aperture **Ø** = 4mm, b) diffraction pattern of the whole EPD, c) diffraction pattern of the pupil aperture limited EPD (blue EPs in the red circle)

The Cross-Random-Sinusoidal distribution, the second case of a Realistic-Random EPD **(Figure II.35a**) has almost a two-fold increase of SNR comparatively to the CS with a SNR = 10.51 dB, almost the same as the Random EPD produces. Similarly to the Periodic and Quasi-Periodic cases, the introduction of irregularity in the addressing of the EP induces an improvement of the SNR. The noise pattern of this EPD also reminds a cross (**Figure II.35 b,c**), rotated around the center due to low randomness in the center of the EPD.

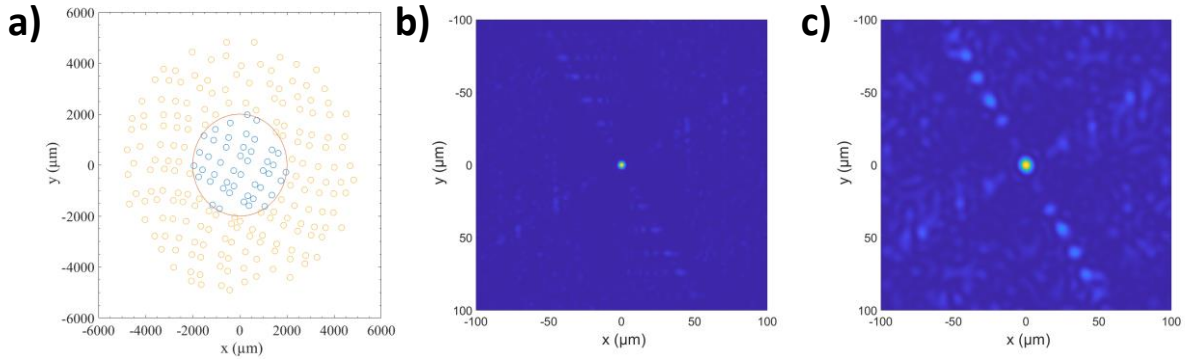

Figure II.35. Self-focusing simulation of Cross Random Sinusoidal distribution: a) CRS EPD with a the pupil aperture Ø = 4mm, b) diffraction pattern of the whole EPD, c) diffraction pattern of the pupil aperture limited EPD (blue EPs in the red circle)

One may conclude from these results the following elements. Firstly, for the maximum number of emissive points per an EPD considered here, and independently of its type, the noise pattern is relatively weak, except for the Periodic distribution. To be able to observe the noise pattern distinctly, one has to either narrow the pupil aperture or to increase the EUC size Λ, that both decrease the number of emissive points. I will investigate these types of simulations in the next sub-sections. The simulations confirm the assumption that randomness significantly improves the SNR.

Secondly, almost same height and thickness of the central peak for a given pupil aperture is observed. As predicted by the theory and shown later, this parameter does not depend on the type of distribution or on the number of EPs, but strongly depends on the numerical aperture of the focusing optical system.

General remark: arbitrary units (a.u.) are used for intensity of the diffraction pattern cross-sections instead of normalized ones. By this way, one can easily distinguish the number of activated emissive points as will be shown on the next paragraph.

5.4.b Self-focusing of various pupil apertures

In the previous subsection, the central peak of the spels is found to be surrounded by a low level of noise when considering a high number of emissive points. In this subsection the influence of the variation of the pupil aperture on the SNR is studied. Another consequence on the broadening of the central peak that depends on ø as expressed by the formula of the first zero of the Airy function:

$$\delta w = 1.22\frac{\lambda f}{ø} \qquad \text{(II.35)}$$

Simulation aperture is chosen according to physiological characteristics of human eye. Human pupil size varies from 2 to 8 mm in general: from 2 to 4 mm in bright environment and from 4 to 8 mm in dark environment. Theoretically, while Ø decrease from 8 to 2 mm the peak width broadens 4-fold according to **Equation (II.32).** Simulations confirm the peak broadening and the SNR degradation. For a pupil aperture reduction from 8 mm to 2 mm the SNR of the Random EPD decreases from 10.63 dB to 2.42 dB respectively. In **Figure II.36** I present the case with the highest-possible pupil aperture Ø=8mm. The SNR = 10.63 dB is the highest value for all distributions with the same initial waist w_1= 25 µm and the same EUC size Λ=600 µm, therefore the highest EPs number per EPD. Later on, the influence of Λ and w_1 on the SNR will be studied.

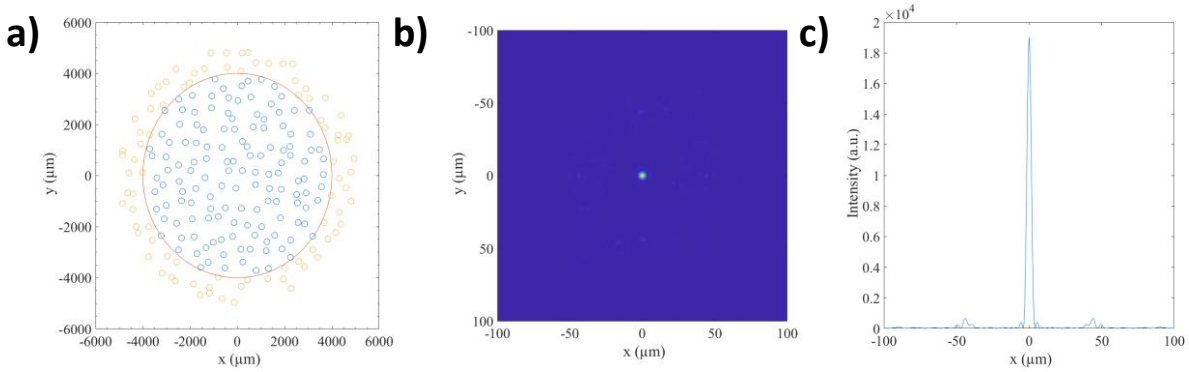

Figure II.36. Self-focusing simulation of Quasi-Random distribution: a) EPD with a the pupil aperture ø = 8 mm (138 EPs), b) diffraction pattern of the EPD, c) cross-section of the diffraction pattern

In **Figure II.37** with a reduction of the pupil aperture ø to 6 mm the number of EPs is reduced from 138 to 78 EPs, however the SNR decreases only by 1.2 dB and equals to 9.44 dB. The peak diameter $2\delta w$ is for simplicity calculated as a distance between the first minima from left to right on the diffraction pattern cross-section. The peak broadening for ø = 6 mm is about 1.5 µm relatively to the initial value δw=3.5 µm for ø = 8mm.

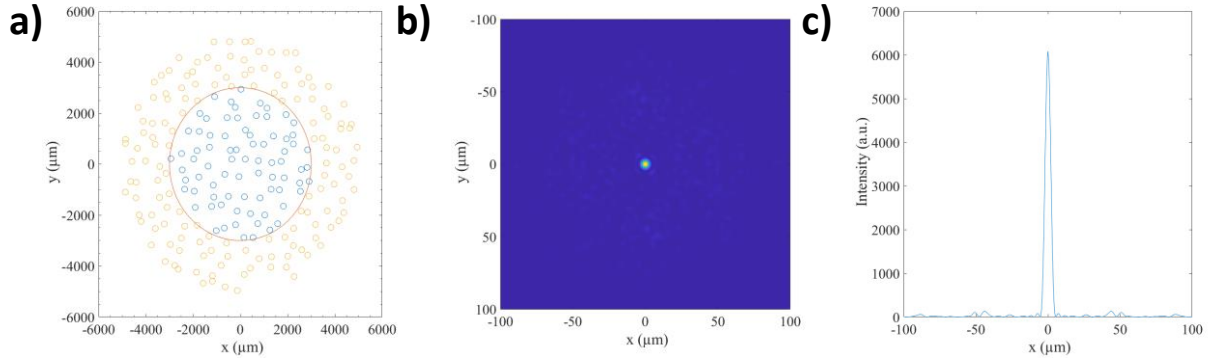

Figure II.37. Self-focusing simulation of Random distribution: a) EPD with a the pupil aperture ø = 6 mm (78 EPs), b) diffraction pattern of the EPD, c) cross-section of the diffraction pattern

Figure II.38 depicts the diffraction pattern with SNR = 7.03 dB for the EPD limited by ø = 4mm – the intermediate size of the eye pupil for day/night regimes. The peak broadening is also about 1.5 µm. In this case 37 EPs per EPD are counted.

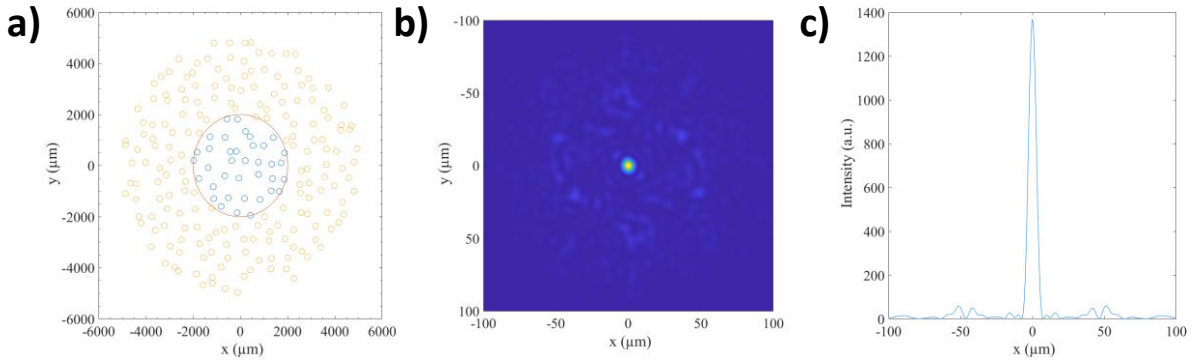

Figure II.38. Self-focusing simulation of Random distribution: a) EPD with a pupil aperture ø = 4 mm (37 EPs), b) the diffraction pattern of the EPD, c) the cross-section of the diffraction pattern

Finally, **Figure II.39** shows the limiting case with Ø = 2 mm. An SNR = 2.42 dB and a peak width $2\delta w$ = 15 µm are obtained. Although the SNR for this case is still higher than the SNR for several other distributions with the wider pupil aperture Ø, one can expect that the formation of images will be difficult with such kind of spel. This case shows the insufficiency of SNR as the only criterion for EPD evaluation and will be completed by the γ-parameter mentioned previously in the next chapters.

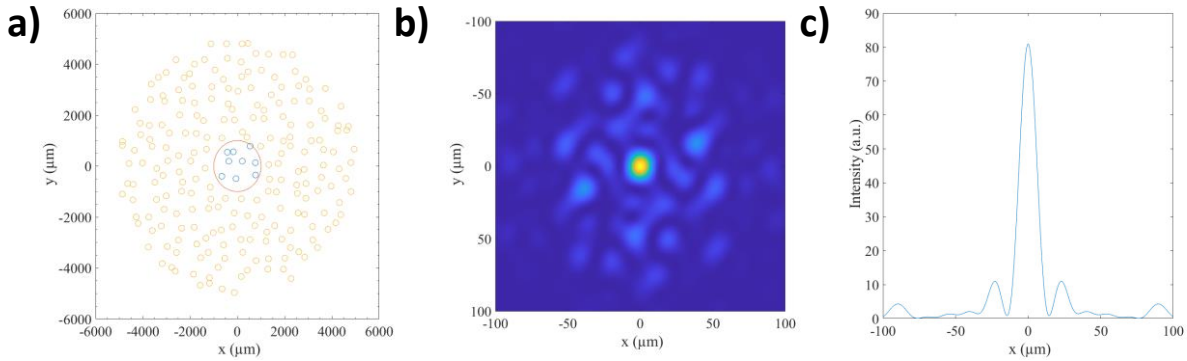

Figure II.39. Self-focusing simulation of Random distribution: a) EPD with a pupil aperture ø= 2 mm (9 EPs), b) the diffraction pattern of the EPD, c) the cross-section of the diffraction pattern

Similar simulations for all sorts of distribution previously discussed with the same initial waist w_1 = 25 µm and the same EUC size Λ = 600 µm have been performed. Results are presented in **Figure II.40** and **Table II.2**. From these supporting materials one can observe self-focusing capability of various EPD and compare them. One can divide the pupil aperture size Ø into three regions: the narrow region with Ø < 4 mm, middle region with pupil aperture Ø between 4 and 6 mm, and wide region with Ø > 6 mm.

Evidently, the Periodic distribution is not suitable due to poor and consistent SNR estimated at about 0.16 dB for the whole pupil aperture range. However, the simple introduction of variations on the periodicity significantly improves the SNR trend for the Quasi-Periodic distribution that reaches 4.62 dB at Ø = 8 mm. In the same time, in the small pupil aperture region the SNR for Quasi-Periodic EPD differs significantly: there is a noticible increase between pupil aperture Ø equals to 4 and 5 mm – the SNR rises from 2.4 dB up to 4.07 dB respectively.

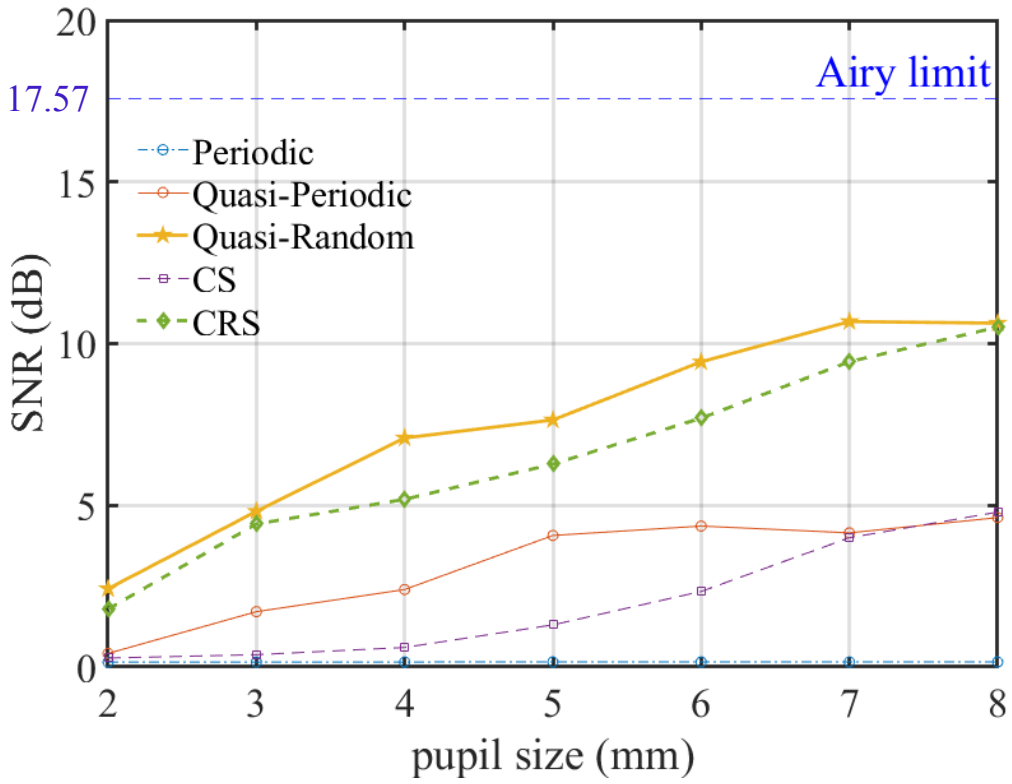

Figure II.40. SNR of Self-Focusing Simulations by the EPD with pupil aperture variation

The Cross-Sinusoidal distribution has the same SNR values as the Quasi-Periodic distribution for wide pupil aperture region where ø equals 7 and 8 mm. For the middle and narrow pupil aperture regions, the CS EPD shows a stable growth trend while ø > 4 mm. Most probably, the EUC size limits randomness in the central region of the CS EPD, as explained before.

The most interesting configuration is the Cross-Random-Sinus distribution due to its high SNR-quality, close to the Quasi-Random EPD. The introduction of irregularity provides an about 5 dB gain relative to the CS distribution all along with the full range of pupil apertures. Both in the narrow and the wide pupil aperture regions, the CRS EPD is close to the Quasi-Random distribution (the ideal case), although there is a 1-2 dB gap in the middle pupil aperture region, that could probably be improved with further research. From **Table II.2** we see that for the same pupil aperture in the mid-wide region the CRS EPDs has about 16-19 EPs per EPD, more than the Quasi-Random distribution. Concluding, one observes a good behavior of the Cross Random Sinusoidal case that can be quite close from the Quasi-Random signal depending on the random

draw, as shown for the case of a 3 mm pupil. This result shows that a realistic addressing configuration could be designed, so as to be close to a theoretical ideal configuration.

Overall, in the narrow pupil aperture region, all distributions provide a PSF that is far from the diffraction limit. It could be caused by the low number of active emissive points contributing to the final intensity pattern. One can increase the number of EPs with the smaller EUC size Λ, however this leads not only towards increasing SNR, but also towards decreasing the number of available EPDs, therefore the number of available pixels that could be projected as spels. This is the so-called resolution/sharpness conflict previously mentioned.

Table II.2 Self-focusing simulation chart for the pupile size aperture variation/type of EPD

EPD	**Periodic**		**Quasi-Periodic**		**Quasi-Random**		**Cross Sin**		**CRS**	
Ø, mm	EP	SNR (dB)	EP	SNR (dB)	EP	SNR (dB)	EP	SNR (dB)	EP	SNR (dB)
8	137	0.16	136	4.62	138	10.63	154	4.79	155	10.51
7	109	0.16	106	4.15	106	10.68	121	3.99	123	9.44
6	73	0.16	73	4.36	78	9.43	93	2.34	94	7.69
5	57	0.16	54	4.07	54	7.63	66	1.3	73	6.28
4	31	0.15	31	2.39	37	7.03	43	0.68	46	5.18
3	21	0.15	21	1.71	20	4.81	25	0.38	29	4.42
2	9	0.15	10	0.42	9	2.42	12	0.28	11	1.79

Further, I propose to compare the most promising distribution from performance/feasibility point of view with the Quasi-Random distribution the ideal EPD in terms of self-focusing capability/PSF.

5.4.c Influence of the eye positioning

The SNR of non-uniform distributions depends on how one chooses the observation point. For the CS and the CRS distributions there is more periodicity in the center of EPD and there is more randomness in the borders as can be seen from **Figure II.23a** or **Figure II.34** and **Figure II.24b** or **Figure II.35**. I chose to compare and analyze the SNR of the CRS EPD regions and the Random distribution, both with the pupil aperture Ø = 4 mm. **Figure II.41a** depicts the CRS distribution divided by zones with the pupil aperture Ø = 4 mm. In **Figure II.41b** regions with the highest and the lowest SNR are highlighted with red and green respectively. **Figure II.41c** compares the SNR

with the EPs number. One can see that randomness plays the essential role for PSF quality: even with only 34 EPs the upper-right region performs 1.5 dB better than the central region with 46 EPs. The uniformity of the CRS distribution is quite moderate: there are 46 EPs in the central region and 28 to 36 EPs in the borders, except the middle right region with 43 EPs. The maximum difference in the EP number is 18 EPs which is more than twice bigger than the same parameter for the Quasi-Random distribution 8 EPs (**0c**).

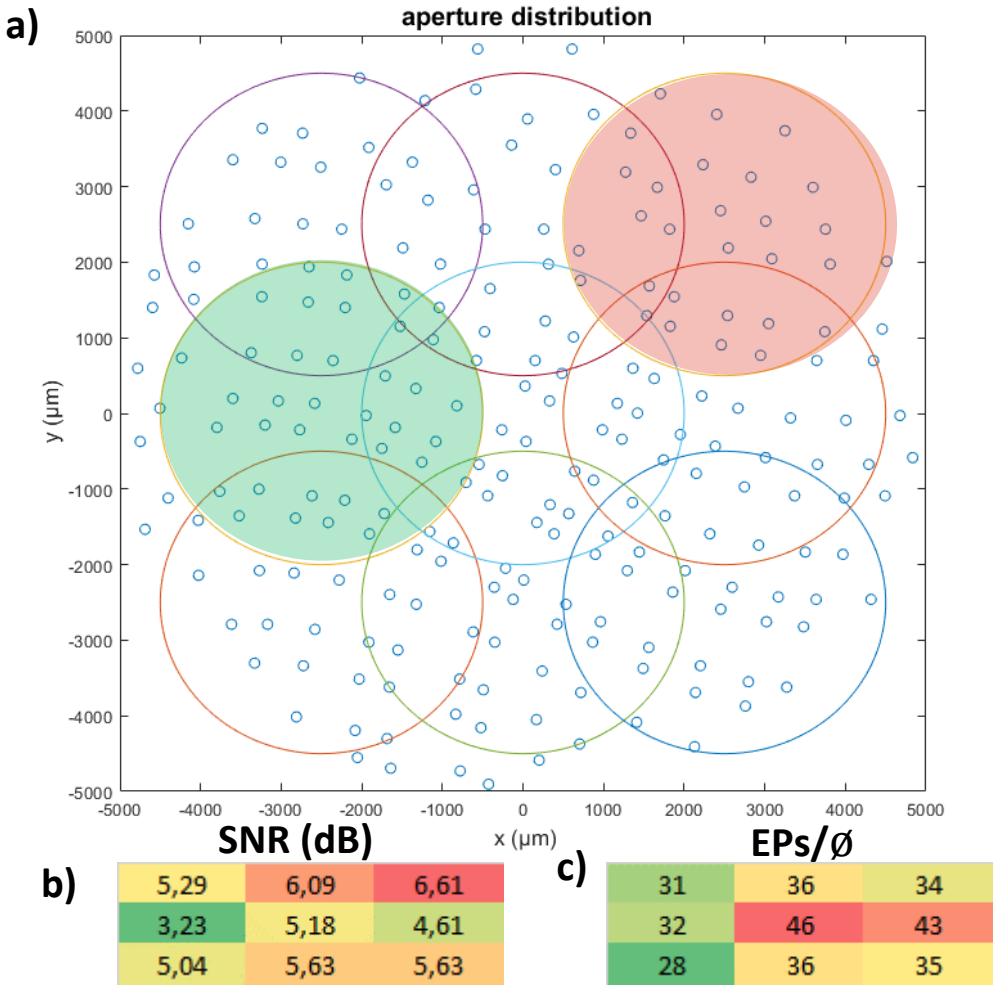

Figure II.41. CRS EPD with varying position of pupil aperture: a) 9 regions limithed by the pupil aperture **ø=4mm** b) SNR for these regions c) EPs number for these regions

The moderate uniformity is also seen from the SNR per region: the maximum difference is 3.37 dB between the highlighted regions (**Figure II.41a/b**). For the Random distribution, this

difference is almost twice lower: 1,7 dB (**0a/b**). The lower left region is chosen deliberately to compare with the low right region, as they have the same number of EPs and the SNR difference of the left region is negligible compared to the central region.

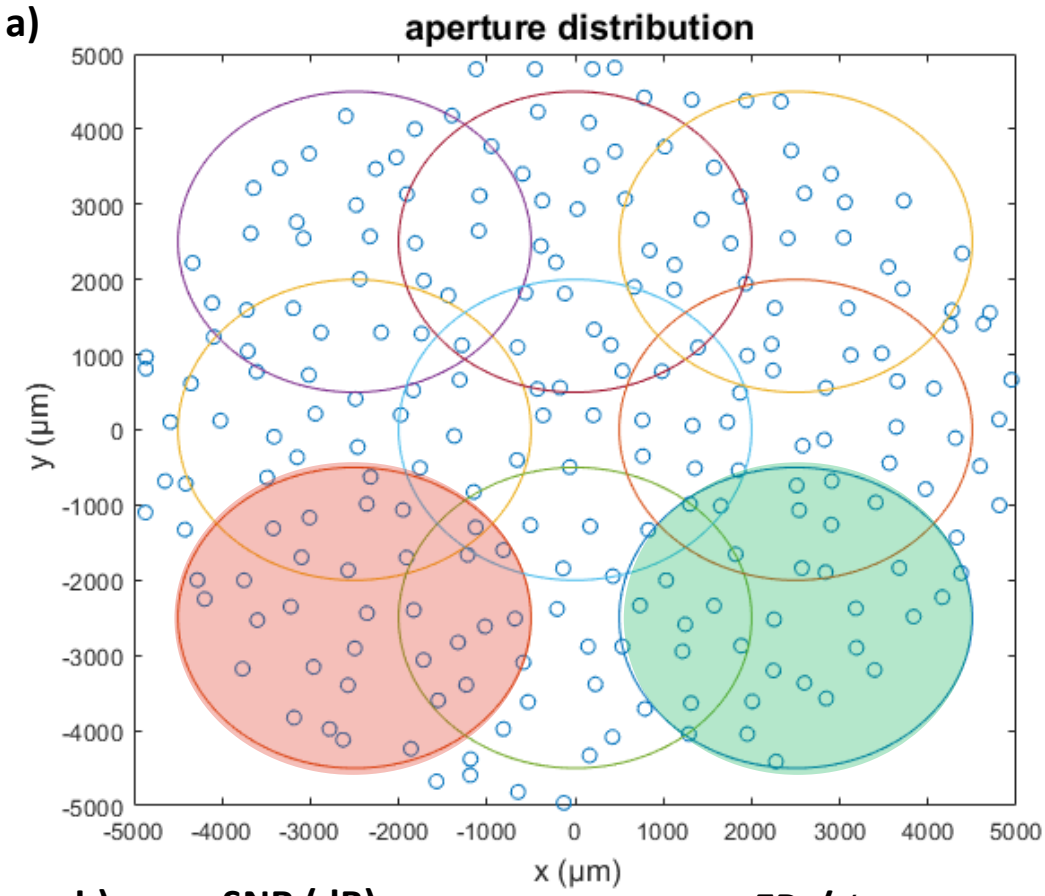

Figure II.42. Quasi-Random EPD with varying position of pupil aperture: a) 9 regions limited by the pupil aperture **Ø** = 4 mm b) the SNR for these regions c) EPs number for these regions respectively

5.4.d Self-focusing of various number of EPs per EPD

One can also vary the EUC size Λ (assuming $\Lambda = \Lambda_1 = \Lambda_2$) which defines the number of EPs per EPD as previously described. The EPDs with Λ in range from 400 to 1000 µm with 200 µm step are simulated. Results are presented in **Figure II.43**. The SNR of the Quasi-Random EPD gradually decreases with increasing EUC size Λ: from 9.48dB down to 2.11 dB. On the contrary, the CRS EPD has the inverted U-shape: equally with the small and big EUC size Λ, it performs worse than with the intermediate value Λ = 600 µm and Λ = 800 µm that shows SNR = 5.19 dB and 4.09 dB respectively. This behaviour is explained by strong periodicity in the central region where the SNR is measured. The periodicity is strongest at the small Λ and the CRS distribution tends to the Periodic EPD in the central region limited by ø = 4 mm as showed in the previous section. However, with the middle EUC size the CRS distribution is comparable to the Quasi-Random EPD: there is a 2-dB offset at Λ = 600 µm and equal SNR for Λ = 800 µm. From **Table II.3** one sees a six-fold decrease in the number of EPs per distribution from the smallest EUC size Λ to the greatest one, as previously explained. The difference of EP number between quasi-Random and CRS EPDs is explained by non-absolute uniformity of CRS distribution. The periodic EPD has almost the same number of EPs as the quasi-Random distribution, both being uniform distributions.

The Quasi-Periodic and CS distributions show strong attenuation in the middle and big EUC size regions, although the Quasi-Periodic EPD performs even better than the CRS distribution at the Λ = 400 µm. The periodic distribution demonstrates the SNR < 1dB all along the whole Λ range. The CRS in the middle Λ region could be a compromise for resolution/sharpness conflict and also an answer for addressing issues due to it's feasibilty, while still having similar SNR to the quasi-Random EDP SNR performance.

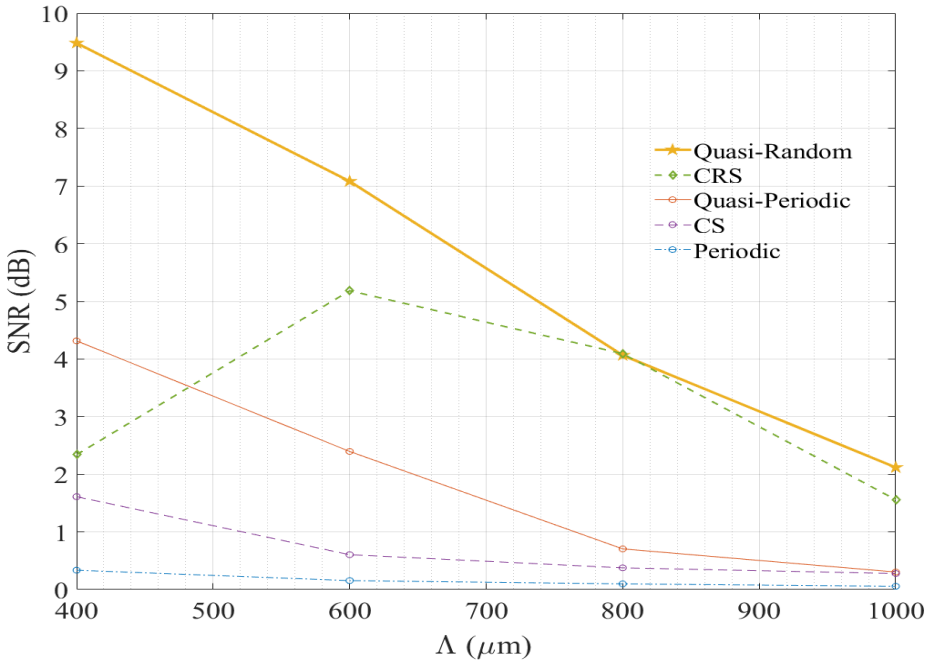

Figure II.43. SNR of Self-Focusing Simulations as a function of the EPD and EUC size Λ

Table II.3 Self-focusing simulation chart for the EUC size Λ variation/type of EPD with the emissive point waist w_1 = 25 µm and limited by the pupil aperture Ø=4mm

EPD	Periodic		Quasi-Periodic		Quasi-Random		Cross Sin		CRS	
Λ (µm)	EP	SNR(dB)	EP	SNR (dB)	EP	SNR (dB)	EP	SNR (dB)	EP	SNR (dB)
400	81	0.36	75	4.31	75	9.48	99	1.61	96	2.34
600	37	0.15	31	2.39	37	7.08	43	0.60	46	5.19
800	21	0.09	16	0.71	20	4.06	24	0.67	24	4.09
1000	13	0.06	15	0.30	12	2.11	16	0.27	16	1.56

5.4.e Self-focusing of various apertures of EP

Another important characteristic is the EP aperture, expressed as a function ot the waist radius w_1.In **Figure II.44** one observes the steady growth of the SNR of all type of EPD with increase of EP aperture w_1. However, the most important region of this graph is outlined in red, where w_1 is between 1.25 µm and 12.5 µm depicted in **Figure II.45.** One can observe a deep downgrade in SNR for Quasi-Random EPD in 1.25-5 µm region. The phenomenon was not deeply investigated and may be caused by simulation artifacts. Therefore, it is important to conduct detailed research for this region.

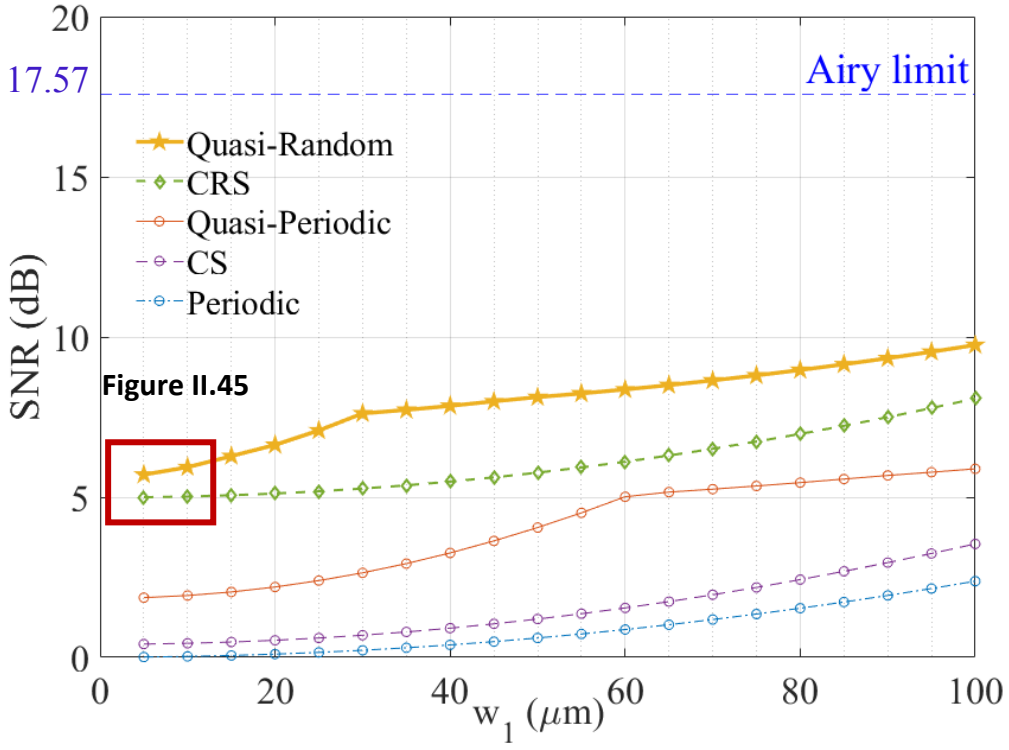

Figure II.44. SNR of Self-Focusing Simulations by the EPD with variation of emissive point waist radius w_1 for the EUC size Λ = 600 µm and the pupil aperture $\emptyset$ = 4 mm

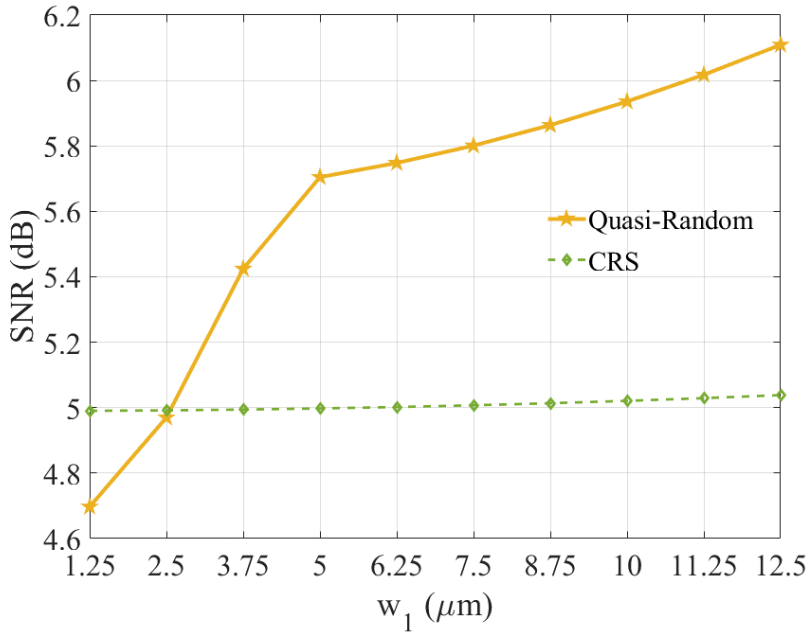

Figure II.45. Quasi-Random and CRS EPD comparison in the emissive point waist region: w_1 varies from 1.25 µm to 12.5 µm of Self-Focusing Simulations by the EPD and emissive point waist w_1 for the EUC size Λ =600 µm and the pupil aperture $\emptyset$ = 4mm

In the region of the small emissive point waists w_1, the CRS distribution performs at a level of about 5 dB. At the same time, the Quasi-Random EPD shows smaller SNR for w_1=1.25 µm, (0.3 dB compare to the CRS) and almost the same at the w_1=2.5 µm. Further there is an SNR growth and the difference between EPD's SNR becomes positive: about 1 dB. However, for technical realizations an EP aperture w_1 between 1 µm and 2.5 µm is the most realistic.

To conclude, the intersection calculation method has been applied and the simulations with the SNR as optimization criterion have been used to find an optimal distribution, both feasible and efficient. These simulations show that the CRS distribution is a good candidate as the first approximation for the concept's EPDs. The CRS performs at the comparative level of SNR for realistic characteristics: pupil aperture, EUC size and EP's aperture. However, analyzing the behavior of this EPD from the image formation side has to be performed to verify such assumption. **Chapter IV** presents the results exploiting γ-parameter. It should be mentioned, that there are also more recent research on the topic of the EPD design, presented in references: [100], [101], [105].

6 Conclusion

As I've shown in this chapter our self-focusing effect implementation for image formation is theoretically possible. However, the whole process requires introducing basic notions that differ from conventional imaging due to our innovative approach. It's useful to keep in mind the difference between a pixel and a spel. A spel is a result of self-focusing onto the retina. To produce such a pattern the conceptual device requires an ensemble of emissive points (EPs) that form an Emissive point Distribution (EPD). This chapter was mainly dedicated to the description of various types of EPDs and to the spels produced by them. I've shown in my simulations that the spel "quality" is strongly dependent on several parameters, namely the number of Emissive points per EPD and the aperture of EP, the type of distribution, especially its randomness and uniformity, the pupil aperture that limits an EPD. These parameters serve for my estimation of the proposed basic design considerations to fill up the emissive surface most effectively. I seek to maximize a number of emissive points, therefore, the EPDs formed by them, and in the same time to obtain the maximal possible quality of spels formed by such EPDs. This requires that an EPD has as much as a possible random distribution of emissive points which are distributed uniformly along the whole emissive surface. I evaluated this using the histograms of the minimal distance. At the same time, designed EPD should be feasible: each EP is an intersection between waveguides and electrodes. They have physical dimensions and requirements, e.g. bending curvature for waveguides that leads to light loss.

I studied 3 main types of distributions: Periodic, Random, and Realistic. Each type has two sub-types, for the first two it expands with a prefix "quasi-". A Realistic distribution searches to imitate Quasi-Random distribution in terms of Randomness that produces the best possible spel for image formation: a thin central peak with low noise around. However, a Random distribution is not feasible, therefore there should be a trade-off between the Random and Periodic distribution. Periodic distribution is perfectly feasible, but the produced signal cannot be used for image formation due to strong noise in form of high thin side peaks. In **Chapter IV** I show the images produced by each type of distribution to evaluate their image formation performance. Therefore, a Realistic distribution is a compromise between Randomness and Feasibility. The research described in this chapter leads me to experimentally validate the self-focusing performance of (Quasi-)Periodic, (Quasi-)Random, and Realistic EPDs. I present it in the next **Chapter III**

Chapter III: Self-focusing experimental evaluation

When you can measure what you are speaking about, and
express it in numbers, you know something about it.
Lord Kelvin

This chapter describes the experimental validation of self-focusing effect to validate the theoretical analysis and simulations presented in the previous chapter.

The **Introduction** highlights the basic idea of our setup to imitate the unconventional NED concept operation.

The **Section 2** describes our setup and characterizes its two main parts: the Emissive system and the Imaging system. The Emissive system is basically imitating our NED concept. The Imaging system is a simplified eye model.

The **Section 3** provides an evidence of self-focusing effect describing its validation process with various pinhole distributions. A solution to overcome specific issues related to the spel evaluation experiment and the dynamic range is presented.

The **Section 4** demonstrates experimental evidence of the influence of the source position (shift and rotation) and of the eye pupil size variation.

The **Section 5** presents the results of self-focusing experiments with a variation of the spectral characteristics to evaluate the impact of the temporal coherence on the image formation. The previously described simulation approach is used to simulate the obtained results with the special characteristics of our source.

1 Introduction

In this chapter, I introduce the setup that allowed us to experimentally validate the self-focusing effect. In **Figure III.1a,** I present our NED concept with spel formation process: there is a spot focalized on the retina thanks to the self-focusing effect. The set of emissive points called Emissive Point Distribution (EPD) generates directive spherical wave fronts with main wave vector $\overrightarrow{k_s}$. Analogously, in **Figure III.1b**, we propose an idea for a possible setup to imitate our NED: a planar wavefront with an angular direction $\overrightarrow{k_p}$ passes through a diffractive optical element (DOE) – a pinholes distribution plate that imitates an EPD. This DOE is placed in front of an optical system consisting of a camera lens and a CMOS sensor that imitates an observer's eye. The setup produces phase-adjusted spherical wavefronts with main wave vector direction $\overrightarrow{k_s} = \overrightarrow{k_p}$. We assume that our validation setup is an adequate model to evaluate our NED concept image formation approach and to investigate its imaging capability on the retina.

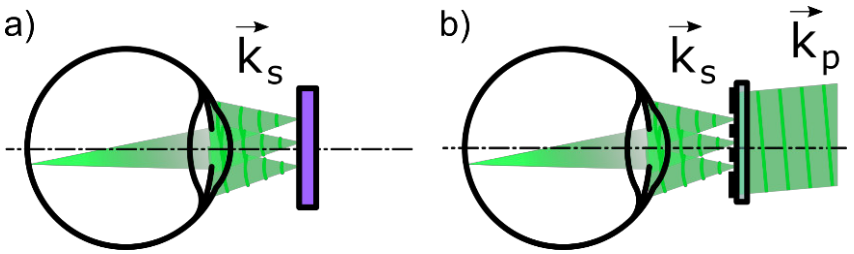

Figure III.1. Comparison of self-focusing NED concept and its validation setup: a) our unconventional NED concept where a distribution of spherical wavefronts is emitted and produces the illusion of a plane wavefront that the eye lens focuses on the retina; b) our validation setup: a laser beam passes through a transmission device consisting in a distribution of pinholes in an opaque metallic layer.

2 General description of setup

This section describes our design choice for self-focusing setup configuration and provides the characterization of its elements. The basic idea of the setup is to imitate our unconventional NED concept that produces a spel into a retina as the result of the self-focusing effect. This setup was assembled in the beginning of 2016, and at that time no solution was ready to implement the concept directly with an emissive surface. In order to get closer from the real concept, other researches have been carried out and are still under way in the laboratory, for example the waveguide part performed by Basile Meynard and Kyllian Millard [95] and the switching part by

Matthias Colard [106]. My PhD was the very first step in an experimental evaluation of the concept so that it leads us to a fairly simple setup, that revealed to be sufficient to validate self-focusing effect. Considering the lack of emissive device, we decided to transpose the demonstration from purely emissive to a transmissive configuration of setup.

Our setup follows the scheme depicted in the **Figure III.1b.** It consists in two main parts: the emissive system that imitates our unconventional NED and the imaging system that mimics a simplified human eye. The main requirement for the emissive system is to have equal output intensity from every emissive point with phase-adjusted wavefronts. The imaging system should have enough resolution and light sensitivity to be able to capture the self-focused spot with its surrounding noise. According to these requirements we solved the next tasks for the setup construction:

- Propose a simple optical design that could be easily used for various experiments.
- Calculate the characteristics of the different optical elements of the setup to ensure proper spel formation by self-focusing effect.
- Define a simple optical system simulating the human eye.

2.1 Main settings and parameters of the setup

Inititially we planned to use a test-bench with an optical system made of two lenses depicted in the Figure III.2. We place an optical fiber as a point source. The emitted energy is transferred via lens $L1$ and $L2$ to generate a planar wavefront at a configurable angle on the diffractive sample located in front of the eye. The point source is placed in a plane located at point A and can take various positions P_{ij}. The image of this distribution is obtained by a first lens $L1$ at point B. A second lens $L2$ images point B to infinity. The image focal point F'_1 of the first lens is imaged at point C by the second lens so that the parallel beams from $L2$ all cross at point C. It is at this point C that we locate our DOE. The various locations of point P_{ij} result in various angular incidence β_{ij} of the beams on the DOE. The mimetic eye is placed behind the DOE. The principle of this setup is based on the optical system used to record the holograms in our NED concept [97].

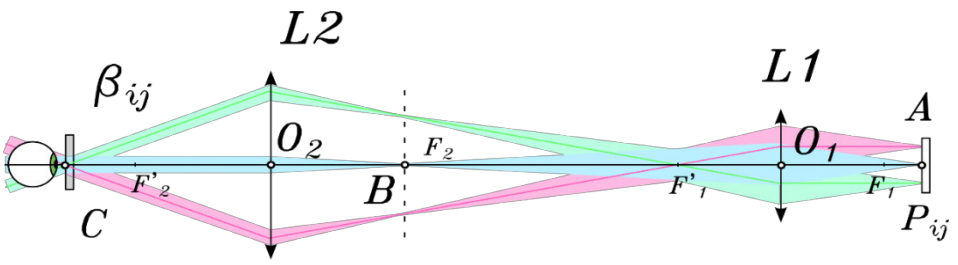

Figure III.2. Initial two-lens self-focusing validation setup

As we were building the setup, I encountered problems related to beam intensity inhomogeneities. Due to multiple reflections in the simple lenses I used at first (plane convex lenses), the beam at the level of the sample shows interference patterns that does not allow to illuminated uniformly the apertures of the DOE. This issue pushed us to evaluate another simple experimental setup. Instead of using an optical system made of two lenses to produce a planar wavefront, I use a free space propagation on a long distance, assuming that if the point source is far enough from the DOE, the spherical wave originating from the emitting point can be approximated by a planar wave. The final self-focusing validation setup is depicted in the **Figure III.3.**

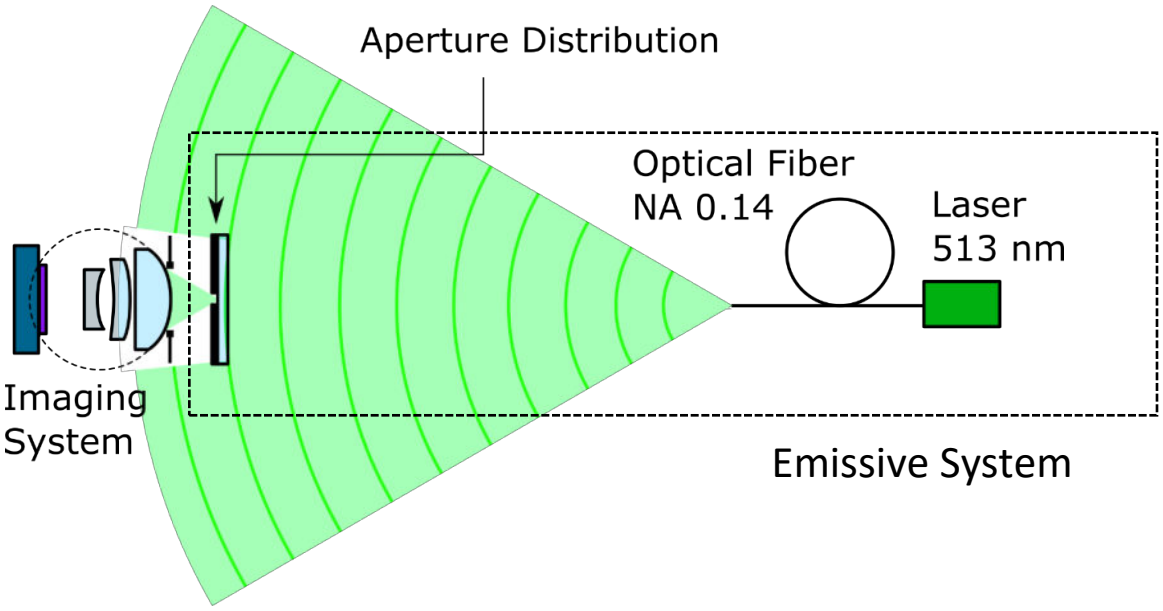

Figure III.3. Experimental setup for self-focusing effect validation consisting of two parts, from left to the right: Imaging system so-called ”mimetic eye” composed of a CMOS sensor and a camera lens. Emissive System: an aperture distribution transmits the quasi planar wavefront originating from a pigtailed laser diode and imitates an EPD.

The emissive system includes a pigtailed laser diode with a single mode optical fiber and the distribution of pinholes in an opaque metallic layer. The imaging system basically mimics a simplified human eye with a camera lens with a focal length f_0=51mm and a high-resolution CMOS sensor with a 3.5 µm pixel size connected to a PC with LabView software. The distance between the aperture distribution sample and the imaging system is about 20 mm and corresponds to a typical eye relief distance.

The main characteristics of the self-focusing validation setup are as follows:

- a single mode laser diode with central wavelength λ = 513 nm with spectral width of about 1 nm and emissive power of about 15 mW;
- a single mode optical fiber with numerical aperture *NA* = 0.14 and core diameter of about 8 µm pigtailed with a FC/PC connector;
- a diffractive optical element (DOE) made of a pinholes distribution with diameters: 25 µm, 50 µm and 75 µm;
- an adjustable diaphragm located behind the DOE (generally adjusted at 3 mm);
- a camera lens (Zeiss Wollensak Raptar 2.04") with 51 mm focal length and a diaphragm with f-number from f/1,5 to f/22;
- a CMOS-sensor from Lumenera with 3.5 µm pixel size, an imaging surface 10.5 x 7.7 mm^2, with 3000 x 2208 pixels;

Between our source and the DOE there is about 53 cm. We have assumed that this distance allows us to consider a planar wavefront incident on the DOE. In practice there is a small difference between our wavefront and a planar wavefront. It induces a small shift in the position of the focus point on the mimetic retina, but can be neglected for this proof of concept experiment.

A planar wavefront coming from $Z = \infty$ is focused in the focal plane of our lens at point *C* as described in **Figure III.4.** The quasi-parallel wavefront coming from S at a distance $Z = 550$ mm is focused at point C' at a distance Z'. We calculate this distance with the :

$$\frac{1}{Z}+\frac{1}{Z'}=\frac{1}{f}; \qquad \text{(III.1)}$$

The spatial shift on the focus point is determined: $Z' - f = 5.2$ mm. This value is not negligible, but we can place the camera on this location to evaluate the self-focusing effect. Indirectly this configuration can describe the self-focusing effect of a NED design that form an image at a given distance. In our concept it should correspond to holographic elements that generate a curve wave front instead of a planar wave front [97].

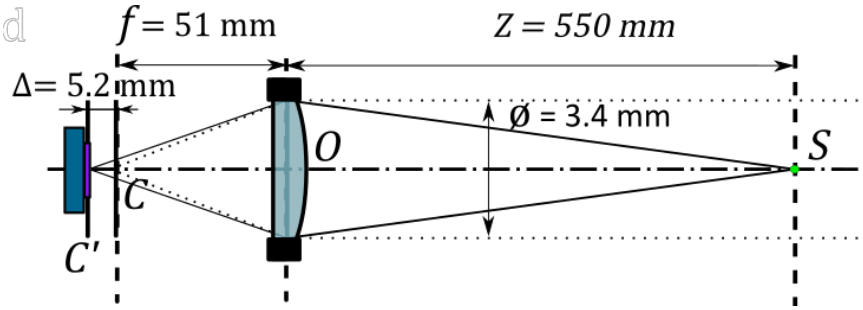

Figure III.4. Path difference between an ideal planar wavefront and the Gaussian beam wavefront generated by the pigtailed laser diode at given distance

2.2 Laser source description

The beam quality is essential for our experiment in order to uniformly illuminate our DOE**.** Our simple system described in **Figure III.3** uses only a small part of the beam coming from the optical fibre**.** Therefore we choose a high brightness laser diode with high quality profile, which is typically allowed by a single mode optical fiber coupled to the laser diode. Another interest of using an optical fiber as a point source is that we can move this element easily in the setup.

We chose a Single Mode Fiber-Pigtailed laser diode from Thorlabs (LP520-SF15). The Laser diode kit is shown in **Figure III.5a**. I show in **Figure III.5b** the laser diode spectrum given by the manufacturer.

Figure III.5. a) Thorlabs Laser Diode Driver Kit includes a laser diode with central wavelength λ ~ 513 nm, LD-Controller, TEC -controller and LD/TEC Mount, b) laser diode spectrum with CWL = 513 nm, FWHM ~ 1 nm

Our pigtailed optical fiber depicted in the **Figure III.6a** has a FC/PC connector that embeds an optical fiber with a numerical aperture NA = 0.14 (given at 1310 nm[12]). We calculate from the NA value the theoretical full divergence angle $\alpha = 2 \cdot \mathrm{asin}(NA) \cong 16°$. To verify this angle, I use the simple measurement setup shown in the **Figure III.6b**.

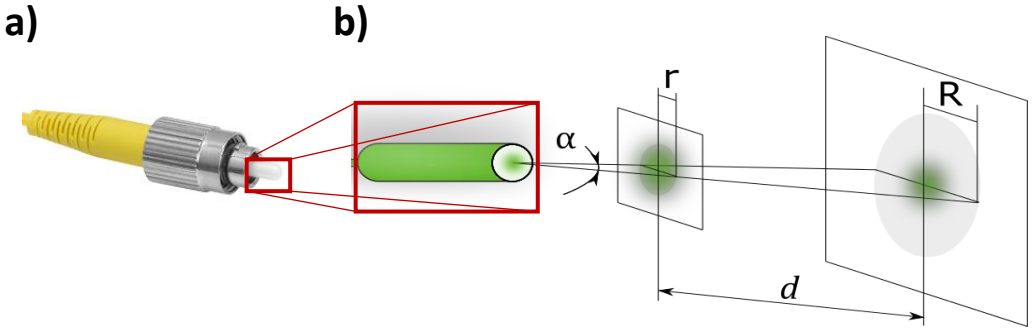

Figure III.6. a) FC/PC connector with 2.5 mm diameter and NA =0.14; b) beam angular divergence measurement process

I approximate the divergence angle α with two measurements of the beam radius at two propagating distances: $\alpha = 2 * arctan\frac{R-r}{d} = 15° \pm 1.5°$.

This value corresponds well with the value calculated from the given NA. I use this experiment to measure the beam intensity in angular coordinate. The cross-section of this measured intensity

[12] https://www.corning.com/media/worldwide/coc/documents/Fiber/SMF-28%20ULL.pdf

beam profile given has a Gaussian shape as shown in the **Figure III.7.** It is approximated by the gaussian function:

$$I(\theta) = I_0 e^{-2\frac{\theta^2}{\omega^2}} \qquad \text{(III.2)}$$

In **Figure III.7**, we use w = 4.86°. It corresponds to an angular radius at one percent of the maximum intensity of about 7 degrees (definition of the NA) that gives a more precise estimation of the numerical aperture at 513 nm.

Our DOE has a typical size of 1 cm in diameter. It stands out from the source at 53 cm, then its angular size is about 0.5° as seen from the fiber extremity. In our setup, the DOE element is centered on the optical axis and therefore according to our measurements presented on the **Figure III.7** the illuminated central region can be assumed as evenly illuminated with a deviation of about 2 %.

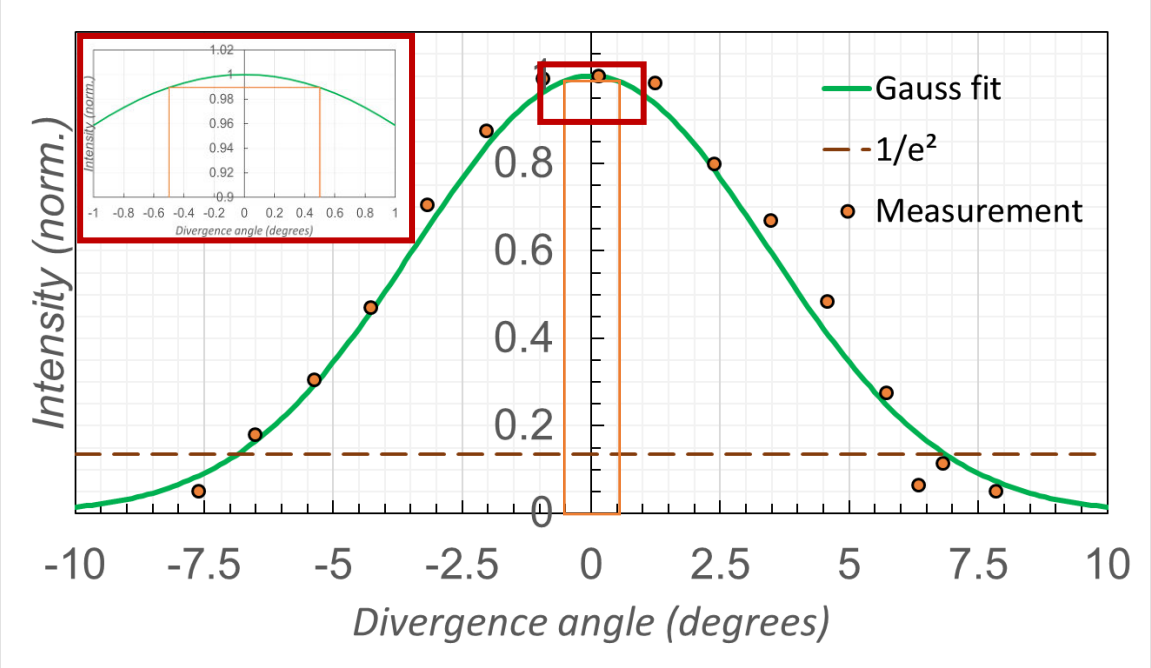

Figure III.7. Normalized intensity beam profile: measurements fitted by Gaussian shape curve (detail shows a zoom on the angular domain covered by the DOE sample)

2.2.a Eye safety

Working with lasers is associated with a certain degree of danger. The most likely is the possibility of eye damage. Due to its spatial properties, laser radiation can focus onto the retina into a very

small spot and thus turn out to be more dangerous for the eye than a conventional light source of the same power. In this sub-section I present laser safety calculations for our setup. According to ANSI Z136.1 (Laser Safety Standard by the American National Standards Institute) our laser relates to the Class 3B laser (output power is between 5 and 499 milliwatts) that may cause eye damage. Therefore, we have to be cautious during laboratory work and apply safety rules and equipment to avoid possible injuries. The core notions for laser eye safety is the **M**aximum **P**ermissible **E**xposure (***MPE***) – the maximal radiant exposure that may be incident upon the eye without causing damage. The **N**ominal **H**azard **Z**one (**NHZ**) – the distance from the laser source where the direct radiation and its reflections are greater than MPE and therefore hazardous (**Figure III.8**).

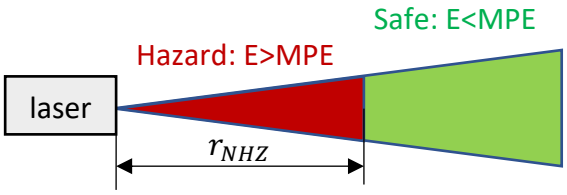

Figure III.8. Core laser safety notions: Maximum permissible exposure (MPE) and Nominal Hazard Zone (NHZ)

For our setup, we use a continues wave (CW) visible range laser (from λ = 400 to 700 nm), the MPE is determined according to ANSI Z136.1:

$$MPE = 1.8\, t^{-1/4}\, mW/cm^2 = 2.55\, mW/cm^2; \qquad \text{(III.3)}$$

With exposure time limited by the human eye's palpebral (blink) reflex $t = 0.25\, s.$

For a given MPE we obtain:

$$r_{NHZ} = \frac{1}{tg\gamma}\left[\frac{4 \cdot P}{\pi \cdot MPE}\right]^{1/2}; \qquad \text{(III.4)}$$

with γ-parameter being the full divergence angle calculated at full width at half maximum. The value of γ-parameter is deduced from **Figure III.7** and is estimated at 7 degrees. Varying the output power P, we can trace a graph of the HDZ distance r_{NHZ} (**Figure III.9**). There are two zones, the first zone where direct radiation and reflections from DOE are hazardous (under the curve, E> MPE) and the second zone above the curve is safe. The r_{NHZ} reaches its maximum at

the output power P=15 mW (maximal output power of our laser diode) where it equals about 10 cm.

The risk of locating the eye at a distance shorter than 10 cm from the optical fiber is very low so that we considered that the experimental setup was not representing laser safety problems. In order to guaranty that no one could get too close from the fiber, we used mechanical protection in the beginning of the beam propagation.

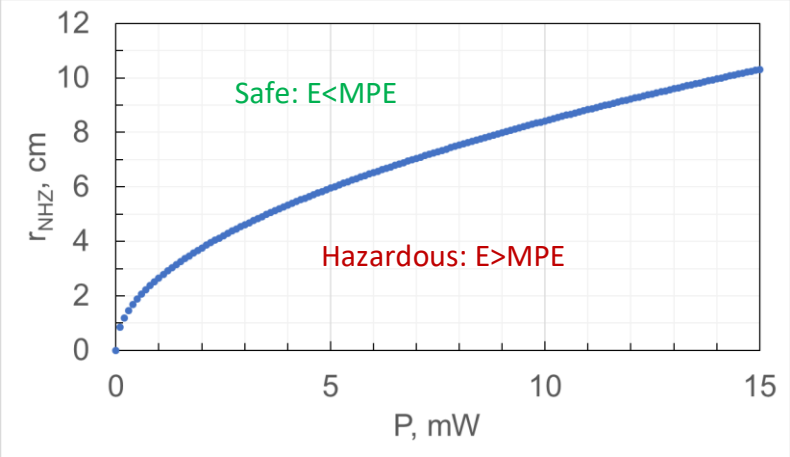

Figure III.9. r_{NHZ} depends as the inverse square root of the laser output power

2.3 Aperture distribution characterization

2.3.a Description of the need

As introduced before, the main requirement for our emissive setup is the homogeneity of output intensity with phase-adjusted wave fronts at each emissive point. Intensity homogeneity is not the only constraint as we must also consider the limited light sensitivity of the imaging system. It limits our choice for the pinhole diameters of the apertures of the DOE.

In our concept, the size of the emissive surface located at the emissive point is an important parameter. It fixes the emission angle of the spherical wave generated by the emissive point and also the number of emissive points we can locate at the surface of the display. We have interest in defining an emissive surface as small as possible. We have given as a reference value a radius of w_1 = 2 µm for the emissive point [3]. If we consider a projected image of 300x300 pixels it leads to a size of unit cell Λ = 600 µm.

If one uses these realistic parameters as a reference to design our transmissive DOE, we can calculate the transmittance of the device as a ratio of one emissive point aperture to the surface of the unit cell:

$$T = \frac{\pi w_1^2}{\Lambda^2}; \qquad \text{(III.5)}$$

The realistic configuration leads to a transmittance of $3{,}5.10^{-3}$ %. This value is too low to be considered in a demonstration setup. We have decided to modify the size of the DOE apertures to have more chance to measure the self-focusing signal, that is the spel formed on the sensor that mimics the retina. Applying **relation III.5**, the transmission is subsequently plotted as a function of the diameter of the circle of the pinholes (the EP aperture) in **Figure III.10**. In our validation setup, this diameter should be a few tens of microns, typically 25 µm. That is to say a transmission close to 0.1%. for the EUC size Λ=600 µm.

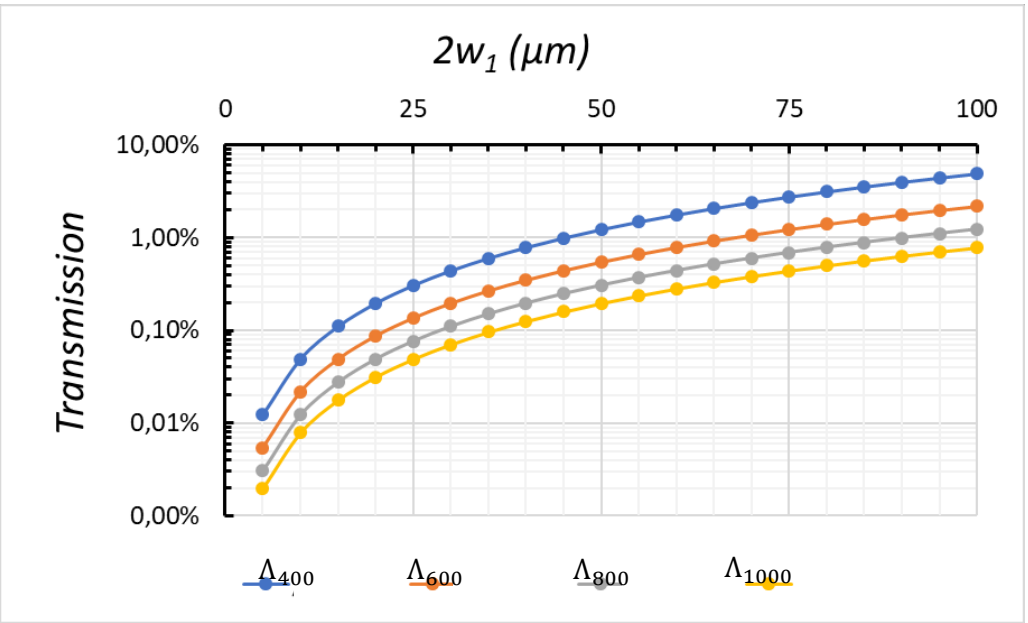

Figure III.10. Relative transmission of a pinhole per an EUC, as a function of the pinhole diameter $2w_1$ and the EUC size Λ equal from 400 to 1000 µm

The goal of this work was also to **characterize the whole spel**, that is, the central focus point and the noise that surrounds it. As given in the published description of the concept [97], the importance of the noise is given by the size w_1 of the emissive aperture. We have taken as an

approximation a Gaussian model to calculate the size w_2 of the noise as a function of w_1. Both parameters are taken as the waist of a Gaussian beam:

$$w_2 = \frac{f\lambda}{\pi w_1}; \quad \text{(III.6)}$$

The realistic radius of 2 µm gives for our 51 mm lens focal length, a noise radius of about 4.3 mm. Considering our sensor surface, there was a risk that we could not cover the whole surface of the noise. For these two reasons, we used aperture surfaces with a factor 10 to 40 as compared to the realistic value and we decided to keep similar unit cell size value.

We decided to manufacture DOE with simple diameter value 25 µm, 50 µm and 75 µm. It corresponds to noise diameters from 1.4 mm to 460 µm that will be easy to characterize on our sensor. Aperture distributions with diameter $2w_1$ 25 µm, 50 µm and 75 µm have been manufactured using maskless lithography on a metallic layer deposited on a glass substrate.

2.3.b Manufacturing method of the aperture distribution masks

A set of aperture distribution was produced by a CEA-LETI spin-off company called Arnano. This company is specialised in the manufacturing of micro patterns and decorations for the market of jewellery and watchmaking and for analogic microform storage. We contact them because their team had already worked with our laboratory for similar applications based on the manufacturing of DOE with similar geometries: a distribution of pinholes in an opaque layer for CGH [107].

The pinhole-making process is based on the maskless direct laser-write lithography (DWL) [108] and performed with the use of microscopic writing equipment (DWL2000 by Heidelberg [109]). The beam impacts a resin layer with approximate 220 nm thickness deposited twice (with 440 nm total thickness) on an opaque substrate made out of a thin glass (SiO_2), coated with an opaque, black chrome layer. After writing, the resin is etched and the chrome layer removed from the glass. Various pinhole distributions have been manufactured with this maskless lithographic process.

The choice of such process stemmed from time/price considerations. The decisive advantage of maskless lithography is to produce samples without the need of creating a photomask resulting in time and cost savings [110]. The writing process is schematically presented in **Figure III.11.** The

acousto-optic modulator (AOM) modulates the laser beam intensity, and the acousto-optic deflector (AOD) deflects the laser beam and performs a scan. After processing, the substrate is diced in several circular samples with ultrasonic dicing.

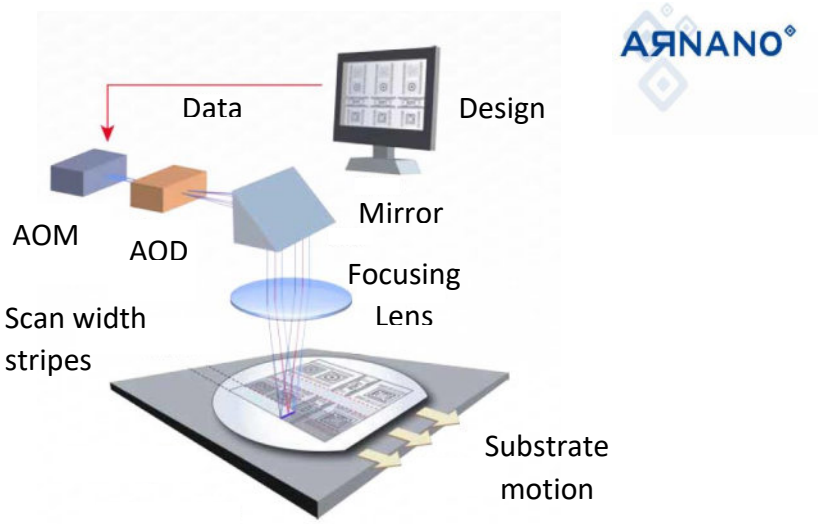

Figure III.11. Direct Laser Writing lithography setup at DWL2000

Laser lithography has slightly shorter exposure times than electron lithography (the maximum exposure time is about 2 hours when filling more than 50% of the substrate), but noticeably longer than photolithography, the exposure time of which does not exceed 1 minute on average. The laser lithography unit is based on a diode laser with an operating wavelength of 405 nm. Substrate sizes range from 5 x 5 mm² to 250 x 250 mm², writing speed is 110 mm²/min and edge roughness accuracy 50nm (3σ)[13]. For focusing, an optical laser with a wavelength of 680nm is used. The samples manufactured with Heidelberg Instruments DWL 2000 has a minimum resolution 0.5 µm with an addressed grid as low as 5 nm. This values are largely sufficient for our need.

2.3.c Aperture distributions design considirations

To properly conduct our experiment, the chrome layer of our sample must have a very low transmission for the signal of the pinholes not to be masked by the signal that passes through

[13] https://heidelberg-instruments.com/product/dwl-2000-4000-laser-lithography-systems/

the opaque layer. As I have shown the transmittance of our samples could vary from 0.1 to 1% of output power or flux. The transmission coefficient of the CR layer must be and order of magnitude below, typically under 0.01 %.

We use the Beer–Lambert law [111] (a complex refractive index in the exponential form of a plane wave produces an exponentially decaying transmittance) to calculate transmittance of the light trough the black chrome layer:

$$I(l) = I_0 e^{-\alpha_\lambda l} \; and \; T = {}^{I(l)}/_{I_0} \Rightarrow T = e^{-\alpha_\lambda l}; \qquad \text{(III.7)}$$

Where $\alpha_\lambda = \frac{4\pi}{\lambda}\kappa_\lambda$ is the absorption coefficient (equivalently, the extinction coefficient κ_λ). The extinction coefficient could be found from the complex refractive index $N = n + i\kappa$, for the wavelength λ = 513 nm , $N = 2.88 + 3.32i$ [112]. Knowing extinction coefficient, we can plot the transmittance as a function of the layer thickness as presented in **Figure III.12**.

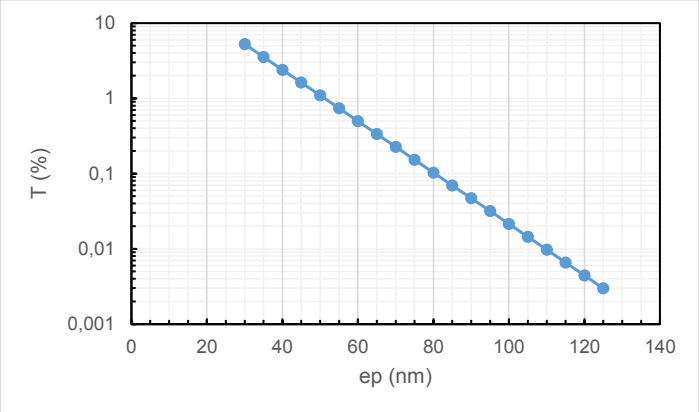

Figure III.12. Transmittance of the black chrome layer for light at wavelength λ = 513 nm as a function of layer thickness

We see that to be an order of magnitude below the transmission of a 25 µm hole in diameter (T ~ 0.1%), one needs a thickness of at least 110 nm of chrome.

The thickness of the chrome layer on our sample is about 200 nm, thereforeit is sufficient for our application. The samples made by Arnano represent the EPD described previously in **Chapter II**. These apertures distributions are simple diffractive optical elements made of distributions of circular apertures (pinholes). They reshape the incident wavefront according to the Huygens-Fresnel principle and produce secondary wavefronts. As a validation, aperture distributions with diameter $2w_1$ 25 μm, 50 μm and 75 μm have been manufactured using maskless lithography on a metallic layer deposited on a glass substrate. Measurements were limited by the detector sensitivity, and therefore should also consider light transmission. A relative transmission is calculated as follows:

Therefore, we decided to fabricate the distributions with three diameters: 25 μm, 50 μm and 75 μm ($2w_1$) as shown in **Figure III.13.** Four EPD types are considered: the Periodic, the Quasi-Random, the CRS and the CS with the varying EUC size Λ from 400 μm up to 1000 μm in 200-μm increment. Several exemplars of distributions with highlighted in red have been manufactured twice, because the chips are quite fragile, and risk of to braking some of them during the experiments is high. I have defined 4 types of distributions: periodic, quasi-random and two kinds of realistic-random, a) Cross-Sinusoidal (CS) and b) Cross-Random Sinusoidal (CRS). We chose 4 EPD types: the Periodic, the Quasi-Random, the CRS and the CS with the varying EUC size Λ ranging from 400 μm up to 1000 μm with a 200 μm increment.

	$2w_1$ (µm)			Λ (µm)					Periodic	Quasi-random	CRS	CS
	25	50	75	400	600	800	1000	3000				
1												
2												
3												
4(47)												
5(48)												
6												
7												
8(53)												
9(54)												
10												
11												
12(49)												
13(50)												
14												
15												
16(51)												
17(52)												
18												
19												
20												
21												
22												
23												
24												
25												
26												
27												
28(57)												
29(58)												
30												
31												
32(59)												
33(60)												
34												
35												
36												
37												
38												
39												
40												
41												
42												
43												
44												
45												
46												

Figure III.13. Table of produced distributions for experimental validation: 4 types of EPD with varying $2w_1$ and Λ

Figure III.14 depicts photographies of three types of DOE made in our 10 mm-diameter opaque metallic layer of black chrome. **Figure III.14a** presents a Periodic distribution with the EUC size $\Lambda = 800$ µm, **Figure III.14b** depicts a quasi-random distribution with the period Λ= 400 µm, **Figure III.14c** shows a CS distribution. The green squared area in the center of the image of the sample

is zoomed in the closed up of **Figure III.14d.** One can see that the circular apertures are well defined and uniform in size.

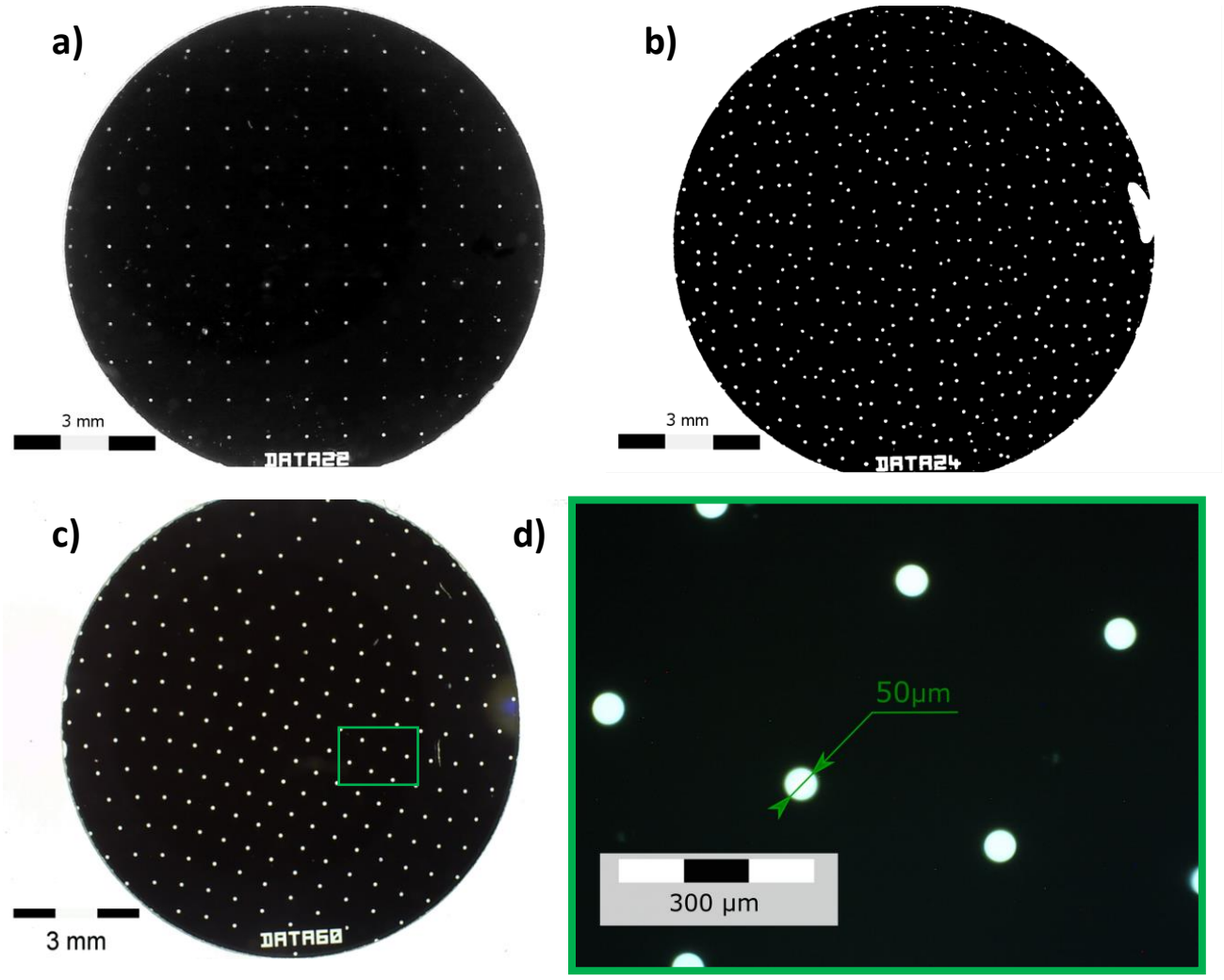

Figure III.14. Photography of two 10mm-diameter DOE samples used for the experiment, a) periodic distribution with the period Λ= 800 µm, b) quasi-random distribution with the period Λ= 400 µm. DOE sample used for the experiment, c) a Realistic (Cross Sinusoidal) distribution with the period Λ= 600 µm with close up squared green region, d) close-up region: the aperture diameter of a pinhole is 50 µm

2.4 Mimetic eye characterization

There are many common points and in the same time differences between a human eye and an optical instrument, i.e. a photo camera that mimics the eye. The goal here was to adapt available materials to evaluate self-focusing efficiency. Ideally, the Imaging part of our setup should

represent a human eye with similar angular resolution. In the same time, for data analysis it was important to obtain a central peak of spel consisted of 7 data points to evaluate the shape of the self-focusing pattern.

Our Imaging system consists of two parts: a lens and a sensor. The first part is a Wollensak Raptar 2.04" Zeiss Camera lens (**Figure III.15a**) with focal length 51 mm and aperture range varying from f/1.,5 to f/22. In order to image a spel over several pixels, while still keeping a sufficiently high signal level, I choose an aperture of f/15 that corresponds to the pupil aperture Ø = 3.4 mm. Such aperture could be considered as an approximately average human pupil size during daytime [37].

Our CMOS senor is a Lumenera LW620 model with surface detection 10.5 x 7.7 mm^2 and resolution 3000x2208 pixels (**Figure III.15b**). We have chosen this sensor for its small pixel size (about 3.5 µm), that could give the best resolution on the evaluation of the spel. The retina contains nerve fibres, light-sensitive rod and cone cells and a pigment layer. Cone distance is estimated at approximately 2.6 µm [113]. The most sensitive region called fovea has about 5°-diameter. With an eye focal length of 23 mm it gives a resolution on the fovea of about 800 pixels.

With our system, the resolution of the 5° foveal diameter is about 1300 pixels. Our mimetic eye gives us a better resolution than the human eye to allows for a precise characterization of the spel.

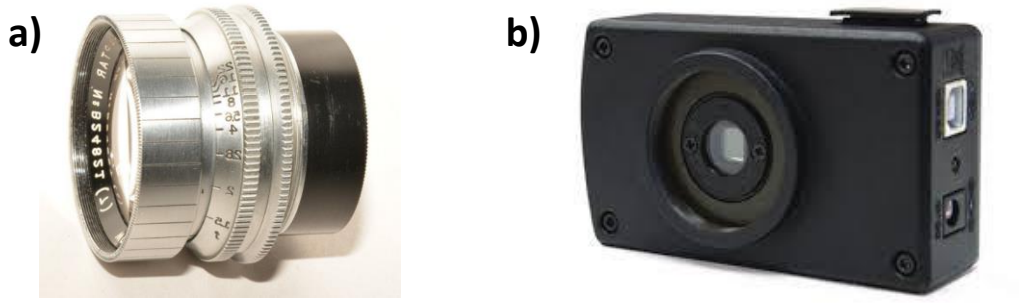

Figure III.15. a) Zeiss Camera lens Wollensak Raptar 2.04", focal length 51 mm f-number: from f/1,5 to f/22,b) the Lumenera LW620 CMOS sensor for mimetic eye : 10.5 x 7.7 mm^2, 3000x2208 pixels with 3.5µm pixel size (square pixel)

As described in **Chapter II** the spel size δw can be estimated by the pupil diameter Ø: $\delta w = 1.22\frac{\lambda f}{ø}$. For a pupil of about 3 mm, we have a spel of diameter $2{\cdot}\delta w$ *= 22 µm.* With a pixel of 3.5

µm we can have 6 pixels per spel in this assembly. For the image formation experiment described in **Chapter IV,** we augmented our resolution up to 13 pixels by replacing the LW620 sensor by a new CMOS-sensor[14] with 1.6 µm pixel size.

2.5 Dynamic range acquisition problem

During my experiments, I faced an issue with the representation of the spel signal due to a limited dynamic of our CMOS sensor. The sensor has an 8-bit coding with intensity value from 0 to 255, where 0 corresponds to intensities below the detection level and 255 corresponds to intensities above the detection threshold. We represent our data in normalized units (n.u.) with a simple division by 255.

A typical diffraction pattern of a spel, as recorded in our setup, is given in**Figure III.16**. We see a peak that corresponds to the signal we want to form in the self-focusing process. We know from our simulations that the signal around the peak is of primary importance to validate our concept (see the **section 5.4** of the **Chapter II**). However, this secondary signal is submerged by stray light that produces some noise. For this reason, we cannot observe the true shape of the curve which is masked by a noise equal to 0.01 *n.u.* To go further in our analysis, I need to improve our signal processing.

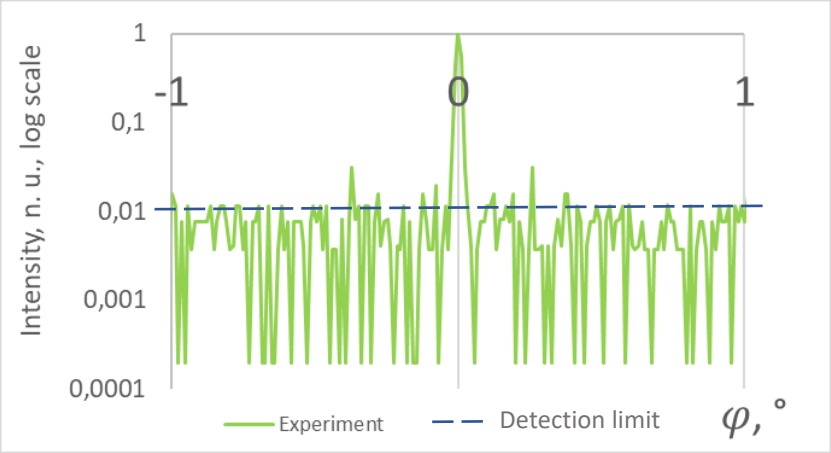

Figure III.16. Experimental data in log scale, the noise caused by stray light hides the Gaussian background around the central peak

[14] https://fr.ids-imaging.com/store/ui-1492le.html

We can observe the true shape of the peak background if we increase the laser power but we lose the peak shape due to the camera saturation (**Figure III.17**). We can use the data if we match it to the peak measurements. To process data, we must know the proportionality value between the luminance intensity of non-saturated measurement (1) and the intentionally saturate measurement (2). We know the ratio of the electrical intensities between measurements (1) and (2) by knowing the power supply of the laser source. It depends on the relation between the applied power and the current. Afterwards, we replace the noise with the Gaussian background. To relate electrical current to light intensity it is necessary to calibrate the source.

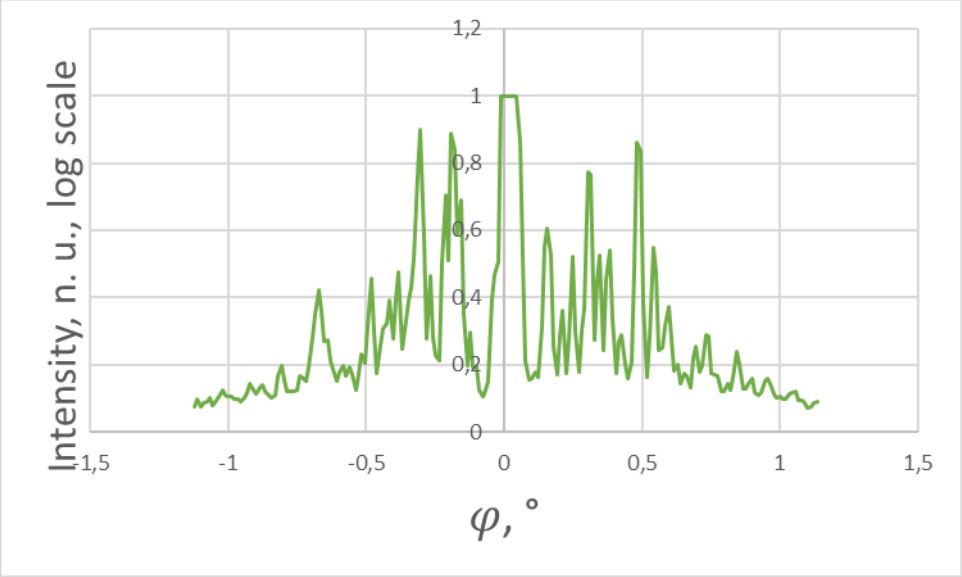

Figure III.17. Overexposure: strong illumination case, the central peak is above the detection threshold, but the surrounding Gaussian background is well observed

I used Optic Power Monitor OPM 150 photodetector (**Figure III.18)** to measure the power of the source. I measured this characteristic with a step of 1 mA. The result is given **Figure III.19**.

Figure III.18. Optical power monitor OPM 150, photodetector for measuring source power

The graph shows that the relationship between I_e and P is not linear. A good approximation is given by a quadratic analytical function (**III.2**):

$$P = (1.8I_e^2 - 0.5I_e + 39.6) \cdot 0.001; \quad \text{(III.8)}$$

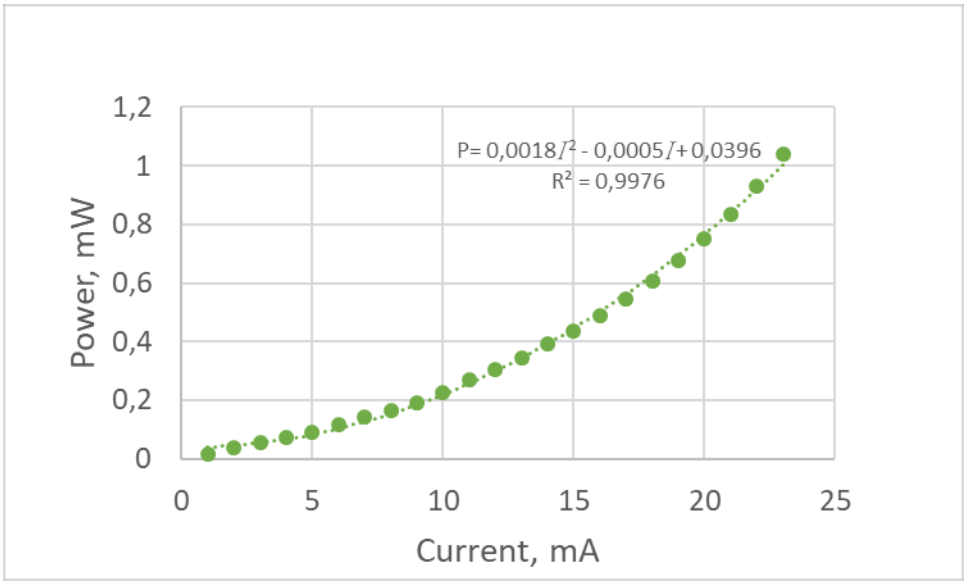

Figure III.19. Relation between Power (P) and Current (I) approximated by a quadratic analytical function

For the diffraction pattern with an exploitable peak we use current I_{e1} = 11.5 mA, for the background we use I_{e2} = 28.9 mA. We used formula (**III.2**) to calculate the relation P_2/P_1. Our coefficient is 5.66. Using it, I obtained the curve with the visible Gaussian background as shown in **Figure III.20**. With this signal processing method, we can expand the dynamic of measurement of 255 values from the initial range [0.01, 1] to the final range [0.0001, 1], which is two orders of magnitude gain.

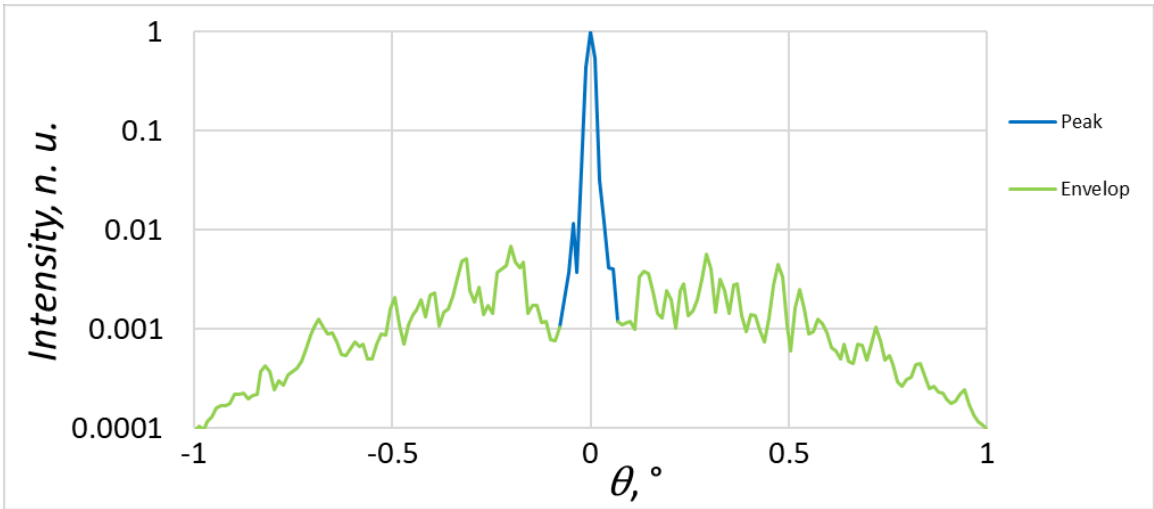

Figure III.20. Corrected data: the superstition of two measures: the central peak taken from Figure III.16. and the Gaussian background of Figure III.17 with the calculated weight coefficient

2.6 Estimation method of the spel central peak

The characterization of the spel is made on the basis of diffraction theory. In that sense, the central peak can be described by an Airy function given by the wavelength and the pupil diameter. However, for the ease of our comparison with experimental results and for the use of the Gaussian model described in the **Chapter IV**, we approximate the central peak with a gaussian function given by **equation III.2**. When we characterize the size of the central peak we can use alternatively the waist of this function (radius at $1/e^2$) or the parameters of the Airy function.

The normalized Airy function is given in **Chapter II** by **Equation II.6**. In **Figure III.21** I show a comparison between the Airy function and a Gaussian approximation. I take as a reference the radius of the Airy function calculated at first zero value, it is estimated as follows [103] :

$$\delta w_0 = 0.61 \frac{\lambda}{NA} ; \qquad \text{(III.9)}$$

where NA is the numerical aperture $\frac{ø}{2f}$.

The half width at half maximum (HWHM) of the Airy function is another way to describe the radius of a peak, given by:

$$\delta w_{0.5} = 0.257 \frac{\lambda}{NA}; \qquad \text{(III.10)}$$

I approximate the Airy function by a Gaussian fit with a waist δw_g supposing that both HWHM are equal. One can deduce the expression of $\delta w_{0.5}$ as a function of δw_g. By solving the equation: $\frac{1}{2} = e^{-2\frac{\delta w_{0.5}{}^2}{\omega g^2}}$ one can find:

$$\delta w_{0.5} = \sqrt{\frac{\ln(2)}{2}} \cdot \delta w_g = 0.59 \cdot \delta w_g; \tag{III.11}$$

Using this equation with **Equation** (**III.10**), one can deduce a relation between the waist and the NA:

$$\delta w_g = 0.43 \frac{\lambda}{NA}. \tag{III.12}$$

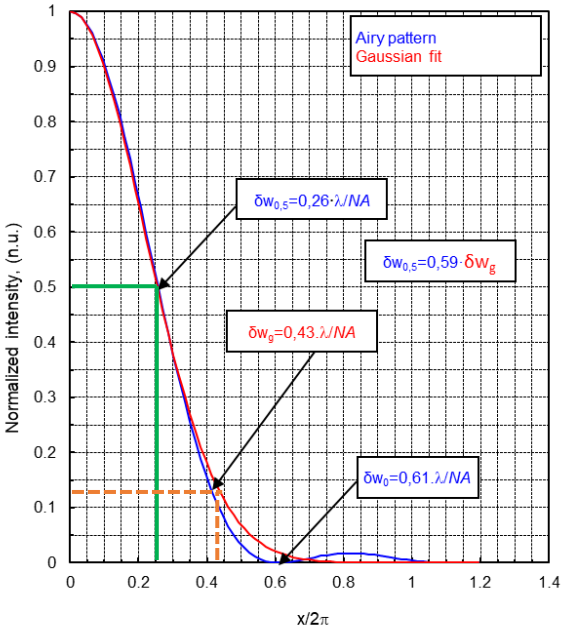

Figure III.21. Airy pattern cross-section and its Gaussian fit approximation, $x = \frac{\pi \emptyset}{\lambda} \varphi$

Finally, we obtain the relation between the Airy disk radius calculated at first zero value and the waist at $1/e^2$:

$$\delta w_g \cong 0.7 \cdot \delta w_0; \tag{III.13}$$

The lateral sizes of the spel radius given at the half maximum, at $1/e^2$ height and at the Airy first zero are presented in **Table III.1** for various pupil diameters at the wavelength λ = 512 nm and the focal length f = 51 mm.

Table III.1 Spel radius sizes for 3 types of definition (given at λ = 512 nm).

Ø, *mm*	*NA*	$\delta w_{0.5}$.(HWHM), μm	$\delta w_g\ (1/e^2)$, μm	δw_0, μm
2	0.019	6.7	11.2	15.9
3	0.029	4.5	7.5	10.6
4	0.039	3.3	5.6	7.9
5	0.049	2.7	4.5	6.4
6	0.059	2.2	3.7	5.3
7	0.069	1.9	3.2	4.5
8	0.078	1.7	2.8	3.9

The proposed Gaussian fit provides a reasonable approximation for a central peak and enables to compare our simulation results with our experimental validation in a simple way using a Gaussian function instead of the Bessel function.

3 Spel formation validation experiment: Remarkable results and comparison with theory and simulations

3.1 Experimental procedure

The measurements for the spel formation validation experiment were performed for samples listed in **Figure III.13** with the fabricated chips. We expect to achieve self-focusing effect using an aperture distribution and compare it with our theory and simulations. My results are obtained with various apertures of the optical system.

I used the LabView program to save images from our CMOS sensor. In order to have the most contrasted images and to overcome noise from lightning, the experiments were performed in the dark. Since each DOE has its own transmission due to different number of pinholes and its diameter as was explained in the previous chapter, I adjusted each time the laser intensity.

In the next section, we show results obtained with DOEs whose main characteristics are as follows:

- the EUC size $\Lambda_1 = \Lambda_2$ for all EPDs is 400 µm, except the single pinhole;
- the pinhole aperture δ = 50 µm for the periodic EPD and a chip with a single pinhole;
- for the quasi-random and the realistic random (both CS and CRS) the pinhole aperture δ = 75 µm.

3.2 Evaluation of the types of EPDs

As I will show below the experimental results are consistent with our simulations and our theoretical analysis presented in the **Chapter II**.

First, I tested our setup on a single pinhole chip that produces a diffractive pattern displayed in the **Figure III.22a**. The waist w_1 of the beam emitted from the pinhole is taken as the radius of the aperture. The angular radius $\Delta\theta$ is a half width on half half-maximum (HWHM) of the blurred signal is then given by the divergence angle of a Gaussian beam:

$$\Delta\theta = \frac{\lambda}{\pi w_1}; \qquad \text{(III.14)}$$

With a pinhole diameter $\delta = 2w_1$=50 µm, an angular radius at half maximum of 18 arcmin (HWHM) is predicted and experimentally observed as shown the **Figure III.22b**. where the angular radius at 1/e² is equal to 30.5 arcmin.

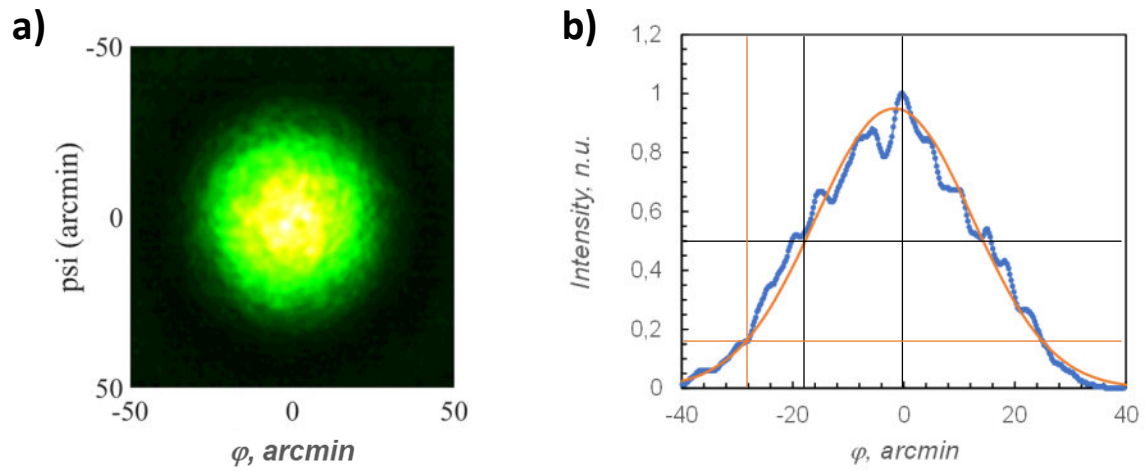

Figure III.22. a) diffraction pattern produced by one pinhole with 50 µm diameter aperture; b) its cross-section in blue and the Gaussian approximation in red,

Figure III.23 shows the typical diffraction pattern resulting from a periodic aperture distribution. For this result I used a DOE with a period Λ=400 µm and with a pinhole diameter $2w_1$ = 50 µm. The periodic aperture distribution generates diffraction orders with an angular period given by λ/Λ. It corresponds to an angular period of 4.4 arcmin, consistent with our measurements (about 4.5 arcmin in average).

Theoretically, central peak waist δw_0= 0.47 arcmin according to **Formula III.9**. As we can see from **Figure III.23c** I measured a SNR about 0.18 dB, that is consistent with the simulation as one can see from **Table II.2:** the mean value is about 0.16 dB.

I present in **Figure III.23** the same Gaussian function as in the **Figure III.22**. It shows that, as predicted by the theory, the diffraction orders are weighted by a Gaussian envelope defined by the individual apertures.

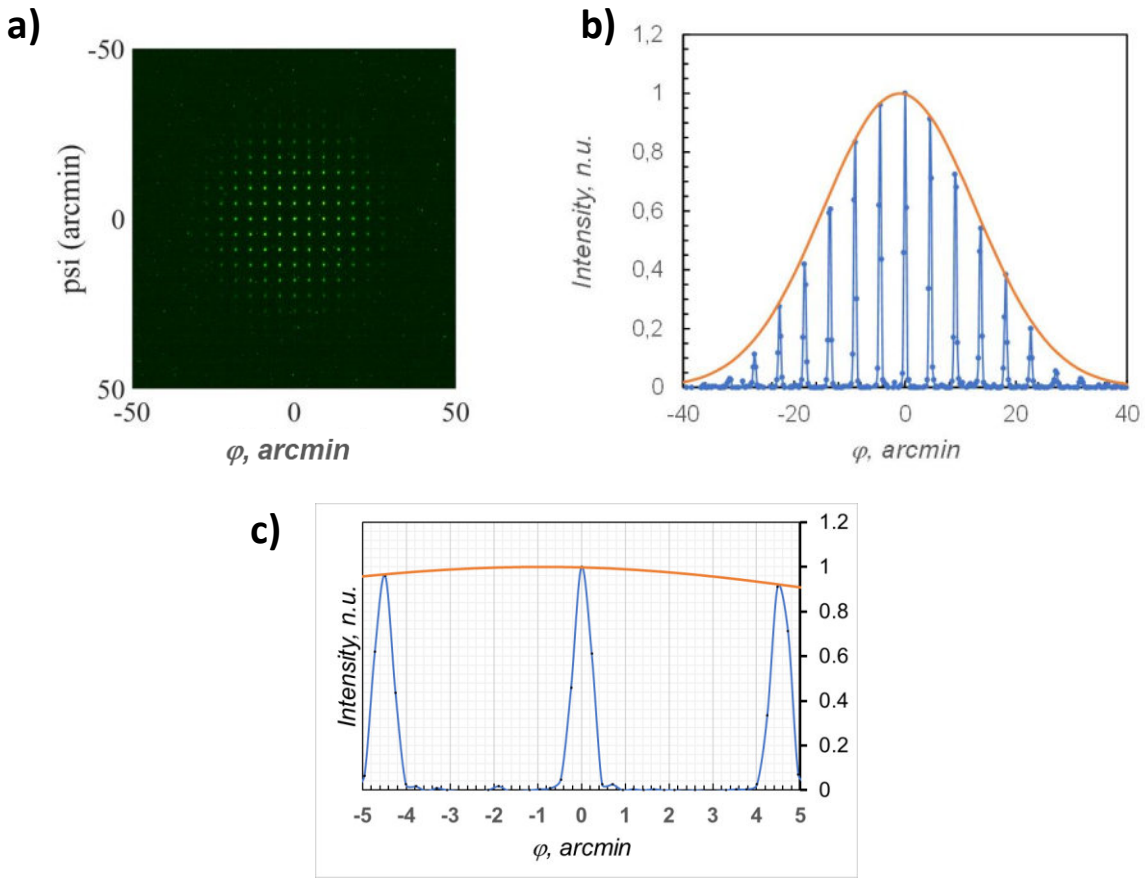

Figure III.23. a) periodic EPD diffraction pattern with pinhole diameter $\delta = 2w_1 = 50$ µm and EUC size Λ = 400 µm and b) its cross-section with a Gaussian envelop approximation c) cross section close up near the central peak

In **Figure III.24**, I show the case of a Quasi-Random distribution with the 400 µm EUC size and a pinhole aperture $2w_1$ = 75 µm. This result confirms the self-focusing behavior for random distribution: we can observe a central peak.

As explained before, I compare the central peak with a Gaussian function. The inset of figure **Figure III.24 b)** shows a good fit obtained with a waist of 0.44 arcmin. If I use **equation III.12** that relates the waist to the numerical aperture I find a correspondence for NA = 0.033. This value indeed corresponds to the actual f number I use: f/# = 15.

As expected the central peak is surrounded by speckle noise.

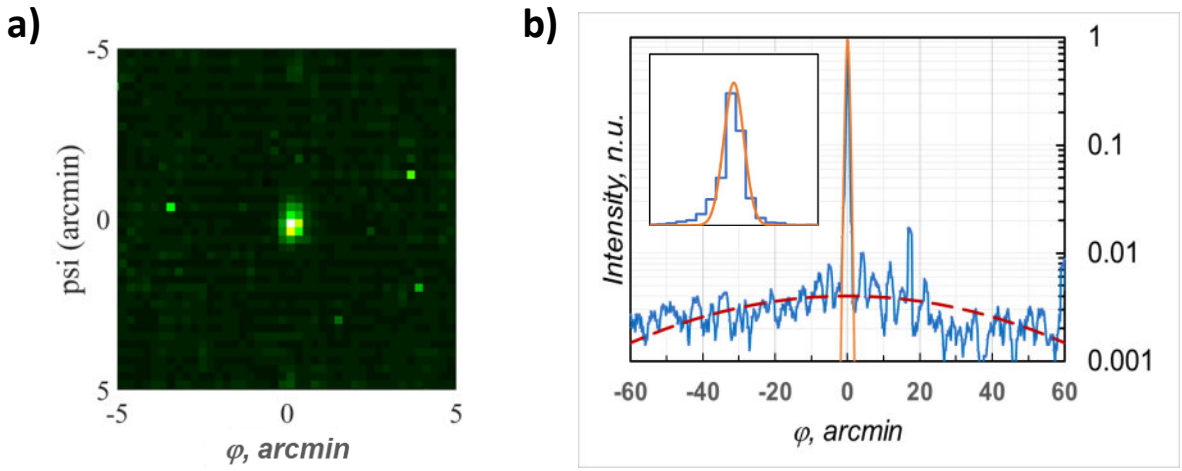

Figure III.24. a) random EPD diffraction pattern with pinhole diameter $2w_1$= 75 µm and EUC size Λ = 400 µm and b) its cross-section with a Gaussian envelop approximation

Below we present the diffraction patterns obtained from Realistic-Random distributions: a Cross Sinusoidal (CS) distribution and a Cross-Random Sinusoidal (CRS) distribution.

The **Figure III.25a** shows the diffraction pattern obtained from the CS distribution with EUC size $\Lambda = 400$ µm and the pinhole aperture $2w_1$ = 75 µm. The CS EPD is intermediate case between the Periodic distribution and the Quasi-Random distribution: although the side-peaks are reduced compared to the Periodic diffraction pattern, the speckle noise is quite distinguishable in the diffraction pattern.

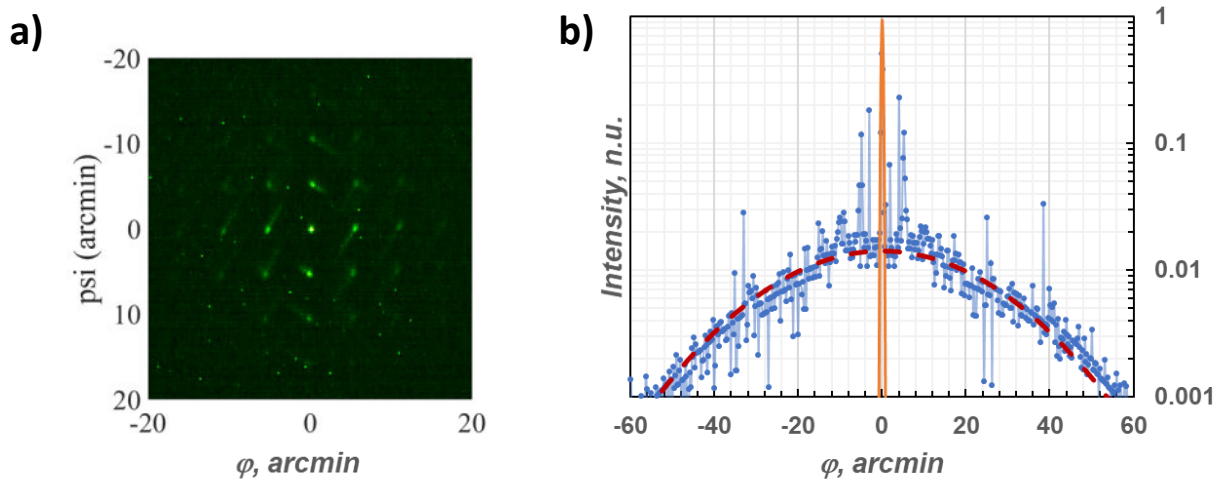

Figure III.25. a) Cross Sinusoidal EPD diffraction pattern with b) its cross-section with a Gaussian envelop approximation

In **Figure III.26a** I finally present the diffraction pattern I have measured from the CRS distribution with EUC size $\Lambda = 400$ µm and the pinhole aperture $2w_1$ = 75 µm. This type of Realistic-Random EPD allows us to slightly reduce side lobes resonances caused by remaining periodicities in the aperture distribution.

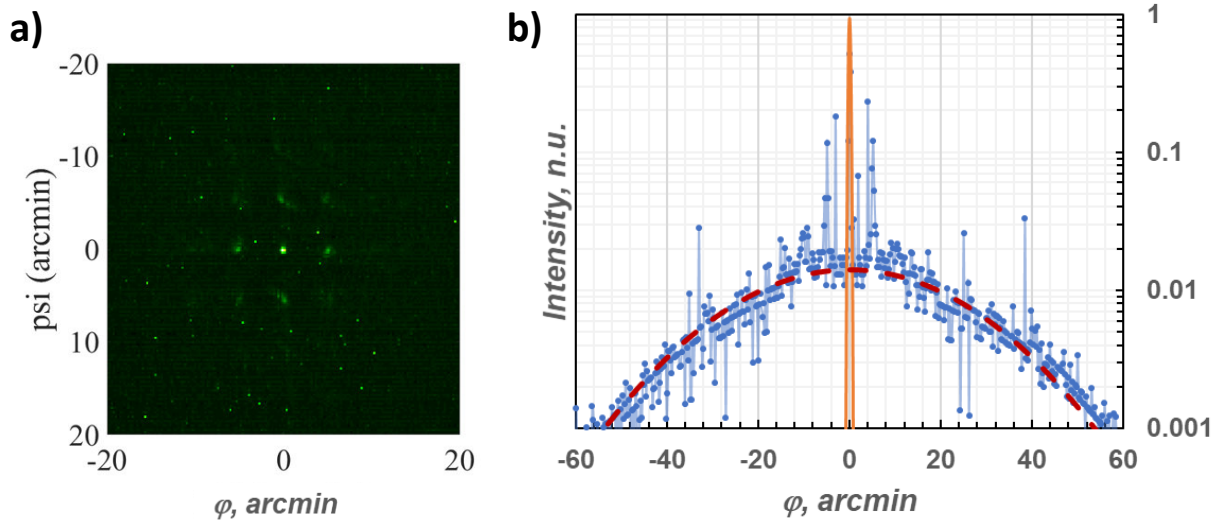

Figure III.26. a) Cross Random Sinusoidal EPD diffraction pattern with b) its cross-section with a gaussian envelop approximation

Although, the SNR of the CS and CRS cross-sections are almost equal, we can see that diffraction patterns significantly differ. This means that the SNR-criteria needs to be complemented with

another criteria that takes into consideration not only the closest side peaks, but the whole energy ratio between the central region and its surrounding. We mentioned previously in **Chapter II** the γ-parameter and we will describe it in the next chapter to analyze image formation behavior of our self-focusing system.

3.3 Summary of the first evaluations

My experimental results confirmed our theoretical assumption and simulations about self-focusing spel formation on the human retina. I experimentally investigated self-focusing behaviour of Periodic, Quasi-Random and Realistic-Random (CS and CRS) distributions and the SNR of corresponding EPDs differs in reasonable limits. The spel formation was demonstrated for Random-type distributions. Simulation results presented in **Chapter II** are valid and confirmed experimentally that the surrounding noise is related to the following EPD characteristics:

- the EP size defines the noise envelop size with the Gaussian-shape;
- the increasing of the EPD randomness level reduces the number of unwanted ghost spel in the noise surrounding;

4 Source position characterization: spel-shift experiment

4.1 Description of the experiment

A projected image on the observer's retina from our display consist of "spels", elementary spots formed by self-focusing effect without lens. The various spel positions define the image as the pixels do in conventional image formation. The next experimental setup was proposed to validate that the position of the spel can effectively be tuned by a change on the emission direction of the EPD.

To change the incidence angle of the beam that reaches the DOE, we move the point source in its plane as in the former setup.

During this experiment I analyze spel-shifting in the approximate range of the fovea region which is about 5°. The setup used for the spel-shift experiment via source positioning is the same as the one used for the spel formation validation. It is shown in the **Figure III.27**.

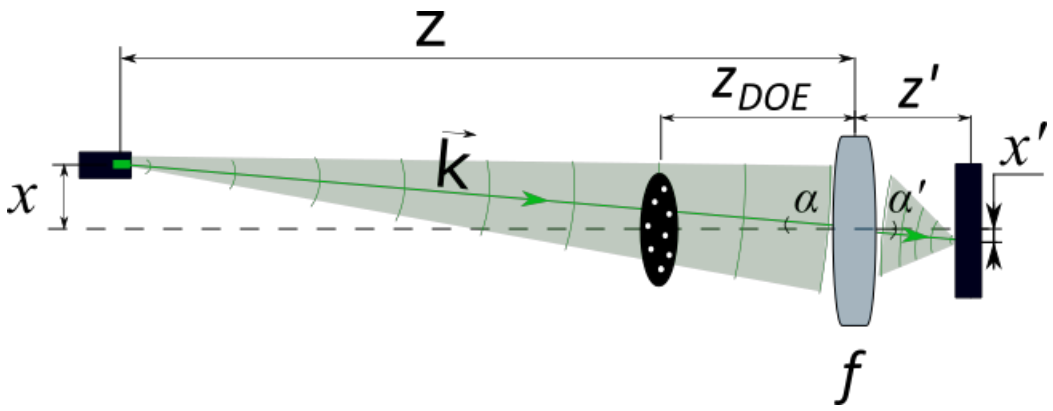

Figure III.27. Spel projection and displacement setup: a DOE stands at the distance z_{DOE} from the lens. A light source is located at a distance *Z* from the lens, in the object plane. An image sensor is located at a distance *z'* from the lens in the image plane.

A Diffractive Optical Element is located at the distance z_{DOE} from our optical system that mimics the eye. A point source is located at a distance *Z* equal to 55 cm, from the imaging system that mimics the human eye. The angle α of the planar wavefront on the DOE plane is given by the distance x that separates the point source from the optical system axis and by the distance Z:

$$\alpha = \tan^{-1}\frac{x}{z}; \qquad \text{(III.15)}$$

The DOE divides the planar wavefront into a distribution of spherical waves thanks to a set of circular apertures, distributed according to an Emissive Point Distribution (EPD) function. The lens focalizes the composite wave into a focus on the image sensor at a location x' given by the angle α and by the imaging distance Z'. In our concept the EPDs generate composite planar wave fronts at Z' = f. In our experiment, the fiber is located at a given distance so that the focus point is located at a distance $Z' \neq f$ given by **Equation III.1**. Then image position is determined as:

$$x' = Z' \cdot \tan\alpha = \frac{Z'}{Z}x \qquad \text{(III.16)}$$

If we put the DOE before the lens, due to the self-focusing effect a focalized spot is observed in the position determined by the same principle.

4.2 Results and discussion

I show in **Figure III.28** the superposition of two measurements corresponding to two source positions (with 5 mm displacement) observed through a quasi-random aperture distribution (cell size 1.6 µm, aperture size 75 µm). We measure as expected a shift on the spel position with very little variation on the speckle noise that surround the spel.

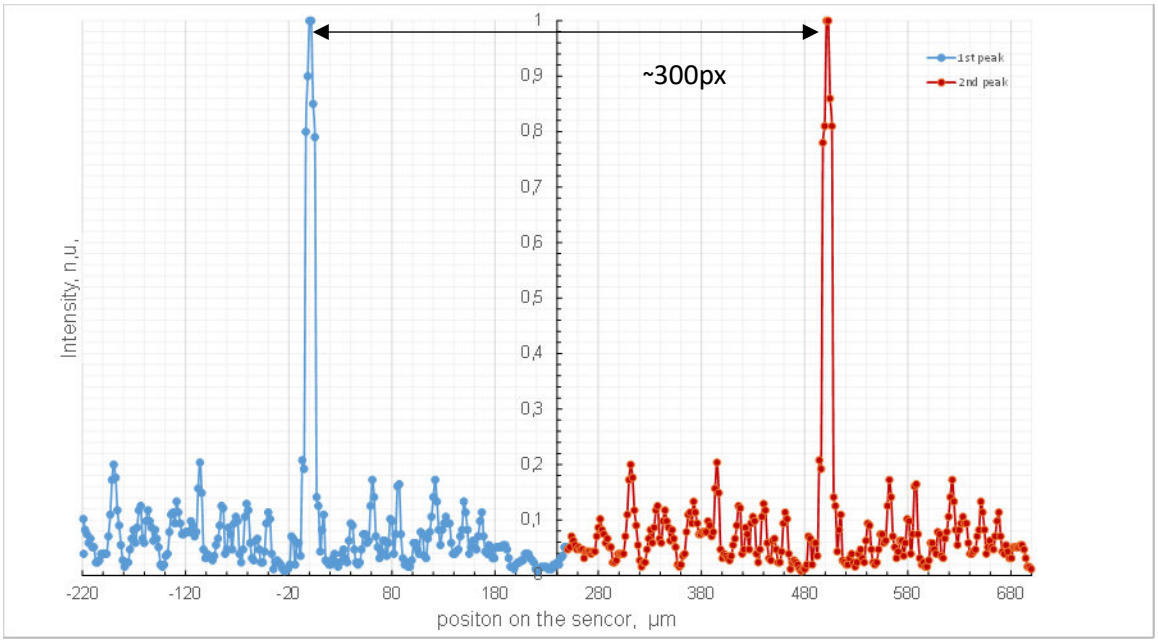

Figure III.28. Spel shift exp on the CMOS-sensor.

I have measured various spel positions depending on the source shift from -25 mm to +25 mm from the optical axis with negligible error estimated at +/- 1 mm on for fiber position (x-axis) and +/- 15 µm on the spel position (x'-axis). The results are given in **Figure III.29**.

The results confirm that the spel displacement is a linear function of source position shift. This result is obvious but is also important as it show that we can evaluate self-focusing in an imaging setup as I show in **Chapter IV**.

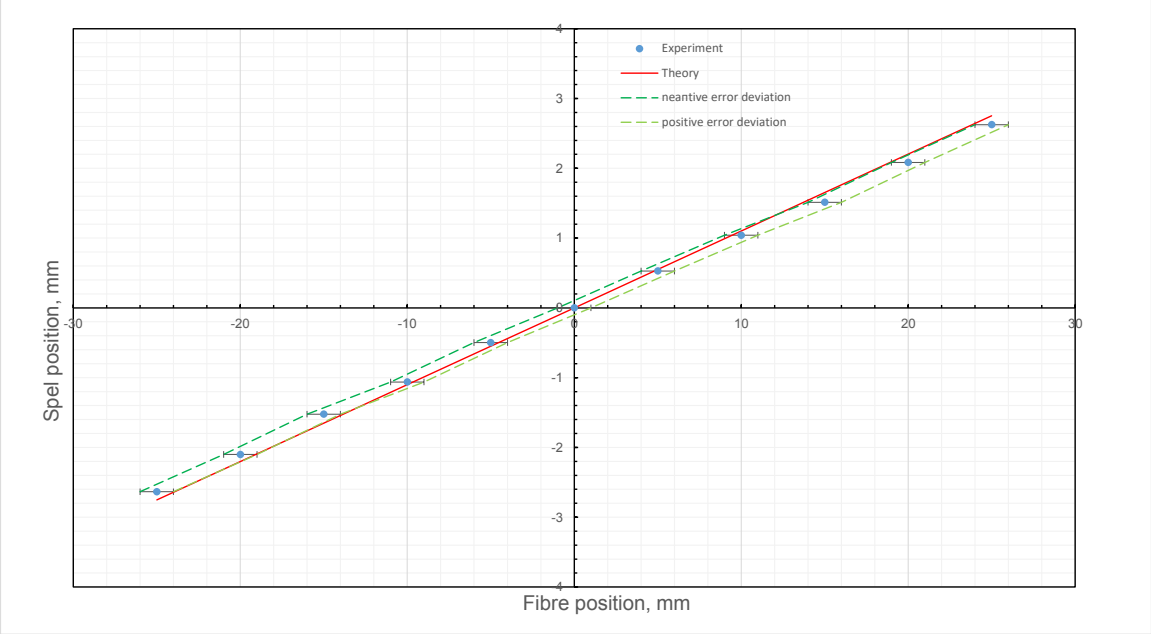

Figure III.29. Spel position depends on laser source position.

5 Coherence experiments

5.1 Principle of the experiment

I show in **Figure III.30** two kinds of coherence characteristics in the propagation of a wave front. First is the spatial coherence that allows to define a spherical wave front with little variation from the centre of curvature. One can typically use a pinhole to improve this characteristic. Second one is the temporal coherence and is related to the spectral dispersion of the wavefront. One use typically a spectral filter to improve this characteristic.

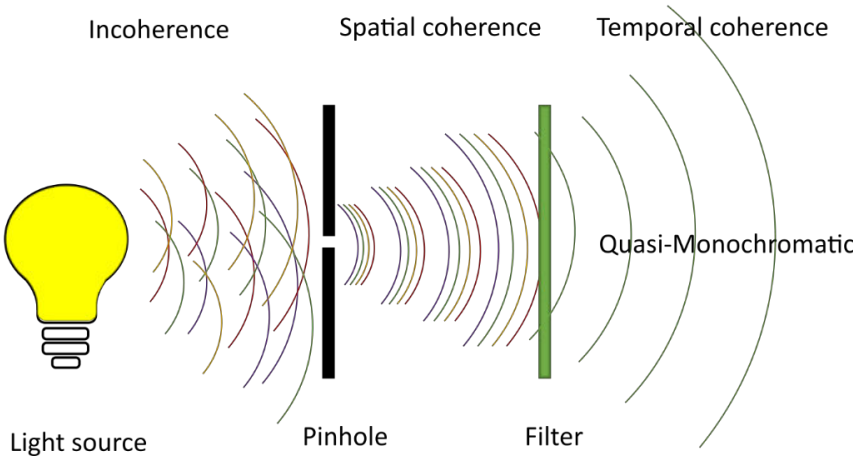

Figure III.30. Spatial (transverse) and temporal (longitudinal) coherence [114]

The self-focusing effect can be seen as an interference phenomenon that produces the spel at a given location. Each spherical wavefront generated by the DOE interferes at the focal point generated by the lens. Interference efficiency is related to the coherence of the interfering beams. In order to evaluate the efficiency of the self-focusing effect, we have investigated the impact of the spectral characteristics of the light beam that impacts the DOE.

5.2 Setup description

In order to evaluate the impact of the coherence on the self-focusing effect, I use the experimental setup depicted **Figure III.31**. It basically inherits from the self-focusing validation setup from **Figure III.3** and only differs in the source part, in order to evaluate the impact of the spectral dispersion of the optical source.

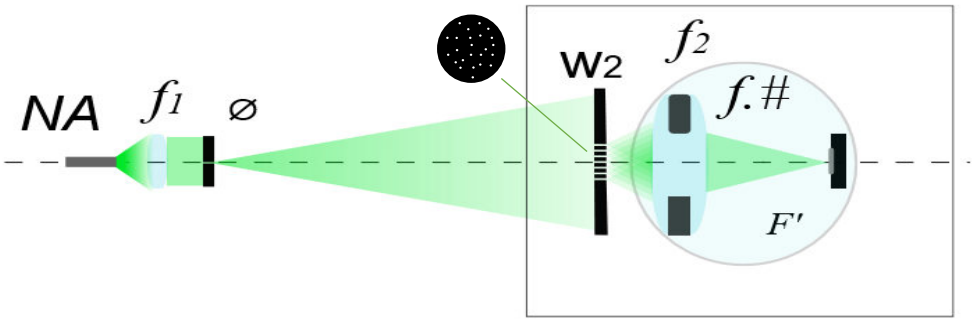

Figure III.31. Coherence experimental setup

I use as a comparison a LED of spectral bandwidth 50 nm with a central wavelength of about 532 nm. **Figure III.32** shows a photography of the LED source and a comparison between its spectrum and the spectrum of the laser diode we used for previous self-focusing validation experiments. The LED is coupled in a lightguide with a 3 mm aperture diameter and a numerical aperture NA = 0.59.

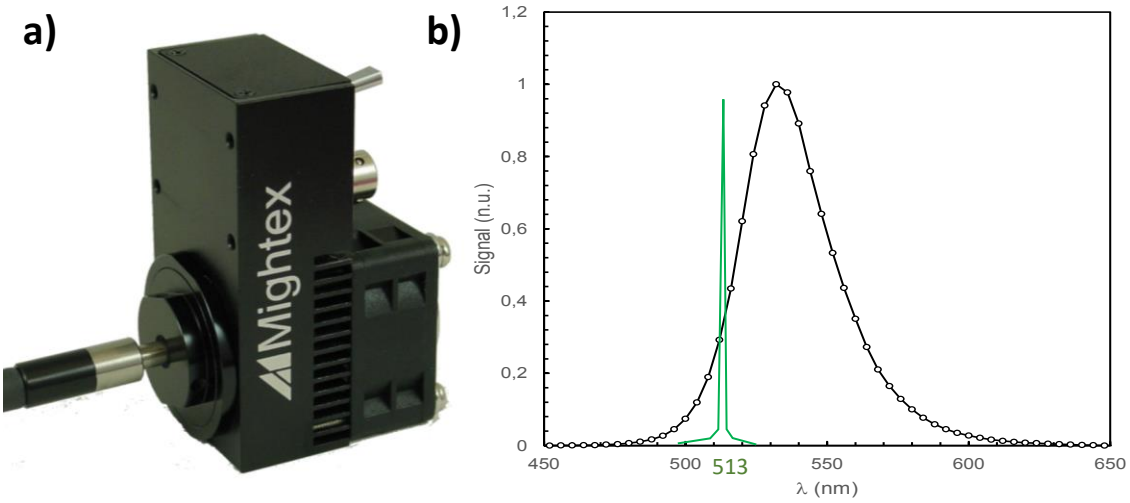

Figure III.32. (a) photography of the LED source, (b) experimental spectrum of the LED (black) and the laser diode (green) used in the experiment.

I use a microscope objective located in front of the light guide as a collimating lens and an aperture of 20 µm to limit the spatial coherence of the optical source. The optical system used to evaluate the self-focusing efficiency consists of our imaging system with a change on the image sensor resolution. We still use the 51 mm focal length objective and we associate it with a CMOS sensor with a pixel size of 1.67 µm that will be described in **Chapter IV**.

We used two types of pinhole distribution on the DOE. The EUC size Λ = 800 µm in the case of the periodic EPD and EUC size Λ = 400 µm in the case of the quasi-random EPD. In both cases the diameter of the DOE apertures is δ = 75 µm.

5.3 Experimental results

In **Figure III.33**, I compare the experimental results of self-focusing of the two types of emissive sources shown in **Figure III.32** for the periodic DOE. In the case of the highly temporal coherence source, the periodic EPD generates a spel with multiple order resonance clearly visible. When the spectral bandwidth of the light source is increased, the self-focusing effect is still efficient for the central peak but vanishes gradually for the resonance orders (**Figure III.33b**). Central peak size is maintained but the width of the lateral resonant peak is progressively increased and the total envelope width decreases (orange curve in **Figure III.33c**). The cross-section of the diffraction pattern for the coherent case is presented in **Figure III.33c** (green curve).

We observe the narrow peaks and a total envelope with δw = 2.8 µm and w_2 = 720 µm. The result is consistent with the theoretical value estimated at $\delta w = 3.6$ µm and $w_2 = 441$ µm.

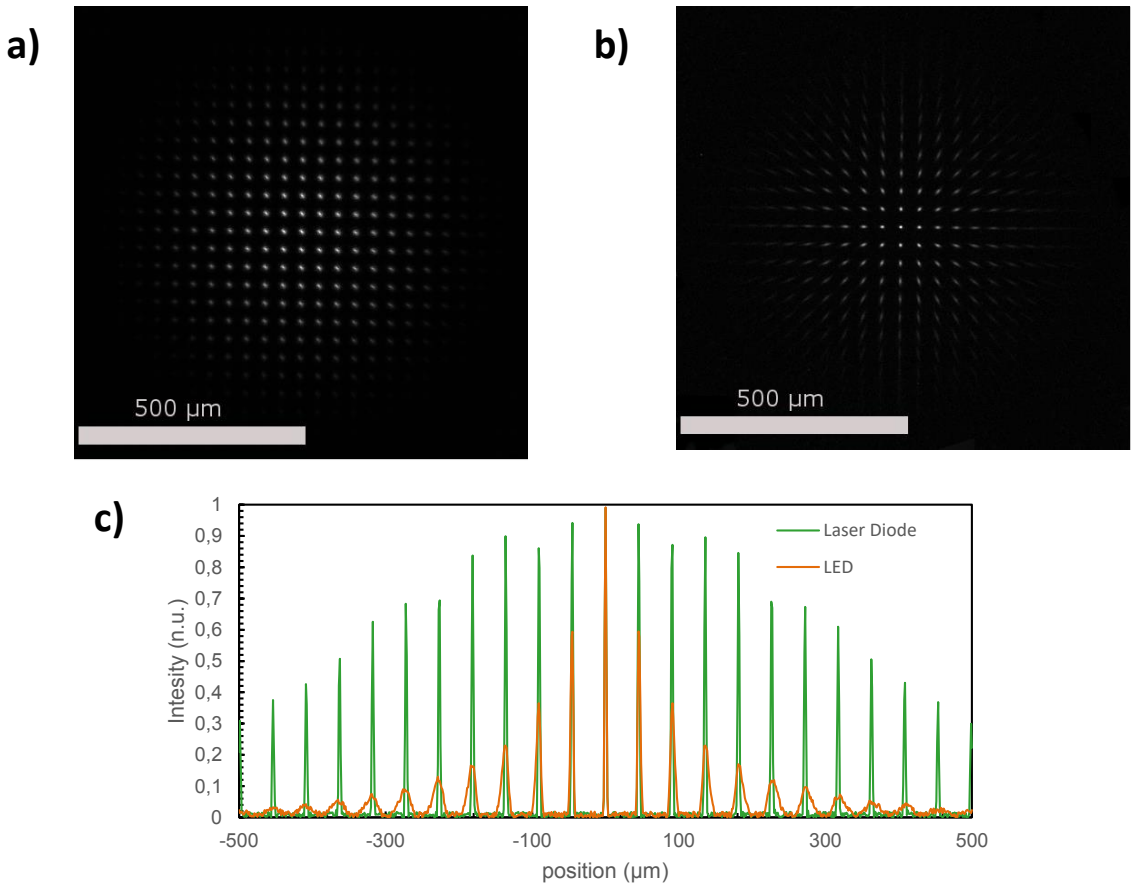

Figure III.33. Experimental results of self-focusing effect with the periodic EPD: a) laser diode 1 nm FWHM, b) LED 50 nm FWHM, c) cross section of the signal after power normalization.

In **Figure III.34,** I compare the cross-sections of diffraction pattern obtained with the laser diode laser and the LED source on the Quasi-Random distribution. The comparison between the quasi-coherent and the low coherent sources shows that the self-focusing effect is still observed in the case of a low temporal coherence beams.

Figure III.34 depicts the signal cross section of the experimental results of the quasi-random EPD. The central peak of the spel is enlarged by the change of the temporal coherence by a factor 2 and the spectral change impacts the speckle figure around the peak. We notice that the speckle figure vanishes from the case of **Figure III.34a** to **Figure III.34.b.**

From the **Figure III.34** it can be seen that experimental data can be approximated by two Gaussians: one for the central peak and the second for the surrounding envelop. We call this approximation the Double Gaussian model, and I will provide more details about it in the next chapter.

This comparison allows to define the characteristics of the Gaussian in both cases:

- Radius at $1/e^2$: wg_1 = 2.8 µm and wg_2 = 141 µm for the peak and the noise in the laser diode case
- Radius at $1/e^2$: wg_1 = 6.5 µm and wg_2 = 200 µm for the peak and the noise in the LED case

with an intensity equal to unity for the peak (G1 = 1) and equal to G2 = 0.065 for the noise.

The increase in size of the peak is interesting as it seems to improve the ratio of energy between the peak and the noise.

If we use a simple model of energy distribution between the peak and the noise we can have a first estimation of the γ-parameter with a simple equation to define the energy in the peak and in the noise:

$$E_j \propto G_j \times {w_j}^2$$

with j = 1 or 2.

Using this simple equation, we approximate a γ-parameter equal to 25 dB in the coherent case and to 18 dB for the incoherent case. It clearly shows that the introduction of incoherence in the process of spel generation can improve the γ-parameter.

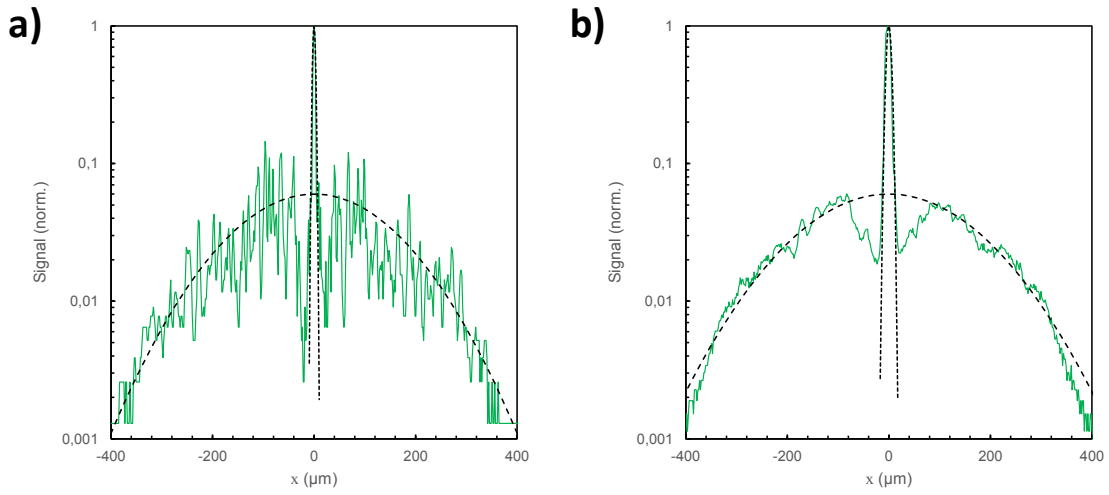

Figure III.34. Experimental results of self-focusing effect with the quasi random EPD: a) laser diode 1 nm FWHM, b) LED 50 nm FWHM. The results are compared with a Double-Gaussian function for the spel and the noise.

5.4 Coherence Simulation

The theoretical analysis of the self-focusing effect has been made for a single wavelength. In this sub-section I provide an evaluation of the temporal coherence impact on spel formation by considering the spectral distribution of the source. My simulations use the multiple interference algorithm described in **Chapter II** implementing a range of wavelength corresponding to the source spectral characteristics.

I reproduce the interference simulation for a set of wavelengths with an intensity given by the spectrum of the source. Each spectral interference figure is added to give the final interference pattern. **Figure III.35** presents the simulation results in the case of a periodic EPD. Both laser diode and LED sources simulation show a good agreement with the experiments depicted in the **Figure III.33.**

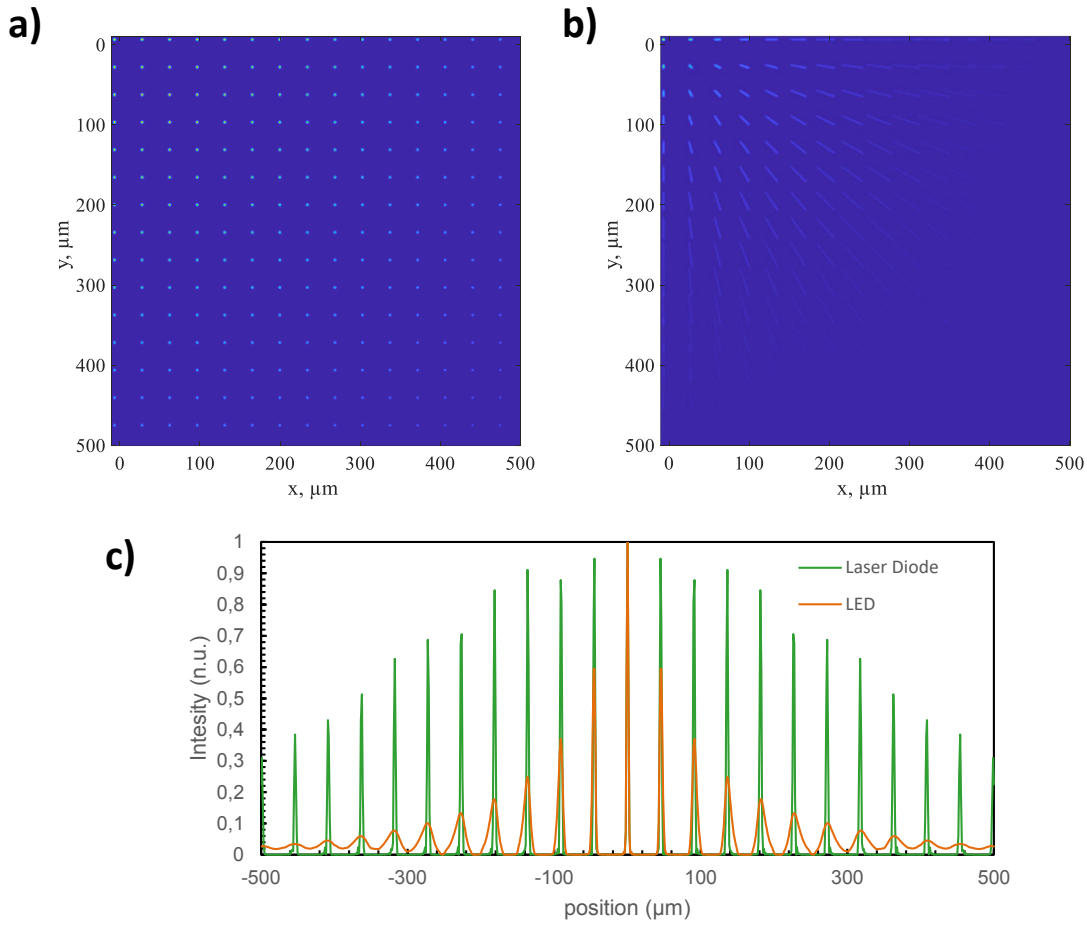

Figure III.35. Simulation results of self-focusing effect in the case of a periodic EPD for a beam with: a) spectral width 1 nm; b) spectral characteristics given by figure 3b; c) cross section comparison of both spectral characteristics.

Since our simulation results agree well with the experiment, we can use our simulation algorithm to analyze the spectral bandwidth impact in the case of the holographical optical element. This optical element is expected to be the last element before the eye in our NED.

In **Figure III.36** I show the spel simulation for a Quasi-Random distribution in the case of holographical optical element (HOE) used for emitting points [115].

The spectral reflection of the HOE is presented in **Figure III.36a**. For our simulations, we use a source with spectral characteristics deduced from this experimental data obtained in the laboratory. The hologram written in a Lippman configuration is compared with the theoretical Bragg response.

The simulation is presented in the **Figure III.36b**. I saturated digitally the intensity to highlight the speckle pattern. **Figure III.36c** shows the cross section of the spel intensity. Similarly, to the case of **Figure III.35c** we notice a speckle that vanishes gradually from the center of the figure.

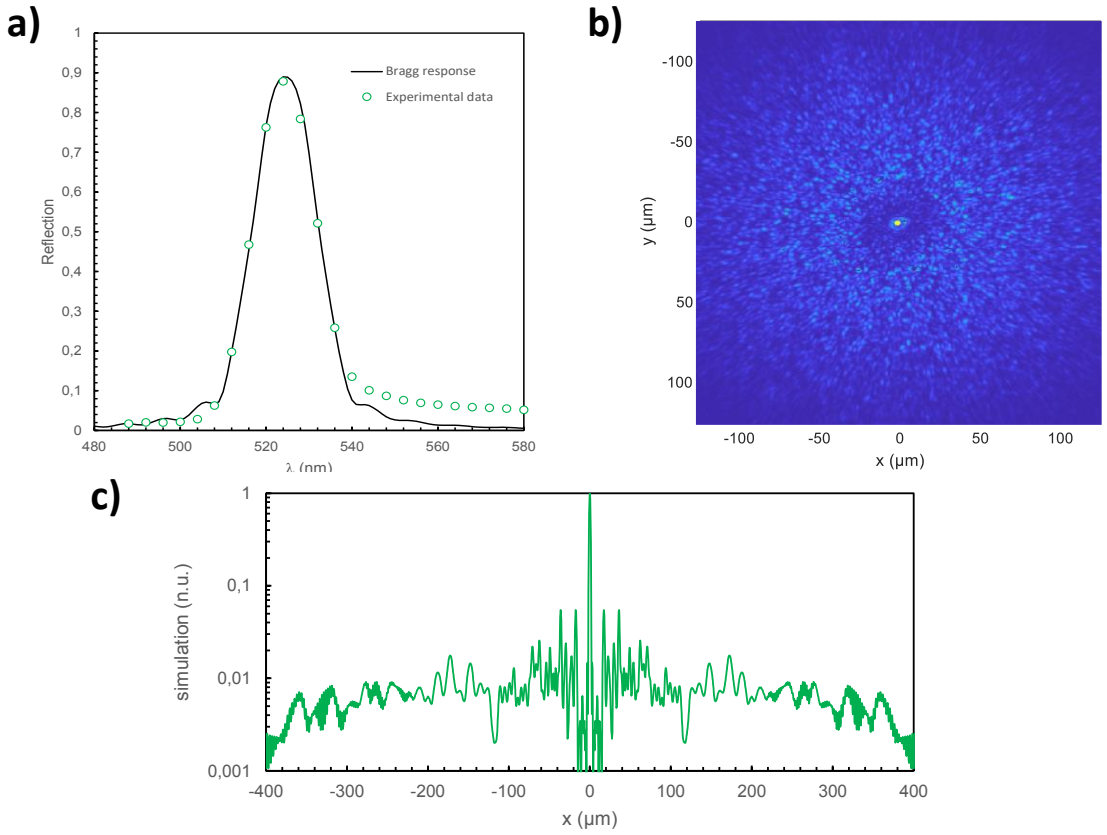

Figure III.36. a) spectral reflection of a hologram recorded in the laboratory (solid line: theoretical Bragg response, green dots: measurements), b) simulation of a spel with a quasi-random EPD and with the hologram spectral characteristics, c) cross section of the spel signal

I have experimentally evaluated the influence of the source spectral bandwidth broadening. It expands the central peak and by the way seems to increase the ratio between the energy of the spel and the energy of the noise. This aspect is particularly important in the case of image formation as we will see in **Chapter IV**.

6 Conclusion

Chapter III was dedicated to experimental validation of self-focusing effect that was not previously used in the context of augmented reality. The experiments were carried out to evaluate self-focusing capabilities for non-conventional display implementation in the augmented reality domain. The results shown in this chapter were firstly presented in 2016 at OSA conference [116] and then published in 2019 in a peer review article [117]. These results confirm the consistency of the experimental results with my simulations presented in **Chapter II**. Since the simulations, and therefore theory, well describe the experiment I consider that our setup sufficiently models our self-focusing concept.

I experimentally demonstrated spel formation with a self-focusing setup that models the unconventional NED. We can observe that the randomness of the distributions plays the central role in the spel/noise ratio. The Quasi-Random distribution showed the most prominent results as a PSF for image formation, however this type of EPD stays is not realistic in view of fabrication. Realistic random distributions lack the sufficient level of randomness exhibiting symmetrical spel-ghost in the diffraction patterns specific to the Periodic distributions.

We therefore have to find a way to increase the energy ratio between the central peak and the surrounding noise. One of the possible ways to decrease the ghost appearance is to modify the source monochromacy. The impact of the spectral bandwidth of the light source used to project the image is investigated in an experimental setup and through multiple interference simulations. I have shown that the self-focusing effect is robust and does not require a highly coherent laser source. Simulations are conducted with first experimental holographic recording data and show that our concept can be implemented with a LED array as primary source.

Each diffraction pattern could be seen as a superposition of the central peak and the surrounding noise. The central peak described as Airy disk is well approximated by a Gaussian fit. The noise envelop is also fitted to a Gaussian function. Therefore, I evaluated the observed diffraction patterns with two Gaussians, the first with high amplitude and thin waist for the peak, and the second with the low amplitude and large waist for the noise. This tool will be further described as a Double-Gaussian model. This model is used in **Chapter IV** to theoretically evaluate the behaviour of the concept as an image forming device.

Chapter IV: Self-focusing image-formation

Ce n'est point l'observation mais la théorie qui m'a conduit à
ce résultat que l'expérience a ensuite confirmé.
Augustin-Jean Fresnel

The goal of my work in this part of the study is to investigate image formation capability of self-focusing effect for a future development of unconventional image projection display concept. Such task could be accomplished with simulations based on simplified spel-formation approach and then validated experimentally with a self-focusing image formation setup. The rigorous spel-formation algorithms based on multiple source interference presented in the **Chapter II** are time-consuming. It was mentioned in the **Chapter III** that a spel could be approximated by two Gaussian functions called **Double-Gaussian (DG) model**. This model is used for two reasons: 1) to qualitatively evaluate the behaviour of the concept prototype as an image-forming device and 2) as a kernel of spel-superposition image formation algorithm. Theoretical evaluation of spel formation quality demands an introduction of previously briefly mentioned **γ-parameter** in addition to SNR that I used previously. I perform image formation simulations with developed spel-superposition algorithm. Simulation results are experimentally validated on the assembled self-focusing image formation setup. A natural constraint for our display concept is so-called **resolution/sharpness conflict**. It demands to balance the quantity and quality of spels projected in the same time.

1 Introduction

The process of image formation in a classical approach of NED consists in a convolution of the image to be formed by the Point Spread Function (PSF) of the optical system. We use $M_{u,v}$ as the matrix that describes the digital image. We consider that the image is formed on a display with square pixels of size and pitch W on the image plane (taking into account the magnification of the optical system). The object that is imaged by the optical system of the NED is described by the following equation on the retinal plane:

$$Obj(\vec{r}) = \sum_{u,v} M_{u,v} \times rect_W\left(\vec{r} - \overrightarrow{r_{u,v}}\right); \quad \text{IV.1}$$

With $rect_W$ the geometric image of the square pixel and $\overrightarrow{r_{u,v}}$ the pixel coordinates. The result of imaging on the sensor by the optical system (an eye in our case) is given by the convolution of the object by the PSF. The expression of the image on the retina is given by:

$$I_{ret}(\vec{r}) = \iint \sum_{u,v} M_{u,v} \times rect_W\left(\vec{s} - \overrightarrow{r_{u,v}}\right) \times PSF(\vec{r} - \vec{s}) \times dx_s \times dy_s \quad \text{IV.2}$$

In the case of our unconventional approach we don't consider a display in the device and the image formation process relies on the distribution of spels on the retina plane. If we define $g(\vec{r})$ as the spel function, the image on the retina is given by the following equation:

$$I_{ret}(\vec{r}) = \sum_{u,v} M_{u,v} \times g\left(\vec{r} - \overrightarrow{r_{u,v}}\right); \quad \text{IV.3}$$

Figure IV.1a illustrates our approach mathematically described by the **formula IV.3**. A digital image matrix $M_{u,v}$ provides an intensity distribution, e.g. a pixelated character "T". Iteratively, all pixels should be transformed into spels starting from the top left corner of the image plane, line by line down to the right bottom corner. Each spel intensity distribution is defined by the spel function $g(\vec{r})$. For the sharpest possible image case a spel is an Airy disk as shown in the scheme. The spel function $g(\vec{r})$ is defined on the whole image projection plane and not only in the small region as schematically shown. The location of each spel is provided by a vector $\overrightarrow{r_{u,v}}$. The resulting intensity on the retina plane $I_{ret}(\vec{r})$ is a sum of all projected spels without any interference: we

suppose that wavelets from different EPDs that forms their spels are not coherently related (coming from different lasers).

Our algorithm let us define the number of spels per pixel projected into the retina. **Figure IV.1b** shows an image of letter "T" coded with 9 pixels that should be projected. Using the described image formation process one can transform those 9 pixels to 9 spels as it shown in **Figure IV.1c,** i.e. 1 spel per pixel. It is possible to increase the image resolution and associate 1 pixel with 4 spels, as presented in **Figure IV.1.d.** Although the image quality should grow with increasing resolution in conventional displays, our concept faces so-call **resolution/sharpness conflict** I mentioned in the **Chapter II**. It is a trade-off between pixels quantity and their quality due to the limited number of emissive points on the display surface. **The higher the quality of one spel, the lower their total number.**

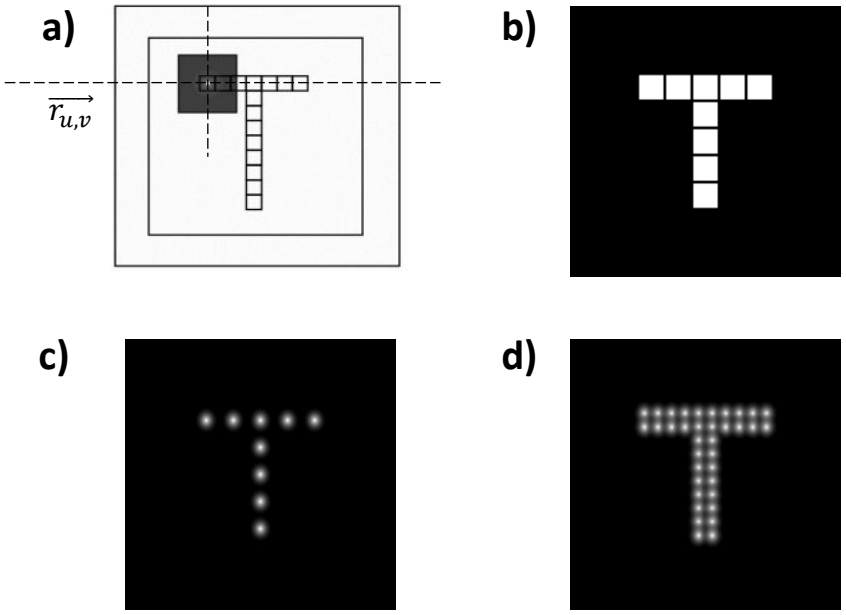

Figure IV.1. Schematic representation of self-focusing image formation: a) principal idea of the image formation algorithm with the DG-model, b) "T" character is a reference image to projection of 9 pixels c) 9 spels projected image, i.e. 1spel per pixel d) 36 spels projected image, i.e. 4 spels per pixel

The result of imaging strongly depends on the knowledge of the spel function. The spel function $g(\vec{r})$ can be rigorously calculated with multiple source interference given in the **equation II.23** from **Chapter II**. Although it provides the exact pattern, it is extremely time consuming when

image contains tens or even hundreds of pixels to project. In order to simplify the image formation analysis, we introduce the double Gaussian model approximation of spel. It let us replace the exact spel pattern with sufficient precision and obtain approximate intensity distribution to qualitatively estimate the image formation capability of our prototype.

I describe in the **Section 2** the simulation tool called **"Double-Gaussian model" (DG-model) approximation** that allows us to calculate the function $g(\vec{r})$ for a given EPD. This development is confirmed experimentally in the **Section 3**.

In the following descriptions valid for small viewing angles, I describe a spel in spatial coordinates *r* or in angular coordinates φ with the corresponding relationship function of *f*, given by the focal length of the imaging system:

$$r = \varphi \times f \qquad \text{IV.4}$$

Such inconsistency of unit use is explained by a need of both angular and spatial size of spels depending on the situation where images are formed. Sometimes it is more convenient to evaluate and analyze simulation and experimental results in spatial coordinates (with reference to the camera plane) or in angular coordinates (when referring to the eye behavior).

2 Spel approximation by Double Gaussian model

In **Chapter III** I introduced Double-Gaussian model to approximate an experimental diffraction pattern and to evaluate my experimental results. As one can see from **Figure IV.2,** each pattern could be presented as a superposition of the central peak or spel (solid blue) and the surrounding speckle noise (solid green).

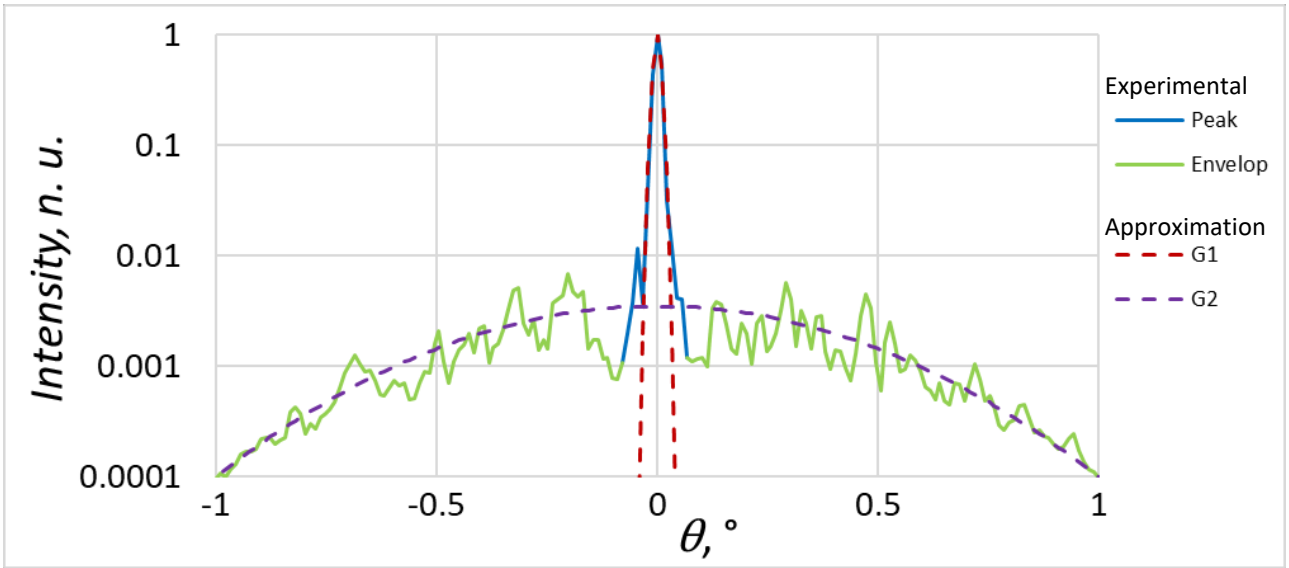

Figure IV.2. Double-Gaussian model: low-cost computational spel approximation for image formation:

Both regions are fitted by Gaussian curves. Each Gaussian G_i is characterized by its intensity distribution as follows:

$$G_i(r) = I_{0i} e^{-2\frac{r^2}{\omega_i{}^2}}; with\ i = 1,2 \qquad \text{IV.5}$$

We consider the spel function $g(\vec{r})$ as a superposition of the two Gaussians $G_i(\vec{r})$:

$$g(\vec{r}) = G_1(\vec{r}) + G_2(\vec{r}) \qquad \text{IV.6}$$

The DG-model requires to know four parameters: two maximum intensities I_{0i} and two waists ω_i. The spel peak size ω_1 is given by relation **III.12** from the previous Chapter: $\omega_1 = 0.86\frac{\lambda}{ø}f$. The noise region is characterized by the waist ω_2 defined by the expression **III.6**: $\omega_2 = \frac{f\lambda}{\pi w_1}$. These four parameters define the total energy of the resulting signal. The total energy of the signal is composed of E_1 and E_2 that represents the energy of the spel and the noise respectively. Since the total energy is a sum of two, I use the error function Erf to calculate the integral of each Gaussian function:

$$Erf(t) = \frac{2}{\sqrt{\pi}} \iint_S I_0\, e^{-2\frac{r^2}{\omega^2}} dr d\theta. \qquad \text{IV.7}$$

The total energy is expressed in a simple way by the integral of the Gaussian function:

$$E_i = 2\pi I_{0i}{\omega_i}^2{}_{i=1,2} \quad \text{IV.8}$$

Considering a normalized description of function $g(\vec{r})$, one can have the following relation:

$$g(0) = I_{01} + I_{02} = 1 \quad \text{IV.9}$$

One can limit the parameters to the waists and to the ratio of energies in both Gaussian representations. It allows us to introduce a **γ-parameter** that describes the ratio of energies between the spel peak and the total self-focused signal. This parameter is expressed in *dB* as follows:

$$\gamma = -10\log\left(\frac{E_1}{E_1 + E_2}\right) = -10\log\left(\frac{I_{01}{\omega_1}^2}{I_{01}{\omega_1}^2 + I_{02}{\omega_2}^2}\right). \quad \text{IV.10}$$

The interest of γ-parameter application is that one can vary the self-focusing signal imaging quality varying γ-parameter. I illustrate the γ-parameter application to the DG-model in **Figure IV.3** showing two limit cases and an intermediate one. The first limit case arises if one applies a large value of γ-parameter, i.e. $\gamma \to \infty$ then the energy of spel becomes negligible: $E_1 \approx 0$ and the total energy of signal contains only the noise part: $E_{\text{total}} \approx E_2$. Therefore, the resulting signal is described by the spel function that is purely the noise envelop: $g(\vec{r}) \cong G_2(\vec{r})$ as presented in the **Figure IV.3a**.

The second limit case arrives if one applies a zero of γ-parameter, i.e. $\gamma = 0$, then the energy of noise becomes negligible: $E_2 = 0$. Therefore, the resulting signal is described by the spel function that is purely the noise envelop: $g(\vec{r}) \cong G_1(\vec{r})$ as presented in the **Figure IV.3b**. In reality, γ-parameter is always somewhere in between these limit values: $0 < \gamma < \infty$. This means that according to the expressions **IV.8-10** we observe a superposition of two Gaussians as presented in the **Figure IV.3c** in the case of γ-parameter ≈ 11dB. The spel function of the resulting signal $g(\vec{r}) = G_1(\vec{r}) + G_2(\vec{r})$ is shown on the **Figure IV.3d.**

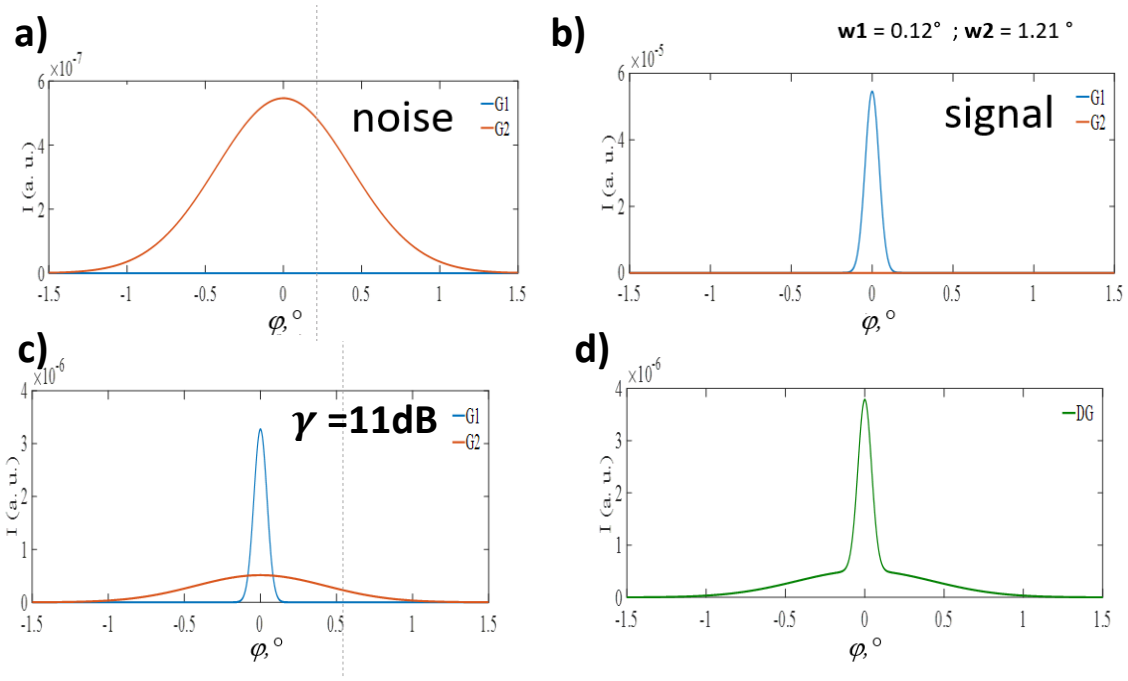

Figure IV.3. Implementation of γ-parameter to Double-Gaussian model for Spel simulation: a) the first limit case with $\gamma \to \infty$ dB; b) the second limit case with $\gamma = 0$ dB; c) the intermediate with case $\gamma \approx 11$dB d) the spel function of the resulting signal

Looking at this example, one can see that the bigger γ-parameter, the more noise in the resulting signal, and vice versa. Therefore, by definition of γ-parameter, the **image quality has inverse relationship with the γ-parameter**.

2.1 Evaluation of Double-Gaussian model approximation of the Airy disk

The Airy disk is the ideal response of an optical system when no aberration or noise is considered. It corresponds to the theoretical response of the beam that focuses on the retina considering only the diffraction. As the Airy disk represents the best achievable "diffraction limited PSF" or spel in our case, it is interesting to evaluate the DG-model approximation of it. **Figure IV.4** shows the Airy disk and its Double-Gaussian fit both in linear and logarithmic scales to illustrate the pattern form. In **Figure IV.4a** one can see that the spel size is defined by the waist δw_g of the first Gaussian G_1 that equals to the HWHM of the Airy disk. However, the second Gaussian G_2 almost merges with the abscissa in this graph and becomes undistinguishable, therefore one needs to draw the Airy disk in the logarithmic scale to clearly see the pattern. In **Figure IV.4b** one can see the Double-Gaussian model approximation of the Airy disk in detail. My method to estimate the

spel central peak is as follows. I chose to match the spel size and the Gaussian fit HWHM. As a consequence, there is a small mismatch for Airy disk and its Gaussian waist at $1/e^2$. This mismatch is negligible as it was shown in the section 2.6 of the **Chapter III.**

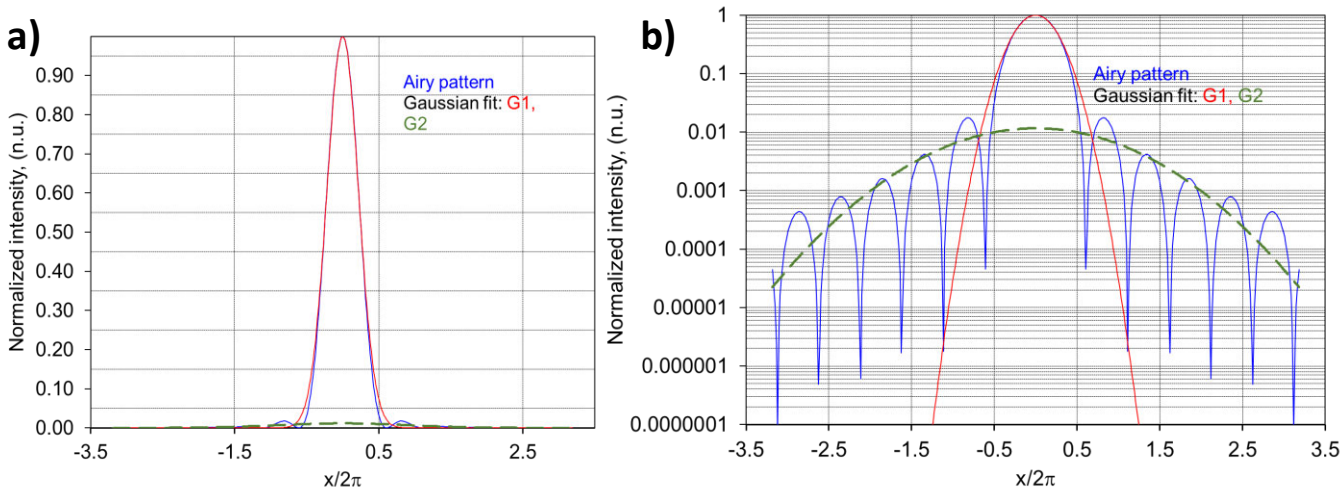

Figure IV.4. Double Gaussian model approximation of Airy disk: the central peak approximated as it was showed in the Chapter III (Figure III.22). a) Double Gaussian fit in linear scale; b) Logarithmic representation of the Double-Gaussian fit of the Airy disk

The waist and the intensity of the second Gaussian G_2 are deduced from expressions **IV.8-10** using γ-parameter**.** I suppose that the first Gaussian contains the energy that corresponds to the energy encountered before the first zeros: $\pm 1.22\pi$. I use the analytical development provided in Born and Wolf [1] to calculate the energy limited to the angular radius φ in the Airy function:

$$E_{Airy}(x) = 1 - {J_0}^2(x) - {J_1}^2(x); \qquad \text{IV.11}$$

With $x = \frac{\pi \text{ø}}{\lambda}\varphi$ and where J_i is the Bessel function of the first kind of i-order, i =1,2. The relation between the waist and the intensity of the second Gaussian G_2 is optimized visually to obtain the best fit of the Airy disk.

In **Figure IV.5** the Airy pattern is presented in logarithmic scale next to its energy integral to highlight how energy is distributed within the several zeros of the function. One can see that 83.7% of energy is encountered before the first zero that I suppose as the spel peak region.

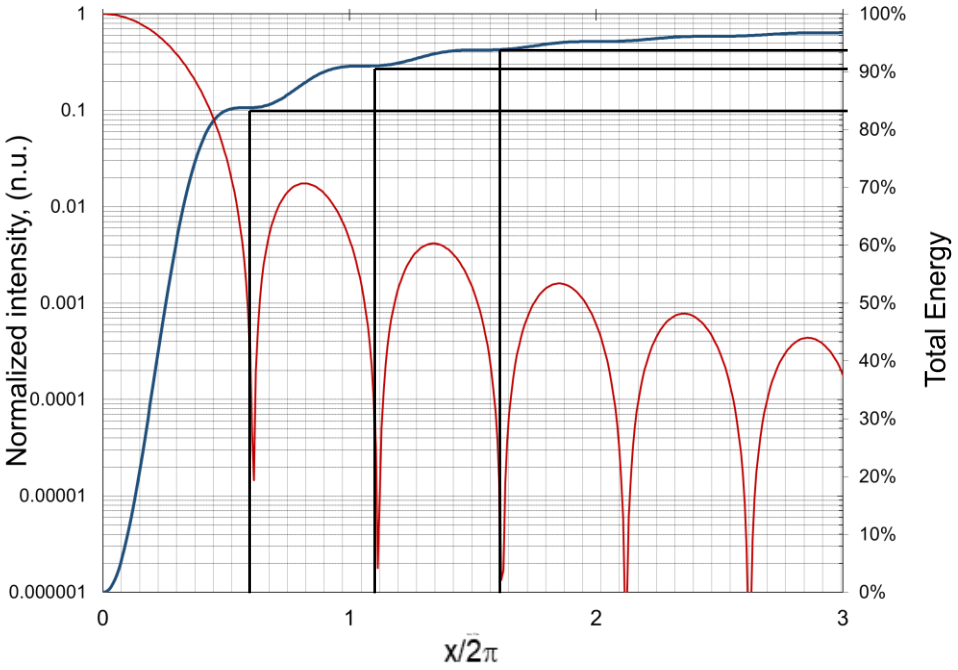

Figure IV.5. Airy pattern in logarithmic scale next to its energy integral in linear scale: 83.7% of energy encountered in the "peak" region.

If I define the **γ-parameter** of the Airy disk as the ratio of energy limited by the first zero and the total energy, then I can estimate a limit value of γ-parameter as follows:

$$\gamma_{Airy} = -10\log\left(\frac{0.837}{1}\right) = 0.77\ dB \qquad \text{IV.12}$$

This result shows that **the minimum theoretical value of γ-parameter is 0.77 dB**. This value along with the parameters of the first Gaussian G_1 let us define the parameters of the second Gaussian G_2. According to the central peak estimation method the first Gaussian G_1 has the next parameters: the normalized maximum intensity $I_{01} = 1$ and spel size $\omega_1 = \delta w_g = 0.43\frac{\lambda}{NA}$, $NA = \frac{ø}{2f}$, as I've shown in the section 2.6 of the **Chapter III**. Therefore, the second Gaussian G_2 has the next parameters: the normalized maximum intensity $I_{02} = 0.0116$ and spel size $\omega_2 = w_2 = 1.8\frac{\lambda}{NA}$. Consequently, it's verified that Airy disk could be mainly represented by the first Gaussian G_1 in linear scale, i.e. if $\gamma = 0.77$ the energy of noise is assumed negligible.

2.2 Resolution/Sharpness conflict

My first image formation simulations showed that the DG approximation seems efficient to give a view of the image that can be reconstructed on the retina. However, while one starts implement the DG-model for image formation, the question arises which value of **γ-parameter** one must use for a particular image; or in other words, **what should be the acceptable image quality?**

Physically, it depends on the number of emissive points that are used for self-focusing of one spel, or in other words the number of EP per EPD that forms a spel. Suppose, we consider a pupil of 6 mm in diameter and an EP size about 5 μm in diameter. The total number of EP in the pupil is given by the ratio of surface between the EP and the pupil. If we consider an EPD composed with 200 EP, then we can define 7200 EPD on the pupil surface. It corresponds to 7200 potential spels on the retina that is to an image of about 84x84 pixels.

If we consider an EPD with 36 EP, then we can define 40 000 EPD on the pupil surface. It corresponds to an image of about 200x200 pixels.

When we consider all these parameters we are confronted to a difficult compromise between the size of the EPD and the number of EPD. Both affect the quality of the image and its resolution in terms of pixel number. **The higher the number of EP per spel (or EP per EPD), the higher its quality, i.e. sharpness, but the lower the total number of spels, i.e. resolution.** This trade-off was mentioned in the Chapter II as **resolution/sharpness conflict:** the EP number per EPD is a **compromise between quality of spel** (γ-parameter) **and number of possible spels N_{sp}**. This conflict is an essential problem of self-focusing image projection display.

Contrary to the introductory figure where I presented self-focused image of letter “T”, the spels in **Figure IV.1c** should have higher quality than the spels in **Figure IV.1d** as I form the image with less pixels. To illustrate the Resolution/Sharpness conflict I provide some qualitative image formation simulations with various γ-parameter. Note, that γ-parameter has arbitrary values to qualitatively illustrate the problem. I use the DG approximation as a kernel of spel-superposition in my image formation algorithm. I simulate the formation of the word “LETI” as shown in **Figure**

IV.6. The descending curve in **Figure IV.6a** shows the principle of **resolution/sharpness conflict:** increasing spel quality (inverse to γ-parameter) decreases the total number of potentially projected spel N_{sp}.

There are two limits: the minimal number of EP per EPD is 1; the maximal spel quality is given by Airy disk γ-parameter equals 0.77 dB.

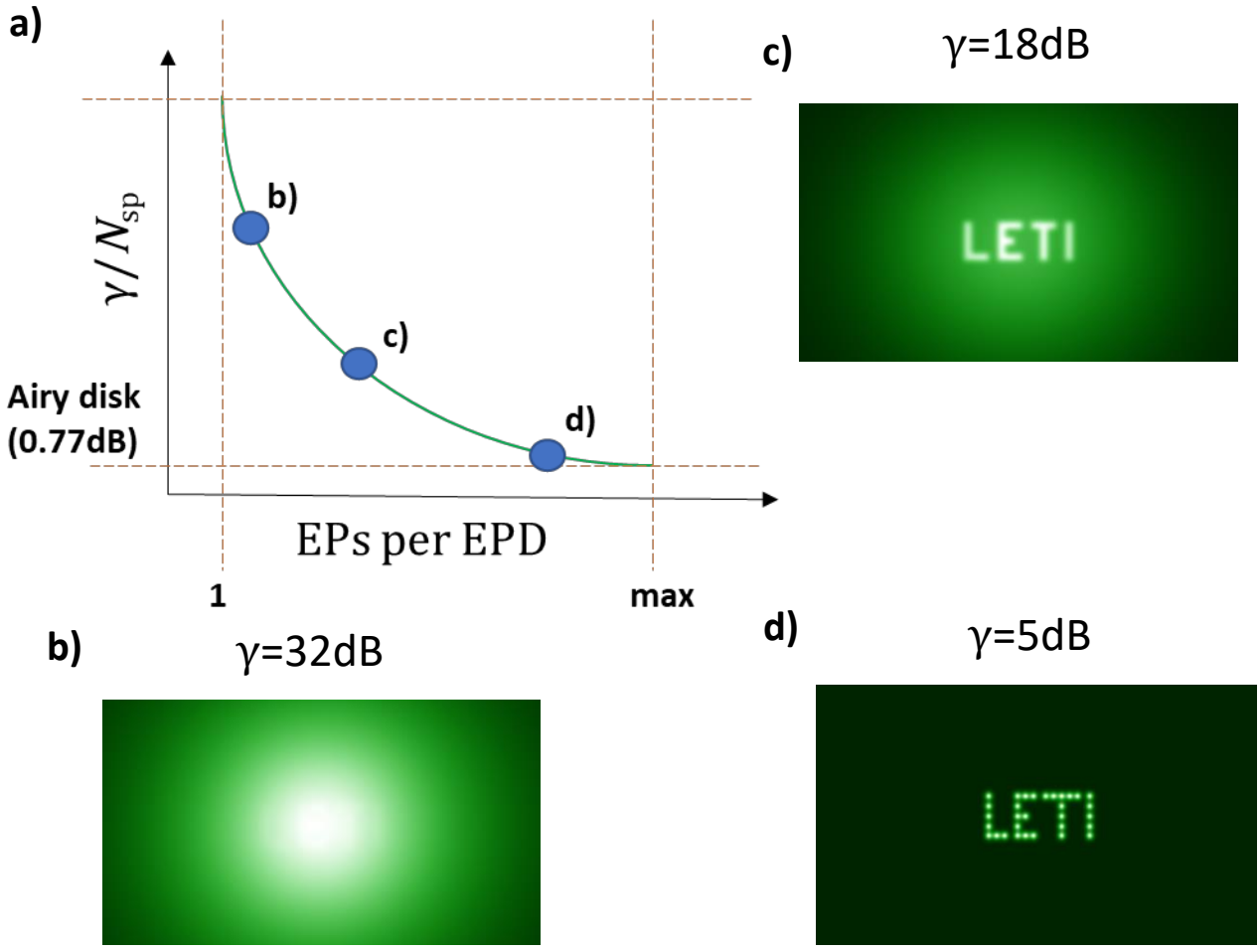

Figure IV.6. Resolution/Sharpness conflict principle illustration: a) the inverse relationship between emissive points per EPD and total number of potentially projected spel N_{sp}. with correspondingly increasing spel quality; b) high resolution low spel quality image, c) compromise case: an image with intermediate values of both N_{sp} and γ-parameter; d) low resolution/high spel quality image

There are three particular points on this curve I chose to illustrate the γ-parameter influence on image formation. The points b), c) and d) corresponds to γ-parameter of value 32 dB, 18 dB and 5 dB respectively. One can see that the "LETI" image presented in **Figure IV.6b** is completely

undistinguishable at $\gamma = 32$ dB although the number of pixel can be high. For the simulation, the number N_{sp} per projected pixel is chosen arbitrary as 25 (5 by 5 spels). In the intermediate case shown in **Figure IV.6c.** γ-parameter equals 18 dB and N_{sp} per projected pixel is 4 (2 by 2 spels). On can observe the moderate quality of image and still a good resolution. I could speculate that somewhere near this region should be an optimum solution for the resolution/sharpness conflict in case of complex images. **Figure IV.6d** presents the high quality spels (γ=5 dB) with low resolution (1 spel per pixel). Due to alpha-numeric type of image the low-resolution case is potentially an adequate choice for such type of images.

Therefore, this short analysis shows that the result of self-focusing imaging depends not only on the physics of the imaging process, but also depends on which type of image we project. Since it was only a qualitative estimation, the exact degradation of the number spels per projected pixel, depending on γ-parameter, has not been considered for this simulation. Such task demands a complex time-consuming research.

First, we should consider the specific behavior of the eye that is a very complex optical system. Then we must take into account the spatial distribution of the EPs in the EPD. It depends on the manufacturing technology of the device (size of the emission points, number of emission points per EPD, etc.) but also a display choice (FOV, angular resolution (in terms of pixel per inch or PPI), etc.) We should then consider reducing as far as possible the number of EP in each EPD to improve the image resolution in terms of number of pixels. However, this task demanded extra-time and competences for our research, hence I preferred to concentrate the rest of my work on the experimental validation of the image formation process. This difficult task of image quality evaluation in the self-focusing concept is currently addressed by another PhD-student in the laboratory. To go further on my research, I present then my work on experimental demonstration of self-focusing image formation validation with the DOE used in the **Chapter III**.

3 Experimental validation of image formation by self-focusing effect

As long as a lensless NED prototype is not fabricated due to its design complexity I propose a simplified setup to validate unconventional self-focusing image formation capability. The main

simplification is replacing the emissive surface of the display by a distribution of pinholes and a monochromatic micro-display with a collimating lens to generate emissive wavefronts.

Our approximation and therefore the obtained results are valid for our concept according to next consideration. I assume that wave propagation from infinity through pinholes distribution is equivalent to the superposition of wavefront from the emissive surface of the unconventional display. Both a pinholes distribution and an EPD have the same pattern of points and are placed in the same distance from the model of human eye. It should be mentioned that there is a main difference between the setup and our concept prototype: there is only one DOE for all spels in the setup while there is one specific EPD for each spel in the concept.

I used a similar approach in the experimental validation of self-focusing effect. The results of multiple interference match with experimental ones. These two facts make us confident in the veracity of the unconventional image formation results.

3.1 General description of setup

To prove experimentally the unconventional image formation capability of our concept I propose a similar setup layout to self-focusing validation setup described in the **Chapter III**. The primary setup is slightly modified and presented in **Figure IV.7**. As previously, there are also 2 main parts: the emissive system and the imaging system. Compared with the emissive system of self-focusing validation setup there is a difference in the wavefront generation or image source. In the modified setup I replace a fibered laser with a micro-display. Initially, we would like to create an image iteratively using the primary setup. It demands to capture spel by spel iteratively as described in our imaging algorithm. However, such approach was not implemented due to low image quality after several iterations: the additive noise component makes the resulting image undistinguishable. Replacement of the bright laser source by a micro-display requires a collimating lens to transfer emitted light up to a DOE and to ensure acceptable radiometric characteristics of the micro display pixels.

As the aperture distribution used in this work has a very low transmission factor due to the small size of the pinholes, a specific high power monochromatic micro-display developed in our

laboratory has been used. This binary microdisplay forms a static image of the word “LETI” with a 13x5 pixels resolution, and a single, isolated pixel is also activated. The size of the pixel is 8x8 µm² with a pixel pitch of 10 µm. Typical brightness for this display is about 3000 Cd/m².

Another modified element is the 3.5 µm pixel size CMOS-sensor that was replaced by another one with 1.67 µm pixel size[15]. Such modification gave a 2-fold gain in resolution to ensure sharp and well-resolved spel projection with 13 pixels per spel (*pps*) instead of 6 *pps*. The spel size $2w \cong 22\ \mu m$ is estimated for the pupil diameter Ø=3.4 mm and the focal length f_2= 51 mm provided by a Zeisss Camera lens Wollensak Raptar 2.04” that was used in the previous setup. The total self-focused signal region w_2 is estimated about 700 μm.

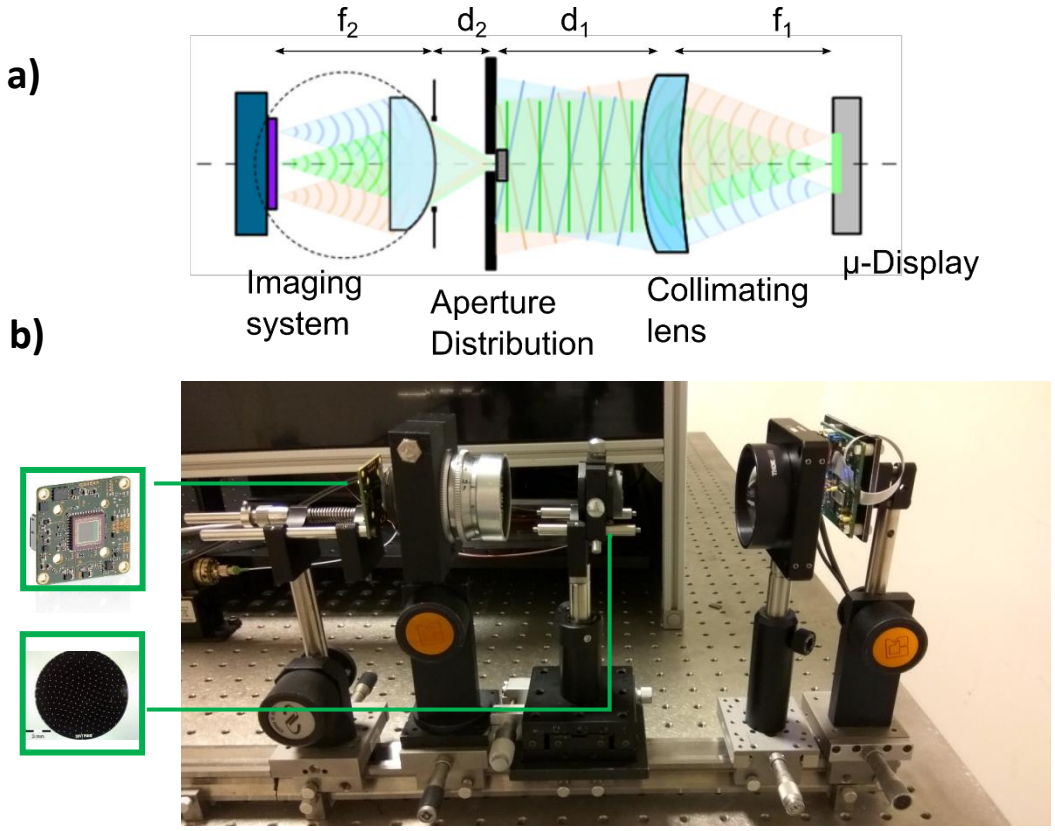

Figure IV.7. Image formation validation setup: a) schematic setup layout; b) a photo of the assembled setup in the laboratory, the distance between the collimating lens and the DOE aperture distribution is shortened for photography compactness; CMOS-sensor and a DOE are zoomed on the left

[15] https://fr.ids-imaging.com/store/ui-1492le.html

3.1.a Main settings and parameters of the setup

Figure IV.7 shows principal view of the setup.

The main characteristics of the setup are as follows:

- The LETI Microdisplay with 10 µm square pixel period, with large effective spectrum length $\Delta\lambda$ ~ 100 nm, central wavelength λ = 508 nm and FWHM ≈ 36 nm, see **Figure IV.8**;
- a collimating lens with focal $f_c = 40$ mm;
- a diffractive optical element (DOE) made of a pinholes distribution with diameters: 25 µm, 50 µm and 75 µm, the size of the DOE is determined by radius $r_{DOE} = 5$ mm;
- an adjustable diaphragm located behind the DOE (generally adjusted at 3 mm);
- a camera lens (Zeiss Wollensak Raptar 2.04") with 51 mm focal length and a diaphragm with f-number from f/1,5 to f/22;
- a CMOS-sensor and a camera lens which presents a simple model of a human eye (UI-1492LE digital camera, USB 2.0, 3840 X 2748 *µm*, 3.2 FPS, CMOS)

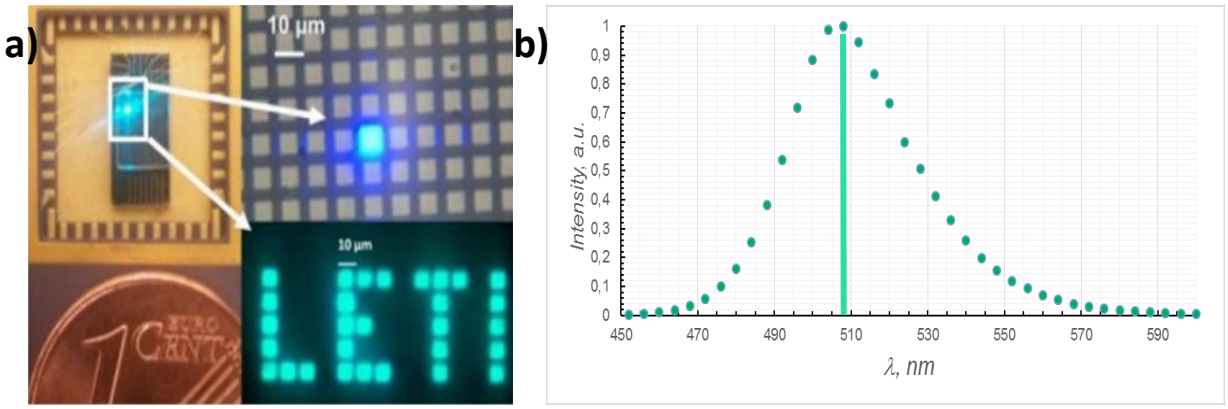

Figure IV.8. LETI's MicroLED-dislpay used in the experimental setup: a) photo of the microdislpay compared with a 1-eurocent coin and a close up on the display region; b) spectrum of the LETI display with maximum at 508 nm and FWHM ≈ 36 nm

The micro-display is placed at the focal point of the collimating lens L_1 and the CMOS-sensor is placed at the focal point of the camera lens L_2. The DOE of radius r_{DOE} is placed at the distance d_1 from the lens L_1 and at the distance d_2 from the lens L_2 with $d_2 \sim f_2$.

The choice of the lens L_1 and of the imaging system f-number is made to recover enough power from the display in order to see the projected image on the imaging sensor through the DOE. The numerical aperture of L_1 is about 0.3.

Using LETI micro-display let us generate a series of planar wavefonts for each pixel u,v defined with wave vector $\vec{k}_{uv}$. We can represent this vector in angular coordinates as:

$$\vec{k}_{uv} = \begin{bmatrix} \sin\rho_{uv}\cos\theta_{uv}; \\ \sin\rho_{uv}\sin\theta_{uv}\,; \\ \cos\rho_{uv}\,. \end{bmatrix} \quad \text{IV.13}$$

Paraxial approximation is used, with δp the display pixel picth:

$$\rho_{uv} = \frac{\delta p}{f_1}\sqrt{u^2+v^2}; \qquad \theta_{uv} = \cos^{-1}\left(\frac{u}{\sqrt{u^2+v^2}}\right). \quad \text{IV.14}$$

Spel coordinates on the CMOS-sensor is defined by the radius vector $\vec{r}_{uv}$ that corresponds to the pixel u,v

$$\vec{r}_{uv} = \begin{bmatrix} f_2\,\rho_{uv}\cos\theta_{uv}; \\ f_2\,\rho_{uv}\sin\theta_{uv}\,. \end{bmatrix} \quad \text{IV.15}$$

3.2 Experimental results

I now present experimental results obtained with the setup. I have evaluated the results of the image forming process on the various EPDs considered in this study. Figures are given in gray level and angular coordinates. To give a better visual rendering the gray scale of the figure is reversed (0 for white and 255 for black).

3.2.a Spel characterization for the QR DOE

Figure IV.9 shows the experimental self-focusing signal from LED-source described in the section 5.2 of **Chapter III**. The spel is approximated by the DG-model. The cross intensities functions are given in spatial coordinates on the CMOS sensor. The DG-model parameters are: I_{01} = 1; w_1 = 6.5 µm; I_{02} = 0.065; w_2 = 200 µm and are consistent with the theoretical values: δw = 6.7 µm and w_2 = 224 µm. From these parameters I deduce γ= 18. This value of γ-parameter is important for the image formation simulations we use latter to compare our experimental results.

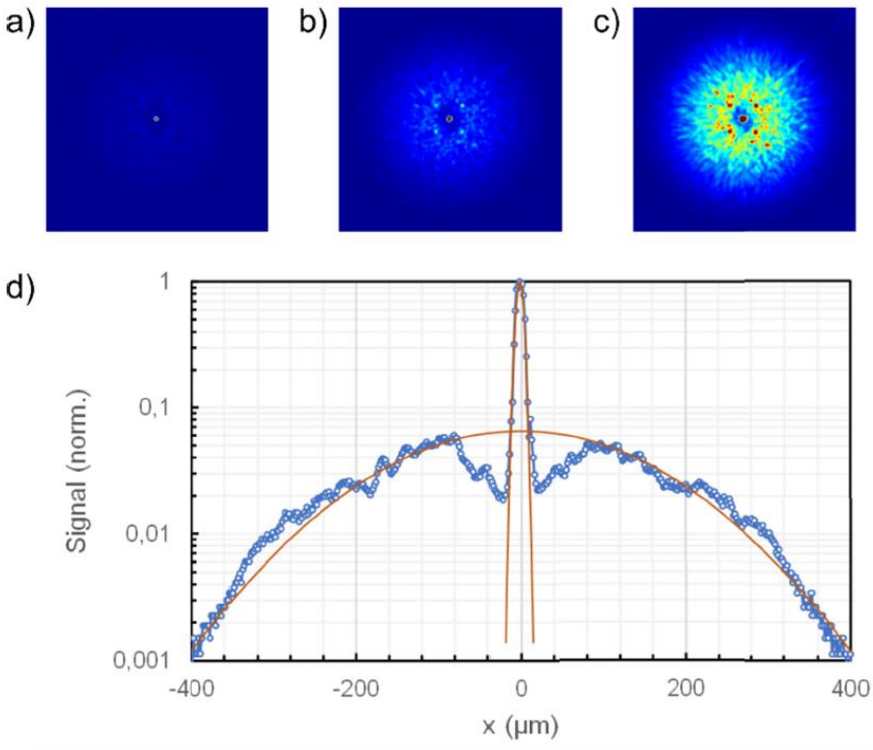

Figure IV.9. Double-Gaussian model for the spel of LED-source. (a), (b) and (c) spel intensity distributions for three LED power (d) cross intensity function of the concatenated images (blue dotted curve) and Gaussian model for the peak and the noise (orange curves).

3.2.b Full pupil result

Firstly, I took a reference image from the display with no aperture distribution. The only factors that disturb image formation are the diffraction and the aberrations of the various lenses. **Figure IV.10** shows the image of the micro display through the full aperture.

As the display has a single illuminated pixel, we can estimate the response of the system to a single planar wavefront. One can see the PSF of the system in **Figure IV.10b**. I can estimate a PSF radius of about 0.01° that corresponds well to the Rayleigh criteria with a F-number of about 15 for our imaging system.

This value can be compared to the angular size of one display pixel on the camera. The pixel pitch divided by the collimating focal distance gives the angular separation between two pixels. It gives an angle of about 10/40 000 ~ 0.003°. This explains why we can't observe any gap in letters as we can see in **Figure IV.10c**.

The PSF radius can also be compared to the image resolution on the camera. With a pixel pitch of 1.67 µm and a focal length of 51 mm, the imaging system has an angular resolution of about 0.002°. The image sensor resolution allows to describe well the PSF but is not able to resolve the pixel display image.

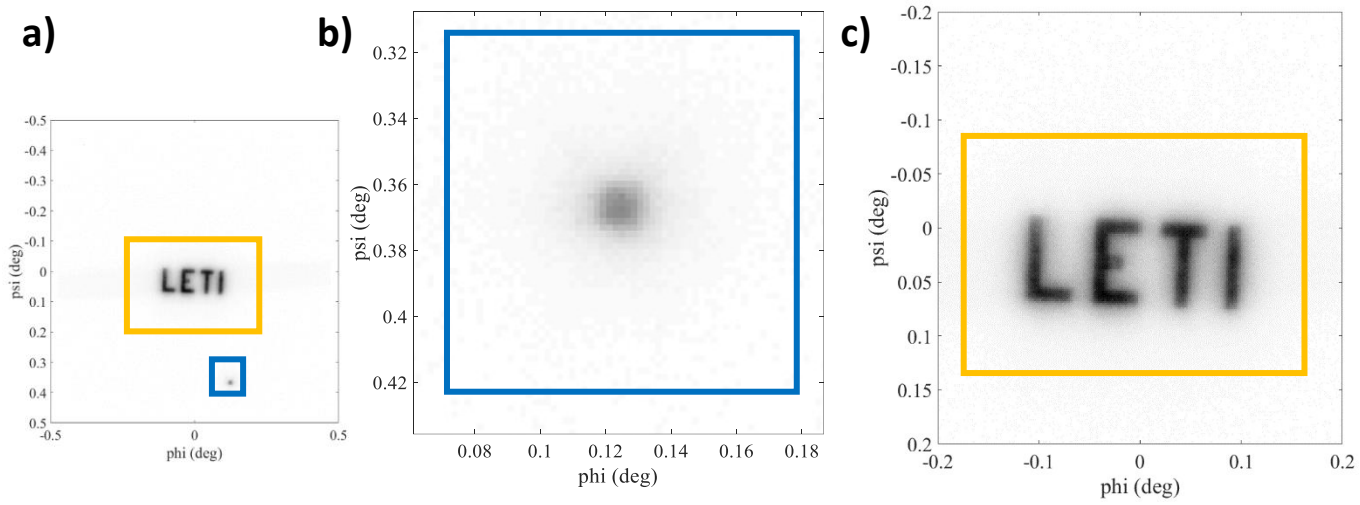

Figure IV.10. Reference image obtained without pinholes distribution: a) the whole image, b) system PSF c) close up of the LETI region

3.2.c Periodic distribution

In **Figure IV.11** one can observe the result of unconventional image formation with periodic pinhole distribution (δ = 75 µm, Λ = 400 µm). As it was predicted multiple images of "LETI" word are observed. In the same image we observe also the response of the single point source (isolated pixel on the display). This PSF is a periodic distribution of resonance peaks. Notably, as distances between peaks and between letters almost the same, the formed image is a slightly shifted superposition of letters "L", "E", "T" and "I". As a result, most contrasted image is letter "E". Diameter of this repeating zone is equal to 0.77°. This value corresponds well with the waist $w_2 = \frac{f\lambda}{\pi w_1}$ given by w_1 the radius of the pinholes.

The distance between the repeated single pixel image on the image sensor is of about 0.078°, it corresponds well to the angular diffraction orders separation related to the periodic distribution and to the wavelength λ/Λ: 0.532 µm/400 µm ~ 0.076°.

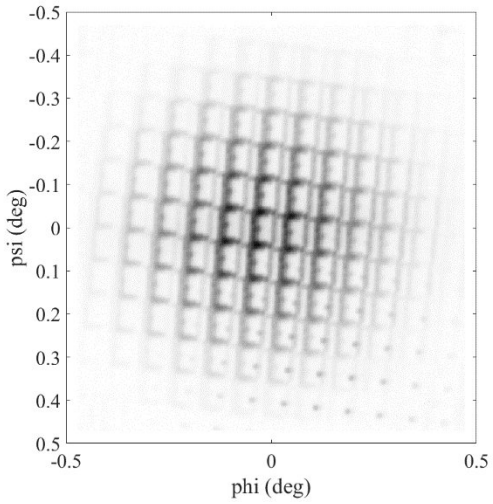

Figure IV.11. Image of the LETI word formed with a periodic distribution of pinholes

3.2.d Random distribution

Random distribution provides the best possible image formed with self-focusing effect. The result image is presented in **Figure IV.12**. Besides the "LETI" word, we can observe a large region w_2 with a Gaussian intensity. In the close up of the same image LETI the letters seem

continuous, one can't observe any gap as it was in the reference image: However, the PSF of the system has similar angular size, so the resolution remains the same.

In contrary, the contrast of the self-focused image is lower than the contrast of the reference image. To calculate the value of the image contrast *k*, we divide difference between $\overline{G_1}$, mean value of grey-level of word zone ("LETI"), and $\overline{G_2}$,the mean value of the grey-level of closest zone with radius 0.2, by $\overline{G_1}$:

$$k = \frac{\overline{G_1} - \overline{G_2}}{\overline{G_1}}. \qquad \text{IV.16}$$

Contrast for reference image is $k_1 \sim 0.95$, contrast for self-focusing image is $k_2 \sim 0.63$.

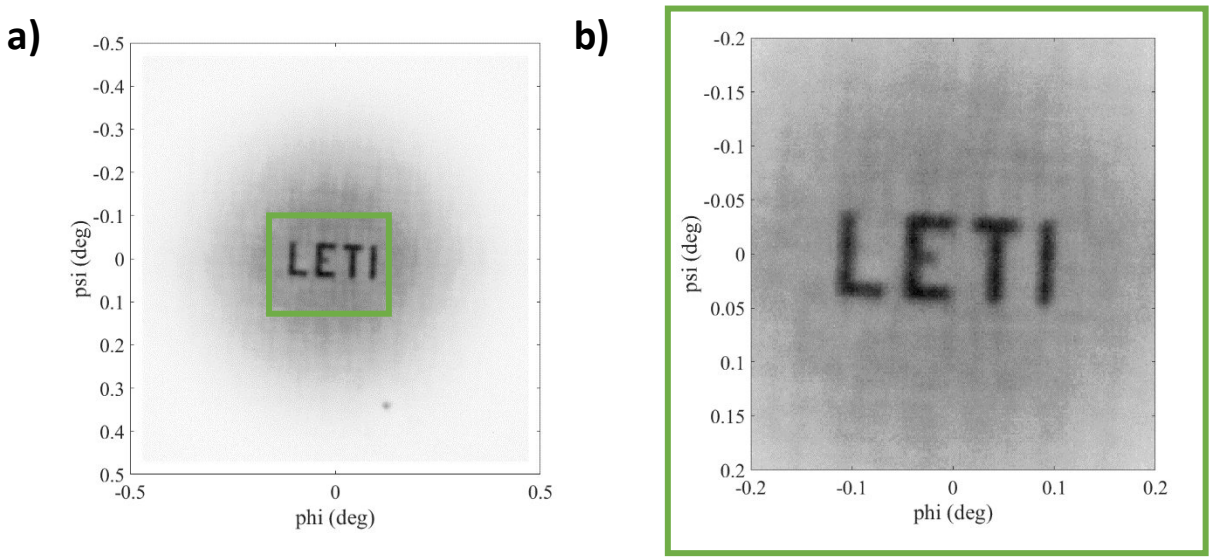

Figure IV.12. Image of the LETI word formed with a quasi-random distribution of pinholes: a) the whole image with, b) the central region

It should be mentioned that semi-random is a distribution of pinholes distributed randomly in the elementary unit cells (EUC) with size $\Lambda_1 \times \Lambda_2$. Dividing the whole surface into smaller regions provides a uniform covering of the display surface by emissive points. Despite this periodic EUC partition, due to the irregularity of the emissive point position in each EUC, the EPD remains random in total.

3.2.e Realistic distribution

One can see in **Figure IV.13** the image formed through realistic EPD.

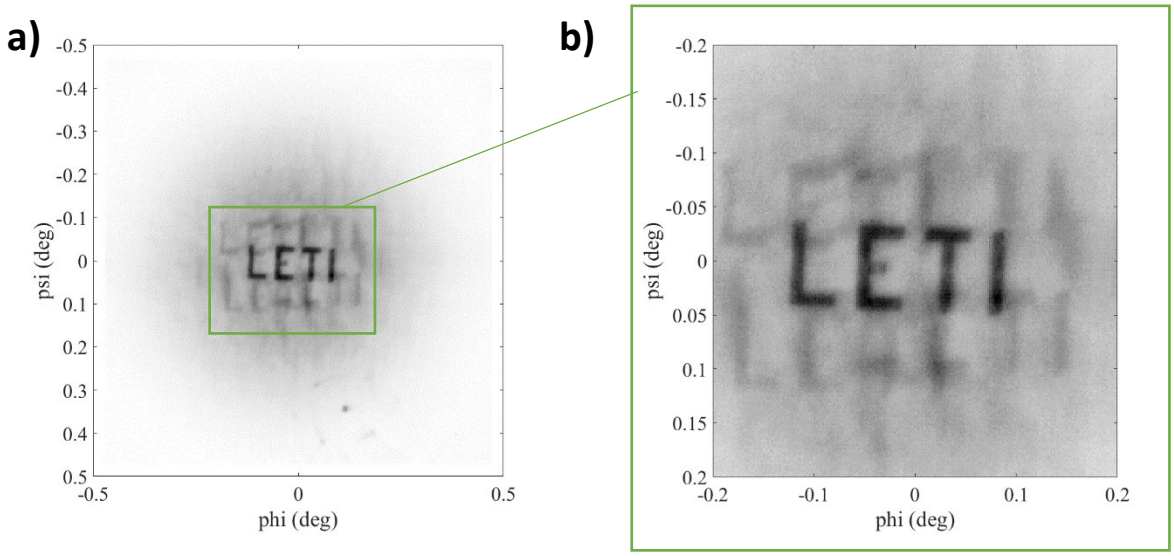

Figure IV.13. Image of the LETI word formed with a realistic distribution of pinholes

LETI image exhibits several side's ghosts which lays on form of PSF: except the central peak there are also some undesirable resonances. It compels us to optimize realistic distribution to achieve single image. However, the best possible image will have a Gaussian halo and the expected contrast is lower than the contrast of the quasi-random distribution k_2. The contrast is measured in range of 0.43 to 0.62 depending on the zone: the ghost regions provides the lower contrast.

3.3 Simulation

The experimentally obtained images can be simulated with double-Gaussian formalism with some modifications for Periodic, Cross Sinusoidal and Cross Random Sinusoidal distributions. I use as image a 13x5 pixels sampling of the acronym "LETI" representative of the micro-display as shown in **Figure IV.14**. For simulation I choose a 130x50 pixels resolution for the whole image, with an emissive-pixel periodicity of the display of 10 pixels, and each emissive zone being itself sampled with 8x8 pixels**.**

Each letter of word “LETI” has 5 display pixels height and 1 or 3 display pixels in length. The distance between each letter is 1 display pixel. LETI image consists of 13 by 5 display pixels in length and height respectively or 130 µm by 50 µm.

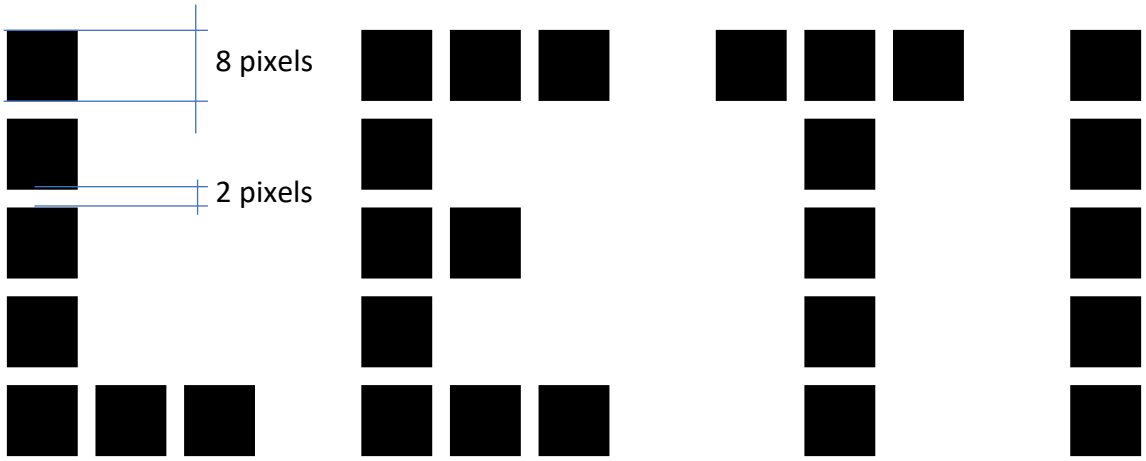

Figure IV.14. LETI image with 130x50 pixels resolution for simulation

Simulations are made on the basis of the double Gaussian model. The results based on the parameters deduced from experimental spel characterization give low correspondence with our experimental measurements and correcting factors must be introduced in values of spel and noise sizes as well as γ-parameter. Both values of the waist must be increased by a factor 1.5 and γ = 15 dB is used instead of γ =18 dB.

3.3.a Simulation implementation

For Quasi-random simulation I use DG model spel function: $g_{qr}(r)$, described in the **equation IV.5.** Periodic distribution case is approximated by spel function: $g_{per}(r)$:

$$g_{per}(\vec{r}) = G_0 e^{-2\frac{\|\vec{r}\|^2}{{w_2}^2}} \sum_{k,l} e^{-2\frac{\|\vec{r}-\vec{r}_{kl}\|^2}{{w_1}^2}} \qquad \text{IV.17}$$

Periodic spel function consists of three terms. The first term G_0 is used to normalize the total energy. The second term is the envelope of the apodization function. The third term is the grid of resonances due to the periodic distribution, vector $\vec{r}_{kl}$ giving the coordinates of the resonant peaks:

$$\vec{r}_{kl} = \begin{bmatrix} k\dfrac{\lambda f_2}{\Lambda} \\ l\dfrac{\lambda f_2}{\Lambda} \end{bmatrix} \qquad \text{IV.18}$$

In the case of CSR, the spel function $g_{CRS}(\vec{r})$ is a compound of DG-model spel function and a resonant spel function.

$$g_{CRS}(\vec{r}) = I_1(\|\vec{r}\|) + I_2(\|\vec{r}\|) + H_0 e^{-2\frac{\|\vec{r}\|^2}{{w_3}^2}} \sum_{qp} e^{-2\frac{\|\vec{r}-\vec{r}_{qp}\|^2}{{w_1}^2}} \qquad \text{IV.19}$$

The first two terms of the equation correspond to the spel and the noise, respectively. The last term corresponds to the ghost peaks that appear at coordinate $\vec{r}_{qp}$ with an angular extension given in the experimental results presented above.

3.3.b Simulation and comparison with experimental results

In **Figure IV.15** I compare the experimental self-focused image produced via quasi-random DOE with a simulation using DG-model spel-function approximation. Correcting factor is introduced to obtain the simulation result close to the experimental one. This correction factor is deduced from middle cross-section comparison presented in **Figure IV.16**. The task is to find the best fit of measured data.

Approximately the correction factor equals 1.5 for the waist size as compared to the result from **Figure IV.9.** The best fit in the curves of **Figure IV.16** is obtained with γ-parameter equal to 15 dB. This value differs from the expected one of about 18 dB.

This difference in the parameters might be due to the difference in the spectral characteristics between the LED source and the pixel of the micro-display. It can be explained also by the change in the setup configuration between the two measures of PSF and Display image.

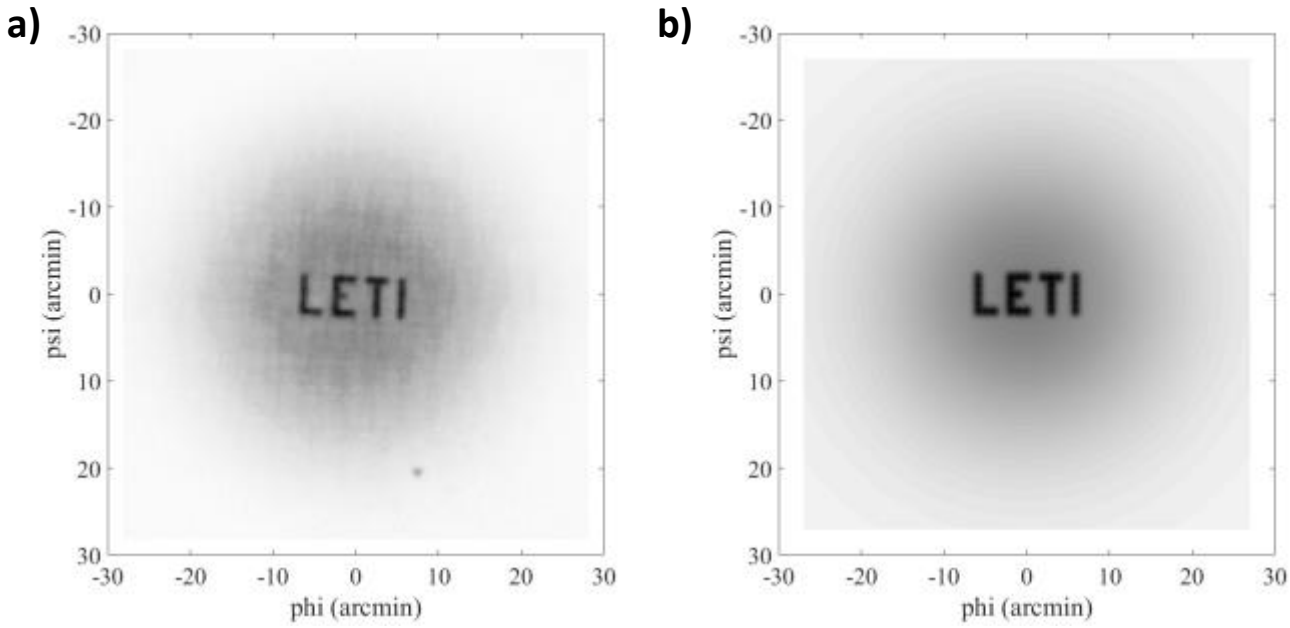

Figure IV.15. Quasi-Random distribution self-focusing images of LETI : a) experimental image, b) simulation with γ=15 dB;

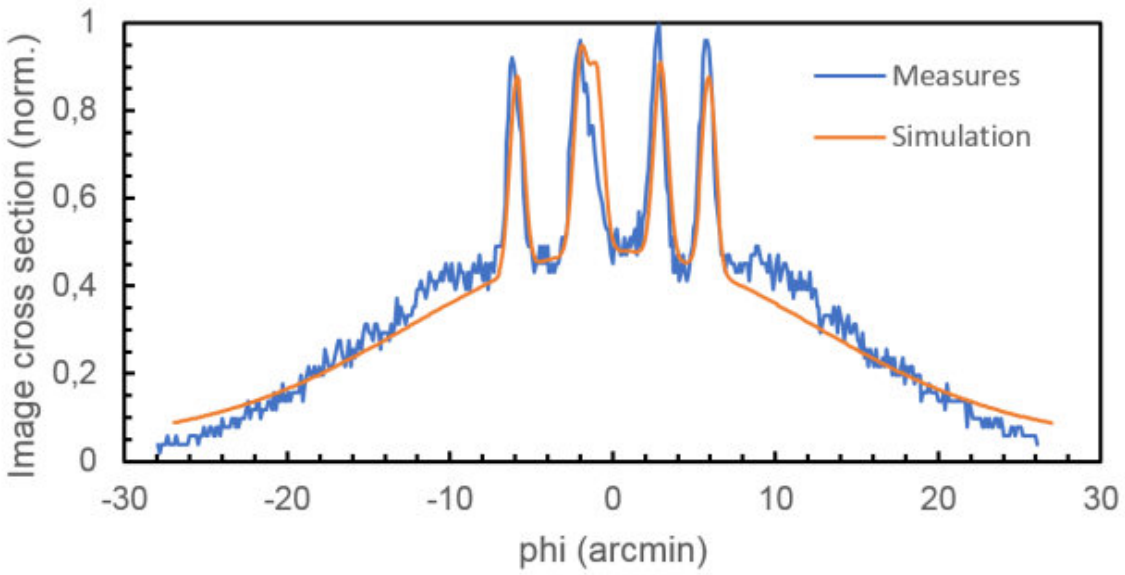

Figure IV.16. Comparison of the middle cross section of the measured and simulated images in the Quasi-Random pinhole distribution/EPD.

Figure IV.17 presents the comparison of the full aperture image with its diffraction limited simulation. Apparently, γ-parameter of our system is higher than theoretical diffraction limited due to aberrations of optical system. We can observe a halo of energy around the experimental image that is not present on the simulation. Although one cannot observe a gap between

measured pixels in the word “LETI”, one can slightly visually distinguish pixels in the simulation image (**Figure IV.17b**). We are here at the limit of the image resolution.

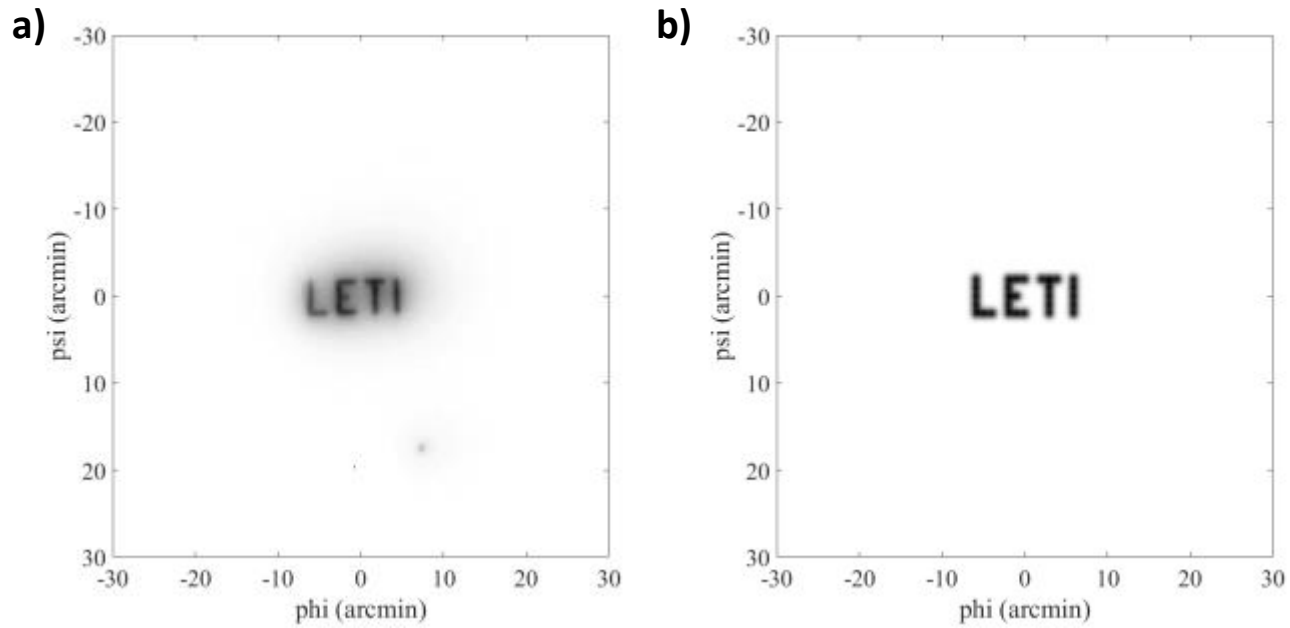

Figure IV.17. Diffraction limited LETI image : a) experimentally obtained, b) simulated with DG-model, $\gamma = 0.77$.

In **Figure IV.18** one can observe almost similar images of “LETI” word oversampling. The experimental image is slightly rotated counterclockwise around the center (**Figure IV.18a**). It’s explained by a small rotation of the DOE sample in its mount.

The simulation in **Figure IV.18b** shows the case of “LETI” word self-focusing with a periodic EPD located aligned with the x/y axis. We should have rotated the simulation to be more similar to the experimental result but our main objective is to recognize the whole image. We observe visually the predominance of the letter “E” due to the particular geometry of the word. The Gaussian envelope seems larger than the experimental one but this visual analysis is difficult.

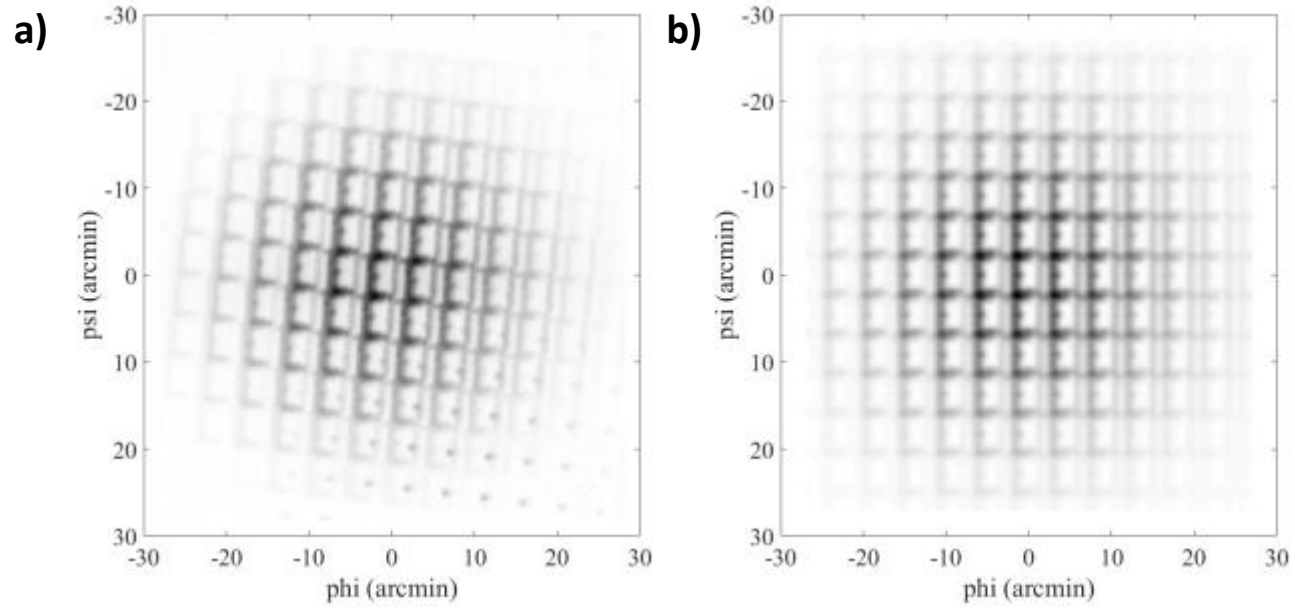

Figure IV.18. Self-focusing image formation of periodic distribution: a) experimental image, b) simulated image

In **Figure IV.19** one can see the comparison of experimental and simulated image of word "LETI" in the case of CRS distribution. As in the previous periodic case, these images differ by location of side ghosts. The nature of this deviation is also the same as previous: the slight rotation of the DOE sample.

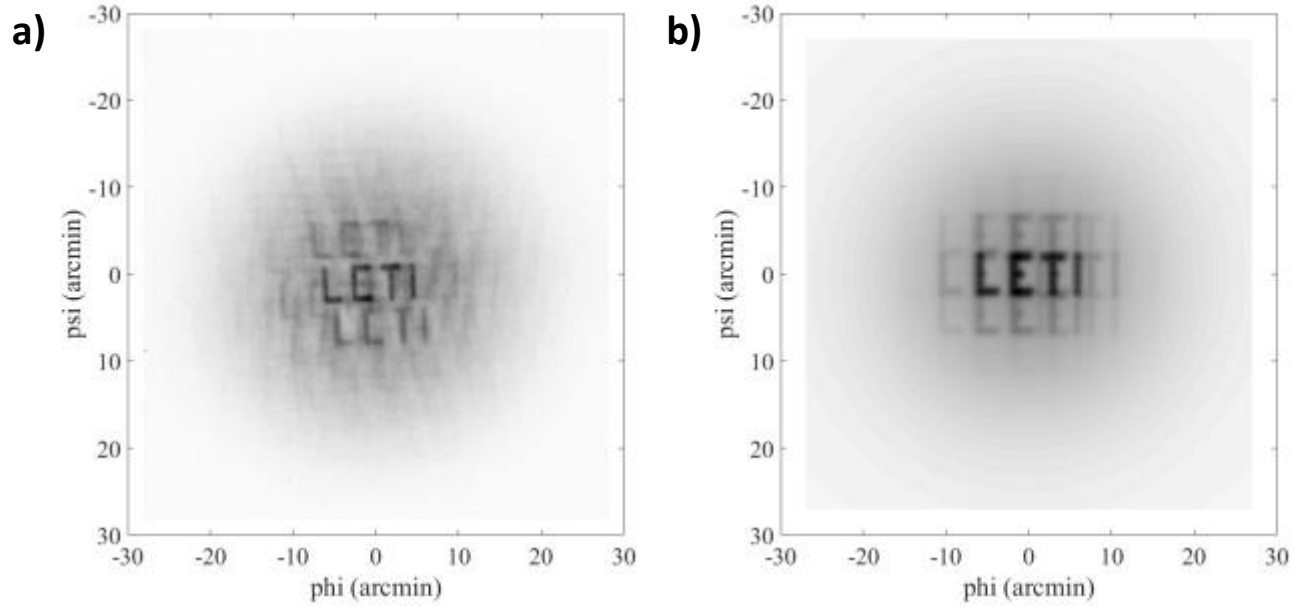

Figure IV.19. Self-focusing image formation of CRS distribution: a) experimental image, b) simulated image

4 Conclusion

In this chapter I presented our approach for unconventional image formation using self-focusing effect. I described Double-Gaussian model for image formation simulations and compared it with experimental results. This model is used in the last section to theoretically evaluate the behaviour of the concept as an image-forming device. Simulations are then compared to experimental measurements of a self-focused image obtained from an optical system that mimics the eye. I analysed self-focusing-image formation and introduced **γ-parameter** to evaluate quality of spel in addition to signal to noise ratio (SNR). For this analysis it is also of primary importance to consider the eye model, particularly in terms of extended sensing dynamic and non-uniform resolution. Specific diffusion behavior of the holographic part of the device also has to be considered for a rigorous analysis of the system performance.

The experimental results confirm the ability to produce an image through the self-focusing effect. The model of a double Gaussian intensity distribution is efficient to describe the imaging process on the retina. It allows for fast simulations as summations of the various spels that form the image.

The display concept we propose works with a set of different Emissive Point Distributions (EPDs) each associated with an image pixel. To be fully representative of the concept, each pixel of the word “LETI” should have been associated with a specific EPD. This configuration is not possible in the frame of this first experiment, as all the display pixels highlight a transmission aperture distribution. CEA is currently investigating the use of a holographic printer, to evaluate a configuration with different EPDs, for a closer-to-real-case application. Nevertheless, even if the aperture distribution is here still common to all the pixels, it anyway well describes the effect of image formation through self-focusing effect, to demonstrate its practical interest.

The main drawback of the device will concern the contrast of the retinal image and the presence of ghost images produced by limited random distributions. The EPDs that have been considered throughout this work are related to simple sinusoidal models, and more complex configurations are currently under investigations to improve the image quality, in the framework of another PhD work.

It is also worth mentioning the influence of the source bandwidth. In particular, the increase of the spectral bandwidth expands the speckle figure around the central peak and tends to increase the ratio between the energy of the spel and the energy of the noise. This aspect still requires an in-depth analysis. However, effects of wavelength and bandwidth have been described experimentally in the **Chapter III**.

The EPD parameters have been chosen in order to simplify the visual analysis. Other laboratory's works are focused on the parameters corresponding to our device with an emissive aperture diameter smaller than 10 µm and an entrance pupil diameter of about 6 mm. The three orders of magnitude difference between these two values make visual analysis difficult if one wants to evaluate on the same graphic the effect of the spel and of the whole surrounding noise.

Conclusion and Perspectives

AR technology is a dynamic domain strongly impacted by the physical limitations of the NED development. CEA-LETI proposed their prototype of such a device. This thesis was the pioneering steps in unconventional image projection prototyping. It was important for our laboratory because it was the starting point of an activity which aims to demonstrate the feasibility of an innovative concept. The main goal of the work was the **theoretical description and experimental validation of the self-focusing effect for the NED-prototype image formation.** The research activity was complicated by the need to start a subject that had not yet been initiated experimentally in the laboratory. The work was also made difficult by the complexity of our concept which implements advanced notions of relatively innovative image formation. I studied diffractive effects involved on the retinal image formation due to self-focusing effect. I analyzed in detail its **imaging performance**. I showed relation between **EPD** and their **spels**. I **evaluated quality of spel-formation**, **simulated self-focusing projection** of our concept and analyzed it with introduced a spel formation quality **γ-parameter**. I assembled an **experimental setup** to validate my theoretical results that I obtained with self-focusing simulation algorithm. I simulated **unconventional imaging** with **simplified spel-formation approach** called **Double-Gaussian (DG) model** and validated it experimentally with a setup. I described a **resolution/sharpness conflict** as a natural constraint for the display prototype. The main results were presented in several conferences:two posters OSA Imaging and Applied Optics Congress 2016 in Heidelberg [116] and 2017 in San-Francisco [118], an oral talk in SPIE Photonics Europe in 2018 [119]. My results contributed to the Optica article that describes general principle of the retinal display concept in 2018 [97]. Main experimental and simulation results of my work were published in Optics Express in 2019 [117].

Overall, the experimental validation of self-focusing effect paved the way for massive and detail research of our laboratory. The prototyping of NED involves a complex association of integrated photonics and holography. Basile Meynard designed and characterized photonic integrated

circuits (PICs) for the concept [95]. Kyllian Millard continued this research [105] and characterized diffraction and transparency to evaluate prototype performance [120].Matthias Colard studied activation elements for pixilated holograms [106], [121], [122] and investigated extraction architectures combining photonics integrated circuits and birefringent liquid crystals [123]. Fabien Rainouard investigated optimal addressing strategies using mathematical models [100], [101], [105].

Bibliography

[1] J. H. Kaas and P. Balaram, “Current research on the organization and function of the visual system in primates,” *Eye Brain*, vol. 6, pp. 1–4, 2014, doi: 10.2147/EB.S64016.

[2] F. Hutmacher, “Why Is There So Much More Research on Vision Than on Any Other Sensory Modality?,” *Front. Psychol.*, vol. 10, Oct. 2019, doi: 10.3389/fpsyg.2019.02246.

[3] R. M. Sapolsky, *Behave: The biology of humans at our best and worst*, Penguin Pr. New York, NY, 2017.

[4] M. Dvornik, *Learning with Limited Annotated Data for Visual Understanding*, Ph.D. diss. UGA, 2019.

[5] M. Billinghurst, A. Clark, and G. Lee, “A Survey of Augmented Reality,” *Found. Trends® Human–Computer Interact.*, vol. 8, no. 2–3, pp. 73–272, 2015, doi: 10.1561/1100000049.

[6] D. R. Berryman, “Augmented Reality: A Review,” *Med. Ref. Serv. Q.*, vol. 31, no. 2, pp. 212–218, Apr. 2012, doi: 10.1080/02763869.2012.670604.

[7] H. Hu *et al.*, “Application and Prospect of Mixed Reality Technology in Medical Field,” *Curr. Med. Sci.*, vol. 39, no. 1, pp. 1–6, Feb. 2019, doi: 10.1007/s11596-019-1992-8.

[8] A. Meola, F. Cutolo, M. Carbone, F. Cagnazzo, M. Ferrari, and V. Ferrari, “Augmented reality in neurosurgery: a systematic review,” *Neurosurg. Rev.*, vol. 40, no. 4, pp. 537–548, Oct. 2017, doi: 10.1007/s10143-016-0732-9.

[9] S. K. Bacca, Jorge; Baldiris, Silvia; Fabregat, Ramon; Graf, “Augmented Reality Trends in Education: A Systematic Review of Research and Applications,” *Educ. Technol. Soc.*, vol. 17, no. 4, pp. 133–149, 2014.

[10] P. Chen, X. Liu, W. Cheng, and R. Huang, “A review of using Augmented Reality in Education from 2011 to 2016,” in *Innovations in Smart Learning*, 2017, pp. 13–18.

[11] R. Palmarini, J. A. Erkoyuncu, R. Roy, and H. Torabmostaedi, “A systematic review of augmented reality applications in maintenance,” *Robot. Comput. Integr. Manuf.*, vol. 49, pp. 215–228, Feb. 2018, doi: 10.1016/j.rcim.2017.06.002.

[12] X. Li, W. Yi, H.-L. Chi, X. Wang, and A. P. C. Chan, “A critical review of virtual and augmented reality (VR/AR) applications in construction safety,” *Autom. Constr.*, vol. 86, pp. 150–162, Feb. 2018, doi: 10.1016/j.autcon.2017.11.003.

[13] F. Schwarz and W. Fastenmeier, “Augmented reality warnings in vehicles: Effects of modality and specificity on effectiveness,” *Accid. Anal. Prev.*, vol. 101, pp. 55–66, Apr. 2017, doi: 10.1016/j.aap.2017.01.019.

[14] J. Peddie, *Augmented Reality: Where We Will All Live*. Springer International Publishing, 2017.

[15] B. C. Kress and I. Chatterjee, “Waveguide combiners for mixed reality headsets: A nanophotonics design perspective,” *Nanophotonics*, vol. 10, no. 1. De Gruyter Open Ltd, pp. 41–74, Jan. 01, 2021, doi: 10.1515/nanoph-2020-0410.

[16] C. Martinez, “US 2015/0370.073 A1,” 2015.

[17] B. C. Kress, “Keys to the Ultimate MR Experience,” in *Kress Optical Architectures for Augmented-, Virtual-, and Mixed-Reality Headsets*, 2020, pp. 19–24.

[18] S. Mann, T. Furness, Y. Yuan, J. Iorio, and Z. Wang, “All Reality: Virtual, Augmented, Mixed (X), Mediated (X,Y), and Multimediated Reality,” Apr. 2018, [Online]. Available: http://arxiv.org/abs/1804.08386.

[19] P. Milgram, H. Takemura, A. Utsumi, and F. Kishino, “Augmented reality: a class of displays on the reality-virtuality continuum,” in *Telemanipulator and Telepresence Technologies*, Dec. 1995, vol. 2351, pp. 282–292, doi: 10.1117/12.197321.

[20] B. C. Kress, “Introduction,” in *Kress Optical Architectures for Augmented-, Virtual-, and Mixed-Reality Headsets*, 2020, pp. 1–4.

[21] B. C. Kress, “Opening Remarks,” in *SPIE AR, VR, MR Industry Talks 2022*, Mar. 2022, p. 70, doi: 10.1117/12.2632760.

[22] P. Balco, P. Bajzík, and K. Škovierová, “Virtual and Augmented Reality in Manufacturing Companies in Slovakia,” *Procedia Comput. Sci.*, vol. 201, pp. 313–320, 2022, doi: 10.1016/j.procs.2022.03.042.

[23] P. A. Sarvari, A. Ustundag, E. Cevikcan, I. Kaya, and S. Cebi, “Technology Roadmap for Industry 4.0,” 2018, pp. 95–103.

[24] G. Smithson, A., Boland, M., Kolo, K., Wheelwright, “VR & AR for Business (Enterprise) White Paper,” 2018.

[25] F. J. Fabozzi, F. J. Jones, and M. J. P. Anson, *The Handbook of Traditional and Alternative Investment Vehicles: Investment Characteristics and Strategies*. John Wiley & Sons, 2010.

[26] C. Chang, K. Bang, G. Wetzstein, B. Lee, and L. Gao, “Toward the next-generation VR/AR optics: a review of holographic near-eye displays from a human-centric perspective,” *Optica*, vol. 7, no. 11, p. 1563, Nov. 2020, doi: 10.1364/optica.406004.

[27] K. Peng, “Kura AR: Ultra High-performance AR Glasses and System,” in *SPIE AVR21 Industry Talks II*, Apr. 2021, p. 62, doi: 10.1117/12.2598237.

[28] B. C. Kress, “Invariants in HMD Optical Systems , and Strategies to Overcome Them,” in *Kress Optical Architectures for Augmented-, Virtual-, and Mixed-Reality Headsets*, 2020, pp. 77–88.

[29] F. W. Weymouth, “Visual Sensory Units and the Minimal Angle of Resolution*,” *Am. J. Ophthalmol.*, vol. 46, no. 1, pp. 102–113, Jul. 1958, doi: 10.1016/0002-9394(58)90042-4.

[30] D. Ren, T. Goldschwendt, Y. Chang, and T. Hollerer, “Evaluating wide-field-of-view

augmented reality with mixed reality simulation," in *2016 IEEE Virtual Reality (VR)*, Mar. 2016, pp. 93–102, doi: 10.1109/VR.2016.7504692.

[31] B. C. Kress, "Human Factors," in *Kress Optical Architectures for Augmented-, Virtual-, and Mixed-Reality Headsets*, vol. 1, 2020, pp. 25–36.

[32] O. Cakmakci and J. Rolland, "Head-Worn Displays: A Review," *J. Disp. Technol.*, vol. 2, no. 3, pp. 199–216, Sep. 2006, doi: 10.1109/JDT.2006.879846.

[33] D. Lanman and D. Luebke, "Near-eye light field displays," *ACM SIGGRAPH 2013 Emerg. Technol. SIGGRAPH 2013*, 2013, doi: 10.1145/2503368.2503379.

[34] N. A. Dodgson, "<title>Variation and extrema of human interpupillary distance</title>," May 2004, pp. 36–46, doi: 10.1117/12.529999.

[35] A. Maimone, A. Georgiou, and J. S. Kollin, "Holographic near-eye displays for virtual and augmented reality," *ACM Trans. Graph.*, 2017, doi: 10.1145/3072959.3073624.

[36] B. C. Kress, "Optical Specifications Driving AR / VR Architecture and Technology Choices," in *Kress Optical Architectures for Augmented-, Virtual-, and Mixed-Reality Headsets*, no. mm, 2020.

[37] M. Bass, *Handbook of Optics: Volume III - Vision and Vision Optics*, 3rd ed. /. New York: McGraw-Hill Education, 2010.

[38] K. Kiyokawa, "A Wide Field-of-view Head Mounted Projective Display using Hyperbolic Half-silvered Mirrors," in *2007 6th IEEE and ACM International Symposium on Mixed and Augmented Reality*, Nov. 2007, pp. 1–4, doi: 10.1109/ISMAR.2007.4538848.

[39] H. Nagahara, Y. Yagi, and M. Yachida, "Super Wide Field of View Head Mounted Display Using Catadioptrical Optics," *Presence Teleoperators Virtual Environ.*, vol. 15, no. 5, pp. 588–598, Oct. 2006, doi: 10.1162/pres.15.5.588.

[40] A. Sisodia *et al.*, "Advanced helmet mounted display (AHMD)," *Head- Helmet-Mounted Displays XII Des. Appl.*, vol. 6557, p. 65570N, 2007, doi: 10.1117/12.723765.

[41] A. Ilie, K.-L. Low, G. Welch, A. Lastra, H. Fuchs, and B. Cairns, "Combining Head-Mounted and Projector-Based Displays for Surgical Training," *Presence Teleoperators Virtual Environ.*, vol. 13, no. 2, pp. 128–145, Apr. 2004, doi: 10.1162/1054746041382375.

[42] H. Benko, E. Ofek, F. Zheng, and A. D. Wilson, "FoveAR: Combining an Optically See-Through Near-Eye Display with Projector-Based Spatial Augmented Reality," in *Proceedings of the 28th Annual ACM Symposium on User Interface Software & Technology*, Nov. 2015, pp. 129–135, doi: 10.1145/2807442.2807493.

[43] G. Kramida, "Resolving the Vergence-Accommodation Conflict in Head-Mounted Displays A review of problem assessments , potential solutions , and evaluation methods," no. October, 2016, doi: 10.1109/TVCG.2015.2473855.

[44] H. Hua, "Enabling focus cues in head-mounted displays," in *Optics InfoBase Conference*

Papers, 2017, vol. Part F44-3, no. 5, pp. 805–824, doi: 10.1364/3D.2017.JTu1F.2.

[45] B. Javidi *et al.*, "Roadmap on 3D integral imaging: sensing, processing, and display," *Opt. Express*, vol. 28, no. 22, p. 32266, 2020, doi: 10.1364/oe.402193.

[46] T. Ando and E. Shimizu, "Head-mounted display using holographic optical element," Feb. 2001, p. 1029804, doi: 10.1117/12.419789.

[47] M. von Waldkirch, P. Lukowicz, and G. Troster, "Defocusing simulations on a retinal scanning display for quasi accommodation-free viewing," *Opt. Express*, vol. 11, no. 24, p. 3220, Dec. 2003, doi: 10.1364/OE.11.003220.

[48] M. von Waldkirch, *Retinal Projection Displays for Accommodation-Insensitive Viewing*, Phd Thesis. 2005.

[49] A. Yuuki, K. Itoga, and T. Satake, "A new Maxwellian view display for trouble-free accommodation," *J. Soc. Inf. Disp.*, vol. 20, no. 10, pp. 581–588, Oct. 2012, doi: 10.1002/jsid.122.

[50] A. Maimone, D. Lanman, K. Rathinavel, K. Keller, D. Luebke, and H. Fuchs, "Pinlight displays: Wide field of view augmented reality eyeglasses using defocused point light sources," 2014, doi: 10.1145/2614066.2614080.

[51] S. C. McQuaide, E. J. Seibel, J. P. Kelly, B. T. Schowengerdt, and T. A. Furness, "A retinal scanning display system that produces multiple focal planes with a deformable membrane mirror," *Displays*, vol. 24, no. 2, pp. 65–72, Aug. 2003, doi: 10.1016/S0141-9382(03)00016-7.

[52] B. T. Schowengerdt, E. J. Seibel, J. P. Kelly, N. L. Silverman, and T. A. Furness III, "Binocular retinal scanning laser display with integrated focus cues for ocular accommodation," May 2003, p. 1, doi: 10.1117/12.474135.

[53] C. Jang, K. Bang, S. Moon, J. Kim, S. Lee, and B. Lee, "Retinal 3D: Augmented reality near-eye display via pupil-tracked light field projection on retina," *ACM Trans. Graph.*, vol. 36, no. 6, 2017, doi: 10.1145/3130800.3130889.

[54] K. Akeley, S. J. Watt, A. R. Girshick, and M. S. Banks, "A stereo display prototype with multiple focal distances," *ACM Trans. Graph.*, vol. 23, no. 3, pp. 804–813, Aug. 2004, doi: 10.1145/1015706.1015804.

[55] G. D. Love, D. M. Hoffman, P. J. W. Hands, J. Gao, A. K. Kirby, and M. S. Banks, "High-speed switchable lens enables the development of a volumetric stereoscopic display," *Opt. Express*, vol. 17, no. 18, p. 15716, Aug. 2009, doi: 10.1364/OE.17.015716.

[56] K. J. MacKenzie, D. M. Hoffman, and S. J. Watt, "Accommodation to multiple-focal-plane displays: Implications for improving stereoscopic displays and for accommodation control," *J. Vis.*, vol. 10, no. 8, pp. 22–22, Jul. 2010, doi: 10.1167/10.8.22.

[57] X. Hu and H. Hua, "High-resolution optical see-through multi-focal-plane head-mounted display using freeform optics," *Opt. Express*, vol. 22, no. 11, p. 13896, Jun. 2014, doi:

10.1364/OE.22.013896.

[58] P. Llull, N. Bedard, W. Wu, I. Tošić, K. Berkner, and N. Balram, “Design and optimization of a near-eye multifocal display system for augmented reality,” in *Imaging and Applied Optics 2015*, 2015, p. JTh3A.5, doi: 10.1364/AOMS.2015.JTh3A.5.

[59] N. Matsuda, A. Fix, and D. Lanman, “Focal surface displays,” *ACM Trans. Graph.*, vol. 36, no. 4, pp. 1–14, Jul. 2017, doi: 10.1145/3072959.3073590.

[60] S. Liu, Y. Li, P. Zhou, Q. Chen, and Y. Su, “Reverse-mode PSLC multi-plane optical see-through display for AR applications,” *Opt. Express*, vol. 26, no. 3, p. 3394, Feb. 2018, doi: 10.1364/OE.26.003394.

[61] K. Rathinavel, H. Wang, A. Blate, and H. Fuchs, “An Extended Depth-at-Field Volumetric Near-Eye Augmented Reality Display,” *IEEE Trans. Vis. Comput. Graph.*, vol. 24, no. 11, pp. 2857–2866, Nov. 2018, doi: 10.1109/TVCG.2018.2868570.

[62] Sheng Liu, Dewen Cheng, and Hong Hua, “An optical see-through head mounted display with addressable focal planes,” in *2008 7th IEEE/ACM International Symposium on Mixed and Augmented Reality*, Sep. 2008, pp. 33–42, doi: 10.1109/ISMAR.2008.4637321.

[63] R. Konrad, E. A. Cooper, and G. Wetzstein, “Novel Optical Configurations for Virtual Reality,” in *Proceedings of the 2016 CHI Conference on Human Factors in Computing Systems*, May 2016, pp. 1211–1220, doi: 10.1145/2858036.2858140.

[64] K. Aksit, W. Lopes, J. Kim, P. Shirley, and D. Luebke, “Near-eye varifocal augmented reality display using see-through screens,” *ACM Trans. Graph.*, vol. 36, no. 6, 2017, doi: 10.1145/3130800.3130892.

[65] D. Dunn *et al.*, “Wide Field of View Varifocal Near-Eye Display Using See-Through Deformable Membrane Mirrors,” *IEEE Trans. Vis. Comput. Graph.*, vol. 23, no. 4, pp. 1322–1331, 2017, doi: 10.1109/TVCG.2017.2657058.

[66] D. Dunn, Q. Dong, H. Fuchs, and P. Chakravarthula, “Mitigating vergence-accommodation conflict for near-eye displays via deformable beamsplitters,” p. 104, 2018, doi: 10.1117/12.2314664.

[67] D. Lanman and D. Luebke, “Near-eye light field displays,” *ACM Trans. Graph.*, vol. 32, no. 6, 2013, doi: 10.1145/2508363.2508366.

[68] A. Maimone and H. Fuchs, “Computational augmented reality eyeglasses,” *2013 IEEE Int. Symp. Mix. Augment. Reality, ISMAR 2013*, pp. 29–38, 2013, doi: 10.1109/ISMAR.2013.6671761.

[69] H. Hua and B. Javidi, “A 3D integral imaging optical see-through head-mounted display,” *Opt. Express*, vol. 22, no. 11, p. 13484, Jun. 2014, doi: 10.1364/OE.22.013484.

[70] F. C. Huang, K. Chen, and G. Wetzstein, “The light field stereoscope: Immersive computer graphics via factored near-eye light field displays with focus cues,” *ACM Trans. Graph.*, vol. 34, no. 4, 2015, doi: 10.1145/2766922.

[71] E. Moon, M. Kim, J. Roh, H. Kim, and J. Hahn, “Holographic head-mounted display with RGB light emitting diode light source,” *Opt. Express*, vol. 22, no. 6, p. 6526, Mar. 2014, doi: 10.1364/OE.22.006526.

[72] L. Shi, F. C. Huang, W. Lopes, W. Matusik, and D. Luebke, “Near-eye light field holographic rendering with spherical waves for wide field of view interactive 3D computer graphics,” *ACM Trans. Graph.*, vol. 36, no. 6, 2017, doi: 10.1145/3130800.3130832.

[73] L. J. Hornbeck, “Digital Light Processing for high-brightness high-resolution applications,” May 1997, pp. 27–40, doi: 10.1117/12.273880.

[74] J. S. Kollin and M. Tidwell, “Engineering Challenges of the Virtual Retinal Display Joel S. Kollin and Michael Tidwell Human Interface Technology Lab, Washington Technology Center University of Washington, Box 352142,” in *Novel Optical Systems Design and Optimization*, 1995, vol. 2537, [Online]. Available: https://doi.org/10.1117/12.216403.

[75] J. P. Rolland, M. W. Krueger, and A. Goon, “Multifocal planes head-mounted displays,” *Appl. Opt.*, vol. 39, no. 19, p. 3209, Jul. 2000, doi: 10.1364/AO.39.003209.

[76] O. Mercier *et al.*, “Fast gaze-contingent optimal decompositions for multifocal displays,” *ACM Trans. Graph.*, vol. 36, no. 6, pp. 1–15, Nov. 2017, doi: 10.1145/3130800.3130846.

[77] P. V. Johnson, J. A. Parnell, J. Kim, C. D. Saunter, M. S. Banks, and G. D. Love, “Assessing visual discomfort using dynamic lens and monovision displays,” in *Imaging and Applied Optics 2016*, 2016, p. TT4A.1, doi: 10.1364/3D.2016.TT4A.1.

[78] G.-A. Koulieris, B. Bui, M. S. Banks, and G. Drettakis, “Accommodation and comfort in head-mounted displays,” *ACM Trans. Graph.*, vol. 36, no. 4, pp. 1–11, Jul. 2017, doi: 10.1145/3072959.3073622.

[79] G. Lippmann, “Épreuves réversibles. Photographies integrates,” in *Comptes Rendus de 1’Académie des Sciences 146*, 1908, pp. 446–451.

[80] D. Fattal *et al.*, “A multi-directional backlight for a wide-angle, glasses-free three-dimensional display,” *Nature*, vol. 495, no. 7441, pp. 348–351, Mar. 2013, doi: 10.1038/nature11972.

[81] K. Akşit, J. Kautz, and D. Luebke, “Slim near-eye display using pinhole aperture arrays,” *Appl. Opt.*, vol. 54, no. 11, p. 3422, 2015, doi: 10.1364/ao.54.003422.

[82] G. Li, D. Lee, Y. Jeong, J. Cho, and B. Lee, “Holographic display for see-through augmented reality using mirror-lens holographic optical element,” *Opt. Lett.*, vol. 41, no. 11, p. 2486, Jun. 2016, doi: 10.1364/OL.41.002486.

[83] A. Maimone and J. Wang, “Holographic optics for thin and lightweight virtual reality,” *ACM Trans. Graph.*, vol. 39, no. 4, Aug. 2020, doi: 10.1145/3386569.3392416.

[84] H.-J. Yeom *et al.*, “3D holographic head mounted display using holographic optical elements with astigmatism aberration compensation,” *Opt. Express*, vol. 23, no. 25, p.

32025, Dec. 2015, doi: 10.1364/OE.23.032025.

[85] G. Kuo, L. Waller, R. Ng, and A. Maimone, “High resolution étendue expansion for holographic displays,” *ACM Trans. Graph.*, vol. 39, no. 4, 2020, doi: 10.1145/3386569.3392414.

[86] X. Xia, Y. Guan, A. State, P. Chakravarthula, T. J. Cham, and H. Fuchs, “Towards Eyeglass-style Holographic Near-eye Displays with Statically,” *Proc. - 2020 IEEE Int. Symp. Mix. Augment. Reality, ISMAR 2020*, pp. 312–319, 2020, doi: 10.1109/ISMAR50242.2020.00057.

[87] H. Mukawa *et al.*, “A full-color eyewear display using planar waveguides with reflection volume holograms,” *J. Soc. Inf. Disp.*, vol. 17, no. 3, p. 185, 2009, doi: 10.1889/JSID17.3.185.

[88] A. W. and B. A. Xiaoyu Miao, “Compact See-Through Display system,” US 2013/0021658.

[89] E. Hecht, *Optics*, 4th ed. Addison-Wesley, 2002.

[90] S. S. Hong, B. K. P. Horn, D. M. Freeman, and M. S. Mermelstein, “Lensless focusing with subwavelength resolution by direct synthesis of the angular spectrum,” *Appl. Phys. Lett.*, vol. 88, no. 26, p. 261107, Jun. 2006, doi: 10.1063/1.2213912.

[91] J. Sun *et al.*, “Large-Scale Silicon Photonic Circuits for Optical Phased Arrays,” vol. 20, no. 4, 2014.

[92] R. Fatemi, A. Khachaturian, and A. Hajimiri, “A Nonuniform Sparse 2-D Large-FOV Optical Phased Array With a Low-Power PWM Drive,” *IEEE J. Solid-State Circuits*, vol. 54, no. 5, pp. 1200–1215, 2019, doi: 10.1109/JSSC.2019.2896767.

[93] R. J. Mailloux, *Phased Array Antenna Handbook*, 2nd ed., vol. 19, no. 2. 2005.

[94] M. Bass, “OPTICAL GENERATION OF THE VISUAL STIMULUS,” in *Handbook of Optics: Volume III - Vision and Vision Optics*, Third., The McGraw-Hill Companies, Inc, 2010, p. 5.4.

[95] B. Meynard, “Dispositif de réalité augmentée basé sur des concepts de couplage guide d ’ onde / hologramme,” 2021.

[96] K. Millard, B. Meynard, D. Fowler, and C. Martinez, “Experimental validation of SiN photonic integrated waveguide arrays at λ = 532 nm for augmented reality display applications,” no. March, p. 59, 2021, doi: 10.1117/12.2582369.

[97] C. Martinez, V. Krotov, B. Meynard, and D. Fowler, “See-through holographic retinal projection display concept,” *Optica*, vol. 5, no. 10, p. 1200, Oct. 2018, doi: 10.1364/optica.5.001200.

[98] J. Chen, W. Cranton, and M. Fih, *Handbook of Visual Display Technology*. 2016.

[99] K. Blankenbach, A. Hudak, and M. Jentsch, “Part X Fundamentals of Driving: Direct Drive, Multiplex, and Passive Matrix,” in *Handbook of Visual Display Technology*, 2016, pp. 621–

649.

[100] F. Rainouard, C. Martinez, and B. Meynard, “Mathematical approach for the design of emissive points distributions for holographic retinal projection devices,” 2020, no. 2, p. JTu3F.17, doi: 10.1364/psc.2020.jtu3f.17.

[101] F. Rainouard, C. Martinez, B. Meynard, O. Haeberlé, and E. Oudet, “Improved mathematical model for a dense network of waveguides and electrodes design,” no. March, p. 55, 2021, doi: 10.1117/12.2578309.

[102] R. Baets and P. E. Lagasse, “Loss Calculation and Design of Arbitrarily Curved Integrated-Optic Waveguides.,” *J. Opt. Soc. Am.*, vol. 73, no. 2, pp. 177–182, 1983, doi: 10.1364/JOSA.73.000177.

[103] M. Born and E. Wolf, *Principles of Optics*, 7th ed. Cambridge University Press, 1999.

[104] B. E. A. Saleh and M. C. Teich, “Fundamentals of Photonics , 2nd Edition,” *Wiley*. 2007.

[105] F. Rainouard, M. Colard, O. Haeberlé, E. Oudet, and C. Martinez, “Optimal dense and random addressing design of emissive points in a retinal projection device,” no. May, p. 31, 2022, doi: 10.1117/12.2620243.

[106] M. COLARD, C. MARTINEZ, and O. HAEBERLÉ, “Switching behavior of pixelated holograms for retinal projection display,” 2020, no. Dmd, p. JTu3F.4, doi: 10.1364/psc.2020.jtu3f.4.

[107] C. Martinez, F. Laulagnet, F. Petit, P. Carre, P. Boulitreau, and N. Oving, “Computer Generated Holographic Dual Storage Concept for Long Term Data Archiving,” in *Imaging and Applied Optics 2014*, 2014, p. DTh2B.4, doi: 10.1364/DH.2014.DTh2B.4.

[108] Yoo, Geonwook and J. Kanicki, “A Maskless Laser-Write Lithography Processing of Thin-Film Transistors,” *Int. Disp. Reasearch Conf.*, p. 71, 2009.

[109] “DWL 2000/4000.” https://heidelberg-instruments.com/product/dwl-2000-4000-laser-lithography-systems/.

[110] T. Sandstrom, A. Bleeker, J. Hintersteiner, K. Troost, J. Freyer, and K. van der Mast, “OML: optical maskless lithography for economic design prototyping and small-volume production,” *Opt. Microlithogr. XVII*, vol. 5377, no. May 2004, p. 777, 2004, doi: 10.1117/12.537391.

[111] D. G. Smith, *Field Guide to Physical Optics*. SPIE, 2013.

[112] P. Johnson and R. Christy, “Optical constants of transition metals: Ti, V, Cr, Mn, Fe, Co, Ni, and Pd,” *Phys. Rev. B*, vol. 9, no. 12, pp. 5056–5070, Jun. 1974, doi: 10.1103/PhysRevB.9.5056.

[113] E. M. Wells-Gray, S. S. Choi, A. Bries, and N. Doble, “Variation in rod and cone density from the fovea to the mid-periphery in healthy human retinas using adaptive optics scanning laser ophthalmoscopy,” *Eye*, vol. 30, no. 8, pp. 1135–1143, Aug. 2016, doi: 10.1038/eye.2016.107.

[114] P. Willmott, *An Introduction to Synchrotron Radiation*. 2019.

[115] C. Martinez, V. Krotov, and D. Fowler, “Holographic Recording Setup for Integrated See-Through Near-Eye Display Evaluation,” in *Imaging and Applied Optics 2017 (3D, AIO, COSI, IS, MATH, pcAOP)*, 2017, p. JTu5A.36, doi: 10.1364/3D.2017.JTu5A.36.

[116] V. Krotov, C. Martinez, and O. Haeberlé, “Multiple beam diffractive setup for intraocular accommodation evaluation,” in *Optics InfoBase Conference Papers*, 2016, pp. 4–6, doi: 10.1364/DH.2016.JT3A.32.

[117] V. Krotov, C. Martinez, and O. Haeberlé, “Experimental validation of self-focusing image formation for retinal projection display,” *Opt. Express*, vol. 27, no. 15, p. 20632, Jul. 2019, doi: 10.1364/oe.27.020632.

[118] V. Krotov, C. Martinez, and O. Haeberlé, “Imaging performance Analysis of a lens-free near to eye display,” in *Optics InfoBase Conference Papers*, 2017, vol. Part F44-3, pp. 2016–2018, doi: 10.1364/3D.2017.JTu5A.5.

[119] C. Martinez, O. Haeberlé, and V. Krotov, “Experimental evaluation of self-focusing image formation in nonconventional near-eye display,” 2018, no. May 2018, p. 22, doi: 10.1117/12.2305930.

[120] K. Millard *et al.*, “Dense silicon-nitride PIC design and manufacturing on transparent substrate for a retinal projector evaluation,” in *Integrated Optics: Devices, Materials, and Technologies XXVI*, Mar. 2022, p. 35, doi: 10.1117/12.2605816.

[121] M. Colard, C. Martinez, and O. Haeberle, “Analysis of new optical addressing strategies for the optimization of retinal projection display,” no. March, p. 29, 2021, doi: 10.1117/12.2578282.

[122] C. Martinez, M.-C. Gentet, P. Legentil, Y. Lee, and M. Colard, “Pixelated holographic reflector recording for retinal projection devices,” no. March, p. 19, 2021, doi: 10.1117/12.2578221.

[123] M. Colard *et al.*, “Study of a liquid crystal impregnated diffraction grating for active waveguide addressing,” in *Emerging Liquid Crystal Technologies XVII*, Mar. 2022, p. 5, doi: 10.1117/12.2607475.

Research Article Vol. 5, No. 10 / October 2018 / Optica 1200

optica

See-through holographic retinal projection display concept

CHRISTOPHE MARTINEZ,[1,*] VLADIMIR KROTOV,[1,2] BASILE MEYNARD,[1] AND DAIVID FOWLER[3]

[1]Display Laboratory, Université Grenoble Alpes, CEA, LETI, DOPT/SNAP/LVE, 38054 Grenoble, France
[2]Laboratory MIPS EA2332, Université de Haute-Alsace IUT Mulhouse, 61 rue A. Camus, F-68093 Mulhouse Cedex, France
[3]Silicon Photonics Laboratory, Université Grenoble Alpes, CEA, LETI, DOPT/SNAP/LP2C, 38054 Grenoble, France
*Corresponding author: christophe.martinez@cea.fr

Received 2 May 2018; revised 16 August 2018; accepted 3 September 2018 (Doc. ID 330487); published 4 October 2018

The field of near-eye see-through devices has recently received significant media attention and financial investments. However, devices demonstrated to date suffer from significant practical limitations resulting from the conventional optics on which they are based. Potential manufacturers seek to surpass these limitations using novel optical schemes. In this paper, we propose such a potentially disruptive optical technology that may be used for this application. Conceptually, our optical scheme is situated at the interface of geometric incoherent refractive imaging and radiative coherent diffractive imaging. The generation of an image occurs as a result of data transmission through a two-dimensional network of optical waveguides that addresses a distribution of switchable holographic elements. The device acts as a wavefront generator, and the eye is the only optical system in which the image is formed. In the following we describe the device concept and characteristics, as well as the results of initial simulations.

OCIS codes: (090.2870) Holographic display; (130.3120) Integrated optics devices; (110.3175) Interferometric imaging; (110.5100) Phased-array imaging systems.

https://doi.org/10.1364/OPTICA.5.001200

1. INTRODUCTION

The fields of augmented reality (AR), mixed reality (MR), and virtual reality (VR) have recently been subject to renewed interest due to the large opportunities offered by smartphone applications. As an extension of this personal, everyday device, smart glasses could allow users to interact directly with their favorite applications without looking at and touching a screen. Such smart glasses could generate new applications in relation to the surrounding analogic world (AR) or to a digitalized world, real or virtual (MR or VR).

To support and anticipate customer expectations, smart glass concepts and devices have been proposed with the help of graphic designers. Impressive marketing material has created a discrepancy between customer perception and the actual technological capabilities of these devices. A thin, light, aesthetically pleasing pair of glasses with low power consumption showing a bright and contrasted image with high resolution and a wide field of view is unfortunately still a dream.

Most development on smart glasses for AR applications is based on a conventional imaging scheme built on the following steps:

(1) Sensing: perception of the surrounding environment by sensors [camera].
(2) Processing: computation of the digital image in relation to the surrounding field of view [micro-processor].
(3) Generating: a display creates the analogic image [micro-display].
(4) Transforming: the real image is transformed into a virtual image seen at large distance to be seen by the viewer [optical system].
(5) Propagating: the photons produced in the image creation process are brought to the eye [free-space or waveguide propagation].
(6) Combining: the virtual image is superimposed on to the surrounding scenery [semireflective, grating, or holographic elements].

These technological functions are difficult to integrate in a compact way, and most of the devices produced for AR applications are still closer to a smart helmet than to smart glasses.

Based on this analysis we have tried to find an unconventional design that takes as a starting point an idealized image of lightweight, discreet smart glasses that has been brought to the consumer and uses alternative technologies to achieve a thin, light, and bright see-through device.

We found that the difficulties encountered in the optical system design are due to the steps 3 to 6 that concern the manipulation of the image from the display to the eye. To circumvent these difficulties, an obvious solution is to emit directly the wavefronts related to the image in front of the eye. This led us to develop a new kind of display that mixes integrated photonics

Research Article Vol. 5, No. 10 / October 2018 / Optica 1201

and digitalized holography [1,2]: integrated photonics brings light from the light sources to the eye as a data transfer system, and holography transforms this data into wavefronts for the image to be projected on the retina.

In Section 2, we describe our display concept. In Section 3, we introduce the concept of the self-focusing effect allowing image formation on the retina. We then present the two main technological constituents of the system in Sections 4 and 5: the integrated photonics light distribution and the digitalized holography, respectively. Sections 6 and 7 describe estimates of the imaging properties and device power consumption, respectively.

2. GENERAL CONCEPT

Image formation into the eye is described in Fig. 1(a): our eye transforms a wavefront coming from the source image and focuses it on the retina. The coordinates of this image point on the retina are given by the angle of the wavefront $\vec{k_p}$ that reaches the cornea.

A conventional display emits light at the level of the image pixels. In a near-eye configuration the spherical wavefront $\vec{k_s}$ generated by each pixel has a curvature that the eye is not able to correct [Fig. 1(b)]. Even if a wavefront has the correct angular orientation, the resulting image point on the retina is blurred. In order to form the image, an optical system is introduced that reduces the curvature of the spherical wavefront and produces the planar wavefront $\vec{k_p}$ with the correct angular coordinates [Fig. 1(c)].

The use of an optical system increases the volume of the optical device and leads to severe constrains in terms of field of view and eye box. Lens-free near-eye displays are possible alternatives that allow generation of planar wavefronts without the use of a single-axis optical system. An example proposed by Maimone *et al.* uses an integral imaging concept [3]. An array of lenses or pinholes, creates a distribution of elementary planar wavefronts with the given angular coordinates $\vec{k_p^i}$ [Fig. 1(d)].

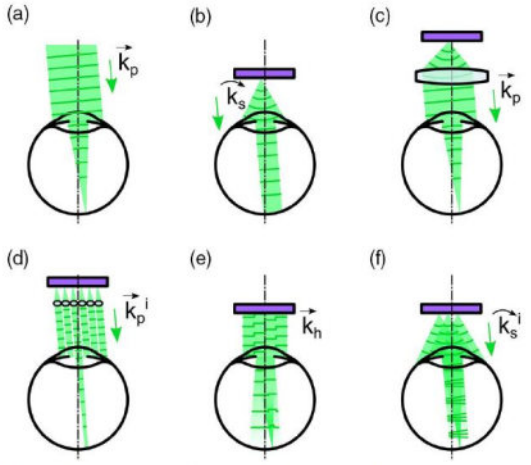

Fig. 1. Imaging into the eye: (a) imaging of a point at infinity, (b) near-eye display, (c) near-eye display with a single optical system, (d) near-eye display with multiple lens/pinholes aperture, (e) near-eye display based on a phased array, and (f) near to eye display according to the CEA concept.

The size of the optical system is decreased due to the reduction in size of the optics. The lens or pinhole array plays the role of a pupil expander and allows the eye box constraint to be relaxed. Another solution proposed by Sun *et al.* consists of a direct emission of a complex holographic wavefront $\vec{k_h}$. The device uses a phased array to generate the phase distribution of the image to be formed on the retina [Fig. 1(e)] [4].

These two solutions rely on a segmentation of the wavefront. The first case uses an incoherent wavefront angular distribution built on a conventional display. The second case uses a coherent wavefront phase distribution built on an unconventional integrated photonics device.

We propose an intermediate solution, situated at the interface of geometric incoherent refractive imaging and radiative coherent diffractive imaging. The wavefront distribution is built in a coherent way by the use of integrated photonics and holography. However, the resulting wavefront is not considered as a complex phase function calculated from the Fourier transform of the image. It is rather built as an incoherent geometrical combination of elementary coherent wavefronts resulting from the image angular point coordinates.

The principle of our concept is described in Fig. 1(f): the display emits a distribution of spherical wavefronts with a given angular orientation $\vec{k_s^i}$. These wavefronts are mutually coherent so that a planar wavefront is generated as described in the Huygens–Fresnel principle. The eye can then focus the generated planar wavefront on the retina with the specified angular coordinate. As the only optical system needed to form the image on the retina is the eye itself, we can imagine a highly integrated architecture as a basis of the display device.

An artist's view of our device is given in Fig. 2. Each emitting point that generates an elementary spherical wavefront is addressed by a waveguide that brings the image data to the outcoupling region. At this location a switchable outcoupling grating extracts the propagated light in the vicinity of a holographic element. This reflective elementary hologram can be considered as an orientated Bragg grating that defines the spherical wavefront angular orientation $\vec{k_s^{i,j}}$.

The surface of the glass is covered by a complex waveguide design that addresses the emissive points distribution (EPD). A distribution of outcoupling electrodes allows the activation/deactivation of the wavefront emission in order to refresh the image formation on the retina. Light that forms the image is

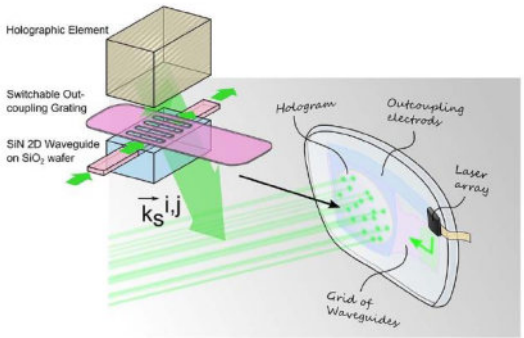

Fig. 2. Artist's view of the see-through display device with a zoom on one emissive point element.

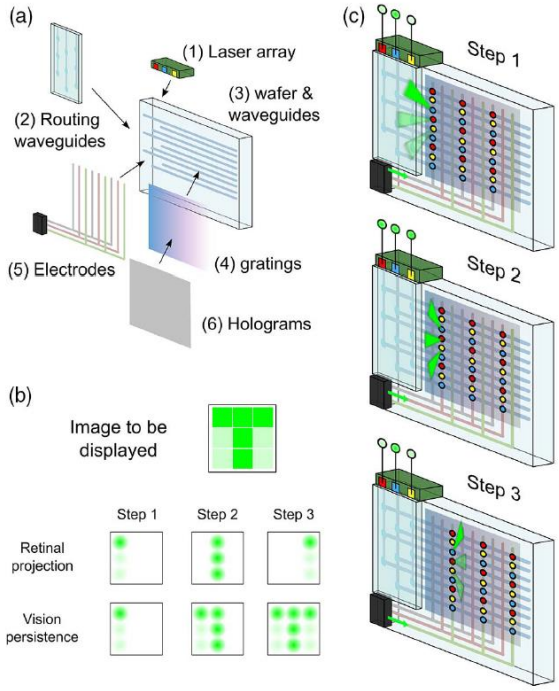

Fig. 3. Principle of the device operation. (a) Exploded view of the device concept, (b) description of the imaging process, and (c) the three steps necessary to project the 3 × 3 pixels image from an array of three laser sources and three electrodes.

generated by an amplitude modulated laser array that is coupled to the waveguide distribution.

If the device is made in transparent materials, with small refractive index variation, we can expect an overall transparency that could allow see-through applications.

The operating principle of the device is described in Fig. 3. In this simple case we show the rendering of a basic image of 3 × 3 pixels. In Fig. 3(a) we have an exploded view of the device: (1) the laser array produces the light used to form the image; (2) the routing waveguides direct the light to the waveguide output distribution; (3) the waveguide output distribution addresses the EPD; (4) the outcoupling grating layer extracts light from guided to free-space optics; (5) the electrode layer enables light extraction at specified locations; and (6) the hologram layer defines light direction and fixes the EPD phase coherence.

Our simple illustration shows the letter "T" scanning image formation in three steps [Figs. 3(b) and 3(c)]. In step 1 we emit three angular directions corresponding to three image pixels. The three lasers are emitting coherent light at three different output power levels at a green wavelength. In the drawing, each green laser is associated with a specific color (red, blue, yellow). A first set of electrodes (gray) is activated, and each light beam guided from the laser is emitted on the glass surface on an EPD of the corresponding color. We have represented only one emitted beam for each laser but each laser, i.e., each angular direction, is associated with a set of emissive holographic points in red, blue, or yellow. At this step the display projects on the retina three points corresponding to the three first angular directions [Fig. 3(b)].

In step 2 a second set of three image pixels is projected. Another set of amplitudes is given to the three laser sources, and another set of electrodes (pink) is activated in order to address the corresponding angular holographic EPD.

The same process is repeated in step 3 to project the last three image pixels. Vision persistence is used to recover the whole image [Fig. 3(b)].

This ambitious concept is based on technological steps that have to be investigated and demonstrated theoretically and practically. One of the first issues concerns the ability to form an image in relation to the Huygens–Fresnel principle. We describe this image-forming method as the self-focusing effect.

3. SELF-FOCUSING EFFECT

A. Theoretical Analysis

The self-focusing effect has already been introduced and demonstrated experimentally by Hong *et al.* in the field of optical data storage [5]. The authors have shown the ability to focus a laser from a combination of phase-adjusted laser beams. More recently this concept has found new applications in LIDAR devices [6].

In our case the self-focusing effect can be described considering both a Gaussian beam model and the multiple interferences phenomenon. Figure 4(a) shows the basic concept of multiple beams focusing into the eye. Our display is located at a distance Z_1 from the eye. The eye is described as a thin lens of focal length f. The retina is located at a distance f from the surface of the eye. The display emits a collection of Gaussian beams from the EPD $M_{u,v}$. The number of emissive points is limited by the entrance pupil Π with diameter D_p, as shown in Fig. 4(b).

The particularity of our concept is that each emitted beam of a given emissive point $M_{u,v}$ propagates according to the same wave vector $\overrightarrow{k_{i,j}}$. Geometrically, after passing through the eye lens, all

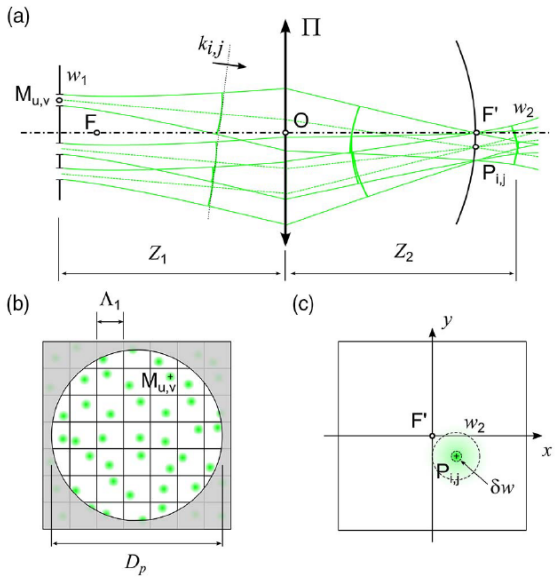

Fig. 4. (a) Principle of the Gaussian beams interferences from the display plane to the retina plane, (b) EPD on the display plane, and (c) the retinal plane.

these parallel beams converge to the same point $P_{i,j}$, located in the focal plane of the eye lens.

We take the approximation of an eye that can be described as a thin lens. According to the Gaussian beam formulation the waist w_1 located at $M_{u,v}$ is imaged by the eye at a distance Z_2 given by

$$Z_2 = f + \frac{f^2 \times \sigma}{\sigma^2 + \frac{\pi^2 w_1^4}{\lambda^2}}, \tag{1}$$

with $\sigma = Z_1 - f$.

Equation (1) shows that if the display is positioned close to the object focal plane of the eye ($\sigma = 0$), the distance Z_2 is close to the focal length. The wavefronts converging on the point $P_{i,j}$ are close to the waist location and can be considered as plane waves with wave vector $\overrightarrow{k_{u,v}}$. The behavior of the beam superposition at the point $P_{i,j}$ can then be described as multiple interfering planar waves. We describe the field of the planar wave as follows:

$$E_{u,v}(\vec{r}) = E_0 \times e^{-i\left(\overrightarrow{k_{u,v}}.\vec{r} + \varphi_{u,v}\right)}, \tag{2}$$

where E_0 is the beam amplitude and $\varphi_{u,v}$ a phase offset.

The interference energy function $I(\vec{r})$ is given by the sum of the beams passing through the eye lens pupil aperture Π as

$$I(\vec{r}) = \left[\sum_{u,v}^{M_{u,v}\in\Pi} E_{u,v}(\vec{r})\right] \times \left[\sum_{u',v'}^{M_{u',v'}\in\Pi} E_{u',v'}(\vec{r})\right]^*. \tag{3}$$

It comes from Eq. (2) that

$$I(\vec{r}) = \sum_{u,v}^{M_{u,v}\in\Pi} \sum_{u',v'}^{M_{u',v'}\in\Pi} E_0^2[\cos(\Delta\varphi_{u,v,u',v'}(\vec{r}))], \tag{4}$$

with the interphase function as

$$\Delta\varphi_{u,v,u',v'}(\vec{r}) = \left(\overrightarrow{k_{u,v}} - \overrightarrow{k_{u',v'}}\right) \cdot \vec{r} + \varphi_{u,v} - \varphi_{u',v'}. \tag{5}$$

If the EPD is coherently phase adjusted for a given angular direction $\overrightarrow{k_{i,j}}$, the relative phase shift verifies that

$$\varphi_{u,v} - \varphi_{u',v'} = \left(\overrightarrow{k_{u,v}} - \overrightarrow{k_{u',v'}}\right) \cdot \overrightarrow{r_{i,j}} \quad \forall\ u, v, u', v'. \tag{6}$$

The interference function can then be expressed as

$$I(\vec{r}) = \sum_{u,v}^{M_{u,v}\in\Pi} \sum_{u',v'}^{M_{u',v'}\in\Pi} E_0^2\left[\cos\left(\left(\overrightarrow{k_{u,v}} - \overrightarrow{k_{u',v'}}\right) \cdot \left(\vec{r} - \overrightarrow{r_{i,j}}\right)\right)\right]. \tag{7}$$

The energy figure on the retina shows a maxima on the point $P_{i,j}$ that is the focus point relative to the emissive distribution $M_{u,v}$.

As a demonstration and for a better understanding of the phenomena, we pursue our theoretical analysis with a 1D emissive distribution in the plane (y, z), as shown in Fig. 5. The wave vector $\overrightarrow{k_u}$ is expressed in relation to the propagation angle α_u as

$$\overrightarrow{k_u} = \frac{2\pi}{\lambda}\begin{vmatrix} \sin(\alpha_u) \\ \cos(\alpha_u) \end{vmatrix}. \tag{8}$$

We consider the center O of the thin lens as the phase reference. The phase offset of Eq. (2) is then expressed as

$$\varphi_u = y_u \times \sin(\gamma_i). \tag{9}$$

The coordinate y_u corresponds to the point N_u, projection of the emissive point M_u on the lens along the $\overrightarrow{k_i}$ direction, characterized by the angle γ_i.

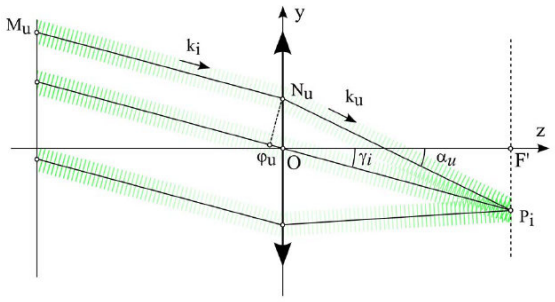

Fig. 5. Simple 2D geometrical representation for the calculation of the interphase function.

The interphase function at the focal plane $z = f$ becomes

$$\Delta\varphi_{u,u'}(y) = \frac{2\pi}{\lambda}[(\sin(\alpha_u) - \sin(\alpha_{u'})) \times y + (\cos(\alpha_u) - \cos(\alpha_{u'})) \times f - (y_u - y_{u'}) \times \sin(\gamma_i)]. \tag{10}$$

If we consider the paraxial approximation, Eq. (10) can be simplified as

$$\Delta\varphi_{u,u'}(y) = \frac{2\pi}{\lambda f}[(y_u - y_{u'}) \times (y - y_i)]. \tag{11}$$

We obtain an equation similar to Eq. (7) showing a maximum of energy at $y = y_i$.

Equation (11) also shows that if the emissive points are distributed in a square periodic grid of period Λ_1, that is, if $y_u = u \times \Lambda_1$, then other maximums of energy occur at the coordinates

$$y = y_i + m\frac{\lambda f}{\Lambda_1}, \tag{12}$$

with m as a relative integer.

Equation (12) is the expression of the order of diffraction of the periodic EPD structure. It shows that the self-focusing effect can effectively focalize the energy at the targeted location but also at periodic resonances. The self-focusing effect could lead to a sharp image on the retina but, as the image is duplicated, the periodic EPD forbids effective imaging. To avoid this resonance effect one solution is to introduce randomness in the EPD, as shown in Fig. 4(b).

B. Simulation

We have simulated the self-focusing effect using the double formalism of the Gaussian beam and multiple beam interference. Equation (3) is used in an iterative way to sum the contribution of an EPD.

We consider a Gaussian beam propagation to describe the amplitude of the beam from the display to the retina. The amplitude of the field in the plane of the display is given in a first approximation by a Gaussian function of waist w_1:

$$E_0(x, y, -Z_1) = \sqrt{\frac{2P_0}{\pi w_1^2}} \times e^{-\left(\frac{x^2+y^2}{w_1^2}\right)}. \tag{13}$$

We consider in this approximation that the waist is equal to the half of the emissive point diameter. The power emitted by each emissive zone is P_0.

Research Article Vol. 5, No. 10 / October 2018 / Optica 1204

The beam propagates from the display to the eye and forms an image of waist w_2 close to the retina:

$$w_2 = \frac{1}{n}\frac{f\lambda}{\pi w_1}, \tag{14}$$

where n is the refractive index inside the eye.

The simulated intensity function I_s is calculated from the summation of the planar beam given in Eq. (3) with a Gaussian beam intensity weighting:

$$I_S(x,y,f) = \frac{2P_0}{\pi w_2^2} \times e^{-2\left(\frac{x^2+y^2}{w_2^2}\right)} \times \frac{I(x,y,f)}{I(0,0,f)}. \tag{15}$$

As an illustration we choose the following simulation parameters that give a simple view of the phenomenon:

- emissive point radius $w_1 = 10$ μm,
- eye lens pupil aperture $D_p = 500$ μm,
- eye lens focal length $f = 23$ mm.

We evaluate the interference figure as a function of the period of the EPD and compare the periodic distribution with a semi-random distribution, defined by a "randomly periodic equation":

$$x_{u,v} = (u + \text{rnd}) \times \Lambda_1,$$
$$y_{u,v} = (v + \text{rnd}) \times \Lambda_1, \tag{16}$$

where rnd is a random number generation function $\in [-0.5{:}0.5]$.

Figure 6(a) shows the case $\Lambda_1 = 400$ μm: only one point of the EPD belongs to the eye lens aperture (red dot on the left figure). The resulting intensity function on the retina shows only the Gaussian beam contribution. The Gaussian beam of waist given by Eq. (14) represents the blurred signal on the retina.

In Fig. 6(b) the EPD period is decreased to 200 μm. We compare the periodic distribution with five points on the EPD (red dots) and the randomly periodic distribution that give four points on the EPD (green dots). The resulting intensity function of both cases shows the periodic self-focusing effect (on the center) and the random self-focusing effect (on the right). Figures 6(c) and 6(d) show the case with $\Lambda_1 = 100$ μm and $\Lambda_1 = 50$ μm.

The choice of the parameter D_p on Fig. 6 allows a good view of the phenomenon as the waist w_1 and w_2 are visible on the same graphic. In the case of periodic EPD, the interfering beams generate a focus that is replicated on a period Λ_2 given by Eq. (12). When randomness is introduce in the EPD, the diffraction orders vanish such that a speckle pattern is formed allowing a single focused spot of the image to be created. The size w_1 of the emissive zone fixes the size w_2 of the speckle distribution, the size D_p of the eye lens aperture Π fixes the radius of the focus δw that tends to the diffraction limit, given by

$$\delta w = 1.22\frac{\lambda f}{D_P}. \tag{17}$$

We compare in Fig. 7 the normalized intensity cross section of the self-focusing signal in the case of a random periodic EPD for $\Lambda_1 = 50$ μm and the theoretical Airy function [7] for a diffracting pupil aperture diameter D_p.

C. Display Analysis

We evaluate the efficiency of the self-focusing effect by measuring the signal-to-noise ratio (SNR) with parameters more consistent with our concept:

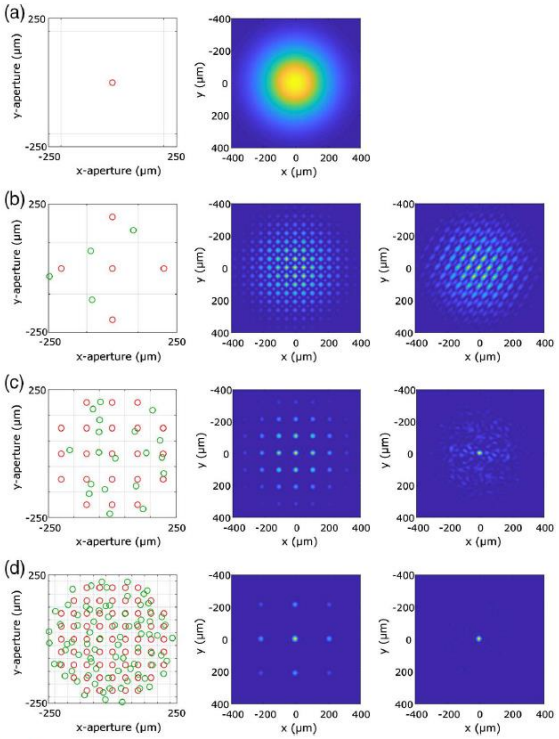

Fig. 6. Results of the self-focusing intensity signal for various EPD configurations. Figures on the left show the EPD in periodic (red dots) and randomly periodic (green dots) cases. Figures in the center and on the right give the intensity distributions for periodic and randomly periodic EPDs. (a) $\Lambda_1 = 400$ μm, (b) $\Lambda_1 = 200$ μm, (c) $\Lambda_1 = 100$ μm, and (d) $\Lambda_1 = 50$ μm.

- emissive point radius $w_1 = 2$ μm,
- eye lens pupil aperture $D_p = 4000$ μm,
- eye lens focal length $f = 23$ mm.

The SNR is calculated according to the equation

$$\text{SNR} = 10\log\left(\frac{I_S(0)}{\max\left(I_s(\vec{r})\right)_{r>\delta w}}\right). \tag{18}$$

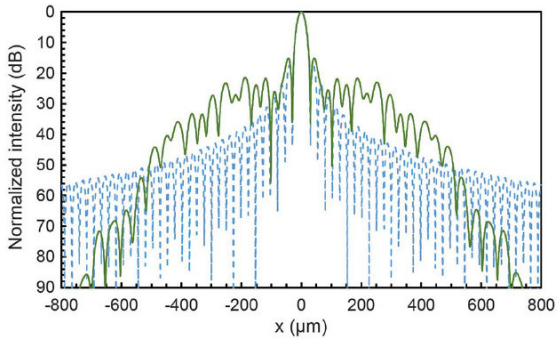

Fig. 7. Comparison between intensity cross section of the self-focusing signal in the random case of Fig. 6(d) (green curve) and the Airy function (dashed blue curve).

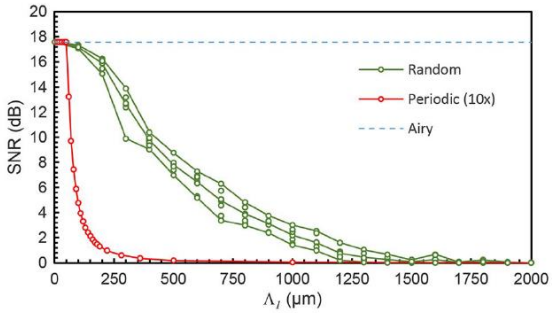

Fig. 8. Results of SNR simulations for six randomly periodic sequences of EPDs (green dots) and for a periodic EPD (red dots, extended by 10 in the abscissa axis). The minimum, mean, and maximum curves of the random sequences are presented by the solid line. The Airy diffraction-limited SNR is also given for comparison.

We compare the results of periodic and randomly periodic EPDs to the theoretical SNR limit given by the first Airy figure maximum [7]:

$$\mathrm{SNR}_{\mathrm{Airy}} = 10\log\left[\left(2\frac{J_1(5.136)}{5.136}\right)^2\right] = 17.57\ \mathrm{dB}. \quad (19)$$

The SNR results of the simulated EPD are shown in Fig. 8. For a better comparison, the periodic case is extended in the x axis ($\Lambda_1 \rightarrow 10 \times \Lambda_1$).

As expected, the results show that randomness greatly improves the SNR and that the choice of the EPD has a strong impact on the imaging process. For a given period Λ_1, the EPD random sequence choice can modify the SNR over several orders of magnitude.

As shown in Fig. 8, we need a small EPD period to increase the SNR and the image rendering. However, for a given emissive point size, the number of available EPDs decreases with the EPD period. As the number of available EPDs is directly related to the number of pixels of the projected image, we have to manage a compromise between the quality and the resolution of the image. This compromise differs from the standard space–bandwidth constraint (for a given display size, sharpness and resolution increase together) [8] and underlines the unconventional aspect of our approach: the increase of the image resolution reduces the image rendering.

The SNR is a first step in the characterization of the self-focusing process. The effective impact of the EPD choice on the image quality, related to resolution sharpness or contrast constraints, is currently under investigation and will be published soon.

The choice of the EPD configuration is also a research topic strongly related to technological constraints. The part of randomness introduced in the EPD must be consistent with the technological solutions used to bring light to the surface of the display. In particular, it must take into account the limitations induced by the waveguide design.

4. WAVEGUIDE DISTRIBUTION ARRAY

The technological principle considered to bring light to the EPD is described in Fig. 9. A waveguide distribution array guides the energy that fixes the amplitude of the emitted signal. The location

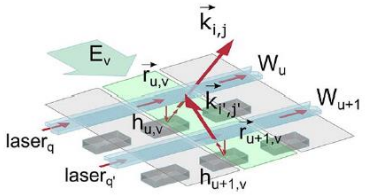

Fig. 9. Principle of signal extraction from the guided mode to free-space propagation.

$r_{u,v}$ of the emitted beam is determined by the intersection between the waveguide W_u and the outcoupling activation electrode E_v. These intersections between the activated electrodes and waveguides define the EPDs. As shown in Fig. 3, various EPDs are activated at the same time as different waveguides are addressed by different lasers.

Figure 9 shows two waveguides W_u and W_{u+1} addressed by two lasers q and q'. The electrode E_v extracts the two signals toward the holographic elements (hoels) $h_{u,v}$ and $h_{u+1,v}$. The two hoels, which belong to the EPD related to the two image point angular coordinates, reflect the signal in the given angular directions $\overrightarrow{k_{i,j}}$ and $\overrightarrow{k_{i',j'}}$.

The device parameters are given in Figs. 10 and 11. Waveguides are designed to propagate a single mode in the visible range, at the wavelength of the hologram maximum efficiency (around 532 nm for the polymer holographic material considered here). One promising technology for the manufacturing of waveguides operational in the visible range is silicon nitride [9]. Typical value parameters for the waveguide thickness e_g and width w_g at these wavelengths are 200 nm and 300 nm. The distance d_g between the waveguides is chosen to limit the coupling to neighboring waveguides. A typical value of 1.5 μm can be considered. The SiN waveguides can be manufactured on transparent glass and covered by a SiO_2 cladding of thickness e_c.

The outcoupling grating is etched in the cladding above the waveguide. A typical grating period for a wavelength of 532 nm is around 400 nm.

The design of the waveguide including coupling/propagation constraints due to the particular random EPD choice is currently investigated theoretically and experimentally.

The electrode that activates the outcoupling grating can be made of a liquid crystal layer as proposed by Buss *et al.* [10]. The width w_e of the electrode fixes the length of the outcoupling grating [Fig. 11(a)]. Typical lengths could be of the order of a few microns. The electrodes are separated by a distance d_e. The total number of emissive points N_{EP} for the whole EPD family is given by the parameters d_e and d_g in relation to the eye pupil aperture

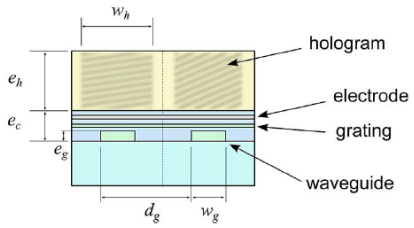

Fig. 10. Cross section of the device showing the wire waveguide and hoel design.

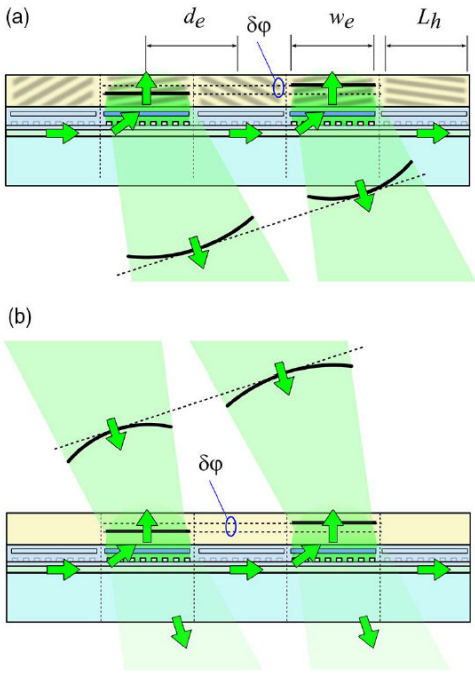

Fig. 11. (a) Lateral section of the device showing the coupling between the waveguide and the hoel. (b) The same figure during the recording process.

$$N_{EP} = \frac{\pi D_p^2}{4 d_e d_g}. \tag{20}$$

The hoels are recorded on a holographic material deposited over the cladding. The thickness e_h of the hologram layer depends on the expected characteristics of the hologram, typical values are about 10 μm to 20 μm. The width w_h of the hoel depends of the recording process and fixes the size w_1 of the EPD elements. The parameters w_h and d_g are not correlated and two neighboring hoels can overlap if $w_h > d_g$. The recording process of the hoel can be compared to the holographic recording process involved in the optical data storage through spatial shift multiplexing [11]. In contrast to holographic data storage, each hologram does not relate to complex data information but to a single angular reference. Each hoel can then be interpreted as an elementary directional Bragg element.

5. DIRECTIONAL HOLOGRAPHIC ELEMENTS

A. General Principle

The principle of light coupling from the waveguide to the hoel has been described in Fig. 9. Here, we present in Fig. 11 the principle of the phase adjustment that allows the efficiency of the interferences produced by the directional hoels.

Figures 11(a) shows a lateral section of the device. A guided wave is extracted in two locations and is reflected by two hoels belonging to the same EPD. The length L_h of the hoel is related to the size of the electrode but is not limited by the interelectrode distance d_e. As for the width of the hologram, its length can exceed d_e so that neighboring hoels can overlap. We have chosen in our simulation a hoel radius that defines a waist $w_1 = 2$ μm of the emitted beam.

As presented in Section 3.A, each EPD must be phase adjusted in order to self-focalize on a specific location of the retina plane. The phase shift $\delta\varphi$ between the extracted beams described in Fig. 11(a) is related to the optical path shift and to the grating distribution. It can hardly be controlled by a nanoscale resolution mask design over the whole device surface. Instead, phase adjustment is guaranteed by the intrinsic nanoscale resolution of the 3D hoel recording process.

The recording process is described in Fig. 11(b). The guided laser light plays the role of the reference beam, and a free-space beam coming from the same laser is used as the object beam. This beam is segmented in a multitude of elementary beams coming from a given angular direction. Activation of the outcoupling electrodes allows the creation of the interference pattern between the reference and the object beams that is recorded by the hoels for a given EPD.

When the reference beam is coupled from the waveguide, the conjugate object beam is generated in a reflective mode, as shown in Fig. 11(a). The phase adjustment is automatically recorded from the original object beam.

B. Recording Setup

In order to record the hoel distribution corresponding to a given EPD, a specific recording setup has to be built. Figure 12 shows the basic concept of the setup. An optical fiber is used to split a laser beam into a reference and an object beam. The object beam is collimated in a two lens optical system from a point source given by the first fiber extremity. First lens L1 makes the image of the fiber extremity on the object focal plane of the second lens L2. The position of this image fixes the angular direction $\overrightarrow{k_{i,j}}$ of the collimated beam. An aperture mask corresponding to the EPD is located on the image focal point of the first lens and is imaged on the hologram layer by the second lens L2. The object beam that impacts the hologram layer is collimated and phase adjusted in relation to the optical fiber position and is segmented in a collection of beam spots defined by the aperture mask. The image of the aperture mask is aligned with the EPD that is activated by the electrodes and by the optical coupling of the second optical fiber in a selected waveguide distribution (shown in the inset of Fig. 12).

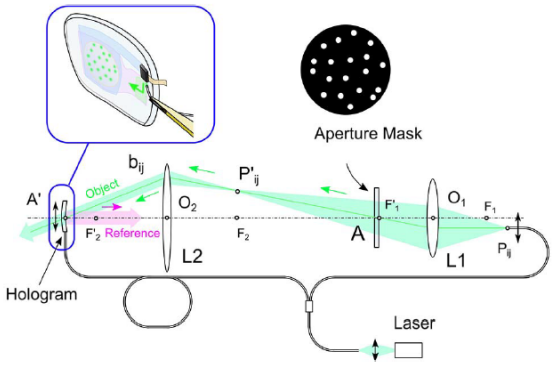

Fig. 12. Recording setup for the hoel distribution manufacturing.

The recording setup shown in Figs. 11(b) and 12 uses a collimated planar object wavefront. It is designed to form an image at infinity for each eye. The modification of the fiber longitudinal position in the recording setup allows the device to form an image at a fixed, given viewing distance by modifying the curvature of the object wavefront. In this case, the management of a symmetric off-axis pixels distribution for each eye should be used to reduce the vergence accomodation conflict (VAC) that usually limits conventional smart glasses approaches [12]. Our concept allows viewing an image in different plane locations with limited VAC. However, the manufacturing process fixes the plane location for a given display device.

Numerous questions remain regarding the technological process for the realization of the holographic device. Uncertainties around the recording duration, the material behavior, and the possible replication methods have to be investigated to validate a potential commercial interest to the concept. However, the impressive achievements of commercially feasible terabit-scale hologram storage and hologram printers imply a technical maturity that should be applicable to our approach [13,14].

We are currently evaluating the hoel recording process and have presented some initial design considerations [15]. A collaboration with a polymeric holographic material supplier has been initiated and should allow us to soon record the first hoel distribution in order to validate the self-focusing effect in an image-forming process.

6. IMAGING PROPERTIES

A. Sharpness/Contrast Issue

The sharpness of an image formed by an optical system is generally characterized by its modulation transfer function (MTF). This function gives the efficiency of the system for the rendering of a spatial frequency with a given contrast. The MTF can be calculated from the Fourier transform of the point spread function (PSF) that is the impulse intensity distribution.

Figure 7 shows the PSF of an optimal self-focusing effect (green curve). The calculation takes into account a perfect lens as the optical imaging system and the signal in its central part is very close to the theoretical diffraction limit. A more realistic approach needs to take into account the specific optical characteristics of the human eye and this poses some specific issues due to the human vision process.

The eye is a complex optical system that does not follow the diffraction theory. Unlike Eq. (17), aberrations in the pupil periphery degrade the MTF as the eye pupil diameter increases [16]. On the other hand, it has been shown that the coherent laser interfering imaging process can alleviate the pupil peripheral aberration distortion and improve the PSF [17]. The question of the effective sharpness of the self-focusing effect in the eye is an open question and needs to be studied with modern eye models and physiologic experiments in a coherent imaging process.

The measurement of the ANSI contrast is also a mean to evaluate the efficiency of an imaging system. It consists in forming a checkerboard image and measuring the ratio of intensity between the dark and white cells. In the case of self-focusing imaging, the PSF can be divided in two parts: a thin central spot and a large noisy speckle contribution, as shown in Fig. 7. This leads us to introduce a double Gaussian model in which the thin central Gaussian spot contributes to the imaging process and the large Gaussian noise reduces the overall contrast [18]. Improving the contrast requires limiting the impact of the large Gaussian contribution. This is done by an optimal EPD design that improves the energy ratio between the two Gaussian contributions and by limiting the number of pixels required to form an image (typically by the use of nonadjacent pixel distribution, as shown below). Characterization of our system in terms of ANSI contrast simulation will be described in an upcoming paper.

B. Resolution/Image Rendering Issue

As we have mentioned in Section 3, the rendering of the image is related to the number of emissive points n_{ep} of a given EPD. This number depends on the eye pupil aperture size and on the choice of the EPD function, in particular, the EPD period Λ_1:

$$n_{EP} = \frac{\pi D_p^2}{4\Lambda_1^2}. \tag{21}$$

The total number of pixels N_{pix} that can be projected on the retina is given by the number of EPDs:

$$N_{pix} = \frac{N_{EP}}{n_{EP}} = \frac{\Lambda_1^2}{d_e d_g}. \tag{22}$$

Equations (21) and (22) confirm that the image rendering given by n_{ep} and the image resolution given by N_{pix} are diverging parameters. Reducing Λ_1 increases the image quality but reduces the resolution.

We can define the following consistent parameters:

- electrode distance $d_e = 4$ µm,
- waveguide distance $d_g = 1.5$ µm,
- EPD period $\Lambda_1 = 600$ µm.

This gives a total number of pixels $N_{pix} = 93{,}750$ that corresponds to a conventional image resolution of about 300 × 300 pixels.

We have simulated in Fig. 13(a) a retinal projection on the basis of an image of 300 × 300 pixels projected on a 15° × 15° field of view (FOV). This artistic view highlights the differences between our retinal projection concept and a conventional display. The image is formed by separated luminous dots rather than by adjacent pixels. The angular distance that separates the dots is not necessarily uniform and can be adapted to the content for a given region of the FOV. In the example the text is projected on the retina with an angular distance between the dots of 3 arcmin and the value is increased to 4.5 arcmin for the GPS pictogram.

Equation (22) leads to low pixel number values. However, even if the resolution of the available image is low, the total number of pixels can be optimized by selecting specific regions in the FOV. This possibility underlines once again the unconventional approach of the concept: the perceived FOV, traditionally given by the product of the resolution with the angular pixel increment, can be increased here for a given constant total number of pixels. The dynamic image addressing for a specific region of the FOV and with a specific resolution is, however, fixed for a given device. Each EPD can be modulated in power emission but not in angular reference.

In terms of image rendering, the dotted aspect of the projected image can modify the perceived resolution and improve the result in comparison to a conventional display due to half-toning visual effects. As an illustration, we compare the same text coded with a resolution of 86 × 9 pixels for an unconventional dots pattern display [Fig. 13(b)] and for a conventional adjacent pixels display [Fig. 13(c)].

Research Article Vol. 5, No. 10 / October 2018 / Optica 1208

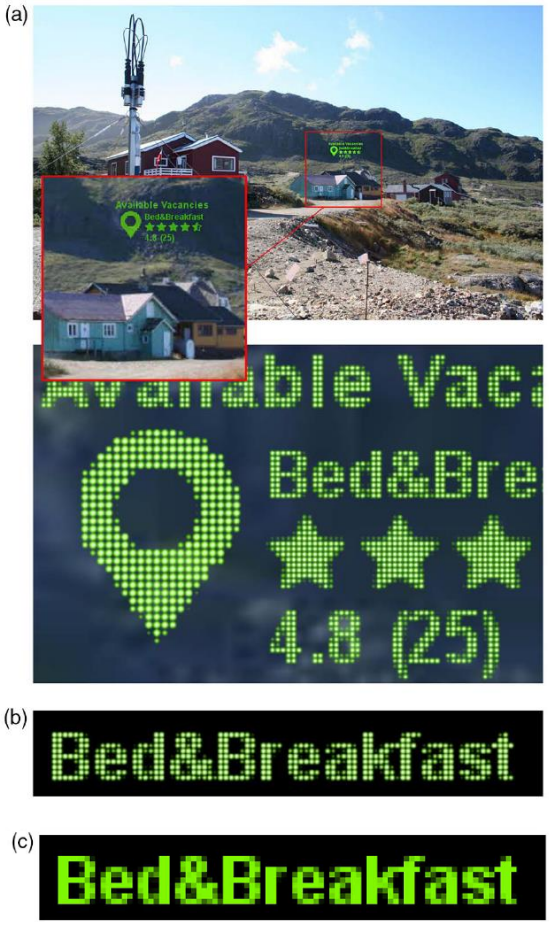

Fig. 13. (a) Simulation of an image projection according to our concept. The image on top shows an external view that covers a 100° wide FOV. The red square presents a projection zone of 15° × 15° with a resolution of 300 × 300 pixels. Over is a zoom on a section of the projected image, with an angular resolution of the text and the GPS pictogram of 3 arcmin and 4.5 arcmin, respectively, (b) detail of the text projected in a dots distribution, (c) detail of the same text resolution projected in an adjacent pixel distribution.

Imaging properties are currently investigated in an extensive study to evaluate the impact of the speckle noise. This theoretical study will be shown by experimental evaluations incorporating visual tests.

7. POWER CONSIDERATIONS

To conclude the technological review of our concept we focus on power considerations to check if the device is consistent with the objective of near-eye integration.

We target the projection of a full bright image on a circular FOV of 15°. The image is characterized by a brightness B. We calculate the power required in relation to the etendue of the eye [Fig. 14]:

$$\Phi_e = B \times \pi^2 \times \frac{D_p^2}{4} \times (\sin(\beta))^2. \tag{23}$$

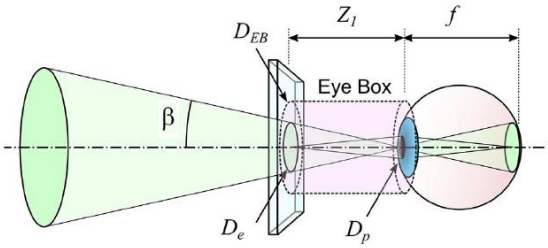

Fig. 14. Description of the etendue and eye box distribution in the intraretinal projection process.

The brightness required in AR applications is estimated to be in the range of 1000 Cd/m^2 to 10,000 Cd/m^2. From Eq. (23), the power that enters the eye is then between 1 μW and 10 μW.

The etendue of the beam seen from the eye is equal to the etendue of the eye seen from the beam. The emitting surface characterized by a diameter D_e is given by the relation

$$D_e = 2 \times Z_1 \times \sin(\beta). \tag{24}$$

One particular advantage of our concept is that the size of the emitting surface that fixes the eye box (EB) is not related to a single-axis optical system. The EB can then be extended by the design of a large waveguide and holographic elements distribution. We note D_{EB} as the diameter of the EB on the display.

The total amount of optical power emitted from the display is given by

$$\Phi_{e\_tot} = \left(\frac{D_{EB}}{D_e}\right)^2 \times \Phi_e. \tag{25}$$

Power considerations are mainly driven by the losses that occur in the device. Losses include coupling loss from the laser array to the waveguide distribution, propagation and outcoupling losses at the device surface, and the loss related to the holographic element efficiency. The losses related to the waveguide design at 532 nm and to the waveguide routing architecture are currently investigated and will be published soon. The efficiency of the holographic elements will depend on the photopolymer material and on the multiplexing strategy. Current performance for photopolymer holographic material shows diffraction efficiency that can reach 98% [14].

We note this overall device efficiency η_d, which leads to the optical power emitted by the lasers:

$$\Phi_{lasers} = \frac{\Phi_e}{\eta_d}. \tag{26}$$

If we suppose an overall device efficiency of 1% and consider a conversion efficiency of 10% for the lasers, it gives a required optical and electrical power of about 1 mW and 10 mW for a brightness of 1000 Cd/m^2 and 10,000 Cd/m^2. This result is an approximation, but it shows that there might be no strong limitation in terms of power consumption. Our low consumption value can be explained by the directivity of the EPD that optimizes the optical power in the direction of the eye and by the proximity between the eye and the display. This may be compared to evaluations of other see-through devices. LiKamWa *et al.* have shown that the LCOS display in the Google glass draws a power between 690 mW and 870 mW, depending on the sensed ambient brightness [19]. This power affects the use of the device and

is not optimized as it does not depend on the projected image. On the contrary, our emissive display adapts its power to the content so that for projecting text information as in the case of Fig. 13 an electric power far lower than 10 mW can be expected.

Another power consideration is that of eye safety. The image is projected on the retina in a scanning mode (Fig. 3) and must not lead to hazard for the retina. Laser safety is based on the calculation of the maximum permissible exposure (MPE) on the cornea. For the case of a collimated laser beam, a blinking reflex of 0.25 s, and a pupil diameter of 7 mm, MPE is about 6.4 J/m^2 [20] and corresponds to a laser power limit of about 1 mW.

In our display the exposure of the cornea for one pixel during 0.25 s is given by

$$E_{\text{pix}} = 4\frac{\Phi_e}{N_{\text{pix}} \times \pi \times D_p^2} \times (0.25\ \text{s}). \tag{27}$$

For the worst case $B = 10{,}000\ \text{Cd}/\text{m}^2$, Eq. (27) leads to an exposure value of $5.10^{-7}\ J/m^2$, which is far below the MPE limit.

The device seems to present no hazard for the eye. However, the case of the blinking reflex can be discussed and long-term laser exposure will have to be studied in more detail.

8. CONCLUSION

We present a complete theoretical overview of an unconventional imaging concept that could allow the development of a near-eye integrated transparent display. We describe the concept of the self-focusing effect that could allow image formation by retinal projection in a lens-free device configuration. The concept is simulated, and first results on evaluation characteristics such as the focus SNR give first insight on the device feature. The waveguide design and hoel concept are introduced, and we give some first perspectives on image rendering, device manufacturability, and power consumption.

Initial limitations are identified in terms of image rendering and commercial implementation. Image resolution is constrained by the waveguide integration and self-focusing efficiency. The use of holographic elements limits the projection to a monochromatic image, and a fast holographic recording process has yet to be demonstrated. These limitations can be balanced by the new opportunities opened by the unconventional imaging approach. In particular, the ability to adapt locally the resolution of the image inside a discontinuous field of view can open interesting applications.

More generally, this research can be seen as a fundamental reflection on the new opportunities for retinal projection that are opened by recent technological achievements in integrated photonics and holography. As our laboratory is strongly involved in conventional microdisplay design and manufacturing for AR/VR/MR applications [21], such investigations may anticipate potential technological evolutions.

Acknowledgment. We thank Pr. Haeberle from Laboratoire MIPS of Université de Haute-Alsace for fruitful discussions on diffraction and holographic issues.

REFERENCES

1. C. Martinez, "Image projection device," U.S. patent 2015/0370073 A1 (December 24, 2015).
2. C. Martinez, V. Krotov, D. Fowler, and O. Haeberle, "Lens-free near-eye intraocular projection display, concept and first evaluation," in *Imaging and Applied Optics*, OSA Technical Digest (Optical Society of America, 2016), paper CW1C.5.
3. A. Maimone, D. Lanman, K. Rathinavel, K. Keller, D. Luebke, and H. Fuchs, "Pinlight displays: wide field of view augmented reality eyeglasses using defocused point light sources," ACM Trans. Graph. **33**, 89 (2014).
4. J. Sun, E. Timurdogan, A. Yaacobi, E. Shah Hosseini, and M. R. Watts, "Large-scale nanophotonic phased array," Nature **493**, 195–199 (2013).
5. S. S. Hong, B. K. Horn, D. M. Freeman, and M. S. Mermelstein, "Lensless focusing with subwavelength resolution by direct synthesis of the angular spectrum," Appl. Phys. Lett. **88**, 261107 (2006).
6. M. Heck, "Highly integrated optical phased arrays: photonic integrated circuits for optical beam shaping and beam steering," Nanophotonics **6**, 93–107 (2017).
7. M. Born and E. Wolf, *Principle of Optics*, 7th ed. (Cambridge University, 1999).
8. A. W. Lohmann, R. G. Dorsch, D. Mendlovic, Z. Zalevsky, and C. Ferreira, "Space-bandwidth product of optical signals and systems," J. Opt. Soc. Am. A **13**, 470–473 (1996).
9. A. Z. Subramanian, P. Neutens, A. Dhakal, R. Jansen, T. Claes, X. Rottenberg, F. Peyskens, S. Selvaraja, P. Helin, B. Du Bois, K. Leyssens, S. Severi, P. Deshpande, R. Baets, and P. Van Dorpe, "Low-loss singlemode PECVD silicon nitride photonic wire waveguides for 532–900 nm wavelength window fabricated within a CMOS pilot line," IEEE Photon. J. **5**, 2202809 (2013). https://doi.org/10.1364/JOSAA.13.000470
10. T. Buß, C. L. C. Smith, and A. Kristensen, "Electrically modulated transparent liquid crystal-optical grating projection," Opt. Express **21**, 1820–1829 (2013).
11. G. Barbastathis, M. Levene, and D. Psaltis, "Shift multiplexing with spherical reference waves," Appl. Opt. **35**, 2403–2417 (1996).
12. G. Wetzstein, "Light field, focus-tunable, and monovision near-eye displays," SID Symp. Dig. Tech. Pap. **47**, 358–360 (2016).
13. L. Hesselink, S. S. Orlov, and M. C. Bashaw, "Holographic data storage systems," Proc. IEEE **92**, 1231–1280 (2004).
14. H. Bjelkhagen and D. Brotherton-Ratcliffe, *Ultra-Realistic Imaging, Advanced Techniques in Analogue and Digital Colour Holography* (CRC Press, 2013).
15. C. Martinez, V. Krotov, and D. Fowler, "Holographic recording setup for integrated see-through near-eye display evaluation," in *Imaging and Applied Optics*, OSA Technical Digest (Optical Society of America, 2017), paper JTu5A.36.
16. F. W. Campbell and R. W. Gubisch, "Optical quality of the human eye," J. Physiol. **186**, 558–578 (1966).
17. B. A. Wandell, *Foundations of Vision* (Sinaur Associates, 1995), p. 54.
18. V. Krotov, C. Martinez, and O. Haeberlé, "Imaging performance analysis of a lens-free near to eye display," in *Imaging and Applied Optics*, OSA Technical Digest (Optical Society of America, 2017), paper JTu5A.5.
19. R. LiKamWa, Z. Wang, A. Carroll, F. X. Lin, and L. Zhong, "Draining our glass: an energy and heat characterization of Google Glass," in *5th Asia-Pacific Workshop on Systems (APSYS)* (2014).
20. F. C. Delori, R. H. Webb, and D. H. Sliney, "Maximum permissible exposures for ocular safety (ANSI 2000), with emphasis on ophthalmic devices," J. Opt. Soc. Am. A **24**, 1250–1265 (2007).
21. F. Templier, L. Dupré, S. Tirano, M. Marra, V. Verney, F. Olivier, B. Aventurier, D. Sarrasin, F. Marion, T. Catelain, F. Berger, L. Mathieu, B. Dupont, and P. Gamarra, "75-1: Invited paper: GaN-based emissive microdisplays: a very promising technology for compact, ultra-high brightness display systems," SID Symp. Dig. Tech. Pap. **47**, 1013–1016 (2016).

Research Article | Vol. 27, No. 15 | 22 Jul 2019 | OPTICS EXPRESS 20632
Optics EXPRESS

Experimental validation of self-focusing image formation for retinal projection display

VLADIMIR KROTOV,[1,2] CHRISTOPHE MARTINEZ,[1,*] AND OLIVIER HAEBERLÉ[2]

[1]*Photonic System Laboratory, Univ. Grenoble Alpes, CEA, LETI, DOPT/SISP/LASP, 38054 Grenoble, France*
[2]*Institut de Recherche en Informatique, Mathématiques, Automatique et Signal (IRIMAS EA7499), Université de Haute-Alsace, IUT Mulhouse, 61 rue A. Camus, F-68093 Mulhouse Cedex, France*
**christophe.martinez@cea.fr*

Abstract: The augmented reality (AR) industry requires both aesthetic designs and high performances of AR devices. This complex dilemma challenges R&D groups from all over the world to improve existing systems or propose new, breakthrough designs. The unconventional concept of direct retinal projection display may be one. It is based on see-through holographic retinal projection, with the image being formed via the so-called self-focusing effect. In this paper, we describe an experimental validation of this self-focusing effect and introduce a possible approach of self-focusing performance evaluation. Experimental image formation capability is demonstrated and compared with simulation results. Main present limitations of the concept are discussed, such as pixel addressing design and image resolution/sharpness conflict.

1. Introduction

Augmented reality (AR) comes smoothly but steadily into our daily life. There are a lot of applications for AR [1,2], in very diverse domains such as medicine and surgery, education construction safety, or maintenance, and numerous others [3–8]. Many scientific groups are in the process of creating their own smart glasses devices [9,10]. In this field, the need to overlay digital information to the surrounding real world usually requires the use of micro-displays. These devices, in turn, require complex optical systems to provide a comfortable vision. Furthermore, the formation of the virtual image of the screen by the device is accompanied by constraints related to the management of pupils that limit the viewing angle and the positioning latitude of the eye while leading to bulky systems.

Bernard Kress and Thad Starner [11] described a wide range of different types of head-mounted displays (HMD). Most of them use conventional approaches for image formation based on the use of a micro-display and an optical system. The CEA proposed in 2014 an original concept of image projection that combines holography, integrated photonics and free space optics [12]. The concept aims at projecting an image into the observer's eye, onto the retina, without any lens. Convergence is provided by the eye through a phenomenon that we describe as self-focusing. This unconventional approach was explained recently for a concept of retinal projection display [13].

The concept is based on the design of an emissive screen close to the eye, where the emission points are duplicated so as to form the illusion of a plane wavefront. This is the case of Fig. 1(a). Thanks to the self-focusing effect, the multiple beams emitted from the display focalize onto the retina without any lens between the emission surface and the eye. The resulting focalized spot corresponds to one Emissive Point Distribution (EPD). An image, composed of several spots, requires a respective number of EPDs, which means that the surface of the display is covered by various EPDs to be able to form an image. Every EPD, in turn, consists in emissive points that are activated simultaneously and coherently for a given EPD, and designed to generate a directive spherical wave front with main wave vector $\vec{k}_s$.

#366745 https://doi.org/10.1364/OE.27.020632
Journal © 2019 Received 6 May 2019; revised 3 Jun 2019; accepted 3 Jun 2019; published 10 Jul 2019

Research Article | Vol. 27, No. 15 | 22 Jul 2019 | OPTICS EXPRESS 20633
Optics EXPRESS

As the wavefronts emitted from every point are phase adjusted for a given EPD and angularly orientated, they produce a resulting planar wavefront of wave vector $\vec{k}_p$. Through multiple interferences the spherical wavefronts focalize the beams onto the retina due to self-focusing effect through the eye pupil.

Self-focusing effect has already been demonstrated experimentally for data storage applications [14]. The use of a distribution of small apertures that approximates the behavior of a large, continuous aperture has also been demonstrated experimentally for astronomical applications [15–17]. However, the unconventional aspect of this approach for display applications opens questions about the perception of the so-formed images on the retina. Theoretical part was discussed previously [13], and we now experimentally investigate the capability of an unconventional image formation directly onto the retina using a device that simulates the self-focusing display concept as shown in Fig. 1(b). A planar wavefront with a given angular direction of wave vector $\vec{k}_p$ passes through a transmission device consisting of a distribution of apertures in an opaque metallic layer. The device simulates a distribution of emitters that generate coherent, phase-adjusted spherical wavefronts $\vec{k}_s$ with main wave vector direction $\vec{k}_p$.

The pinhole distribution represents the EPD and the device is placed in front of an optical system that mimics the eye.

In this article, we present first experimental results of unconventional image formation for the concept of retinal projection display developed by our laboratory. Section 2 presents the choice of the EPD and the mathematical development used to evaluate the randomness of the distributions. The third section describes the experimental validation of the self-focusing effect. Various EPDs are evaluated and a double Gaussian model is introduced to describe the signal formed by a central peak and a surrounding noise. This model is used in the last section to theoretically evaluate the behavior of the concept as an image-forming device. Simulations optical system that mimics the eye.

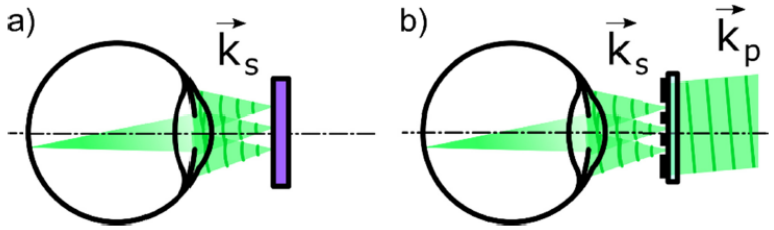

Fig. 1. Self-focusing image formation: (a) concept of near to eye display where a distribution of spherical wavefronts is emitted and produces the illusion of a plane wavefront that the eye lens focuses on the retina; (b) our validation setup: a laser beam passes through a transmission device consisting of a distribution of pinholes in an opaque metallic layer.

2. Emissive points distribution for self-focusing

The EPD design plays a dominant role for self-focusing, therefore the best distribution to implement must be found. We introduce some possible solutions and discuss their advantages and drawbacks. As previously shown [13], the best theoretical EPD for image formation is a random distribution. However, such a solution represents a technological challenge for the device manufacturing and the EPD addressing.

On the opposite, the easiest solution for the device manufacturing and addressing is a periodic EPD, but this solution is not acceptable from the image formation point of view. Hence, a compromise is to be found, such as a quasi-random distribution.

We introduce the Emissive Unit Cell (EUC) to refer to the elementary building block of the display. EUC is a region with sizes Λ_1 and Λ_2, composed by one emissive point from each

Research Article | Vol. 27, No. 15 | 22 Jul 2019 | OPTICS EXPRESS 20634
Optics EXPRESS

EPD. As described in [13], each emissive point corresponds to the intersection of a waveguide and an electrode. To provide the interference phenomenon, each EPD is addressed by a single laser. Image formation is then conceived in a scanning mode with a frequency that depends on the number of lasers used to project the image. It comes that each EUC will be addressed by several lasers n_{laser} and electrodes n_{elect} that fixes the number of the pixels N of the projected image:

$$N = n_{elect} n_{laser} \tag{1}$$

The size of the EUC is then given by the distances between rows of waveguides d_g and between columns of electrodes d_e :

$$\begin{aligned} \Lambda_1 &= n_{elect} d_e \\ \Lambda_2 &= n_{laser} d_g \end{aligned} \tag{2}$$

A simple way to solve the addressing problem is to create a 2D grid of periodically-distributed, straight electrodes. The coordinates of the EPD $x_{i,j}$ and $y_{i,j}$ are then given by the equation:

$$\begin{aligned} x_{i,j} &= \Lambda_1 i \\ y_{i,j} &= \Lambda_2 j \end{aligned} \tag{3}$$

Another solution for the EPD is to define a quasi-random distribution inside the EUC:

$$\begin{aligned} x_{i,j} &= \Lambda_1 \left(i + rnd \right) \\ y_{i,j} &= \Lambda_2 \left(j + rnd \right) \end{aligned} \tag{4}$$

Where rnd is a random number, with $rnd \in [0:1]$.

This solution is theoretically interesting but is hard to implement in practice because of an intersection distribution between a waveguide and an electrode trajectory function. To generalize the addressing problem, we define these two trajectory functions as $f_e(x,y)$ and $f_g(x,y)$. Solving the EPD design problem then requires solving the intersection equation between a distribution of waveguide and electrode function.

With respect to Eqs. (3) and (4), this can be done in two ways. First by keeping a periodic distribution:

$$\left(x_{i,j}, y_{i,j} \right) = f_e \left(x + \Lambda_1 i, y \right) \cap f_g \left(x, y + \Lambda_2 j \right) \tag{5}$$

Secondly by introducing a random access addressing:

$$\left(x_{i,j}, y_{i,j} \right) = f_e \left(x + \Lambda_1 \left(i + rnd \right), y \right) \cap f_g \left(x, y + \Lambda_2 \left(j + rnd \right) \right) \tag{6}$$

To facilitate the determination of the intersections between f_e and f_g we choose to describe these functions as the trajectory of a moving particle. The location $\vec{r}(x, y)$ of the particle is given by the time varying relation:

$$f: \quad \vec{r}\left(t + \delta t \right) = \vec{r}\left(t \right) + \vec{V}\left(t \right) \delta t \tag{7}$$

The velocity function $\vec{V}(t)$ that fixes the trajectory is defined by a time varying amplitude and direction:

$$\vec{V}\left(t \right) = \begin{bmatrix} v_0\left(t \right) \cos\left(\alpha\left(t \right) \right) \\ v_0\left(t \right) \sin\left(\alpha\left(t \right) \right) \end{bmatrix} \tag{8}$$

In this work, we choose a simple sinusoidal model with the following definition:

Research Article | Vol. 27, No. 15 | 22 Jul 2019 | OPTICS EXPRESS 20635
Optics EXPRESS

$$v_0(t) = v_0 = const.$$
$$\alpha(t) = \alpha_0 \cos\left(\frac{2\pi}{t_0} t\right) \tag{9}$$

Starting from these equations, we calculate the intersections of the functions f_e and f_g according to the two cases described in Eq. (5) (Cross Sinusoidal distribution CS) and (6) (Cross Random Sinusoidal distribution CRS). The resulting EPDs are given in Figs. 2(e) and 2(g). It consists on a set of N_{EPD} points. The cases of periodic and quasi-random distributions are described in Figs. 2(a) and 2(c) respectively.

The physical process involved in self-focusing is based on a multiple interference phenomenon. It can be described as a superposition of series of Young's fringes figure, with a period and an orientation given by the amplitude and orientation of the vector $\vec{u}_{p,q}$ that connects two interfering emissive points p and q from a given EPD.

The efficiency of the self-focusing effect is related to the number and to the diversity of this vector distribution. To evaluate this diversity, we introduce the histogram of the minimal distance distribution.

We first calculate the distribution of the minimal distance s from a point to its neighbors:

$$s_p = \min\left(\left|u_{p,q}\right|\right)_{q \in EPD} \tag{10}$$

We consider the case of a square EUC: $\Lambda_1 = \Lambda_2 = \Lambda$. The histogram is calculated with a number N_h of bins calculated between 0 and Λ:

$$h_q = \sum_{p=1}^{N_{EPD}} \left[0 < \left(s_p - q\frac{2\Lambda}{N_h} \right) \le \frac{2\Lambda}{N_h} \right] \tag{11}$$

The histograms of the various EPDs are presented Fig. 2, right part. In the case of the periodic distribution, the histogram is a Dirac located at the period of the distribution, see Fig. 2(b). The histogram is a large distribution for the quasi-random EPD as shown in Fig. 2(d). The choice of a sinusoidal design for the waveguides and electrodes allows to enlarge the histogram function particularly in the case of the random access, case of Fig. 2(h) with respect to the periodic one, as depicted in Fig. 2(f).

This first mathematical approach to the design of the EPD shows some orientations that will be followed in next investigations to improve the histogram distribution in order to achieve better self-focusing performances.

To validate the link between the EPD histogram and the self-focusing behavior, the various EPDs considered in this study have been manufactured in an opaque layer, and experimentally evaluated using an optical set-up that transposes the self-focusing behavior from an emissive to a transmissive configuration.

Research Article | Vol. 27, No. 15 | 22 Jul 2019 | OPTICS EXPRESS 20636
Optics EXPRESS

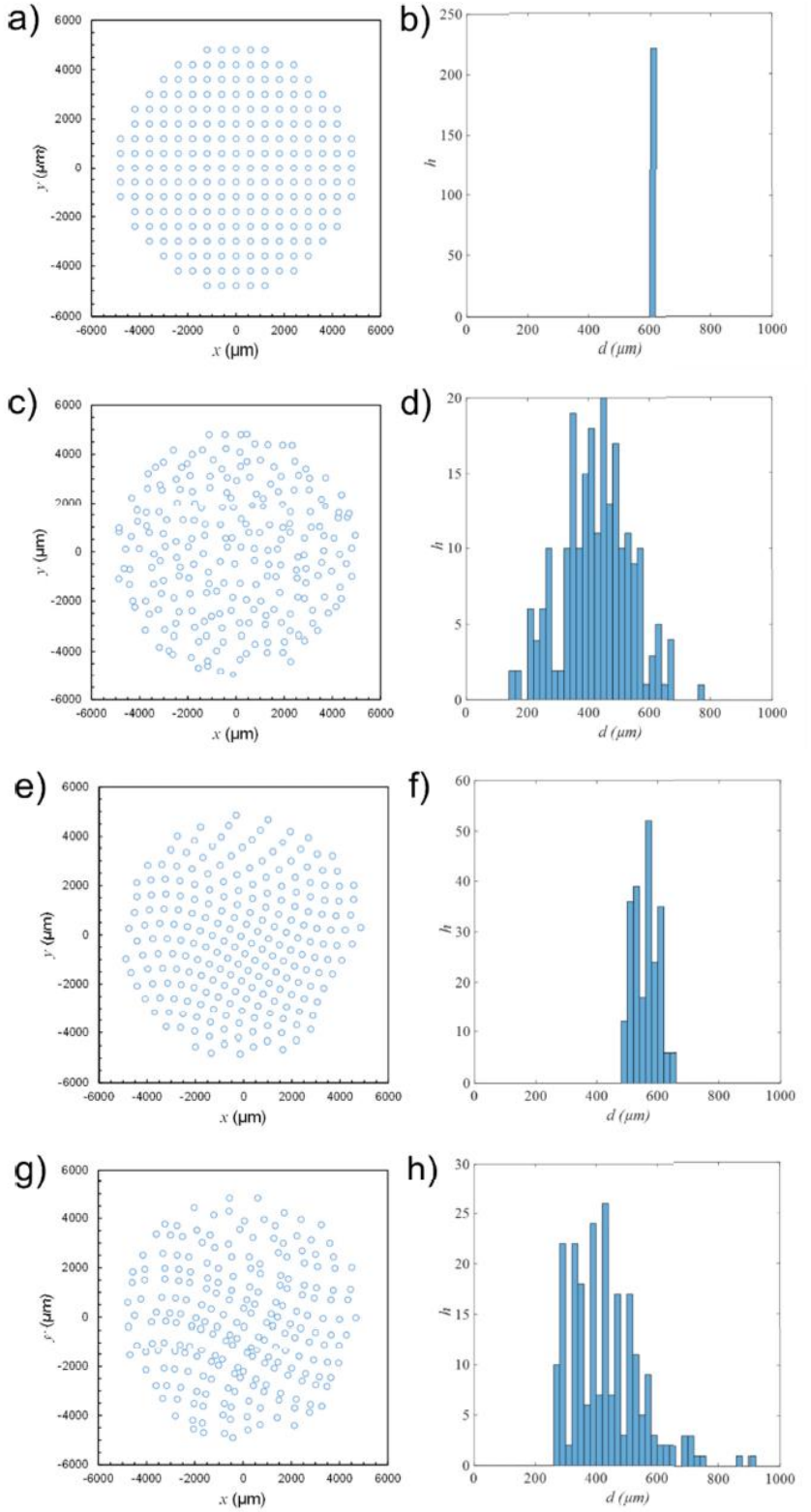

Fig. 2. Calculated distributions and their histograms of the closest distance between the nearest pinholes: (a) and (b) periodic distribution; (c) and (d) quasi-random distribution; (e) and (f) CS distribution; (g) and (h) CRS distribution.

Research Article | Vol. 27, No. 15 | 22 Jul 2019 | OPTICS EXPRESS 20637
Optics EXPRESS

3. Experimental validation of self-focusing effect

3.1. Set-up description

The optical set-up consists in a 513 nm laser diode, emitting through an optical fiber. The beam impacts an opaque sample made out of a thin glass, coated with an opaque, black chrome layer. A distribution of apertures of various sizes and distribution functions has been etched through the opaque layer with a maskless lithographic process Fig. 3(a) [18]. In order to simulate a phase-adjusted emission through the EPD, the fiber laser is located at a large distance from the sample. The beam incident on the EPD sample can then be considered as representing a planar wave, as shown in Fig. 3(b).

Beyond the aperture distribution sample, we evaluate the self-focusing effect with an imaging system that mimics the eye. We use as optical system an objective with a focal length f_0 = 51 mm and a high resolution 6.6 MegaPixels monochrome CMOS sensor with a 3.5 µm pixel size. The distance between the aperture distribution sample and the optical system is about 20 mm.

3.2. Experimental results

The first results given in Figs. 4(a) and 4(b) present the case of a single aperture. In this case self-focusing does not occur, and one observes the blurred image of the aperture. Figure 4(a) shows the intensity of the beam measured on the CMOS sensor in angular coordinates. Figure 4(b) depicts the cross section of the signal.

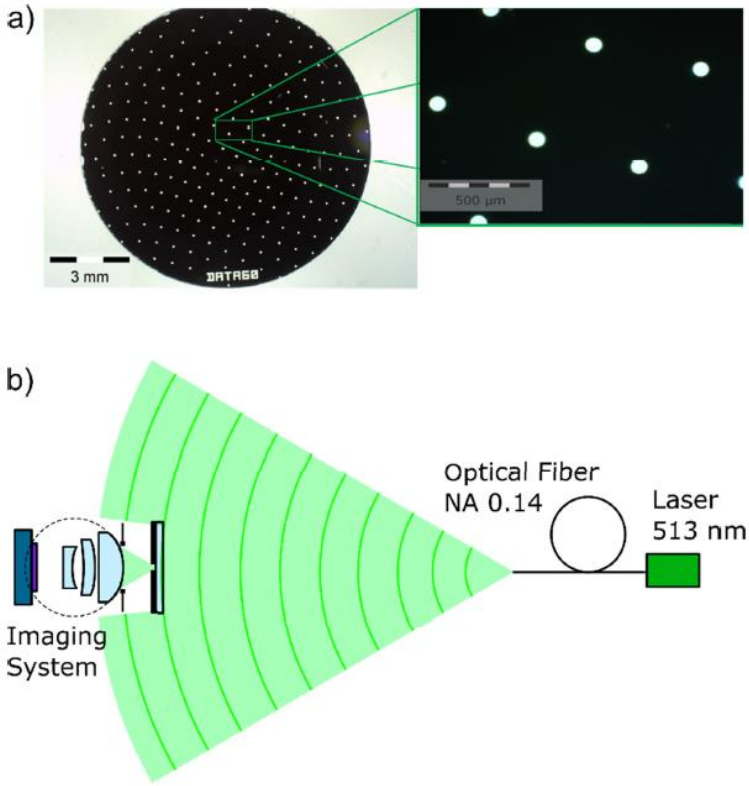

Fig. 3. Experimental set-up for self-focusing effect validation: (a) pictures of a sinusoidal periodic apertures distribution mask, (b) set-up description.

Research Article | Vol. 27, No. 15 | 22 Jul 2019 | OPTICS EXPRESS 20638
Optics EXPRESS

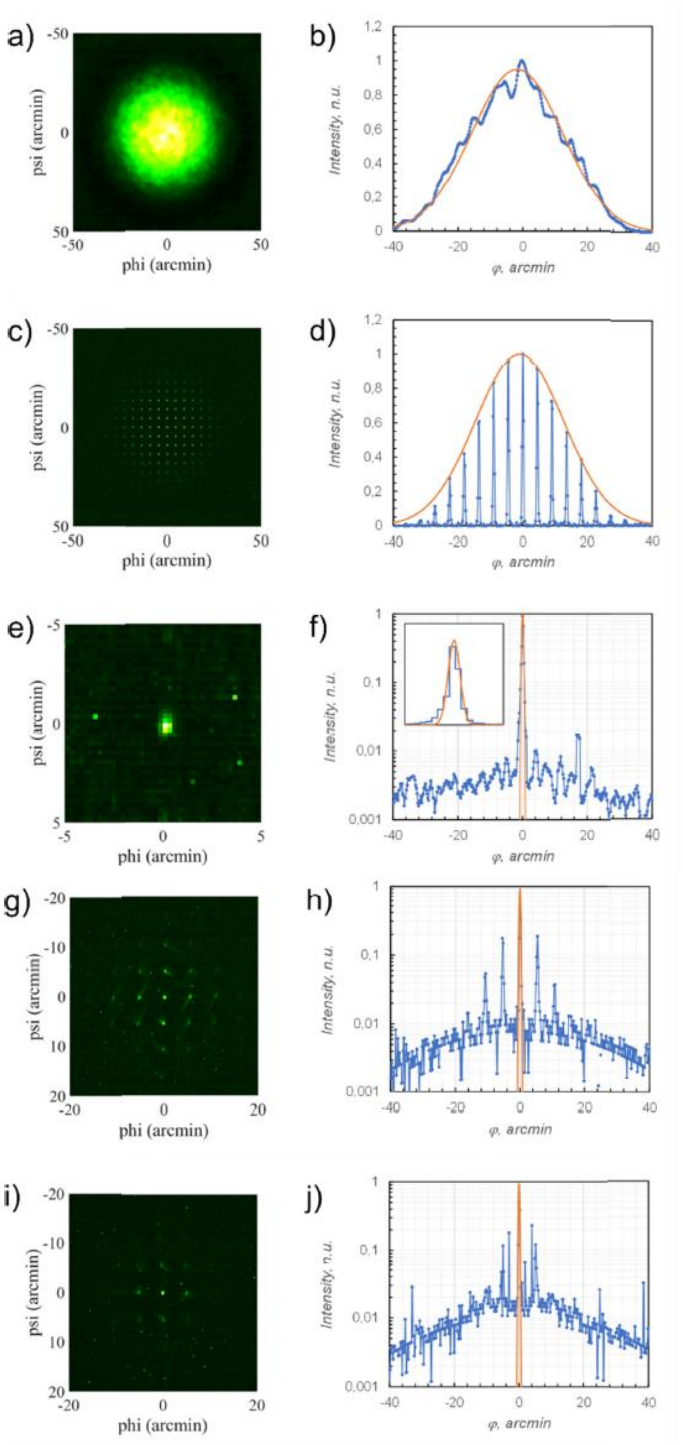

Fig. 4. Diffraction patterns produced by various EPD, on the left the image on the image sensor (in green false color), on the right the intensity cross section compared with Gaussian function: (a) and (b) one pinhole; (c) and (d) periodic distribution; (e) and (f) quasi-random distribution; (g) and (h) CS distribution; (i) and j) CRS distribution. Figure (f), (h) and (j) are plotted in logarithmic intensity scale. Inset in Fig. (f) is a detail of the spel theory/measurement comparison in linear scale near 0 arcmin.

Research Article | Vol. 27, No. 15 | 22 Jul 2019 | OPTICS EXPRESS 20639
Optics EXPRESS

We use Gaussian beam formalism as described in [13]. The waist w_0 of the beam emitted from the aperture is taken as the radius of the aperture. The angular radius $\Delta\theta$ (HWHM) of the blurred signal is then given by:

$$\Delta\theta = \frac{\lambda}{\pi w_0} \tag{12}$$

With a 50 µm diameter aperture, an angular radius of 22 arcmin is calculated. The value is consistent with the value of the waist deduced from the Gaussian model of Fig. 4(b) (waist 30 arcmin).

Figures 4(c) and 4(d) describe the image resulting from a periodic aperture distribution. The period Λ of the 50 µm diameter apertures distribution is 400 µm. The periodic aperture distribution generates diffraction orders with an angular period given by λ/Λ. It corresponds to an angular period of 4.4 arcmin, consistent with our measurements.

Figures 4(e) and 4(f) describe the case of a quasi-random distribution calculated on a 400 µm periodic EUC. These results confirm the self-focusing behavior. One observes a central peak, that we name spel (for elementary spot), with an angular radius $\delta\theta$ (first zero of the Airy function) given by the entrance pupil diameter D_p:

$$\delta\theta = 1.22\frac{\lambda}{D_p} \tag{13}$$

The aperture of the optical system is given by the choice of the f#. In order to image a spel over several pixels, while still keeping a sufficiently high signal level, we choose an aperture of f/15 that corresponds to D_p = 3.4 mm. The calculated angular radius of 0.6 arcmin is consistent with the measurements (the inset of Fig. 4(f) shows the cross section pixel signal of the spel and a Gaussian model with waist 0.45 arcmin).

The signal outside of the spel is distributed as speckle noise.

Figures 4(g) and 4(h) show the result for the CS distribution. The resonant contribution is strongly reduced, compared to Fig. 4(d), but speckle noise still presents remaining peaks, compared to Fig. 4(f).

Finally, the choice of a CRS distribution allows for reducing the contribution of the unwanted peak, as shown on Figs. 4(i) and 4(j).

3.3. Analysis

The experimental results confirm that the self-focusing effect implemented with a random EPD allows for isolating a spel on the retina. This behavior is accomplished at the price of a speckle noise surrounding the spel. The characteristics of this noise contribution are related to the EPD:

- the size of the emissive points fixes the size of the noise envelop,
- the type of the EPD reduces the number of unwanted ghost spel in the noise,
- the number of points in the EPD fixes the signal to noise ratio between the spel and the noise.

To evaluate the impact of the noise on the imaging performance of the self-focusing effect, we introduce a double Gaussian model to describe the spel and the noise. Figure 5 shows a cross section of the spel for the quasi-random EPD case.

One can separate the signal in two contributions:

- the spel is described by a first intensity Gaussian function with a waist w_1,
- the noise is described by a second intensity Gaussian function with a waist w_2.

Both intensity functions are described by the Gaussian beam formula:

Research Article | Vol. 27, No. 15 | 22 Jul 2019 | OPTICS EXPRESS 20640
Optics EXPRESS

$$I_i(r) = I_{0i} e^{-2\left(\frac{r}{w_i}\right)^2}{}_{i=1,2} \tag{14}$$

I_{0i} being the maximum intensity of the signal that fixes the total energy of the signal:

$$E_i = 2\pi I_{0i} w_i^2{}_{i=1,2} \tag{15}$$

The size of the spel w_1 is given by the total pupil aperture:

$$w_1 \sim 0.7\delta\theta f_0 = 0.86\frac{\lambda f_0}{D_p} \tag{16}$$

The size of the noise contribution w_2 is given by the pinhole aperture diameter d_p as for the case of Eq. (12):

$$w_2 = 2\frac{\lambda f_0}{\pi d_p} \tag{17}$$

The terms E_1 and E_2 represent the energy contains in the spel and in the noise, respectively. We define the parameter γ as the ratio in dB between the energy of the spel and the energy of the self-focused signal:

$$\gamma = -10\log\left(\frac{E_1}{E_1 + E_2}\right) = -10\log\left(\frac{I_{01} w_1^2}{I_{01} w_1^2 + I_{02} w_2^2}\right) \tag{18}$$

Figure 5 shows the experimental characterization of the spel in the case of a random EPD with the aperture diameter d_p = 75 µm. To fit both Gaussian models, three intensities of the LD are used to overcome the limited CMOS sensor dynamic: Fig. 5(a) to Fig. 5(c).

The cross intensities functions are given in spatial coordinates on the CMOS sensor. The double Gaussian parameters are: I_{01} = 1; w_1 = 6.5 µm; I_{02} = 0.065; w_2 = 200 µm and are consistent with the theoretical value given by Eqs. (16) and (17): w_1 = 6.7 µm and w_2 = 224 µm. The Gaussian model parameters give a noise ratio γ = 18.

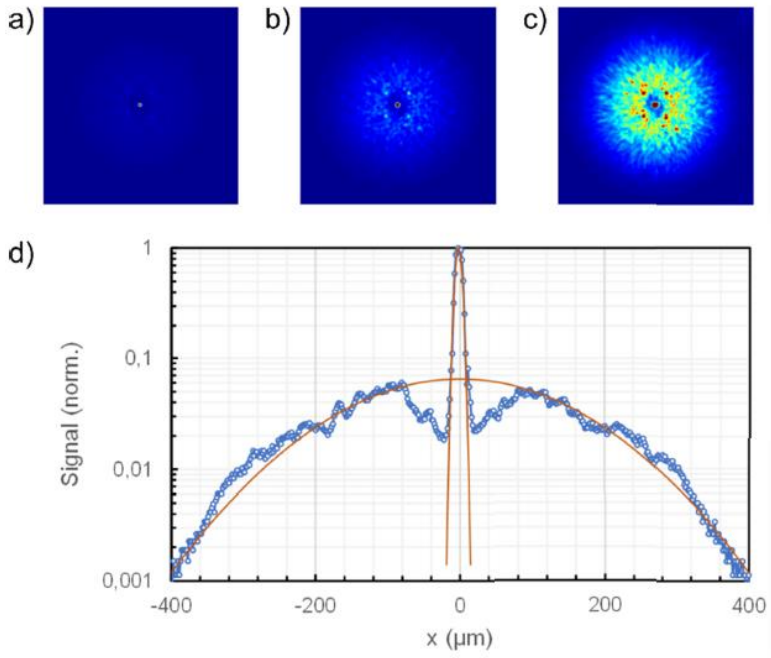

Fig. 5. Double-Gaussian model for the spel. (a), (b) and (c) spel intensity distributions for three LD power (d) cross intensity function of the concatenated images (blue dotted curve) and Gaussian model for the peak and the noise (orange curves).

Research Article | Vol. 27, No. 15 | 22 Jul 2019 | OPTICS EXPRESS 20641
Optics EXPRESS

The double Gaussian model has the great interest to give an analytical expression for the spel that can be used to evaluate the image forming process involved in self focusing as a function of γ.

4. Self-focusing image formation

4.1. Imaging process simulation

Simulation of imaging process in conventional imaging is based on the convolution of an image by the Points Spread Function (PSF) of the optical system. This process related to linear systems traduces the continuity of the image in the object and image plane of the optical system. Here, one has to consider a process with no image in the object plane of the optical system, and an image representation that is not continuous in the image plane. The simulation can still be made on the basis of the convolution with the optical response of the system, but we must consider here the image as a series of Dirac that localize the spels on the retina.

Considering an image formed onto the retina by a succession of spels with positions on the retina given by the vector $\vec{r}_{u,v}$ and an intensity given by the matrix $M_{u,v}$, one describes the spel intensity distribution with the function $g\left(\vec{r}\right)$. The image I_{ret} on the retina is given by the sum of the spel contributions:

$$I_{ret}\left(\vec{r}\right)=\sum_{u,v}M_{u,v}g\left(\vec{r}-\vec{r}_{u,v}\right) \tag{19}$$

We must here underline the specificity of the imaging process in self-focusing. In conventional optics the image on the retina is expressed by:

$$\tilde{I}_{ret}\left(\vec{r}\right)=\iint\sum_{u,v}M_{u,v}rect_{W}\left(\vec{s}-\vec{r}_{u,v}\right)PSF\left(\vec{r}-\vec{s}\right)dx_{s}dy_{s} \tag{20}$$

The function $rect_W$ represents the geometric image of the square pixel on the retina (with size and pitch W) and traduces the continuity of the image as a succession of adjacent squares with size given by the display characteristics and the magnification of the optical system.

According to Eq. (20), if we consider a micro display with resolution N_l x N_c pixels, an optical system gives the same result $\tilde{I}_{ret}\left(\vec{r}\right)$ for an image of size N_l /2 x N_c/2 or for the same image oversampled by a factor 2.

In the case of self-focusing imaging, the oversampling by a factor 2 leads to an increase of a factor 4 on the number of spels and modifies the resulting image. This effect is described in Fig. 6. The image to be displayed is the letter T and is shown in Fig. 6(a) as given in a conventional display with adjacent pixel. In self-focusing each pixel can be represented by one spel as in Fig. 6(b), by four spels as in Fig. 6(c) or more. Increasing the number of spel is supposed to increase the image quality. However, as the total number of emissive points is fixed for a given display, increasing the number of spel reduces the number of emissive points allocated to each spel. This reduction of the EPD size degrades each individual spel, and by this way is supposed to degrade the overall image quality.

A compromise must be found between the number of spel and the efficiency of the spel in terms of image quality, so-called resolution/sharpness conflict. The goal of this paper being to present first experimental validations of self-focusing imaging, this complex aspect of self-focusing will not be more discussed here.

Research Article | Vol. 27, No. 15 | 22 Jul 2019 | OPTICS EXPRESS 20642
Optics EXPRESS

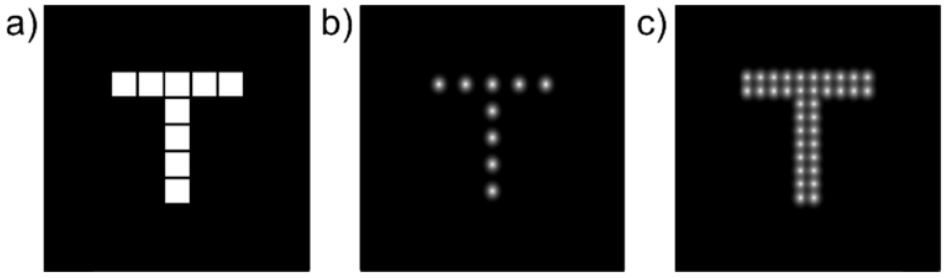

Fig. 6. (a) Image of the letter "T" coded with 5x5 pixels, (b) self-focusing imaging with one spel per pixel and (c) self-focusing imaging with four spels per pixel.

4.2. Experimental set-up

The set-up used to evaluate self-focusing imaging is described in Fig. 7. As we don't have yet retinal display devices, the principle of the validation is to pass through a distribution of apertures as in the case of Fig. 3. The objective is not to generate a single planar wave through our EPD but a series of planar wave that project an image onto the retina. We use a micro-display with a pixel size δ and a collimating optics with focal f_c as wavefront generator.

Each pixel u,v of the display generates a wavefront of vector $\vec{k}_{u,v}$ with the angular coordinates:

$$\vec{k}_{u,v} = \begin{bmatrix} \sin(\rho_{u,v})\cos(\theta_{u,v}) \\ \sin(\rho_{u,v})\sin(\theta_{u,v}) \\ \cos(\rho_{u,v}) \end{bmatrix} \tag{21}$$

With the angular relations given in the paraxial approximation:

$$\begin{aligned} \rho_{u,v} &= \frac{\delta}{f_c}\sqrt{u^2+v^2} \\ \theta_{u,v} &= \cos^{-1}\left(\frac{u}{\sqrt{u^2+v^2}}\right) \end{aligned} \tag{22}$$

The wavefronts are transmitted to the imaging system through the apertures holes of the EPD and form the spels of the image at coordinates $\vec{r}_{u,v}$ on the CMOS sensor that mimics the retina.

$$\vec{r}_{u,v} = \begin{bmatrix} f_0\rho_{u,v}\cos(\theta_{u,v}) \\ f_0\rho_{u,v}\sin(\theta_{u,v}) \end{bmatrix} \tag{23}$$

The microdisplay used in this work is depicted on Fig. 8. As the aperture distribution used in this work has a very low transmission factor due to the small size of the pinholes, a specific high power monochromatic microdisplay developed in our laboratory has been used. This binary microdisplay forms a static image of the word "LETI" on a 13 x 5 pixels resolution, and a single, isolated pixel is also activated. The size of the pixel is 8 x 8 μm^2 with a pixel pitch of 10 µm. Typical brightness for this display is about 3000 Cd/m^2 [19].

For these measurements, the resolution of the sensor is increased and a new CMOS sensor is used with a smaller 1.67 µm pixel size.

Research Article | Vol. 27, No. 15 | 22 Jul 2019 | OPTICS EXPRESS 20643
Optics EXPRESS

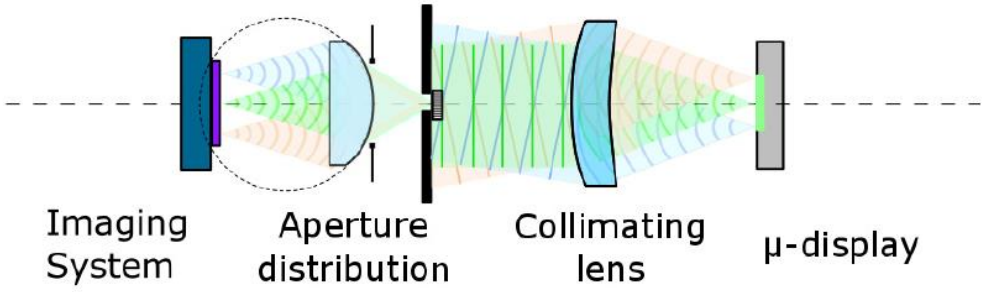

Fig. 7. Optical set-up used to evaluate self-focusing imaging.

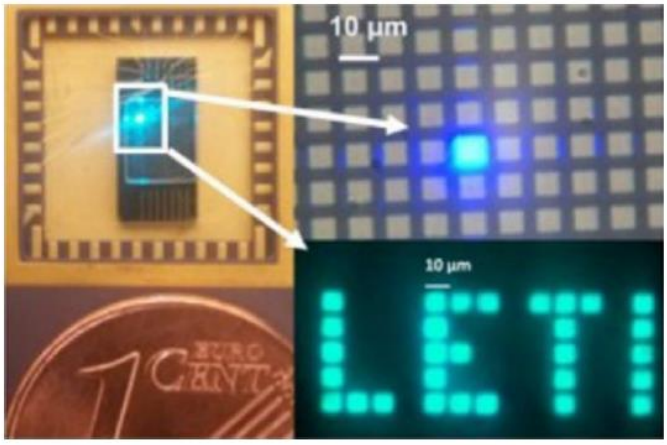

Fig. 8. MicroLED display used to generate the image wavefront. On the left the display size compared with 1 eurocent; on the right the magnification of the display with an isolated activated pixel as well as the "LETI" acronym.

4.3. Experimental results

We show on Fig. 9 the results of the image forming process on the various EPDs considered in this study. Figures are given in gray level and angular coordinates. To give a better visual rendering the gray scale of the figure is reversed. Figure 9(a) shows the image of the micro display without any aperture. It represents the perfect image only limited by the aberration of the optical system. Due to a too low energy level, the experimental evaluation of the imaging process through a single aperture was not possible.

Figure 9(b) shows the imaging through a periodic aperture distribution (d_p = 75 µm, Λ = 400 µm). We observe a duplication of the elementary image as expected from the theory. Figures 9(c) and 9(d) show the result of imaging through the quasi-random and CRS EPDs.

Research Article | Vol. 27, No. 15 | 22 Jul 2019 | OPTICS EXPRESS 20644
Optics EXPRESS

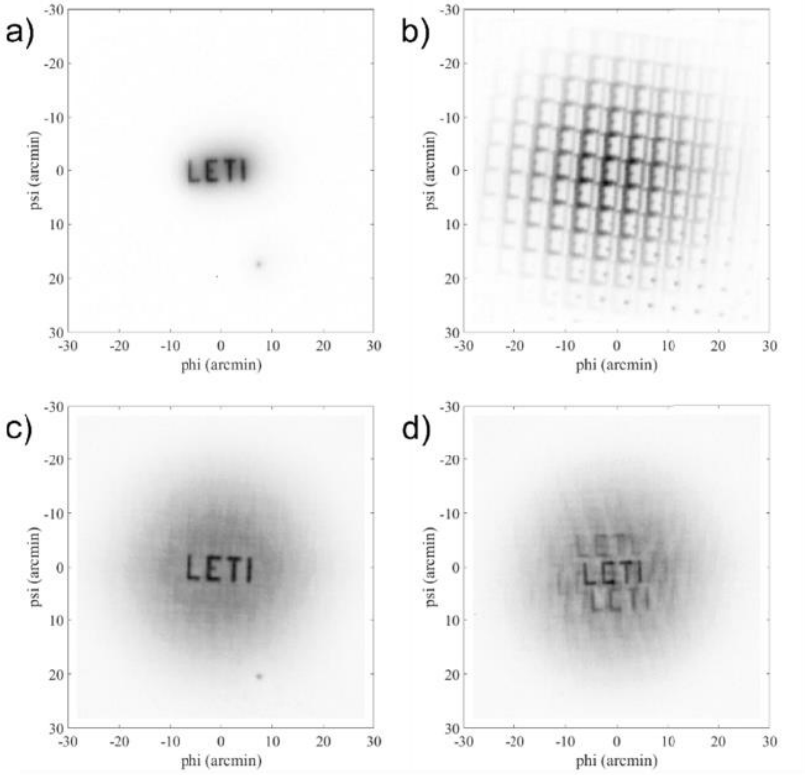

Fig. 9. Results on the experiment (a) diffraction limited, (b) periodic distribution, (c) quasi-random EPD and (d) CRS EPD.

4.4. Simulation results

We use as image a 13 x 5 pixels sampling of the acronym "LETI" representative of the micro-display of Fig. 8. We choose a 130 x 50 pixels resolution for the whole image, with an emissive-pixel periodicity of the display of 10 pixels, and each emissive zone being itself sampled with 8 x 8 pixels.

Simulations are made on the basis of the double Gaussian model. The results based on the parameters given from Fig. 5 give low correspondence with our experimental measurements and correcting factors must be introduced in the value of w_1, w_2 and γ as given by Eqs. (16)–(18). Both values of the waist must be increased by a factor 1.5 and a noise ratio of 15 dB is used instead of 18 dB.

Figure 10(a) shows simulation for a conventional imaging behavior. We use the double Gaussian model with a ratio factor γ ~0 dB.

We simulate the case of a periodic EPD with a function that describes the spel distribution as shown on Fig. 4(c). The following definition is used for g (with the corrected waist values):

$$g_{per}\left(\vec{r}\right) = G_0 e^{-2\frac{\|\vec{r}\|^2}{w_2^2}} \sum_{k,l} e^{-2\frac{\|\vec{r}-\vec{r}_{k,l}\|^2}{w_1^2}} \tag{24}$$

First term G_0 is used to normalize the total energy. Second term is the envelope of the apodization function. Third term is the grid of resonances due to the periodic distribution, vector $\vec{r}_{k,l}$ giving the coordinates of the resonant peaks:

Research Article | Vol. 27, No. 15 | 22 Jul 2019 | OPTICS EXPRESS 20645
Optics EXPRESS

$$\vec{r}_{k,l} = \begin{bmatrix} k\dfrac{\lambda f_0}{\Lambda} \\ l\dfrac{\lambda f_0}{\Lambda} \end{bmatrix} \tag{25}$$

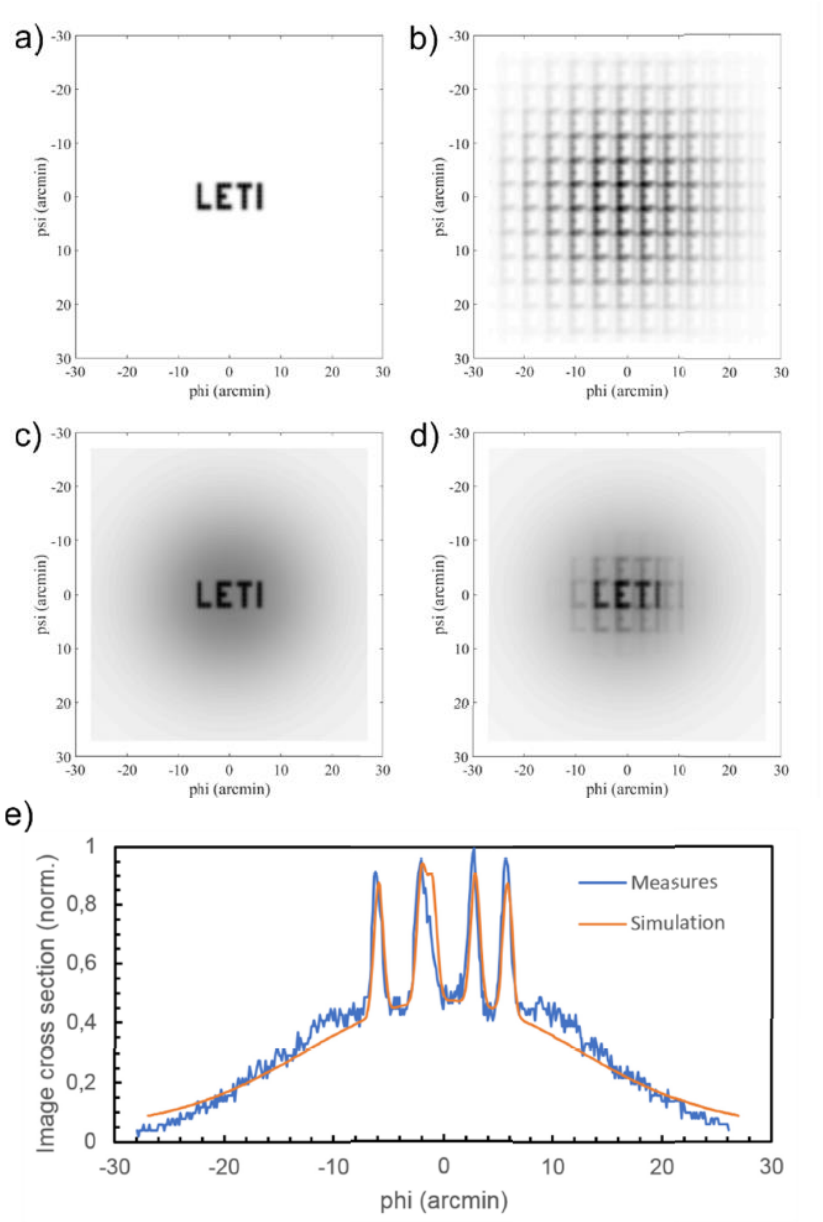

Fig. 10. Results on the imaging simulation process (a) diffraction limited, (b) periodic distribution, (c) quasi-random EPD, (d) CRS EPD and (e) comparison of the middle cross section of the measured and simulated images in the quasi-random EPD.

Figure 10(b) gives the result of the simulation. One can see that the repetition of the resonant peaks prevents the recognition of the word LETI, as observed in the measurements and as predicted by the theory.

The quasi-random distribution is simulated with the double Gaussian formalism:

$$g_{qr}(r) = I_1(r) + I_2(r) \tag{26}$$

Research Article | Vol. 27, No. 15 | 22 Jul 2019 | OPTICS EXPRESS 20646
Optics EXPRESS

The simulation result given in Fig. 10(c) is used as a comparison between theory and experiment. Figure 10(e) compares the cross section of the experimental and simulated image made on the middle of the image in the quasi-random case. This case is used as a reference as it corresponds to the optimal imaging result for the EPD design. Correcting factors are determined to give the best fit between the two curves. Note that the Cross Sinusoidal and Cross Random Sinusoidal distributions (CS and CRS) distributions are easier to fabricate but don't correspond to an optimal distribution realistic with our manufacturing capabilities. Future work will focus on determining such distributions with better self-focusing performances than CS and CRS. Note also that the brightness of the image is not strongly modified by the kind of EPD used, as long as the main characteristics of the EPD (size and density of the apertures) remain the same.

We can now recognize in Fig. 10(c) the word LETI surrounded by a strong noise contribution that degrades the contrast.

The CRS case is described by a function that mixes the formalism of Eqs. (24) and (26).

$$g_{CRS}\left(\vec{r}\right) = I_1\left(\left\|\vec{r}\right\|\right) + I_2\left(\left\|\vec{r}\right\|\right) + H_0 e^{-2\frac{\left\|\vec{r}\right\|^2}{w_3^2}} \sum_{q,p} e^{-2\frac{\left\|\vec{r}-\vec{r}_{q,p}\right\|^2}{w_1^2}} \qquad (27)$$

The first two terms of the equation correspond to the spel and the noise, respectively, as in Eq. (24). The last term corresponds to the ghost peaks that appear at coordinate $\vec{r}_{q,p}$ with an angular extension w_3 given in the experimental results of Fig. 4(i).

Figure 10(d) gives the result of image simulation with the CRS distribution. The image of the word LETI can be recognized but some ghost images appear at the ghost peak location as in the measurements.

4.5 Analysis

The experimental results confirm the ability to produce an image through the self-focusing effect. The model of a double Gaussian intensity distribution is efficient to describe the imaging process on the retina. It allows for fast simulations as summations of the various spels that form the image.

The main drawback of the device will concern the contrast of the retinal image and the presence of ghost images produced by limited random distributions. The EPDs that have been considered throughout this paper are related to simple sinusoidal models, and more complex configurations are currently under investigations to improve the image quality.

The best fit between simulation and measurements in Fig. 10 requires introducing some correcting factors. This correction can be explained by the difference in spectral characteristics between the laser diode used in Fig. 5 (FWHM ~1 nm) and the pixel of the microLED display used in Fig. 9 (FWHM ~30 nm) [20].

The EPD parameters have been chosen in order to simplify the visual analysis as shown on Figs. 9 and 10. Future work will focus on the parameters corresponding to our device with an emissive aperture diameter smaller than 10 µm and an entrance pupil diameter of about 6 mm. The three orders of magnitude difference between these two values make visual analysis difficult if one wants to evaluate on the same graphic the effect of the spel and of the whole surrounding noise as in Fig. 10(e).

For this analysis it is also of primary importance to consider the eye model, particularly in terms of extended sensing dynamic and non-uniform resolution. Specific diffusion behavior of the holographic part of the device also has to be considered for a rigorous analysis of the system performance [21].

It is also worth mentioning the influence of the source bandwidth. In particular, the increase of the spectral bandwidth expands the speckle figure around the central peak and tends to increase the ratio between the energy of the spel and the energy of the noise. This

Research Article | Vol. 27, No. 15 | 22 Jul 2019 | OPTICS EXPRESS 20647
Optics EXPRESS

aspect still requires an in-depth analysis, however, effects of wavelength and bandwidth have been described experimentally in [20], to which the interested reader is referred.

Then, the display concept we propose works with a set of different Emissive Point Distributions (EPDs) each associated with an image pixel. To be fully representative of the concept, each pixel of the word "LETI" should have been associated with a specific EPD. This configuration is not possible in the frame of this first experiment, as all the display pixels highlight a transmission aperture distribution. We are currently investigating use of a holographic printer, to evaluate a configuration with different EPDs, for a closer-to-real-case application. Nevertheless, even if the aperture distribution is here still common to all the pixels, it anyway well describes the effect of image formation through self-focusing effect, to demonstrate its practical interest.

5. Conclusion

After the introduction of a new concept of retinal projector [13], we studied an implementation of the imaging process through the self-focusing effect. This first experimental demonstration allows introducing first elements of design for an Emissive Point Distribution consistent with the requirement of the addressing process through the intersection of sinusoidal waveguides and electrodes. First results are positive, but show that more complex addressing design has to be found in view of improving the visual rendering of the retinal projection.

Main limitations of the concept have been highlighted. The noise generated by the sampling of the planar wave by a series of spherical waves is a first limitation, inherent to the concept. Its reduction requires a compromise between the size and the number of the EPD, that is, between the resolution and the sharpness of the image (resolution/sharpness conflict). It is well described by a simple double Gaussian model that allows for fixing a signal to noise design parameter γ.

Another limitation is the presence of ghost images, directly related to the choice of the EPD and to its actual degree of randomness.

The link between γ, the EPD definition, the sampling and the angular size of the images is difficult to establish and will require pursuing research with the introduction of a more detailed eye model, in order to finely tune the image formation parameters, which are specific to this new image projection modality.

Finally, a natural extension of this work would be to study application for colors display. Here, monochrome demonstration of the self-focusing effect is provided, but the use of multiple wavelengths is possible, using same EPD for all the pixels of the image. It could allow for evaluating the spectral behavior of the self-focusing effect in a red-green-blue (RGB) configuration. However, in the case of the originally proposed retinal display concept [12,13], each EPD is to be associated with a specific hologram that fixes the emissive angle. As holograms are selective in wavelength, one would then have to use three separate holographic layers in order to encode three EPD color families for full RGB display.

Acknowledgments

The authors would like to thank both anonymous reviewers for their valuable suggestions to improve the manuscript.

References

1. B. Kress, E. Saeedi, and V. Brac-de-la-Perriere, "The segmentation of the HMD market: optics for smart glasses, smart eyewear, AR and VR headsets," Proc. SPIE **9202**, 92020D (2014).
2. M. Billinghurst, A. Clark, and G. Lee, "A Survey of Augmented Reality," Found. Trends Human–Comp. Inter. **8**, 73–272 (2015).
3. A. Meola, F. Cutolo, M. Carbone, F. Cagnazzo, M. Ferrari, and V. Ferrari, "Augmented reality in neurosurgery: a systematic review," Neurosurg. Rev. **40**(4), 537–548 (2017).

Research Article | Vol. 27, No. 15 | 22 Jul 2019 | OPTICS EXPRESS 20648
Optics EXPRESS

4. J. W. Yoon, R. E. Chen, E. J. Kim, O. O. Akinduro, P. Kerezoudis, P. K. Han, P. Si, W. D. Freeman, R. J. Diaz, R. J. Komotar, S. M. Pirris, B. L. Brown, M. Bydon, M. Y. Wang, R. E. Wharen, Jr., and A. Quinones-Hinojosa, "Augmented reality for the surgeon: Systematic review," Int. J. Med. Robot. **14**(4), e1914 (2018).
5. J. Bacca, S. Baldiris, R. Fabregat, S. Graf, and Kinshuk, "Augmented Reality Trends in Education: A Systematic Review of Research and Applications," J. Educ. Technol. Soc. **17**(4), 133–149 (2014).
6. P. Chen, X. Liu, W. Cheng, and R. Huang, "A review of using Augmented Reality in Education from 2011 to 2016," in *Innovations in Smart Learning. Lecture Notes in Educational Technology*, E. Popescu, Kinshuk, M. K. Khribi, R. Huang, M. Jemni, N.-S. Chen, and D. G. Sampson (eds). (Springer, 2017).
7. R. Palmarini, J. A. Erkoyuncu, R. Roy, and H. Torabmostaedi, "A systematic review of augmented reality applications in maintenance," Robot. Comput.-Integr. Manuf. **49**, 215–228 (2018).
8. X. Li, W. Yi, H.-L. Chi, X. Wang, and A. P. C. Chan, "A critical review of virtual and augmented reality (VR/AR) applications in construction safety," Autom. Construct. **86**, 150–162 (2018).
9. K. Akşit, W. Lopes, J. Kim, P. Shirley, and D. Luebke, "Near-eye varifocal augmented reality display using see-through screens," ACM Trans. Graph. **36**(6), 189 (2017).
10. A. Maimone, A. Georgiou, and J. S. Kollin, "Holographic near-eye displays for virtual and augmented reality," ACM Trans. Graph. **36**(4), 85 (2017).
11. B. Kress and T. Starner, "A review of head-mounted displays (HMD) technologies and applications for consumer electronics," Proc. SPIE **8720**, 87200A (2013).
12. C. Martinez, "Image projection Device," US patent 2015/0370073 A1 (2015).
13. C. Martinez, V. Krotov, B. Meynard, and D. Fowler, "See-through holographic retinal projection display concept," Optica **5**(10), 1200–1209 (2018).
14. S. S. Hong, B. K. P. Horn, D. M. Freeman, and M. S. Mermelstein, "Lensless focusing with subwavelength resolution by direct synthesis of the angular spectrum," Appl. Phys. Lett. **88**(26), 261107 (2006).
15. P. S. Salvaggio, J. R. Schott, and D. M. McKeown, "Laboratory validation of a sparse aperture image quality model," Proc. SPIE **9617**, 961708 (2015).
16. A. Jiang, S. Wang, Z. Dong, J. Xue, J. Wang, and Y. Dai, "Wide-band white light sparse-aperture Fizeau imaging interferometer testbed for a distributed small-satellites constellation," Appl. Opt. **57**(11), 2736–2746 (2018).
17. F. Eisenhauer, G. Perrin, W. Brandner, C. Straubmeier, K. Perraut, A. Amorim, M. Schöller, S. Gillessen, P. Kervella, M. Benisty, C. Araujo-Hauck, L. Jocou, J. Lima, G. Jakob, M. Haug, Y. Clénet, T. Henning, A. Eckart, J.-P. Berger, P. Garcia, R. Abuter, S. Kellner, T. Paumard, S. Hippler, S. Fischer, T. Moulin, J. Villate, G. Avila, A. Gräter, S. Lacour, A. Huber, M. Wiest, A. Nolot, P. Carvas, R. Dorn, O. Pfuhl, E. Gendron, S. Kendrew, S. Yazici, S. Anton, Y. Jung, M. Thiel, É. Choquet, R. Klein, P. Teixeira, P. Gitton, D. Moch, F. Vincent, N. Kudryavtseva, S. Ströbele, E. Sturm, P. Fédou, R. Lenzen, P. Jolley, C. Kister, V. Lapeyrère, V. Naranjo, C. Lucuix, R. Hofmann, F. Chapron, U. Neumann, L. Mehrgan, O. Hans, G. Rousset, J. Ramos, M. Suarez, R. Lederer, J.-M. Reess, R.-R. Rohloff, P. Haguenauer, H. Bartko, A. Sevin, K. Wagner, J.-L. Lizon, S. Rabien, C. Collin, G. Finger, R. Davies, D. Rouan, M. Wittkowski, K. Dodds-Eden, D. Ziegler, F. Cassaing, H. Bonnet, M. Casali, R. Genzel, and P. Lena, "GRAVITY: Observing the Universe in Motion," Messenger (Los Angel.) **143**, 16–24 (2011).
18. V. Krotov, C. Martinez, and O. Haeberlé, "Multiple beam diffractive setup for intraocular accommodation evaluation," in *Imaging and Applied Optics 2016* (2016), paper JT3A.32.
19. F. Templier, L. Dupré, B. Dupont, A. Daami, B. Aventurier, F. Henry, D. Sarrasin, S. R. Berger, and F. Olivier, L. Mathieu, "High-resolution active-matrix 10-µm pixel-pitch GaN LED microdisplays for augmented reality applications," Proc. SPIE **10556**, 105560I (2018).
20. C. Martinez, V. Krotov, and O. Haeberlé, "Experimental evaluation of self-focusing image formation in unconventional near-eye display," Proc.SPIE **10676**, 106760N (2018).
21. C. Martinez, B. Meynard, and Y. Lee, "Multiplexed pixelated hologram recording process for retinal projection device," Proc. SPIE **10944**, 109440N (2019).

Résumé en français de la thèse :

ETUDE DE LA FORMATION D'IMAGE PAR AUTO-FOCALISATION POUR LE DEVELOPPEMENT D'UN DISPOSITIF VISUEL NON CONVENTIONNEL DE LA REALITE AUGMENTEE

Vladimir Krotov

Thèse soutenue le 8 décembre 2022

ECOLE DOCTORALE : Mathématiques, Sciences de l'Information et de l'Ingénieur (ED 269)
Discipline : Electronique, Optronique et Systèmes

Directeur de thèse : Pr Olivier Haeberlé - IRIMAS – UR UHA 7499 - Mulhouse

Encadrant au CEA : Dr Christophe Martinez, CEA-Leti – Grenoble

Jury de soutenance :

Pr. Olivier HAEBERLE	Université de Haute-Alsace	Directeur de thèse
Dr. Christophe MARTINEZ	CEA-LETI	Encadrant de thèse
Pr. Eric LACOT	Université Grenoble Alpes	Rapporteur
Pr. Huges GIOVANNINI	Aix-Marseille Université	Rapporteur
Dr. Elise GHIBAUDO	Grenoble INP	Examinatrice
Dr. Kristina IRSCH	Institut de la Vision	Examinatrice

Contexte général :

Le Laboratoire Visualisation Eclairage du Département Optique et Photonique du CEA Leti Grenoble travaille en collaboration avec l'IRIMAS (équipe IMTI du Pr Olivier Haeberlé) sur le domaine des dispositifs visuels appliqués à la réalité augmentée. Dans ce domaine les prototypes développés sont fortement limités par des contraintes de conception optique liées aux principes de base de l'optique géométrique. Pour s'affranchir de ces contraintes et proposer des dispositifs conformes à l'attente du grand public des concepts d'architecture optique innovants sont étudiés par plusieurs équipes de recherche dans le monde. Notre laboratoire a proposé en 2013 un concept ambitieux basé sur l'association de technologies en photonique intégrée, en holographie et sur la mise en œuvre d'effet diffractifs. C'est dans ce cadre que s'inscrit la thèse intitulée :

« **ETUDE DE LA FORMATION D'IMAGE PAR AUTO-FOCALISATION POUR LE DEVELOPPEMENT D'UN DISPOSITIF VISUEL NON CONVENTIONNEL DE LA REALITE AUGMENTEE »**

de Vladimir Krotov.

Cette thèse est la première à aborder ce sujet de recherche aussi bien au CEA-Leti qu'à l'IRIMAS. Elle est tout particulièrement orientée vers la compréhension, la simulation et l'évaluation des effets diffractifs.

Introduction

La perception visuelle est très importante et peut être considérée comme cruciale pour les êtres humains. Elle occupe une place prépondérante parmi nos sens, ce qui reflète le fait que nos comportements sont fortement orientés vers la vision. Cependant, notre monde est sursaturé de données visuelles de toutes sortes : à chaque minute, les gens partagent des centaines de milliers de photos et de vidéos sur divers réseaux sociaux et envoient des dizaines de millions de messages par l'intermédiaire de tous les types de messageries. Cela nous pousse à la limite de la capacité de perception humaine : notre cerveau a évolué dans des circonstances extrêmement différentes de celles dans lesquelles nous vivons aujourd'hui. D'une certaine manière, cela rappelle la course de la Reine rouge : "Il faut courir tout ce que l'on peut pour rester au même endroit et si l'on veut aller ailleurs, il faut courir au moins aussi vite que cela !"

Une façon de surmonter cet obstacle est de laisser les algorithmes d'intelligence artificielle, comme l'apprentissage automatique et l'apprentissage en profondeur, traiter ces données volumineuses et nous fournir des résumés et des recommandations. Cela pourrait être basé sur les données provenant de l'internet des objets (IoT) : tous nos appareils intelligents - montres, téléphones, lunettes, même les voitures et les maisons - seront connectés et échangeront des données sur l'internet. Parallèlement, nous aurons besoin d'un dispositif permettant de percevoir visuellement et auditivement les informations à venir afin de prendre des décisions. Les technologies immersives telles que la réalité augmentée, virtuelle

et mixte constituent un moyen idéal de fournir des informations : leur grande efficacité dans divers domaines de l'activité humaine tels que l'éducation, la médecine, l'ingénierie, etc. a déjà été prouvée.

L'un des exemples de technologies immersives est un système optique proche de l'œil qui affiche des informations (Figure 1). Il peut s'agir d'un affichage monté sur la tête ou le casque (Head up Mounted Display) ou d'un système d'affichage de l'information de type lunettes intelligentes.

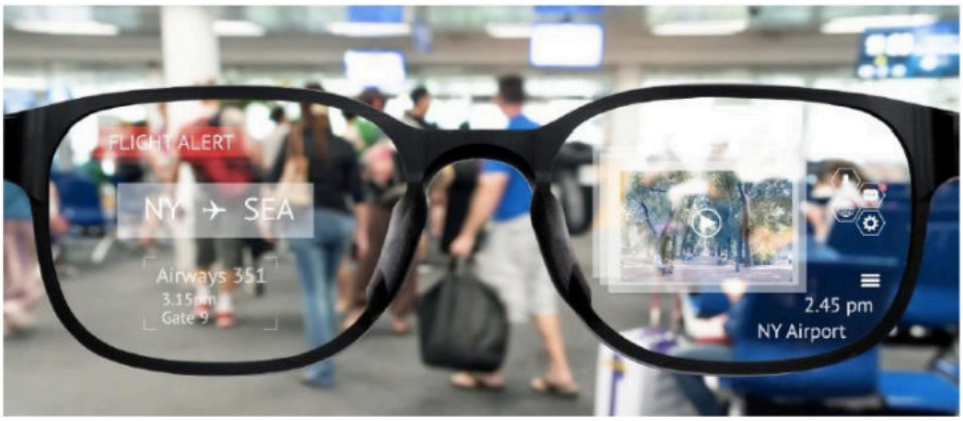

Figure 1. Vue artistique de lunettes intelligentes pour la réalité augmentée : l'information est affichée en surimpression sur un écran, qui permet aussi la vue de la scène réelle.

Ces écrans à vision directe (Near-Eye Displays - NED) font partie de notre vie quotidienne et des géants transnationaux comme Microsoft, Google, Facebook, Apple, Sony, etc. (la liste pourrait être assez longue) commercialisent leurs solutions ou se consacrent activement à la recherche et au développement (R&D). Ces appareils sont loin des attentes des consommateurs nourries par les images futuristes des livres et des films de science-fiction. Le processus de conception d'appareils ergonomiques (à la fois esthétiques et performants) exige des équipes de R&D qu'elles fassent des compromis entre de nombreux paramètres et propriétés de conception. La plupart de ces paramètres et propriétés sont interdépendants et il faut toujours trouver un compromis entre les performances élevées et les attentes esthétiques de l'utilisateur. Ce dilemme complexe met les groupes de R&D du monde entier au défi d'améliorer les systèmes existants ou de proposer de nouvelles conceptions révolutionnaires.

Il y a plusieurs années, le CEA-LETI a proposé un concept non conventionnel d'écran de projection rétinienne sans lentille au plus proche des yeux. Il est basé sur un effet d'autofocalisation qui ne nécessite aucune optique mais seulement l'œil de l'observateur. Dans cette thèse, nous fournissons le contexte nécessaire pour comprendre les considérations de conception d'un tel affichage de projection rétinienne holographique non conventionnel, en décrivant l'état de l'art de la réalité augmentée et le système visuel humain (HVS). Nous expliquons ensuite le concept en détail et présentons un aperçu théorique de l'effet d'autofocalisation, qui est au cœur du concept. Notre description théorique est évaluée par des simulations et validée expérimentalement

Le document principal de cette thèse se compose de quatre chapitres et d'une conclusion.

Le chapitre I présente le contexte nécessaire, les objectifs de recherche, les défis et les contributions. L'état actuel des connaissances dans le domaine de l'affichage à proximité des yeux est décrit, ainsi que les systèmes visuels humains, et nous présentons les principaux problèmes liés à l'affichage à proximité des yeux.

Le chapitre II présente notre concept et introduit l'effet d'autofocalisation avec les notions de base liées à notre affichage non conventionnel, telles que le point émissif (EP), la distribution des points émissifs (EPD), la cellule unitaire émissive (EUC) et le spel (point élémentaire autofocalisé sur la rétine). Nous présentons les limites de conception de ce type d'affichage autofocalisé et nos tentatives pour les surmonter.

Le chapitre III décrit la première validation expérimentale de l'effet d'autofocalisation. Nous présentons notre dispositif et sa caractérisation. Les sous-chapitres décrivent essentiellement diverses expériences de validation de l'effet d'autofocalisation.

Le chapitre IV est consacré à la formation d'images non conventionnelles. Je décris le modèle double gaussien pour les simulations de formation d'images et le compare aux résultats expérimentaux. La formation d'images autofocalisées est analysée et j'introduis le paramètre γ pour évaluer la qualité de l'image en plus du rapport signal/bruit (RSB).

Dans la conclusion et les perspectives, les principaux résultats sont soulignés, avec une liste de publications et une vue d'ensemble des recherches connexes effectuées par notre groupe depuis 2018.

Je donne à la suite un court résumé de ce travail.

Description du travail effectué

Le travail de thèse a consisté dans un premier temps à l'assimilation du concept complexe de production d'image par projection rétinienne. Ce travail focalisé sur un concept originellement proposé par le CEA s'est également accompagné d'une étude bibliographique pour comprendre les contraintes particulières du domaine des lunettes intelligentes pour la réalité augmentée. Dans ce domaine, la nécessité de superposer une information digitale au monde réel nous environnant, sur un dispositif mobile, impose l'utilisation de micro-écrans. La vision confortable de ces micro-écrans nécessite l'utilisation d'un système optique complexe intégrant notamment un élément de combinaison appelé « combiner ». La formation de l'image virtuelle de l'écran par le dispositif s'accompagne de contraintes liées à la gestion des pupilles qui limitent l'angle de vision et la latitude de positionnement de l'œil tout en conduisant à des systèmes volumineux.

La compréhension de ces contraintes a été conduite en analysant les solutions alternatives de la littérature. Ces solutions se basent généralement sur des concepts d'écran conçus de manière angulaire plutôt que spatiale. La vision angulaire même si elle nous apparait moins familière est le phénomène central de la vision humaine qui perçoit les objets avant tout par leur taille angulaire.

De fait, le travail en début de thèse a consisté à la compréhension du fonctionnement de l'œil. La résolution angulaire de l'œil en zone fovéale et périphérique, sa réponse à une dynamique de signal, l'influence de la pupille, tous ces éléments ont été analysés dans le but d'optimiser notre dispositif de projection rétinienne et dans la perspective de la construction d'un dispositif d'analyse digital expérimental simulant l'œil humain.

Une grosse partie du travail de thèse a consisté à mettre en place les outils de simulations mathématiques et à confronter les résultats avec notre compréhension du dispositif.

En complément de l'approche simulation, le processus de formation des spels et de formation expérimentale d'une image a aussi été validé. Tout d'abord le montage de formation des spels a été étudié sur la base de la variation des paramètres géométriques d'alignement. La problématique de la cohérence a également été analysée expérimentalement et théoriquement.

La fin de la thèse concerne la démonstration expérimentale du processus de formation d'une image par l'effet d'auto-focalisation. Sur le nouveau montage, le point source initial est remplacé par une collection de points sources de différentes intensités qui produisent des fronts d'ondes dans différentes directions angulaires. Ces fronts d'onde produisent des spels à différentes positions sur la matrice de détection et permettent ainsi de visualiser la formation d'une image. Pour matérialiser ces points source, un micro-écran émettant à 532 nm fabriqué au laboratoire a été utilisé.

Les principaux points de cette démarche sont décrits ci-après.

Concepts

Un écran conventionnel est composé de pixels, unités élémentaires d'une surface émettrice ou d'un écran. En suivant les règles simples de l'optique géométrique, on peut trouver la projection d'un tel pixel sur la rétine à travers une combinaison de lentilles. Notre concept propose une autre approche pour projeter l'image sur la rétine. Il s'agit d'une approche non conventionnelle qui permet d'éviter un système optique entre l'œil du spectateur et l'écran. Chaque pixel d'un écran conventionnel produit un front d'onde sphérique et il existe deux approches conventionnelles pour le rendre planaire afin de permettre à l'œil de focaliser l'image sur la rétine.

La première approche consiste à placer l'écran au moins à la distance du point le plus proche (environ 25 cm pour un "œil normal"), ce qui correspond à la vision libre ou à la vision dite newtonienne.

La seconde approche concerne les écrans proches des yeux : un système optique est placé entre l'écran et l'œil pour rendre le front d'onde incident planaire ; sinon, la courbure du front d'onde produite par le pixel ne peut pas être corrigée par le cristallin de l'œil.

Il existe plusieurs solutions non conventionnelles pour concevoir un NED sans optique intermédiaire entre l'œil du spectateur et l'écran. Notre approche repose sur la combinaison de plusieurs fronts d'onde sphériques cohérents en phase provenant de points émissifs (EP) selon le principe de Huygens-Fresnel pour produire une enveloppe de front d'onde planaire. Ce front d'onde résultant est quasi-planaire et peut être focalisé par le cristallin sur la rétine sous la forme d'un motif simple autofocalisé ou spel (du français "spot élémentaire"). Nous appelons un ensemble de ces EP une distribution de points émissifs (EPD). Par conséquent, chaque spel correspond à une EPD définie, c'est-à-dire à un certain nombre de EP, et non pas simplement à un point émissif comme dans un cas conventionnel (pixel). L'orientation angulaire de chaque EP est donnée par l'indice k de son vecteur d'onde □ (figure II.4).

La Figure 2 décrit ce concept général :

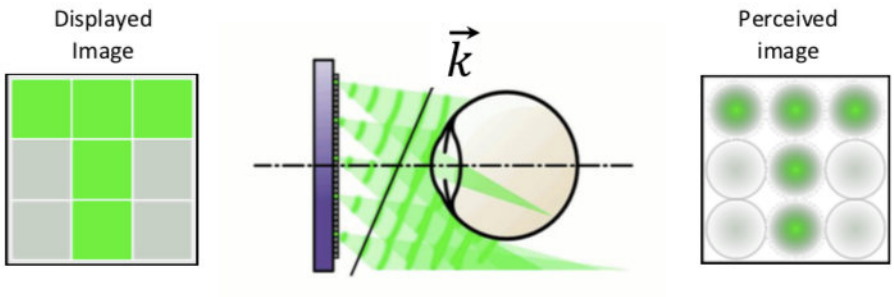

Figure 2 : Un affichage non conventionnel fonctionnant sur le principe de l'effet d'autofocalisation. Un ensemble de points émissifs répartis sur l'ouverture du système produit un faisceau d'interférence suivant une direction angulaire donnée □. Il génère un front d'onde planaire qui devient un signal de focalisation (spel) sur le plan focal après avoir traversé la lentille de l'œil

Un point fondamental est donc l'étude de la meilleure EPD possible, ce qui signifie que nous devons connaître des paramètres tels que le nombre de points émissifs et le type de distribution. La qualité d'une EPD est directement liée à ces caractéristiques. Théoriquement, le meilleure spel réalisable, correspondant à la figure d'Airy, est produite par une surface entièrement recouverte de points émissifs. Ce cas est presque identique à l'incidence de la lumière provenant de l'infini à travers une ouverture de taille égale à la surface émissive. La réduction du nombre de points émissifs nous amène à rechercher une distribution qui comporte beaucoup moins de points émissifs, mais qui, en même temps, focalise toujours une tache de qualité acceptable. Il a été démontré que les EPD de types périodiques produisent des rebonds latéraux périodiques autour de la tache centrale, tandis que les EPD aléatoires les réduisent presque à des valeurs insignifiantes, ne laissant qu'une tache centrale focalisée. Par conséquent, le nombre d'EP par EPD est un compromis entre la qualité du spel (SNR de la PSF et son pic par rapport à l'énergie de la zone environnante) et le nombre de spels possibles. C'est ce que nous appelons le conflit résolution/netteté.

Dans cette étude, j'utilise 3 types principaux de distributions avec 2 variations pour chacun d'entre eux : périodique et quasi-périodique, aléatoire et quasi-aléatoire, réaliste-aléatoire (Cross-Sinusoidal (CS) et Cross- Random-Sinusoidal (CRS)). L'acceptabilité de la conception d'un point de vue pratique est examinée. Elle devrait fournir en même temps une capacité de formation d'image adéquate en termes de qualité d'image et de nombre de pixels, ainsi que la faisabilité de la fabrication d'un tel EPD.

Une distribution réaliste cherche à imiter une distribution quasi-aléatoire qui produit la meilleure forme possible pour la formation de l'image : un pic central fin avec peu de bruit autour.

Cependant, une distribution aléatoire n'est pas réalisable du point de vue de l’adressage des EP, c'est pourquoi il faut trouver un compromis entre la distribution aléatoire et la distribution périodique. La distribution périodique est parfaitement réalisable, mais le signal produit ne peut pas être utilisé pour la formation d'images en raison d'un bruit important sous la forme de pics latéraux minces et élevés. Par simulation, on obtient les images produites par chaque type de distribution afin d'évaluer leur performance en matière de formation d'images.

Par conséquent, une distribution réaliste est un compromis entre le caractère aléatoire et la faisabilité. Les recherches durant cette thèse m'ont amené à valider expérimentalement les performances d'autofocalisation des EPD (quasi-)périodiques, (quasi-)aléatoires et réalistes.

Simulations

Sur la base de ce principe la thèse s'est donc orientée sur la partie diffractive qui constitue le phénomène physique de formation des images sur la rétine. Pour s'affranchir du dispositif optique classique entre l'œil et l'écran, notre concept repose sur un écran émettant directement des faisceaux angulaires, interprétables par l'œil.

La focalisation sur la rétine ne se fait pas par une optique externe mais par un effet de diffraction appelé autofocalisation. Cet effet repose sur l'émission d'une collection de faisceaux élémentaires, accordés en phase et émis suivant une direction angulaire commune. Leur pénétration dans la cornée et leur propagation dans le cristallin et l'humeur vitreuse produit, par interférence multiple, un point de résonnance appelé spel (spot élémentaire). La position du spel sur la rétine est définie par l'orientation d'émission de la collection de faisceaux.

La Figure 3 donne le schéma de calcul du spel par le phénomène d'interférence.

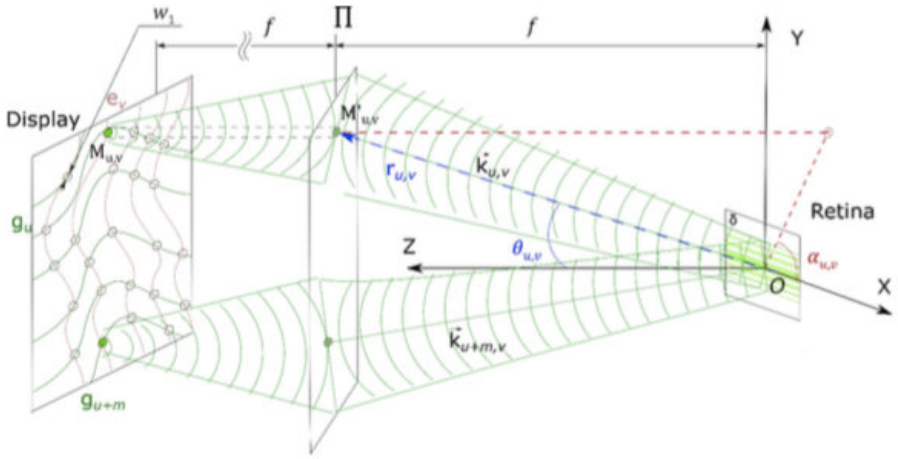

Figure 3 : Principe de simulation d'interférences multiples

A partir des outils de simulations construits au laboratoire, j'ai évalué les performances de formation des spel en fonction des distributions de point d'émission. Ces distributions sont réparties spatialement à la surface de l'écran suivant des fonctions imposées par les contraintes d'adressage de l'écran. Chaque point d'émission doit en effet pouvoir être activé ou désactivé de manière simultanée avec la distribution de points qui lui correspond. Cette activation se fait de manière électronique suivant une amplitude qui fixe l'intensité du spel produit sur la rétine. Cette problématique d'adressage optique/électronique est classique dans le domaine des écrans.

Nous avons étudié les différentes options d'adressage employées sur les écrans et avons analysé quelle évolution du type d'adressage pourrait servir au mieux notre concept. Les contraintes sur l'adressage lui ont permis de définir des fonctions de répartition de distribution de points d'émission pouvant être testées expérimentalement.

La figure 4 décrit les différentes configurations d'EPD avec une analyse de la répartition des points avec un outil d'histogramme des distances aux plus proches voisins.

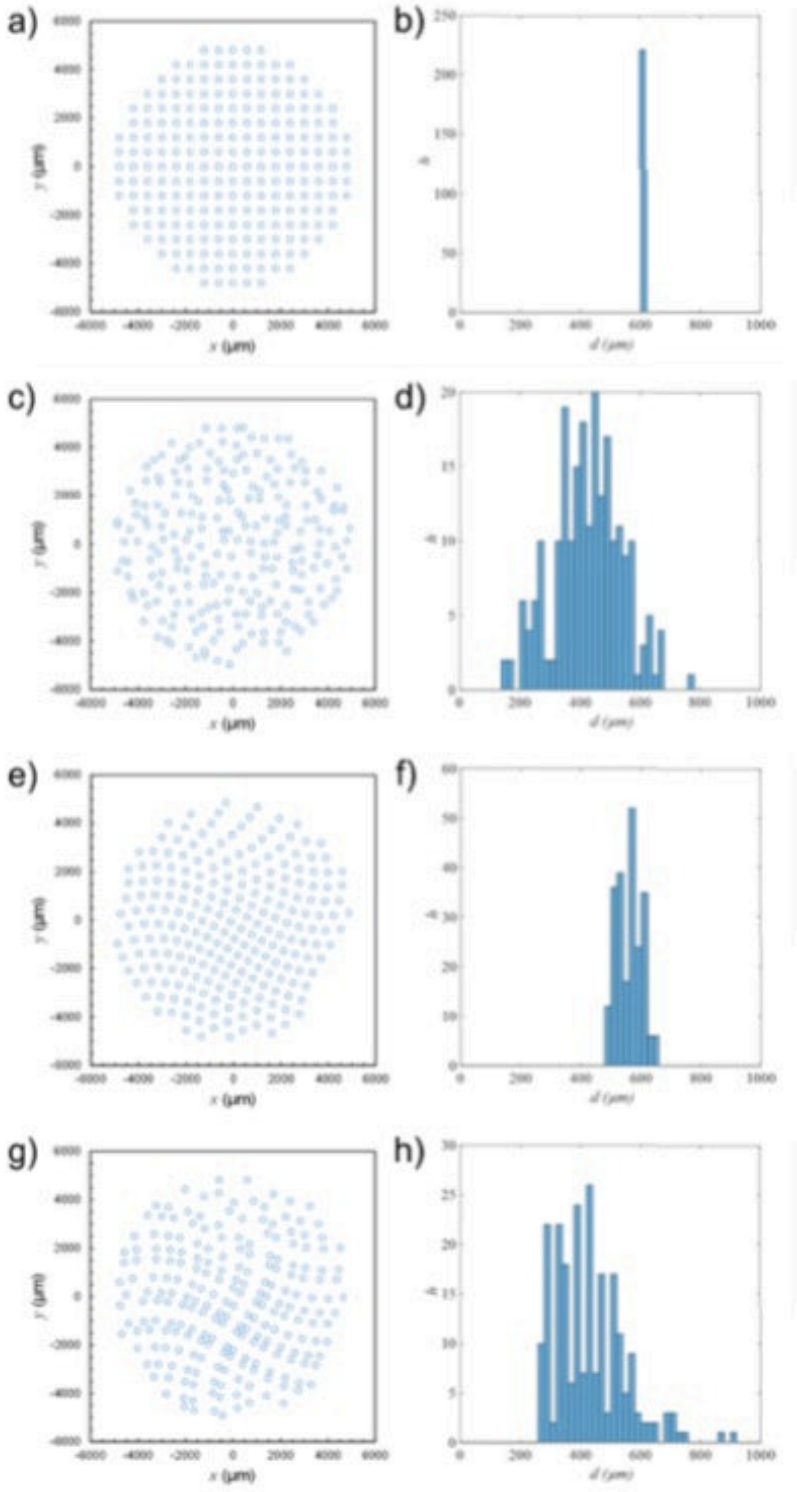

Figure 4 : Distributions calculées et leurs histogrammes de la distance la plus proche entre les EP leur plus proche voisin : (a) et (b) distribution périodique ; (c) et (d) distribution quasi-aléatoire ; (e) et (f) distribution CS ; (g) et (h) distribution CRS.

Résultats expérimentaux

De manière à confronter les résultats des simulations avec la réalité physique du procédé d'autofocalisation, un montage expérimental a été construit dans la gamme de longueur d'onde caractéristique du dispositif. Il consiste en un point d'émission de lumière laser à 532 nm placé à grande distance d'une surface opaque percée d'ouvertures. Les ouvertures permettent de simuler des points d'émission de faisceaux accordés en phase, la surface percée fait ainsi office d'écran d'émission. Un dispositif simulant l'œil vient à la suite de cette surface de manière à former un spel sur un capteur matriciel. La haute résolution du capteur permet l'analyse fine du spel, il a mis en évidence la séparation en double gaussienne.

Le montage optique se complète d'une réalisation technologique pour les distributions d'ouvertures. Suivant nos recommandations, un fournisseur extérieur a réalisé par lithographie sans masque des ouvertures calibrées sur une couche de chrome noir. Ces échantillons seront testés en diffraction et constituent des éléments de diffraction optique (DOE). Un ensemble de paramètres ont ainsi été étudiés : la taille des ouvertures, les familles de distribution avec différents degrés de répartition aléatoire et la densité d'ouverture par unité de surface. Certaines puces ont été dupliquées pour évaluer de possibles problèmes de reproductibilité technologique. Au total c'est un ensemble de 54 échantillons qui a été réalisé.

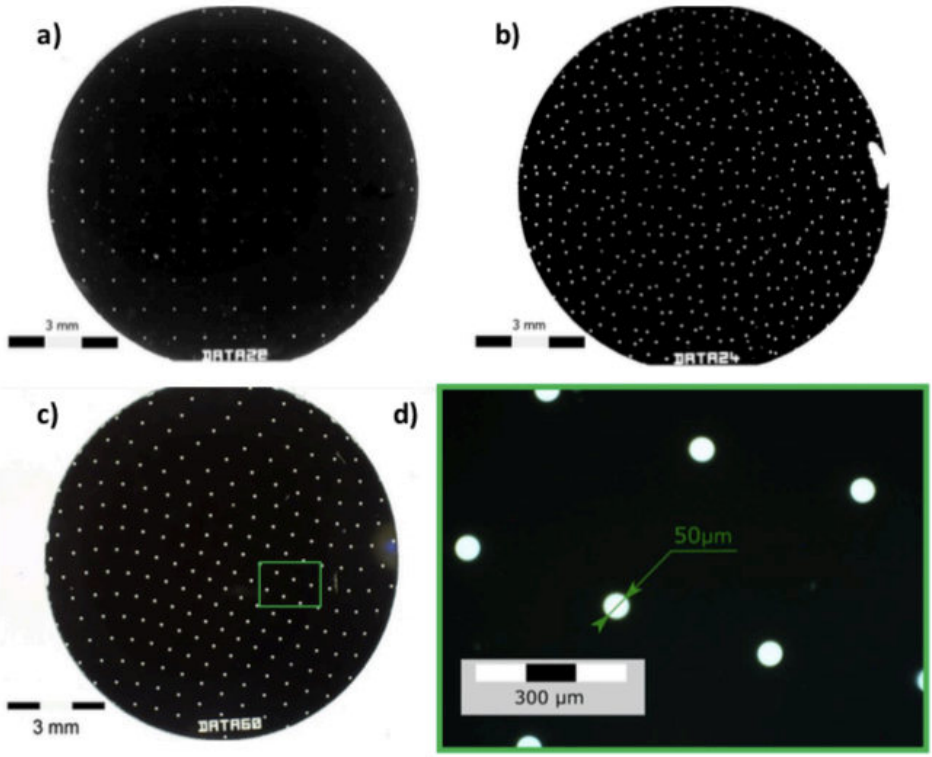

Figure 5 : Photographie de deux échantillons DOE de 10 mm de diamètre utilisés pour l'expérience, a) distribution périodique avec la période 800 µm, b) distribution quasi-aléatoire avec la période 400 µm, c) distribution réaliste (sinusoïdale croisée) avec la période 600 µm avec un détail représenté en gros plan en d), le diamètre d'ouverture est de 50 µm.

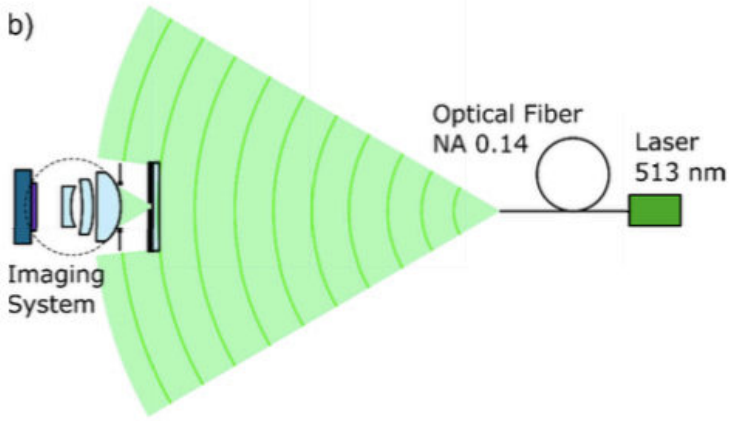

Figure 6 : Dispositif expérimental pour la validation de l'effet d'autofocalisation.

L'analyse expérimentale des échantillons (Figures 5 et 6) permet de valider le comportement du phénomène d'auto-focalisation. Il permet également de conforter les tendances apportées par les résultats des simulations.

J'ai ainsi pu démontrer expérimentalement la formation de spels avec un dispositif d'autofocalisation qui modélise le NED non conventionnel. Nous avons observé que le caractère aléatoire des distributions jouait un rôle central dans le rapport spel/bruit. La distribution quasi-aléatoire a donné les meilleurs résultats en tant que PSF pour la formation d'images, mais ce type d'EPD n'est pas réaliste du point de vue de la fabrication. Les distributions aléatoires réalistes n'ont pas le niveau d'aléatoire suffisant pour éviter des résonnances "fantômes" dans les figures de diffraction.

Il faut donc trouver un moyen d'augmenter le rapport énergétique entre le pic central et le bruit environnant. L'un des moyens possibles de réduire l'apparition de fantômes est de modifier la monochromie de la source. L'impact de la largeur de bande spectrale de la source lumineuse utilisée pour projeter l'image est étudié dans un dispositif expérimental et au moyen de simulations d'interférences multiples.

J'ai montré que l'effet d'autofocalisation est robuste et ne nécessite pas une source laser hautement cohérente. Les simulations sont effectuées avec les premières données expérimentales d'enregistrement holographique et montrent que notre concept peut être mis en œuvre avec un réseau de LED comme source primaire.

On retiendra en particulier que chaque figure de diffraction peut être considérée comme une superposition d'un pic central et de bruit environnant. Le pic central décrit comme un disque d'Airy est bien approximé par une fonction gaussienne. L'enveloppe de bruit est également ajustée à une fonction gaussienne. J'ai donc évalué les figures de diffraction observées à l'aide de deux gaussiennes, la première avec une amplitude élevée et une taille fine pour le pic, et la seconde avec une faible amplitude et une taille large pour le bruit.

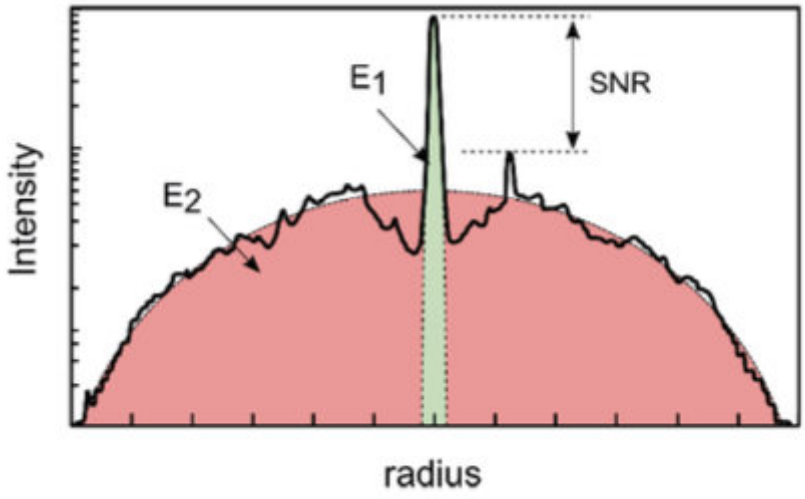

Figure 7 : Approximation d'un spel par une double gausienne

J'avais montré théoriquement comment une EPD peut être évaluée du point de vue de la localisation de l'EP. Le caractère aléatoire de la distribution et la dispersion de l'histogramme ont été caractérisés. Cette méthode donne une première vue quantitative de l'efficacité du dispositif dans le plan émissif.

Cependant, il est nécessaire de caractériser son impact sur le plan de la rétine. A l'aide d'outils de simulation de la spel sur la rétine, j'ai étudié deux paramètres pour l'évaluer de manière quantitative. Ces deux paramètres sont le SNR et le paramètre , décrits Figure 7.

Le rapport signal à bruit (Signal to Noise Ration SNR) est un rapport entre l'intensité du pic central et l'intensité la plus élevée de la zone environnante :

$$SNR = 10log\left(\frac{I_{peak}}{I_{ghost}}\right) = 10log\left(\frac{I_S(0)}{max\left(I_s(\vec{r})\right)_{r>\delta w}}\right)$$

Une autre mesure importante de la qualité du signal est le rapport entre l'énergie de crête centrale et l'énergie totale du signal, appelé paramètre γ :

$$\gamma = -10\log\left(\frac{E_1}{E_1 + E_2}\right)$$

Les résultats expérimentaux obtenus pour les EPD considérées sont synthétisés sur la Figure 8.

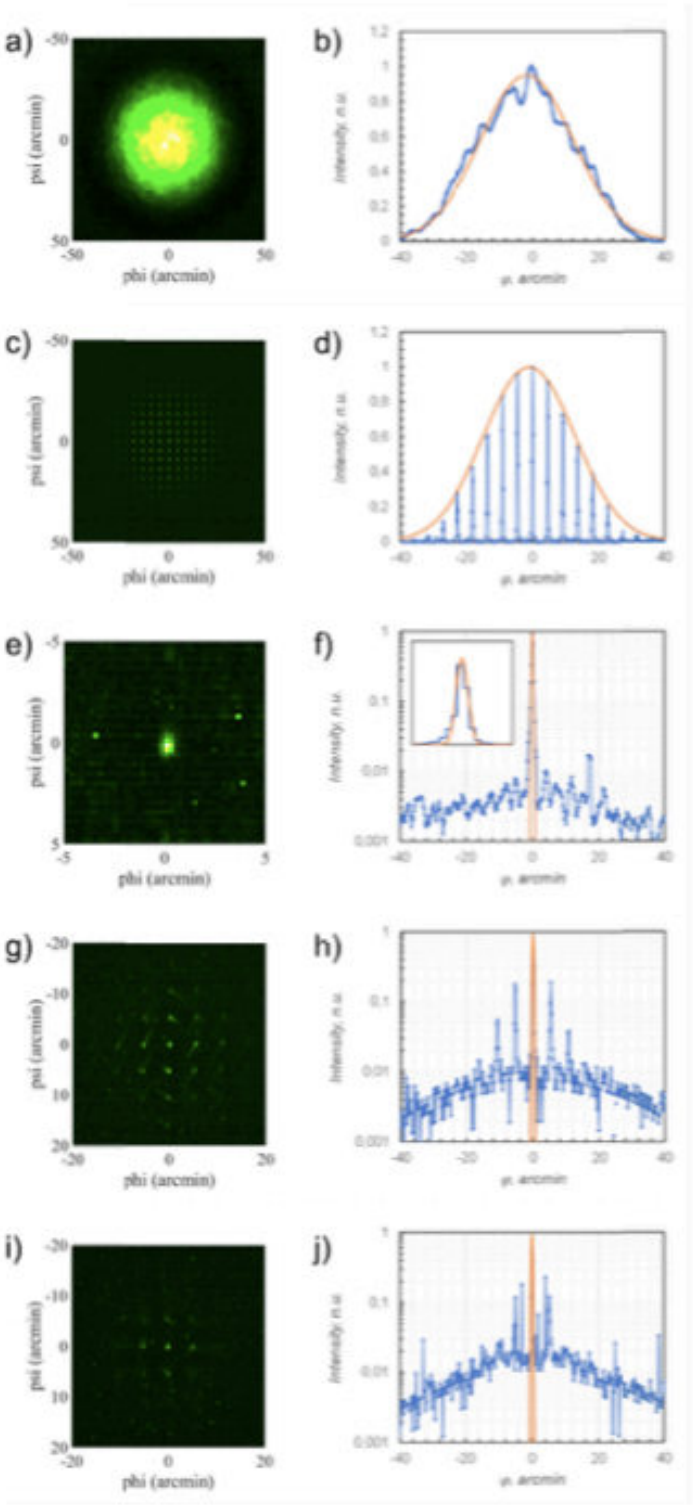

Figure 8 : Figures de diffraction produites par différentes EPD, à gauche l'image sur le capteur d'image (en fausse couleur), à droite la section transversale d'intensité comparée à une fonction gaussienne : (a) et (b) un seul EP ; (c) et (d) distribution périodique ; (e) et (f) quasi-aléatoire ; (g) et (h) CS ; (i) et j) CRS. Les figures (f), (h) et (j) sont représentées sur une échelle logarithmique. L'encadré de la figure (f) est un détail de la comparaison théorie/mesure du spel à l'échelle linéaire près de 0 arcmin.

Conclusion et perspective

La technologie associée au domaine de la réalité augmentée est un domaine dynamique fortement impacté par les limitations physiques du développement des NED. Le CEA-LETI a proposé un concept de rupture d'un tel dispositif. Cette thèse a constitué une étape pionnière dans le prototypage de projections d'images non conventionnelles. Elle était importante pour mon laboratoire d'accueil car elle était le point de départ d'une activité visant à démontrer la faisabilité d'un concept innovant. L'objectif principal du travail était la description théorique et la validation expérimentale de l'effet d'autofocalisation pour la formation de l'image du prototype NED. L'activité de recherche a été compliquée par la nécessité d'aborder un sujet qui n'avait pas encore fait l'objet d'expériences en laboratoire. Le travail a également été rendu difficile par la complexité de notre concept qui met en œuvre des notions avancées de formation d'image relativement innovantes.

J'ai étudié les effets de diffraction impliqués dans la formation de l'image rétinienne grâce à l'effet d'autofocalisation. J'ai analysé en détail ses performances en matière d'imagerie. J'ai montré la relation entre les EPD et leurs spels. J'ai évalué la qualité de la formation des spels, simulé la projection autofocalisante de notre concept et l'ai analysée en introduisant un paramètre γ de qualité de la formation des spels. J'ai mis en place un dispositif expérimental pour valider les résultats théoriques que j'ai obtenus avec l'algorithme de simulation de l'autofocalisation. J'ai simulé l'imagerie non conventionnelle avec une approche simplifiée de la formation de spel appelée modèle double gaussien (DG) et je l'ai validée expérimentalement avec un dispositif. J'ai décrit un conflit résolution/netteté comme une contrainte naturelle pour le prototype d'affichage.

Les principaux résultats ont été présentés dans plusieurs conférences : deux posters au congrès OSA Imaging and Applied Optics 2016 à Heidelberg et 2017 à San-Francisco, un exposé oral à SPIE Photonics Europe en 2018. Mes résultats ont contribué à l'article d'Optica qui décrit le principe général du concept d'affichage rétinien en 2018. Les principaux résultats expérimentaux et de simulation de mon travail ont été publiés dans Optics Express en 2019.

Dans l'ensemble, la validation expérimentale de l'effet d'autofocalisation a ouvert la voie à des recherches massives et approfondies dans notre laboratoire. Le prototypage du NED implique une association complexe de photonique intégrée et d'holographie. Basile Meynard puis Kyllian Millard ont conçu et caractérisé des systèmes photoniques intégrés (PIC) pour ce concept. Matthias Colard a étudié les éléments d'activation pour les hologrammes pixellisés et a étudié les architectures d'extraction combinant des circuits intégrés photoniques et des cristaux liquides biréfringents. Fabien Rainouard a étudié les stratégies d'adressage optimales à l'aide de modèles mathématiques.

LISTE DE TRAVAUX ET PUBLICATION RESULTANTS DE CE TRAVAIL DE THESE

Posters dans des conferences internationales

"Multiple beam diffractive setup for intraocular accommodation evaluation,"
V. Krotov, C. Martinez, and O. Haeberlé,
Imaging and Applied Optics 2016, OSA Technical Digest (online) (Optical Society of America, 2016), paper JT3A.32.

"Lens-Free Near-Eye Intraocular Projection Display, Concept and First Evaluation,"
C. Martinez, **V. Krotov**, D. Fowler, and O. Haeberlé
Imaging and Applied Optics 2016, OSA Technical Digest (Optical Society of America, 2016), paper CW1C.5

"Imaging Performance Analysis of a Lens-Free Near to Eye Display,"
V. Krotov, C. Martinez, and O. Haeberlé,
Imaging and Applied Optics 2017 (3D, AIO, COSI, IS, MATH, pcAOP), OSA Technical Digest (online) (Optical Society of America, 2017), paper JTu5A.5.

"Holographic Recording Setup for Integrated See-Through Near-Eye Display Evaluation,
C. Martinez, **V. Krotov**, and D. Fowler,
Imaging and Applied Optics 2017, OSA Technical Digest (Optical Society of America, 2017), paper JTu5A.36

Présentation orale dans des conférences internationales avec actes

"Experimental evaluation of self-focusing image formation in nonconventional near-eye display", C. Martinez, **V. Krotov** and O. Haeberlé, in Digital Optics for Immersive Displays 2018 (SPIE Photonics Europe, Strasbourg-France, 22 - 26 April 2018) [paper 10676-22]

Articles de journaux avec comité de lecture

“See-through holographic retinal projection display concept”,
C. Martinez, **V. Krotov,** B. Meynard and D. Fowler,
Optica 5, pp.1200-1209 (2018)

“Experimental validation of self-focusing image formation for retinal projection display”
V. Krotov, C. Martinez, and O. Haeberlé
Opt. Express 27, pp. 20632-20648 (2019)